

**CONTROLLED SYNTHESIS OF METAL  
OXIDE BASED FUNCTIONAL AND  
BIFUNCTIONAL NANOPARTICLES AND  
THEIR APPLICATIONS.**

**A THESIS SUBMITTED TO THE  
UNIVERSITY OF PUNE  
FOR THE DEGREE OF DOCTOR OF PHILOSOPHY**

**IN  
CHEMISTRY**

**BY  
SUBAS KUMAR MUDULI**

**DR. K. VIJAYAMOHANAN  
(RESEARCH GUIDE)**

**DR. SATISHCHANDRA B. OGALE  
(RESEARCH CO-GUIDE)**

**PHYSICAL AND MATERIALS CHEMISTRY DIVISION  
NATIONAL CHEMICAL LABORATORY  
PUNE – 411 008  
INDIA**

**JUNE 2011**

TO  
ALMIGHTY,  
MY PARENTS  
AND  
MY LOVELY WIFE





राष्ट्रीय रासायनिक प्रयोगशाला  
(वैज्ञानिक तथा औद्योगिक अनुसंधान परिषद)  
डॉ. होमी भाभा रोड, पुणे - 411 008. भारत  
**NATIONAL CHEMICAL LABORATORY**  
(Council of Scientific & Industrial Research)  
Dr. Homi Bhabha Road, Pune - 411008. India



## CERTIFICATE

This is to certify that the work presented in the thesis entitled **“CONTROLLED SYNTHESIS OF METAL OXIDE BASED FUNCTIONAL AND BIFUNCTIONAL NANOPARTICLES AND THEIR APPLICATIONS”** by **SUBAS KUMAR MUDULI**, submitted for the degree **Doctor of Philosophy in Chemistry** was carried out under our supervision at the Physical and Materials Chemistry Division, National Chemical Laboratory, Pune, 411008, India. All the materials from other sources have been duly acknowledged in the thesis.

Dr. K. Vijayamohan  
(Research Guide)

Dr. Satishchandra B. Ogale  
(Research Co-Guide)

Date :

Place : Pune

Communications Channels  
+91 20 25902000  
+91 20 25893300  
+91 20 25893400

Fax +91 20 25902601 (Director)  
+91 20 25902660 (Admin.)  
+91 20 25902639 (Business Development)

URL : [www.ncl-india.org](http://www.ncl-india.org)

## **DECLARATION**

I hereby declare that the thesis entitled “**CONTROLLED SYNTHESIS OF METAL OXIDE BASED FUNCTIONAL AND BIFUNCTIONAL NANOPARTICLES AND THEIR APPLICATIONS**” submitted for the degree Doctor of Philosophy in Chemistry to the University of Pune, has been carried out by me at the Physical and Materials Chemistry Division of National Chemical Laboratory, Pune under the joint supervision of Dr. K. Vijayamohan and Dr. Satishchandra B. Ogale. Such material as has been obtained by other sources has been duly acknowledged in this thesis. The work is original and has not been submitted in part or full by me for any other degree or diploma to other University.

Date:  
National Chemical Laboratory  
Pune – 411 008

Subas Kumar Muduli  
(Research Student)

## *Acknowledgements*

*There are so many people, whose support, encouragement and inspiration are very much obligatory to accomplish major achievements in life, especially, if it involves the elements of fulfilling one's cherish dreams. For me, this thesis is such an important destiny and I am indeed indebted to lot of people for their well wishes and blessings for completing this journey. I take this opportunity to acknowledge and extend my sincere gratitude towards all those people who have been involved, directly or indirectly, to make the research work described in this thesis possible.*

*I would like to express my deep sense of gratitude to Dr. K. Vijayamohan for giving me an opportunity to pursue Ph.D. with him. I am always indebted for his scientific advice, trust, continuous support, and co-operation during the course of this work. I am very fortunate to have been associated with him and to have learnt several things from him.*

*I would also like to offer my sincere admiration to my co-guide Dr. Satishchandra B. Ogale for all his help, support, suggestion and advice during the course of this study. His innovating thinking and high spirited attitude have inspired me to conduct and complete my doctoral research. He has not only grafted my scientific skills and knowledge but also moulded me into a better human being. I thank him for this endless support filled with patience and enthusiasm during my whole tenure of PhD. I feel very fortunate to be able to learn lots of things from him.*

*I wish to thank Dr. S. Sivram, former Director of NCL, Dr. Sourav Pal, Director, NCL and Dr. Anil Kumar, HOD, Physical and Materials Chemistry Division, for providing the infrastructure and facilities for the research. I thank CSIR, Govt. of India, for my research fellowship.*

*My heartfelt gratitude to Dr. B.L.V. Prasad, Dr. P. Poddar, Dr. I. S. Mulla, Dr. V. Ravi, Dr. P. A. Joy, Dr. Absar Ahmad, Dr.(Mrs.) Joti Jog & Mrs. Suguna Adhyantaya for their advice & help. I am highly indebted to Dr. K.R. Patil, Mr. Gholap, Mrs. Rupali & Mr. Gaikwad for helping me a lot in characterising my samples. Timely help from Mr. Dipak, Mr. Punekar & the entire library staff for excellent facilities is gratefully acknowledged. I wish to acknowledge all my teachers from primary schools to master's level who educated and nurtured me academically to reach at this destiny. Special thanks are due to all collaborators Dr. B. B. Kale, Dr. Seema Verma, Dr. V. Ravi, and Dr. S. N. Kale. I also take this opportunity to thank all*

*our international collaborators Prof. Sung-Hwan Han, Prof. Beatrice Hannover, Prof. Wegdan Ramadan and Dr. Won-joo Lee.*

*I can never forget the help from my seniors, Dr. Hrushikesh, Dr. Sneha, Dr. Kashinath, Dr. Rajesh, Dr. Sarfaraj, Dr. Anup, Dr. Tushar, Dr. Balchandra, Dr. Mahima, Dr. Meera, Dr. Kanan, & Dr. Bhaskar for their mentoring & care during my initial research days. A special thanks to all my labmates Vivek, Abhimanu, Prasad, Guru, Onkar, Vishal, Datta, Abhik, Rohan, Pradeep, Dr. Parvez, Anil, Pravarthana, Meenal, Shruti, Mandakini, Reshma, Puja, Shradha, Dr. Sarika, Anirudh, Dhanya, Harish Sir, Ashish Sir & Dr. Hema Singh who have helped me in all possible ways & created a cheerful and cooperative atmosphere during the tenure of my work at NCL. I will always cherish memories of these days with you people.*

*I would also like to express my sincere thanks to all my divisional colleagues Dr. Atul, Dr. Shekhar, Jayasis, Dhanraj, Dr. Deepti, Dr. Manasi, Dr. Priyanka, Dr. Vijay, Mangesh, Pankaj, Nagesh, Sudarsan, Dr. Sanjay, Dr. Umesh, Dr. Imran, Dr. Ramya, Dr. Sheetal, Dr. Maggie, Adish, Dr. Pratap, Vilas, Anal, Ravi, Prakash, Anil, Raja, for their friendly interactions. I also extend my thanks to several other friends in NCL, Dr. Seetaram, Dr. Sabita, Dr. Gokarneswar, Dr. Rosy, Dr. Suman, Dr. Sivaram, Dr. Sashi, Dr. Bhuban, Dr. Ramakanta, Dr. Atulkumar, Dr. Pitambar, Chakadola, Jeetu, Raju and Pushpanjali for their valuable help & support.*

*As always, it is impossible to mention everybody who had an impact on this work although there are those whose spiritual support is even more important. I find no words to express my feelings for my parents, whose moral support, blessings, love, sacrifice, care & constant encouragement throughout my life. This thesis is also a culmination of a dream for my elder brother Sushant whose support has always played a key role in my career. I wish to extend my sincere gratitude to my grandfather, late grandmother & all other relatives for their blessings & love. Finally, a very special appreciation is due to my lovely wife G. S. Karubaki not only for her constant encouragement but also for her patience, unconditional love & understanding throughout.*

*Subas Kumar Muduli*

## List of Abbreviations

1-D	One-Dimensional
2-D	Two-Dimensional
3-D	Three-Dimensional
AFM	Atomic Force Microscopy
AM	Air Mass
BE	Binding Energy
BET	Brunauer Emmett Teller
BSE	Backscattered Electrons
CA	Citric Acid
CB	Conduction Band
CIS	CuInSe <sub>2</sub>
CIGS	Cu(In,Ga)Se <sub>2</sub>
CNTs	Carbon nanotubes
CVD	Chemical Vapor Deposition
DMS	Diluted Magnetic Semiconductor
DOS	Density of States
DRS	Diffuse Reflectance Spectroscopy
DSSC	Dye Sensitized Solar Cell
EDX/EDS	Energy Dispersive Analysis of X-rays
EIS	Electrochemical Impedance Spectroscopy
ESCA	Electron Scanning for Chemical Analysis
FESEM	Field Emission Scanning Electron Microscope
FF	Fill Factor
FTIR	Fourier Transform Infra-red
FTO	Fluorine doped Tin oxide
FWHM	Full Width at Half Maximum
HMT	Hexamethylene tetramine
HOMO	Highest Occupied Molecular Orbital
HRTEM	High Resolution Transmission Electron Microscope
IPCE	Incident photon-to-current conversion efficiency
ITO	Indium doped Tin Oxide
J <sub>sc</sub>	Short circuit current density

LHE ( $\lambda$ )	Light harvesting efficiency at wavelength $\lambda$
LUMO	Lowest Unoccupied Molecular Orbital
LED	Light Emitting Diodes
MWCNTs	Multi-Walled Carbon Nanotubes
NPs	Nanoparticles
ODA	Octa-decyl Amine
PL	Photo-luminescence
PLD	Pulsed Laser Deposition
$P_{\max}$	Maximum power
PVP	Polyvinyl Pyrrolidone
QDs	Quantum Dots
SAED	Selected Area Electron Diffraction
SAM	Self-Assembled Monolayers
SCF	Supercritical Fluid
SCW	Supercritical Water
SE	Secondary Electrons
STM	Scanning Tunnelling Microscope
SPM	Scanning Probe Microscopy
SWCNTs	Single Walled Carbon Nanotubes
TIP	Titanium tetra isopropoxide
TMO	Transition Metal Oxide
TEM	Transmission Electron Microscope
UV-VIS-NIR	Ultraviolet-Visible-Near TON Turn Over Number
XPS	X-ray Photoelectron
XRD	X-ray Diffraction
VB	Valence Band
$V_{oc}$	Open circuit potential
TCO	Transparent Conducting Oxide
ZFC-FC	Zero Field Cooled-Field Cooled

# Table of Contents

<b>1</b>	<b>Chapter-1: Introduction</b>	<b>1-44</b>
1.1	Preamble	2
1.2	Properties of Nanomaterials	5
1.2.1	Surface effects	5
1.2.2	Electronic properties	6
1.2.3	Optical properties	8
1.2.4	Magnetic properties	11
1.2.5	Mechanical properties	12
1.2.6	Melting point	13
1.3	Metal Oxide Nanomaterials	13
1.3.1	Titanium Dioxide (TiO <sub>2</sub> )	14
1.3.2	Zinc oxide (ZnO)	17
1.4	Applications of Nanomaterials	19
1.4.1	Solar Cell Application (Clean Energy)	19
1.4.1.1	Dye-sensitized Solar cells (DSSC)	22
1.4.1.2	A history with photography	22
1.4.1.3	Basic principles of dye-sensitized solar cells	24
	A concept of 'excitonic' solar cell	
1.4.1.4	Electron transfer processes in DSSC	27
1.4.1.5	Photovoltaic Cell Performance	29
1.4.1.6	Structure of DSSC	30
1.5	Objective and outline of the thesis	35

1.6	References	36
<b>2</b>	<b>Chapter-2</b>	<b>45-74</b>
	<b>Synthesis and Characterizations Techniques</b>	
2-I	Section-I	46
	Synthesis Technique	
2-I.1	Hydrothermal methods	47
2-I. 2	Sol-gel technique	50
2-I. 3	Co-Precipitation Method	52
2-I. 4	Fabrication of Dye Sensitized Solar Cells	52
2-II	Section-II	54
	Materials Characterisation Techniques	
2-II. 1	X-ray diffraction (XRD)	54
2-II. 2	UV-VIS Spectroscopy	56
2-II. 3	Raman Spectroscopy	58
2-II. 4	Fourier Transform IR Spectroscopy	60
2-II. 5	Transmission electron microscopy (TEM)	61
2-II. 6	Scanning Electron Microscope (SEM)	63
2-II. 7	Dye sensitized solar cells (DSSC) characterization	65
2-II. 7. 1	Solar Simulator	67
2-II. 7. 2	Solar Cell Efficiency Measurements	68
2-II. 7. 2 .1	Open-circuit voltage (Voc)	69
2-II. 7. 2 .2	Short-circuit current (I <sub>sc</sub> )	70
2-II. 7. 2 .3	Fill factor (FF)	70
2-II. 7. 2. 4	Solar-to-electric-power conversion efficiency ( $\eta$ )	71
2-II. 7. 3	Incident photon-to-current conversion efficiency	71

(IPCE) Measurements

2-II. 7. 4	Electrochemical Impedance Spectroscopy (EIS)	72
2-III	References	73
<b>3</b>	<b>Chapter-3</b>	<b>75-89</b>
	<b>Semiconductor-Metal (TiO<sub>2</sub>-Au) Nanocomposites for DSSC</b>	
3.1	Introduction	76
3.2	Experimental Methods	77
3.2.1	Preparation of TiO <sub>2</sub> -Au Nanocomposite	77
3.2.2	Characterization	77
3.2.3	Measurements	78
3.3	Results and Discussion	78
3.4	Conclusions	88
3.5	References	88
<b>4</b>	<b>Chapter-4</b>	<b>90-120</b>
	<b>TiO<sub>2</sub>-MWCNTs/Graphene Nanocomposites for DSSC application</b>	
4.1	Introduction	91
4-I	Section-I	92
	TiO <sub>2</sub> -MWCNTs Nanocomposites	
4-I.1	Introduction	92
4-I.2	Experimental	94
4-I.2.1	Materials	94
4-I.2.2	Preparation of TiO <sub>2</sub> -MWCNT nanocomposite	94
4-I.2.3	Characterization	94
4-I.2.4	Measurements	95
4-I.3	Results and Discussion	95

4-I.3.1	Crystal Structure of TiO <sub>2</sub> -MWCNTs nanocomposite	95
4-I.3.2	Morphological Characterization	98
4-I.3.3	FT-IR spectra	100
4-II	Section-II	106
	TiO <sub>2</sub> -Graphene Nanocomposites	
4-II.1	Introduction	106
4-II.2	Experimental	107
4-II.2.1	Preparation of TiO <sub>2</sub> -Graphene nanocomposite	107
4-II.2.2	Characterization techniques	107
4-II.2.3	I-V Measurements	108
4-II.3	Results and Discussion	108
4-II.3.1	X-ray Diffraction	108
4-II.3.2	Raman Spectroscopy	109
4-II.3.3	Transmission Electron Microscopy (TEM) Data	110
4-II.3.4	Atomic Force Microscopy (AFM) Study	111
4.2	Conclusions	114
4.3	References	115
<b>5</b>	<b>Chapter-5</b>	<b>121-156</b>
	<b>TiCl<sub>4</sub> Treatment of TiO<sub>2</sub> and ZnO</b>	
5-I	Section-I	122
	TiCl <sub>4</sub> treatment of TiO <sub>2</sub> Nanoparticles for DSSC	
5-I.1	Introduction	122
5-I.2	Experimental Method	122
5-I.3	Results and discussion	123
5-II	Section-II	129

ZnO based DSSC	
5-II.1	Introduction 129
5-II.2	Experimental Method 130
5-II.2.1	Synthesis of ZnO nanoflowers by hydrothermal method 130
5-II.2.2	Preparation of ZnO nanostructures by using different capping Agents 130
5-II.2.3	Fabrication of dye-sensitized solar cell 130
5-II.3	Characterization 131
5-II.4	Results and discussions 131
5-III	Section-III 134
	TiCl <sub>4</sub> Treatment of ZnO Mesostructures for Shape Preserving Chemical Transformations for DSSC Applications
5-III.1	Introduction 134
5-III.2	Experimental Section 136
5-III.2.1	Preparation of ZnO Flowers 136
5-III.2.2	Preparation of ZnO rods on FTO and ITO 136
5-III.2.3	Preparation of ZnO spheres and flakes 137
5-III.2.4	Preparation of TiO <sub>2</sub> Nanoparticles 137
5-III.2.5	Fabrication of dye sensitized solar cell 138
5-III.2.6	TiCl <sub>4</sub> Treatment of ZnO Structured Films 138
5-III.3	Characterization 139
5-III.4	Results and discussions 139
5-III	Conclusions 152
5-IV	Reference 152

<b>6</b>	<b>Chapter-6</b>	<b>157-162</b>
	<b>Conclusions and Future Scope</b>	
6.1	Summary of the thesis	158
6.2	Scope for future work	159
<b>7</b>	<b>List of Publications</b>	<b>161</b>
<b>8</b>	<b>Patents</b>	<b>162</b>

# **Chapter-1**

## **Introduction**

*This chapter presents the premise of the thesis. It introduces the field of nanotechnology, in general with an emphasis on the unique properties of nanomaterials followed by portrayal of their applications. The main focus of this thesis is metal oxide nanomaterials for Dye Sensitized Solar Cell application; therefore a brief history of solar cells and the relevant metal oxide nanomaterial systems has been presented. In the end, the chapter summarizes the outline-- the chapter wise division, of the thesis.*

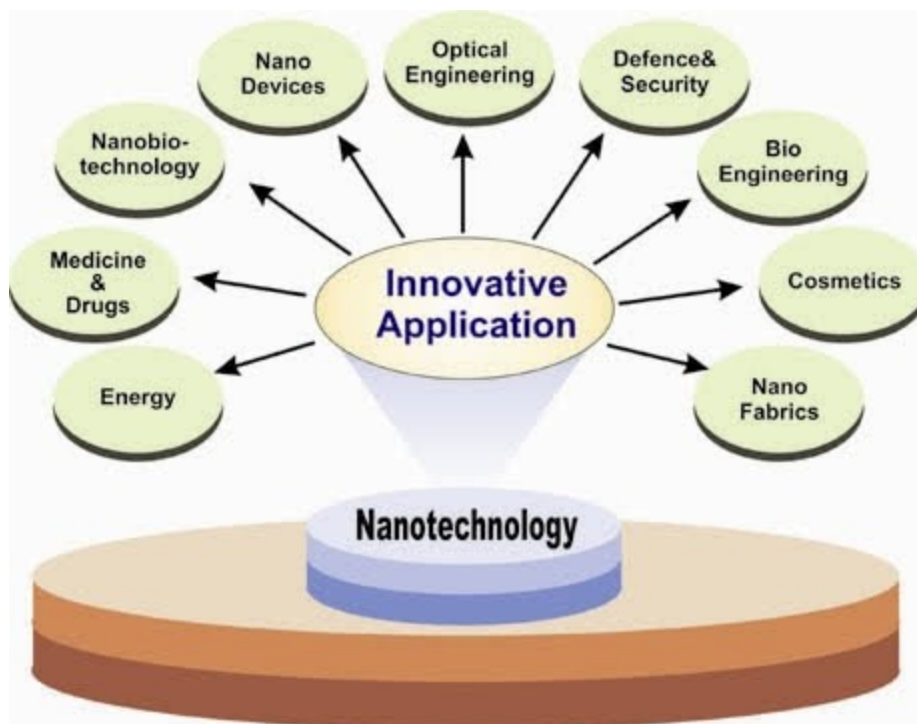


*Figure-1.1 Different applications of Nanotechnology [1].*

## 1.1 Preamble

Nanotechnology, which exploits materials of dimension smaller than 100 nm, possesses tremendous potential to address many scientific and technological challenges, faced by mankind in a variety of fields as described in figure 1.1. This is in accord with Richard Feynman's speech back in 1959, when he described a vision – “to synthesize nanoscale building blocks with precisely controlled size and composition, and assemble them into larger structures with unique properties and functions” [2]. This vision has sparked the imagination of a generation of researchers. Nowadays, this small word ‘Nano’ has become so famous that almost every common person in the society knows ‘Nano’ being something to be ‘very small’ although only few of them know its actual meaning. Actually ‘Nano’ is a Greek word; meaning dwarf. Mathematically a ‘Nano’ means one billionth. Thus,  $1 \text{ nm} = 10^{-9} \text{ m}$ . To get a sense of the nano scale, a human hair measures 80,000 nanometers across or just ten hydrogen atoms in a line make up one nanometer. The thing, which is smaller than a nanometer in size, is just a loose atom or small

molecule floating in space. Thus, in practice nanostructures are the smallest solid things, which are practically possible to make or ever has made. Any engineered object with at least one of its dimensions less than 100 nm is called as a ‘Nanomaterial’. In fact, the nanoscale is unique because it is in the range of the size where the familiar everyday materials properties dominated by quantum mechanical phenomena causing these materials to display many novel and interesting electrical, optical, electronic, magnetic and chemical properties usually not achieved by their bulk counterparts. An overview of the typical dimensional ranges of various materials approaching the nanosize region is shown in figure 1.2.

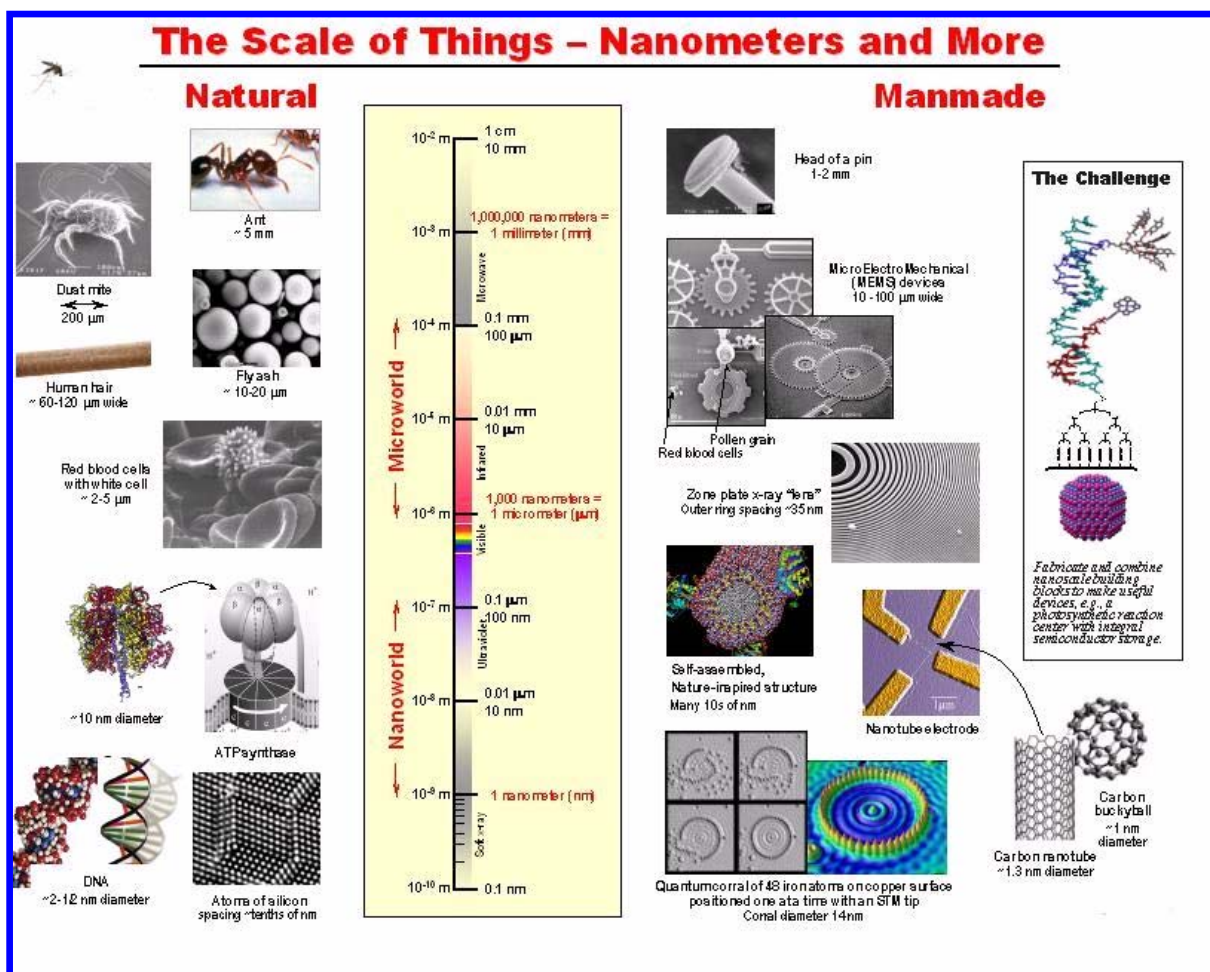
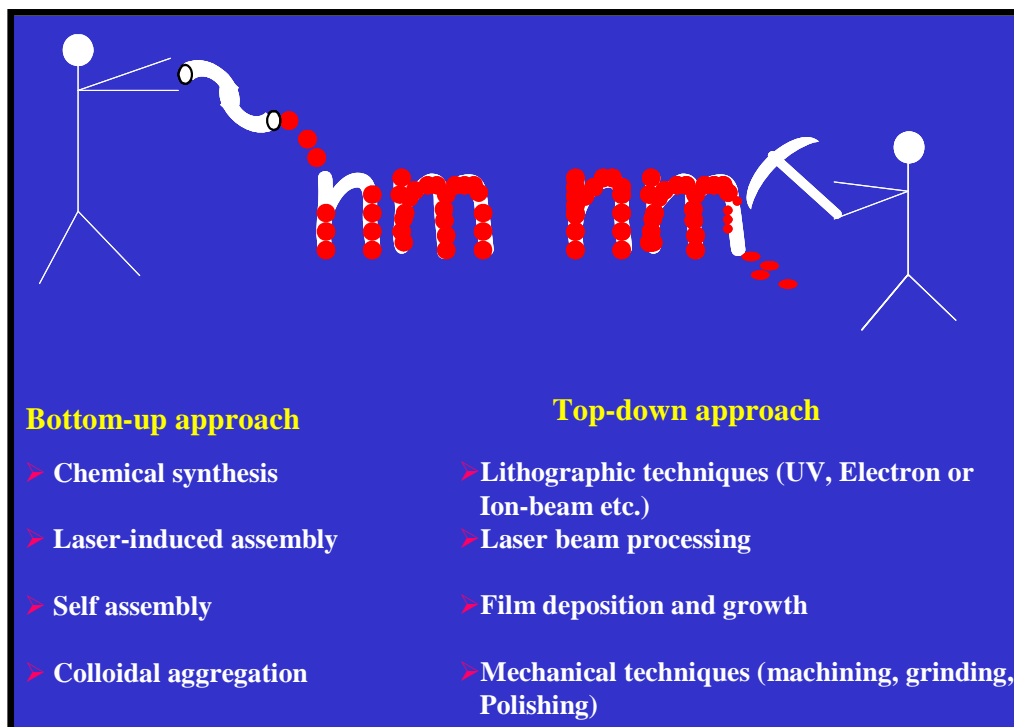


Figure-1.2 Naturally occurring and manmade materials. [[www.understandingnano.com](http://www.understandingnano.com)]

Last two decades evidenced the exponential growth of activities in the field of nanoscience research. During the last few years, there has been a more directional effort towards the controlled synthesis of inorganic/organic nanomaterials of specific sizes, different shapes and stoichiometric compositions. The projected potential in this respect has led to a significant growth of activity in the fields of a) reproducible growth of nanomaterials with different uniform compositions and controlled shapes and sizes, b) their systematic studies by different reliable techniques such as SPM, TEM, various spectroscopy techniques etc. and c) exploration of these nanomaterials for novel potential technological applications.



**Figure-1.3** Schematic showing Nanostructure synthesis approaches with classifications.

The first task in this direction is the synthesis of nanomaterials. There are two broad approaches to synthesize nanomaterials viz. Top-Down and Bottom-Up approach as shown in figure 1.3. Top-Down approach mainly involves the physical processes for nanomaterials synthesis. This approach can make nanomaterials in large quantities but with less control on the size, shape and uniformity in composition. Bottom-Up approach

mainly involves colloidal chemical synthesis methods and self-assembly. This approach can produce nanomaterials with uniform compositions and controlled size/shapes although the yield of such a reactions is relatively low.

In order to exploit the potential of the synthesized nanomaterials effectively, it is that they must be of same size and shape since their properties are largely size and shape dependant. Thus, to synthesize nanomaterials of same size and shape while maintaining their compositional uniformity, it is crucial for to understand the actual nanomaterial formation kinetics and their synthesis mechanism. A thorough understanding of nanomaterials formation kinetics and synthesis mechanism will help to engineer the nanoparticles growth to uniform and controlled size, shape, and composition. Moreover, it is still difficult to synthesize the uniformly doped nanomaterials, nanocomposites/core/shells and multi-component complex nanomaterials.

It is expected that these uniformly size and shaped nanomaterials will find important applications in areas including energy (solar cells, water splitting), environment (photocatalysis, sensing) and biomedicine (hyperthermia, biolabelling).

## 1.2 Properties of Nanomaterials

### 1.2.1 Surface effects

The surface atoms of a particle have fewer adjacent coordinating atoms as compared to the core atoms. So, the surface atoms are more active than the core atoms. Due to this, surface of a material determines the material characteristics like light emission, solubility etc. As the size of the particle decreases, a larger number of its constituent atoms occupy the surface (shown in figure 1.4). The reason behind this can be understood from a simple calculation given below.

Consider a spherical particle of radius “r”,

$$\text{Surface area of the particle} = S = 4\pi r^2$$

$$\text{Volume of the particle} = V = (4/3) \pi r^3$$

$$\text{So, the surface to volume ratio} = (S/V) = (3/r)$$

As can be seen, the surface to volume ratio is inversely proportional to 'r'. So, as the size of the particle decreases, the surface effects become more prominent.

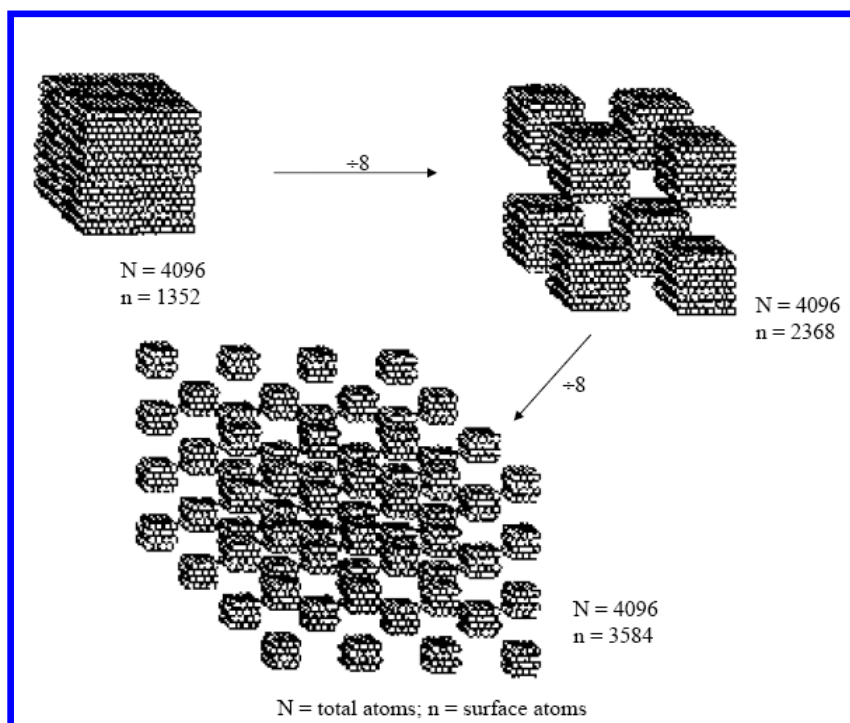


**Figure-1.4** Decrease in the particle size leads to increase in surface to volume ratio of the nanoparticles [3, 4].

### 1.2.2 Electronic properties

Electronic structures of nanoparticles are very different from their bulk form as illustrated in figure 1.5(a) and (b). Nanocrystals lie in between the atomic/molecular limit of discrete density of electronic states and the bulk crystalline limit of continuous bands. At given temperature, size- dependant property variations occur significantly in semiconductors, as compared to metals, insulators, and van-der Waals or molecular crystals. In each case, the density of states is discrete at the band edges. Because we know bands of a solid are centered about atomic energy levels, with the width of the band related to the strength of the nearest neighbor interactions. As a function of increasing size, the center of a band develops first and the edges develop last. In the case of Vander-Waals or molecular crystals, the nearest-neighbor interactions are weak and the bands in the solid are very narrow, and as a consequence not much size variation in optical or electrical properties is expected or observed in the nanocrystal regime.

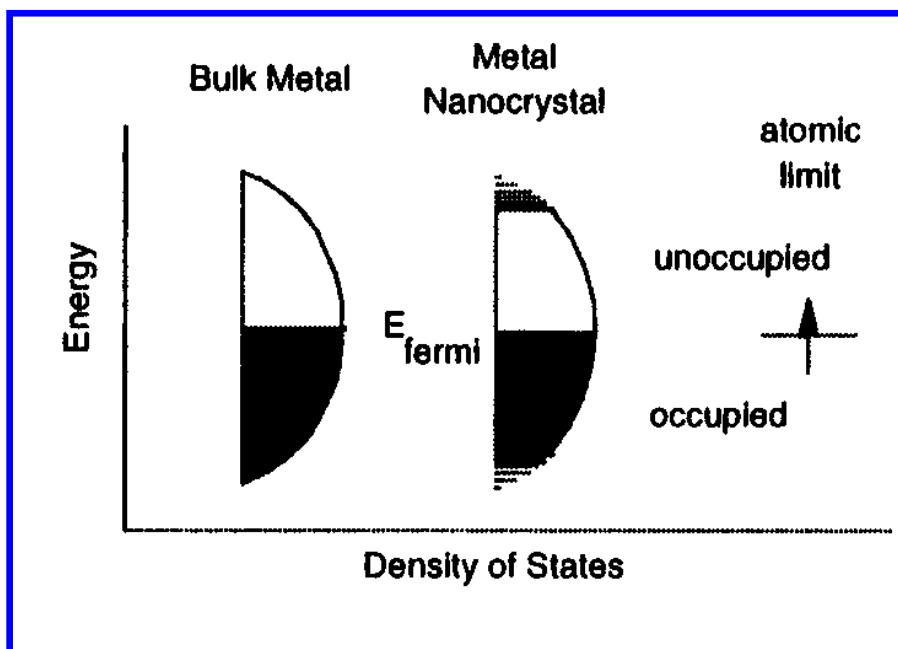


**Figure-1.5(a)** Comparative electronic structures of metals in bulk form, nano form and isolated atoms [5].

In metals, the band gap is zero and Fermi level lies in the center of a band, thus relevant energy level spacing is negligible, and at temperatures above a few kelvin, the electrical and optical properties more closely resemble to those of a continuum, even in relatively small sizes (tens or hundreds of atoms) [6]. When a metal is divided finely, the continuum of the electronic states breaks down. The discreteness of the energy levels can be measured in terms of average spacing between the successive quantum levels namely Kubo gap. Such changes come under the so-called quantum size effects [7, 8]. As the size of metal nanocrystals is reduced, they can show insulating behavior due to the changes in the electronic structure. This transition is called the size-induced metal–insulator transition.

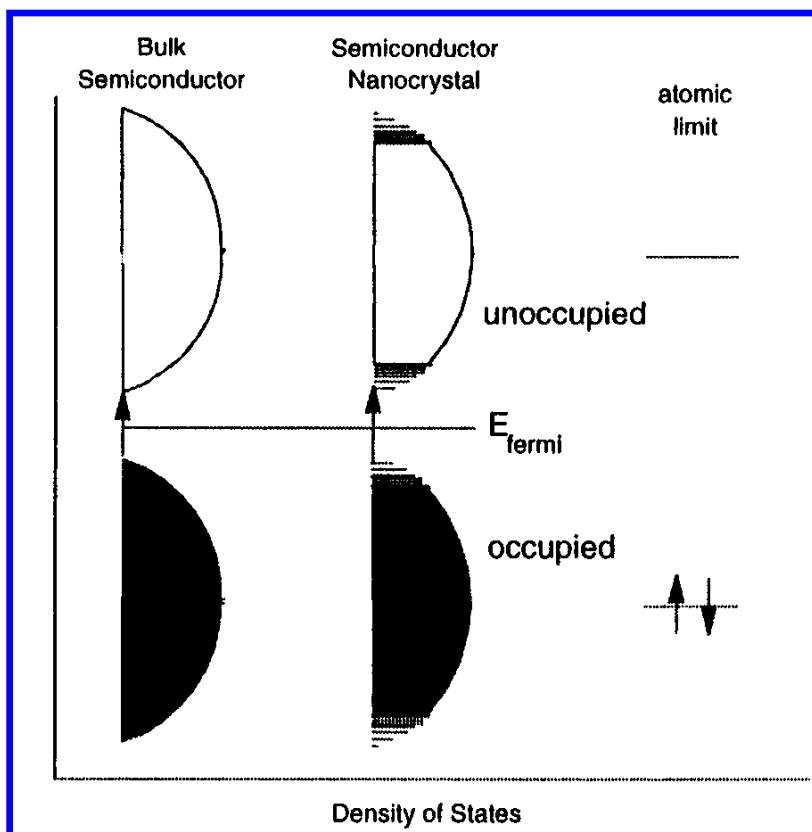


**Figure-1.5(b)** Density of states in semiconductor nanocrystals [5].

In semiconductors, however, the Fermi level lies between two bands, so that the edges of the bands dominate the low-energy optical and electrical behavior. The band gap of semiconductors increases with decreasing size due to reduction in the band width in the nano-regime due to both decreased number of atoms and weakening of nearest neighbour interactions. This is the most striking effect in the semiconductor nanocrystals that leads to the massive changes in optical properties as a function of the size [ 9].

### 1.2.3 Optical properties

Metal nanoparticles show different optical properties from their bulk form figure 1.6 [10]. These properties are dependent on composition, size, shape and surrounding medium of the nanoparticles [11]. It varies from visible region to NIR region depending on the size and shape of the nanoparticles [12]. This effect appears due to interaction of electromagnetic radiation with the electron cloud present on the surface of metal

nanoparticles. Gold, silver and copper nanoparticles are known to exhibit unique optical properties in visible and in NIR region within certain size limit of particles [10].

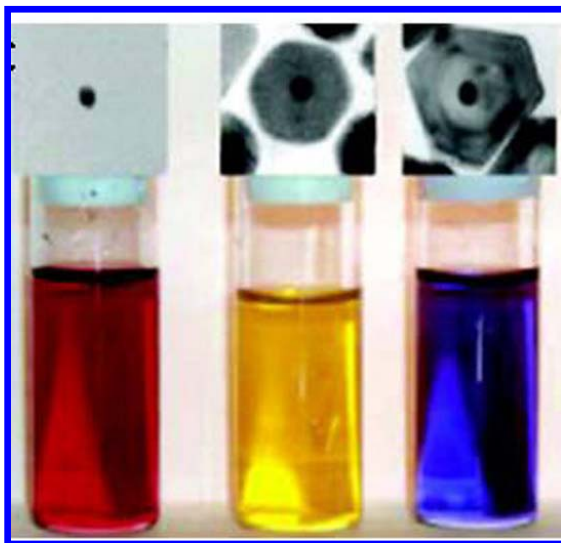


**Figure-1.6** Nanoparticle solutions demonstrating the variation of optical properties i.e. colour with respect to change in composition [13].

### Surface plasmon resonance

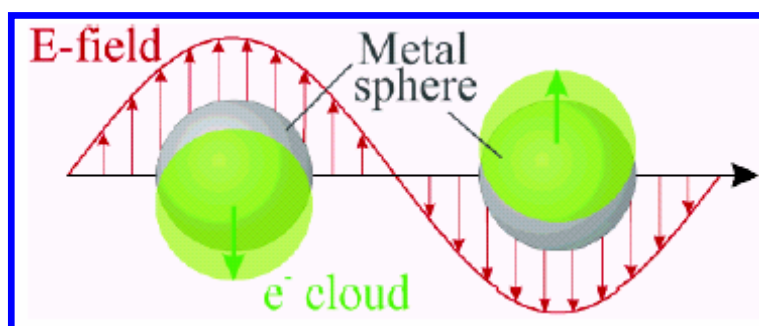


**Figure-1.7** Schematic of plasmon oscillation for a sphere, showing the displacement of the conduction electron charge cloud relative to the nuclei [10].

Large number of atoms present on the surface of nanoparticles contributes electron cloud on the surface of nanoparticles. As shown in the figure 1.7, the movement of these free electrons under the influence of the electric field vector of the incoming light leads to a

dipole excitation across the particle. This induces positive polarization charge on cationic lattice. This charge acts as a restoring force, and brings back electron cloud to its original position, thus causing the oscillations of the electron cloud.

Thus, the electron density within a surface layer, the thickness of which is about equal to the screening length of a few angstroms, oscillate, whereas the density in the interior of the particle remains constant. This phenomenon is called surface plasmon resonance, and has been explained by Mie in 1908, based on the Maxwell's equation of scattering [14]. The absorption spectrum of particles in a given solvent can be calculated from optical constants of the bulk metal. The absorption spectrum of spherical particles of sizes between 3 to 20 nm does not strongly depend on particle size. This is because the particles are below the size at which higher order term in the Mie formulae for the absorption constant becomes significant. Thus, one has to regard only the dipole term, which depends only on the total metal concentration in the solution and not on particle size. The absorption coefficient  $\alpha$  is calculated from equation given below

$$\alpha = \frac{18\pi}{\ln 10} \frac{10^5}{\lambda} \frac{Mn_0^3}{\rho} \frac{\epsilon_2}{(\epsilon_1 + 2n_0^2) + \epsilon_2^2} \dots\dots\dots(1.1)$$

where,  $\lambda$  is the wavelength of light in nanometers,  $M$  and  $\rho$  are the molecular weight and density of the metal,  $n_0$  is the refractive index of the solvent and  $\epsilon_1$  and  $\epsilon_2$  are the real and imaginary parts of the dielectric constant of the metal. When the size of the particles becomes smaller than the mean free path of the electrons, the absorption bands are broadened; this is accounted for by using size-corrected values of  $\epsilon_2$ . [10, 15]

$$\epsilon_2 = \epsilon_{2(bulk)} + \left( \frac{\omega_p^2}{\omega^2} \right) \left( \frac{V_F}{R} \right) \dots\dots\dots(1.2)$$

where,  $\omega$  is the light frequency,  $\omega_p$  the plasmon frequency,  $V_F$  the electron velocity at the Fermi level and  $R$  the particle radius ( $R/V_F$ , mean time of the free movement of the electrons). From the equation 1.1, resonance with the incident light reaches at the wavelength where the negative value of  $\epsilon_1$  of the metal is equal to twice the dielectric

constant of the medium. In other words, any changes in the electron density near surface of nanoparticles will lead to changes in the plasmon absorption. This surface sensitivity of colloidal nanoparticles has been used to study adsorption/chemisorption of biomolecules etc. [16-22]. Several applications are emerging based on the surface plasmon resonance properties of nanoparticles. Applications based on optical properties in the visible region are receiving considerable scientific interest due to its promising technological development. In plasmonics, transfer of the electromagnetic energy from one place to another has been shown efficiently with the help of nanoparticles arrays. Nanoparticles arrays in these cases are used as wave guide [23].

### **1.2.4 Magnetic properties**

Nanomaterials show novel magnetic properties [24-26]. As depicted in figure 1.8, magnetic nanoparticle, below a critical size  $r_c$ , can contain only a single magnetic domain which means that all the spins of the particle are coupled in the same direction, and the particle behaves as a single magnetic dipole. Hence, to change the magnetization, the domain needs to be rotated instead of moving the domain wall.

For a particle size smaller than the single domain size, the spins can be easily affected by the thermal fluctuations and the originally ferromagnetic material shows superparamagnetic nature [27]. This can be understood from the equation  $KV = 25 k_{\beta} T_B$  where  $V$ ,  $k_{\beta}$  and  $T_B$  are the volume of a single particle, Boltzmann constant and blocking temperature respectively [28]. From this equation, it can be seen that as the particle size decreases, the magnetic anisotropy energy  $KV$  (the energy difference involved in changing the magnetization direction from a low-energy direction or easy axis to a high energy direction or hard axis) also decreases. For a given particle,  $K$ ,  $V$  and  $k_{\beta}$  would be constant and the thermal energy would be a function of the blocking temperature. Above the blocking temperature, the thermal energy is sufficient to flip the spins in the magnetic material; hence, the material will not show any hysteresis loop. Consequently, for superparamagnetic materials, a hysteresis loop is obtained only below its blocking temperature. In case of superparamagnetic materials, a plot of the magnetization ( $M$ ) and the ratio of the magnetic field and the temperature ( $H/T$ ) produce a universal curve for all

temperatures above  $T_B$ . Superparamagnetism is also related to the relaxation rate and is sensitive to the characteristic time scale of measurement.

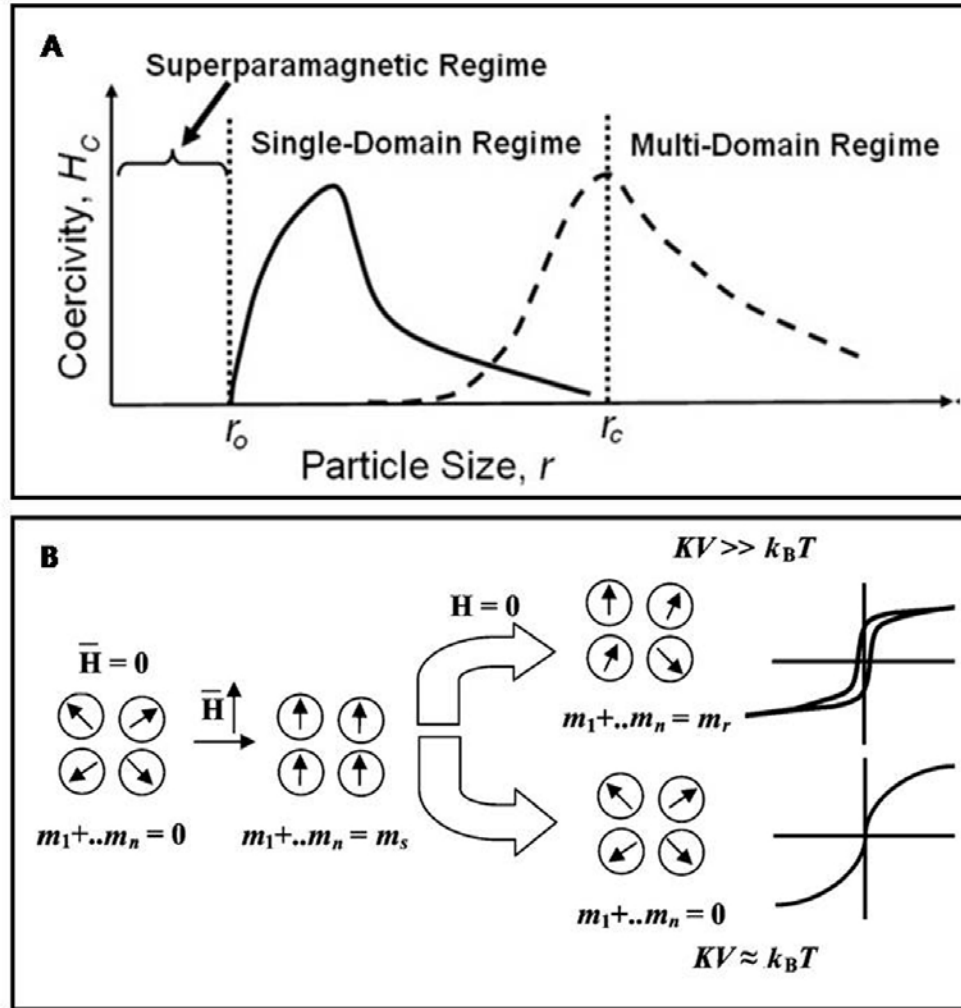


**Figure-1.8A)** Schematic showing the change in the coercivity of a ferromagnetic particle with the diameter in the superparamagnetic, single-domain and multi-domain regions [29]. **B)** Illustration of superparamagnetism [30].

### 1.2.5 Mechanical properties

Mechanical strength of the material depends on several parameters such as impurities, dislocations etc. More defects in materials lead to less mechanical strength. Thus, due to small cross sections and less number of imperfections, nano materials such as nano wires and nano rods show enhanced mechanical strength. Since imperfections are

thermodynamically more energetic, small size of nanomaterials eliminates imperfections in the crystal and acquires better mechanical strength [31].

### **1.2.6 Melting point**

Metal nanoparticles below 100 nm of size have low melting point than its bulk form. Number of surface atoms increases with decrease in the size of nanoparticles. Since it decreases the co-ordination number of atoms, atoms on the surface can be easily rearranged than those atoms present inside nanoparticles, thus melting process starts at lower temperature leading to decrease in melting point [32].

### **1.3 Metal Oxide Nanomaterials**

Metal oxides play a very important role in many areas of chemistry, physics, and materials science [33-37]. The metal elements are able to form a large diversity of oxide compounds [38]. These can adopt a vast number of structural geometries with an electronic structure that can exhibit metallic, semiconductor, or insulator characteristics. The metal oxides are used in the fabrication of microelectronic circuits, piezoelectric devices, sensors, fuel cells, solar cells, coatings for the passivation of surfaces against corrosion, and as catalysts. For the control of environmental pollution, catalysts or sorbents that contain oxides are employed to remove the CO, NO<sub>x</sub>, and SO<sub>x</sub> species formed during the combustion of fossil-derived fuels [39, 40]. The most active areas of the semiconductor industry involve the use of oxides [41]. Thus, most of the chips used in computers contain a metal oxide component.

Metal oxide nanoparticles can exhibit unique chemical properties due to their limited size and a high density of corner or edge surface sites. Bulk oxides are usually robust and stable systems with well-defined crystallographic structures. However, the growing importance of surface free energy and stress with decreasing particle size must be considered. The changes in thermodynamic stability associated with size can induce modification of cell parameters and structural transformations [42-45]. To display mechanical or structural stability, the nanoparticle must have a low surface free energy. As a consequence of this requirement, phases that have a low stability in bulk materials

can become very stable in nanostructures. This structural phenomenon has been detected in  $\text{TiO}_2$ ,  $\text{VO}_x$ ,  $\text{Al}_2\text{O}_3$  or  $\text{MoO}_x$  oxides [43, 45, 46]. Size-induced structural distortions associated with changes in cell parameters have been observed in nanoparticles. As the particle size decreases, the increasing number of surface and interface atoms generates stress/strain and concomitant structural perturbations [47-49].

In any material, the nanostructure produces the so-called quantum size or confinement effects which essentially arise from the presence of discrete, atom-like electronic states. The general electronic effects of quantum confinement experimentally probed on oxides are related to the energy shift of exciton levels and optical band gap [50, 51]. Theoretical studies for oxides show a redistribution of charge when going from large periodic structures to small clusters or aggregates which must be roughly considered to be relatively small for ionic solids while significantly larger for covalent ones [52-57]. The degree of ionicity or covalency in a metal-oxygen bond can however strongly depend on size in systems with partial ionic or covalent character [42].

Many oxides have wide band gaps and a low reactivity in their bulk state [58]. A decrease in the average size of an oxide particle does in fact change the magnitude of the band gap [50, 59], with strong influence in the chemical reactivity [60, 61]. In the case of nanostructured oxides, surface properties are strongly modified with respect to two-dimensional (2D) infinite surfaces, producing solids with unprecedented sorption or acid/base characteristic [62]. Furthermore, the presence of undercoordinated atoms (like corners or edges) or O vacancies in an oxide nanoparticle should produce specific geometrical arrangements as well as occupied electronic states located above the valence band of the corresponding bulk material [63-65]. In our studies, we have investigated on n-type  $\text{TiO}_2$  and  $\text{ZnO}$  nanomaterials.

### **1.3.1 Titanium Dioxide ( $\text{TiO}_2$ )**

Titanium dioxide ( $\text{TiO}_2$ ) is one of the most prominent materials used in various industrial applications related to catalysis, e.g., the selective reduction of  $\text{NO}_x$  in stationary sources [66, 67], photocatalysis for pollutant elimination [68] or organic synthesis [69],

photovoltaic devices [70], sensors [71], and paintings [72]. Additional applications of importance include its use as a food additive [73], in cosmetics [74], and as a potential tool in cancer treatment [75]. The (n-type) semiconductor properties of TiO<sub>2</sub> materials are essential in accomplishing these functions. The Ti-O bond appears to have an increasing covalent character with the oxygen content of the oxide, so the departure of Ti<sup>n+</sup> from the formal oxidation state grows from +2 to +4 [76]. Experimental approaches to scale down the primary or intrinsic particle size of TiO<sub>2</sub> to the nanometer scale are now actively investigated to improve its current applications and to reach more advanced ones such as its use in electrochromic devices [77]. As a general result, the nanostructure induces an increase in surface area with concomitant enhancement of the chemical activity and also of the photochemical and photophysical activities with a potential reduction of light scattering.

TiO<sub>2</sub> occurs in nature in three different polymorphs, which, in order of abundance, are rutile, anatase, and brookite. As an extended (bulk) system, rutile is thought to be the thermodynamic stable phase, although, based in calorimetric and theoretical investigations, there is a controversy in the literature about whether the rutile or the anatase is in fact the stable polymorph. When the primary particle size is scaled down, a thermodynamic analysis of phase stability indicates that surface free energy and stress contributions stabilize anatase below a certain size close to 15 nm [45]. Above such limit, brookite and rutile appear to have very close free energy values up to a size close to 35 nm, above which rutile seems the stable phase [45, 78]. The nanostructure of the TiO<sub>2</sub> material strongly affects the phase behavior, tuning the thermal stability and corresponding phase transformation of the polymorphs. Concerning anatase samples, the anatase to rutile phase transformation occurs in a broad temperature range, from around 723 to 1273 K [79-82]. As it is obvious, grain/particle size growth and phase transformation are parallel phenomena during a thermal treatment of a nanostructured solid, but in TiO<sub>2</sub> the size-dependent relative stability of the polymorphs [45] interrelates these two variables, in turn making difficult the identification of thermodynamic and kinetic parameters present in the phase transition. On heating, the following transformations are seen: anatase to brookite to rutile, brookite to anatase to rutile,

anatase to rutile, and brookite to rutile. These transformation sequences imply very closely balanced energetics as a function of particle size.

As a semiconductor used in photochemical and photophysical applications, one critical parameter is the band gap energy and characteristics. The band gap of bulk  $\text{TiO}_2$  lays in the UV region i.e. 3 eV for the rutile phase and 3.2 eV for the anatase phase. Although the extended/bulk anatase material is an indirect band gap semiconductor, the nanostructured anatase  $\text{TiO}_2$  samples are likely direct semiconductors [83, 84]. For indirect band gap semiconductors, the valence to conduction band electronic transition is electrical dipole forbidden, vibrationally allowed, and photon assisted (i.e., both energy and momentum of the electron-hole pair change) while direct band gap transitions are dipole allowed. The absorption at threshold but particularly the emission of light is thus stronger for the direct systems, resulting in a more efficient management of light and in potentially improved photochemical or physical performances for nanostructured materials.

Electrical/ionic conductivity is the other type of property of  $\text{TiO}_2$  materials that can be modulated by nanostructure and has current technological applications in the field of sensors or photoelectronic devices. The metal/ $\text{TiO}_2$  contact is used at low temperatures in sensor devices. At high temperatures,  $\text{TiO}_2$  can be easily reduced, and this decisively influences conductivity. Bulk defects result in n-type doping and high conductivity [85], and are of various types such as doubly charged oxygen vacancies,  $\text{Ti}^{3+}/\text{Ti}^{4+}$  interstitials, and planar defects such as crystallographic shear planes [85, 86], while surface defects are mostly ascribed to undercoordinated Ti anions and (doubly charged) oxygen vacancies [87]. Their presence, characteristics, and development under reductive atmospheres as a function of temperature are less defined for nanostructured materials. Grain boundaries, on the other hand, strongly influence electrical conductivity as measured by impedance spectroscopy [88].

$\text{TiO}_2$  is regarded as the most efficient and environment friendly photocatalyst and has widely used and studied for photodegradation of various pollutants [89], diseased cells,

harmful bacteria and viruses [90], in cancer treatment etc. [91]. On the similar footings, undoped [92]/doped [93]  $\text{TiO}_2$  can also be used for water splitting. In these photoreactions, recombination of photogenerated charge carriers is the main problem. This is solved by attaching different metal NPs (Au, Ag, Pt) to the  $\text{TiO}_2$  nanostructures [94]. Another important area where  $\text{TiO}_2$  nanomaterials are directly used is photovoltaics. More specifically Dye Sensitized Solar Cell (DSSC) or Grätzel cell consisting  $\text{TiO}_2$  layer where different size and shaped titania nanomaterials are used [95].

### 1.3.2 Zinc oxide (ZnO)

Zinc oxide nanostructures have attracted much attention in recent years because of the strong dependence of their optical properties on the crystallite size and morphology. The lack of a centre of symmetry in wurtzite, combined with large electromechanical coupling, results in strong piezoelectric and pyroelectric properties and the consequent use of ZnO in mechanical actuators and piezoelectric sensors. In addition, ZnO is a wide band-gap (3.37 eV) compound semiconductor that is suitable for short wavelength optoelectronic applications. The high exciton binding energy (60meV) in ZnO crystal can ensure efficient excitonic emission at room temperature and room temperature ultraviolet (UV) luminescence has been reported in disordered nanoparticles and thin films. ZnO is transparent to visible light and can be made highly conductive by doping.

In terms of structural properties, ZnO is a polar crystal with a number of alternating planes composed of tetrahedrally coordinated  $\text{O}^{2-}$  and  $\text{Zn}^{2+}$  ions, stacked alternately along the c-axis [96]. Thus, a ZnO crystal consists of a positively charged plane (001) terminated with zinc and a negatively charged plane terminated with oxygen [97]. On the other hand, ZnO has its unique ability to form a variety of nanostructures such as nanowires, nanoribbons/nanobelts, nanocombs, nanorings, nanocages, nanocastle, nanospheres, nanofibers, nano-tetrapods and heterostructures [98-118]. In addition, ZnO nanostructures are one of the most promising materials for the fabrication of chemical and biosensors due to having exotic and versatile properties including biocompatibility, nontoxicity, chemical and photochemical stability, high specific surface area, optical

transparency, electrochemical activities, high electron communicating features and so on [119-121].

ZnO has attracted a great deal of attention for its potential uses in UV light emitters, piezoelectric transducers, gas sensors, transparent conductive films and photovoltaic cells etc. [122]. Like TiO<sub>2</sub> nanomaterial, ZnO nanostructures are used in dye-sensitized solar cells. The band gap and conduction band edge of ZnO is similar to that of TiO<sub>2</sub> (anatase). ZnO has higher electron mobility (205-1000 cm<sup>2</sup> V<sup>-1</sup> s<sup>-1</sup>) than TiO<sub>2</sub> (~0.1-4 cm<sup>2</sup> V<sup>-1</sup> s<sup>-1</sup>), which should favor electron transport [123]. The chemical stability of ZnO is rather poor compared with that of TiO<sub>2</sub>; it dissolves under both acidic and basic conditions.

Mesoporous ZnO electrodes can be prepared from a paste containing ZnO nanoparticles, followed by doctor-blading or screen printing onto FTO substrates and sintering. The best result so far was reported by Saito and Fujihara who used a commercial ZnO powder (20 nm sized particles) and 90 min dye adsorption time at 60 °C (0.3 mM N719 in ethanol) [124]. They obtained 6.6% efficiency at AM 1.5 G (100 mW cm<sup>-2</sup>). In earlier work, longer dye-adsorption times were used, and abnormal dye uptake was observed. Keis et al. found that dye precipitation can take place in the ZnO mesoporous structure [125]. Some dissolution of ZnO by the acidic carboxylic anchoring groups of the sensitizer can take place. The resulting Zn<sup>2+</sup> ions form insoluble complexes with the N3/N719 dye, causing precipitation of these complexes in the pores of the film. This gives rise to a filter effect (inactive dye molecules), so that net yield for charge carrier injection is decreased, whereas the light-harvesting efficiency is increased during the sensitization process due to the large number of dye molecules in the film. Thus, careful control of the dye adsorption conditions is necessary for ZnO-based DSSCs.

## 1.4 Applications of Nanomaterials

The existing and promising applications of nanomaterials include UV protection, photocatalysis, photovoltaics, sensing, and electrochromics as well as photochromics. Wide-band-gap semiconductor ( $\text{TiO}_2$  and  $\text{ZnO}$ ) NPs are used in dye sensitized Solar cells to generate photovoltaic electricity. Nanocrystalline  $\text{CdS}$ ,  $\text{CdTe}$ ,  $\text{ZnS}$  made by sol-gel are the candidates for light emitting phosphors. Batteries in portable electronic equipments like mobile phones, laptops need to be light-weight with high energy density storage capacity. Nano-materials like aerogels made by sol-gel are the candidates for the separator plates in batteries. CNTs and polymer nanocomposites have proved to be viable as anti-stacking packing. Current medical implants, such as orthopaedic implants and heart valves, are made up of titanium and SS alloys, since they are bio-compatible. Nanocrystalline  $\text{ZrO}_2/\text{SiC}$  can be the good alternatives as bio-implants. The enormous potential for nanotechnology is to be applied to gene and drug delivery. Functionalized NPs can be used as vehicles and are capable of targeting specific diseased cells. These contain both therapeutic agents that are released into the cells and a sensor that controls the release.

### 1.4.1 Solar Cell Application (Clean Energy)

As the world is becoming more advanced in technology and economy, more energy is being consumed to keep up with the development and the demand on energy boomed over the past years. In 2010, the annual world primary energy consumption increased by 2.7% to 441 exajoules and is estimated to augment steeply to 762 exajoules by the year of 2030 [126]. Presently, the energy economy is still highly dependent on three forms of fossil fuels - oil, natural gases and coal with percentages of 36.4%, 23.5% and 27.8%, respectively [127]. However, the world will shortly come to an end of fossil fuels as the world's primary energy resource. With a daily consumption of 82.5 million barrels, oil might run out in around 40 years at current reserves-to-production (R/P) ratio. A better synopsis is for natural gases that can last for about 60 years and coal, being the most abundant, for 150 years [126]. Meanwhile, the increasing awareness that the unpleasant environmental pollution arising from the combustion of these feedstocks necessitates

urgent promotion of alternatives in renewable energy sources to cover the substantial deficit left by fossil fuels.

Of all the available technologies producing renewable energy, photovoltaic energy is a hot topic in current research. One simple reason is that the Earth receives  $1.2 \times 10^{17}$  W insolation or  $3 \times 10^{24}$  Joule energy per year from the Sun and this means covering only 0.13% of the Earth's surface with solar cells with an efficiency of 10% would satisfy our present needs [95(a)]. Apart from the abundance of potentially exploitable solar energy, photovoltaic cells also have other competitive advantages such as little need for maintenance, off-grid operation and silence, which are ideal for usage in remote sites or mobile applications.

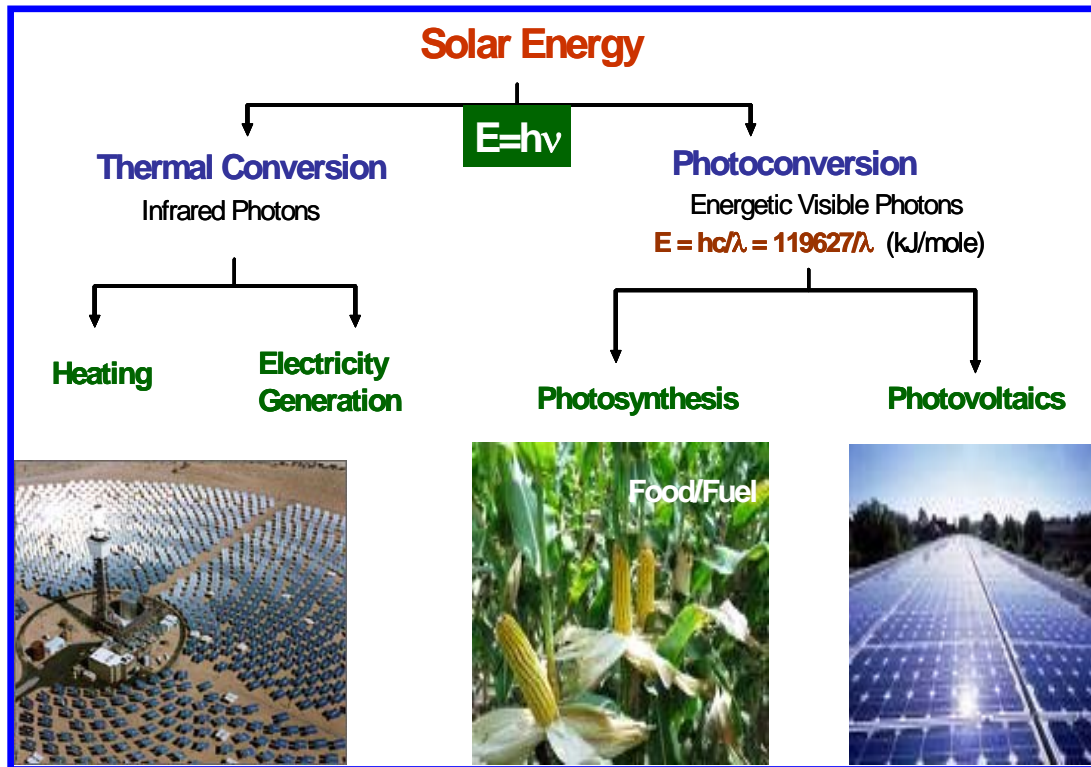


*Figure-9 Schematic diagram of various applications of solar energy.*

Solar cell production has grown at about 30% per annum over the past 15 years. The conventional solar cells of today, **the first generation** solar cells are based on single crystalline silicon. The estimated total installed capacity in 2010 was 7.8 GW.<sup>23, 24</sup>

## Chapter-1

Silicon-based systems make up around 90% of the current PV market. The production cost is presently around \$3/Wp but is highly dependent on the price of the silicon material.

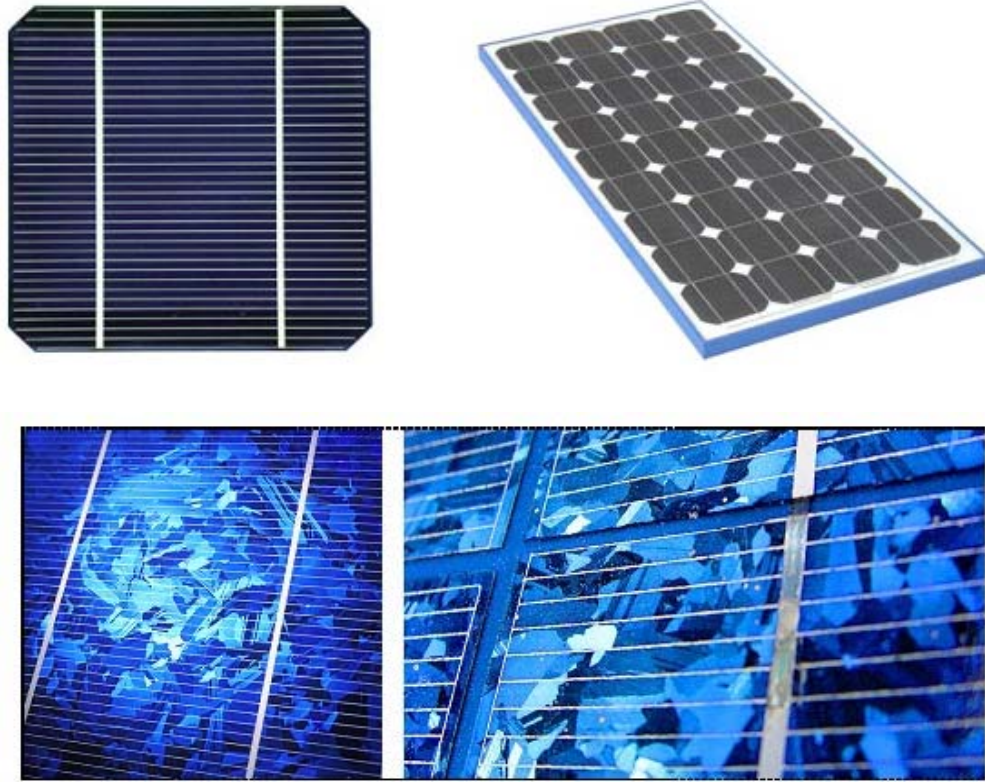


**Figure-1.10** Silicon solar cells. [[http://sovoxglobal.com/cell\\_classification.html](http://sovoxglobal.com/cell_classification.html)]

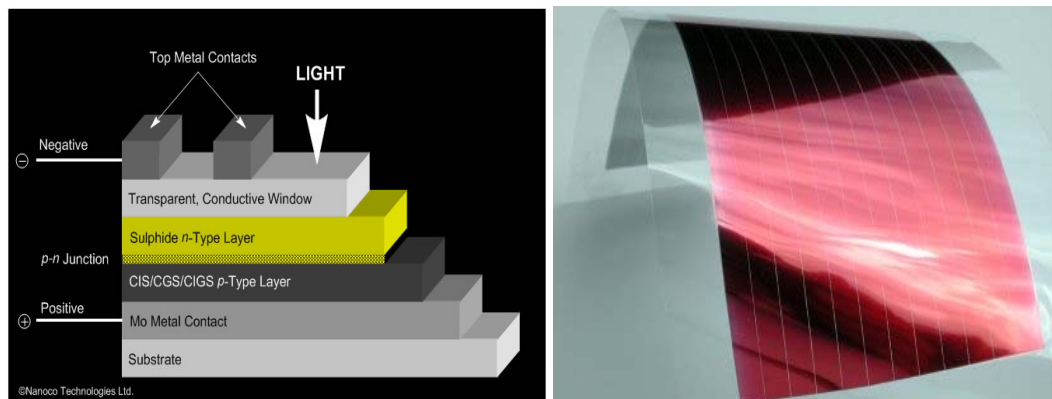


**Figure-1.11** Schematic diagram of Copper Indium Gallium Selenide (CIGS) solar cell with its module. [[http://sovoxglobal.com/cell\\_classification.html](http://sovoxglobal.com/cell_classification.html)]

**The second generation** solar cells were developed, such as polycrystalline and amorphous silicon, thin-film deposits of silicon, CdTe, CuInSe<sub>2</sub>, (CIS) and Cu(In,Ga)Se<sub>2</sub> (CIGS), as well as multijunction cell technology. These devices were initially designed to be high-efficiency but later turned out to be of the advantages in the mass of material and production cost compared to single crystalline silicon devices.

Both first and second generation solar cells are based on single junction devices. Calculated thermodynamic efficiency limits in single junction solar cells (31%) assume that absorption of an individual photon results in the formation of a single electron-hole pair and that all photon energy in excess of the energy gap is lost as heat. This so-called Shockley-Queisser limit can be overcome by the use of various types of so-called third generation solar cell devices [128]. In the 1990s; new concepts of solar cells were conceived and realized. These technologies mainly include dye-sensitized solar cells, polymer solar cells, and nanocrystalline solar cells, all of which are now known as **third generation photovoltaics** since they are very different from the previous semiconductor devices as they do not rely on a traditional p-n heterojunction to separate photogenerated charge carriers. Instead, they form a ‘bulky’ junction where charge separation takes place. Because of the low-cost materials and easy fabrication, these technologies are expected to take a significant share in the fast growing photovoltaic areas.

### **1.4.1.1 Dye-sensitized Solar cells (DSSC)**

#### **1.4.1.2 A history with photography**

In 1837, almost at the same time when Becquerel found the photovoltaic effect, Louis Daguerre made the first “daguerreotype” photographic image onto a mirror-polished surface of silver bearing a coating of silver halide particles, which is now considered as the beginning of photography. The silver halides used in photography have band gaps ranging from 2.7 to 3.2 eV, and are therefore not photoactive for wavelengths longer than 460 nm, lacking the sensitivity to the mid-visible spectral and red light. An improvement was made in 1873 by a German photochemist, Vogel, via the dye sensitization of silver halide emulsions, leading to an extended photoresponse into the red and even infrared regions and the first panchromatic film rendering a realistic black and white picture

[129]. In 1887, Moser intuitively observed the first case of dye-sensitized semiconductor electrode when using the dye erythrosin on silver halide electrodes [130]. However, it was not until 1960s that people clearly understood the operating mechanism is the electron injection from a photo-excited state of the dye molecules into the conduction band of the n-type semiconductor substrates, following the work of Namba and Hishiki [131], Tributsch and Gerischer et al. [132-134] on zinc oxide. Those prototype dye-sensitized cells were characterized with poor dye anchorage (mostly physisorbed) on semiconductor surface and low conversion efficiencies restricted by the limited, weak light absorption (in the order of 1 to 2%) of the dye monolayer on the planar surface. Thicker dye layers increased the resistance of the system without adding to the current generation [135], which disappointed Gerischer and led him not to “follow the idea of constructing a photocell based on this effect with earlier experiments” [136]. Incremental improvements were then achieved both in the chemisorption of sensitizers [137-139], electrolyte redox chemistry and the judicious selection of photoelectrode materials [136, 139-145]. Most semiconductors such as CdS, CdSe, GaP and Si underwent serious photocorrosion or even normal corrosion in the dark, thus a stable, wide band-gap semiconductor, TiO<sub>2</sub>, became the material of choice, following the successful demonstration of direct photolysis of water with TiO<sub>2</sub> [146, 147]. To solve the absorption dilemma, the concept of using dispersed particles to provide a sufficient interface emerged first [148], then photoelectrodes with high surface roughness were employed to generate multiple reflections at a rough surface, permitting the capture of most of the incident light by a monolayer of a dye with a high molar extinction coefficient [149, 150]. All these improvements finally led to the announcement in 1991 of the sensitized nanocrystalline photovoltaic device with a conversion efficiency at that time of 7.1 -7.9 % under solar illumination and 12% in diffuse daylight [151]. With the discovery of the N3 sensitizer and the later panchromatic “black dye”, the power to electricity conversion efficiency was pushed well over 10% [152, 153].

### 1.4.1.3 Basic principles of dye-sensitized solar cells

#### A concept of 'excitonic' solar cell

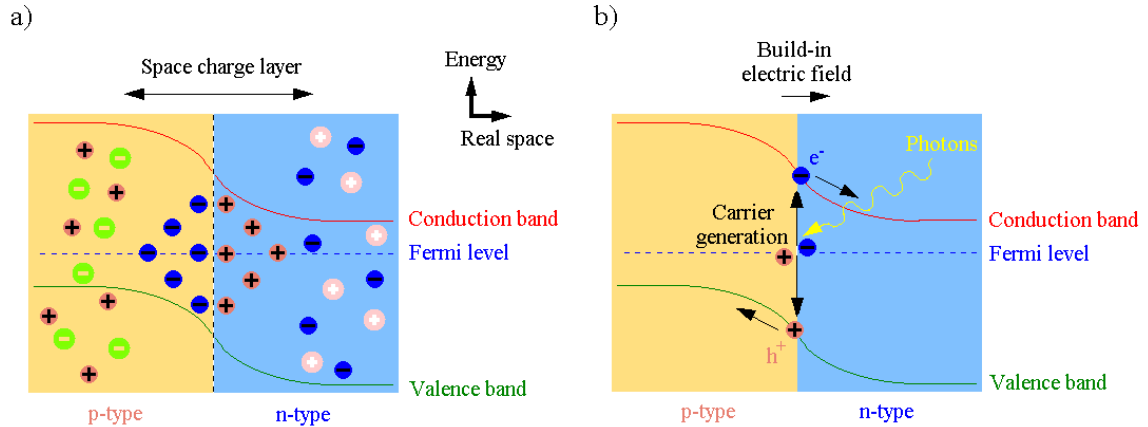


**Figure-1.12** a) Energy band diagram of a conventional p-n junction solar cell in the case of short circuit condition; b) Charge separation under illuminations.

Conventional photovoltaic cells are built on p-n junctions of silicon and other inorganic semiconductors. Figure 1.12a depicts the energy band diagram of a p-n junction after thermal equilibration of positive and negative charge carriers. Due to the concentration difference between the p and the n type semiconductor, holes move to the n region and electrons to p region. The uncompensated charges induced by the diffusion generate a built-in electric field at the junction and impair further percolation of charge carriers since the orientation of the electric field is contrary to the direction of the carrier diffusion. At equilibrium, no net charge diffusion occurs and a depletion region is formed, which is also referred to as a space charge layer. In the case of illumination as shown in figure 1.12b, absorption of photons with energy higher than a threshold, the band gap, results in generation of excitons which interact via coulombic forces. Considering that excitons will recombine after a certain time with emission of photons or phonons (heat), therefore only those created in or close to the space charge layer can be separated by the built-in electric field and contribute to the photocurrent. Since both electrons and holes coexist in the same chemical phase, these cells are called minority

carriers devices and their efficiencies are highly dependent on the ability of photogenerated minority carriers (for example, electrons in a p-type material) to be collected out of devices before recombining with the majority carriers (holes, in this case) [154].

On the contrary, with an electron-conducting phase (n-type semiconductor) and a hole conducting phase (redox species or hole conductors) forming a “bulky” heterojunction, Dye Sensitized Solar Cells (DSSCs) are majority carrier devices where electrons and holes are separated in two chemical phases. A schematic of the interior of a DSSC showing the principle of how the device operates is shown in figure 1.13.

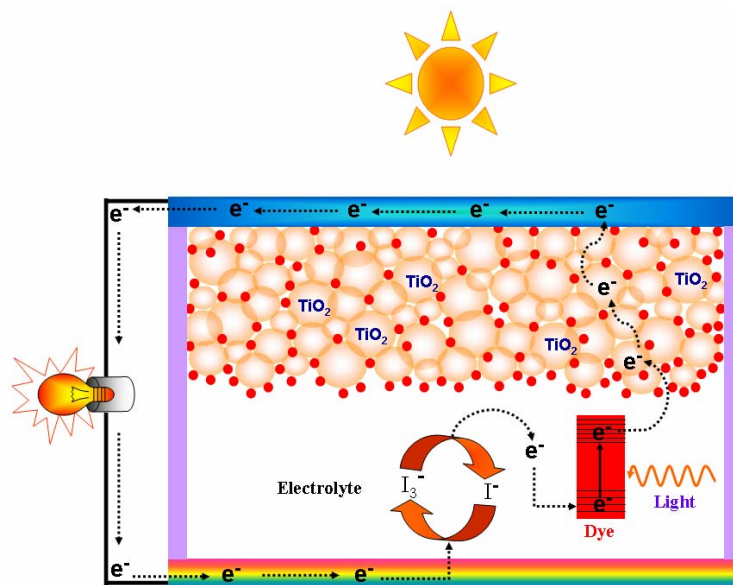


**Figure-1.13** Schematic overview of a dye-sensitized solar cell.

The typical basic configuration is as follows: At the heart of the device is the mesoporous oxide layer composed of a network of  $\text{TiO}_2$  nanoparticles that have been sintered together to establish electronic conduction. Typically, the film thickness is  $\sim 10 \mu\text{m}$  and the nanoparticle size 10-30 nm in diameter. The porosity is 50-60%. The mesoporous layer is deposited on a transparent conducting oxide (TCO) on a glass substrate. The most commonly used substrate is glass coated with fluorine-doped tin oxide (FTO). Attached to the surface of the nanocrystalline film is a monolayer of the charge-transfer dye.

Photoexcitation of the latter results in the injection of an electron into the conduction band of the oxide, leaving the dye in its oxidized state. The dye is restored to its ground state by electron transfer from the electrolyte, usually an organic solvent containing the iodide/ triiodide redox system. The regeneration of the sensitizer by iodide intercepts the recapture of the conduction band electron by the oxidized dye. The  $I_3^-$  ions formed by oxidation of  $I^-$  diffuse a short distance ( $<50 \mu\text{m}$ ) through the electrolyte to the cathode, which is coated with a thin layer of platinum catalyst, where the regenerative cycle is completed by electron transfer to reduce  $I_3^-$  to  $I^-$ . Following are the some numbers for typical materials and relative concentrations of the different species in the mesoporous system under normal working conditions (1 sun illumination):

- Under working conditions there are about 10 electrons per  $\text{TiO}_2$  particle.
- More than 90% of electrons in  $\text{TiO}_2$  are trapped and  $<10\%$  in the conduction band.
- There are  $\sim 10\,000$  adsorption sites for  $\text{H}^+$  on an 18 nm (diameter)  $\text{TiO}_2$  particle.
- A  $\text{TiO}_2$  particle (18 nm) has  $\sim 600$  dye molecules on the surface.
- Each dye molecule absorbs a photon once per second.
- The flux of electron injection into the  $\text{TiO}_2$  particle is  $\sim 600 \text{ s}^{-1}$ .
- Under working conditions, about 1 dye per 150  $\text{TiO}_2$  particles is in its oxidized state.
- The total volume fraction of the solutes in the electrolyte is  $\sim 10\text{-}20\%$ .
- In the pore volume around the  $\text{TiO}_2$  particle, there will be  $\sim 1000 I^-$  and  $200 I_3^-$  ions.
- The concentration of iodine,  $I_2$ , is  $<1 \mu\text{M}$ , that is, about one free iodine per 10 000  $\text{TiO}_2$  particles.

For a DSSC to be durable for more than 15 years outdoors, the required turnover number is  $10^8$ , which may be satisfied by the ruthenium complexes [155]. The voltage generated under illumination corresponds to the difference between electrochemical potential of the electron at the two contacts, which generally for DSSC is the difference between the Fermi level of the mesoporous  $\text{TiO}_2$  layer and the redox potential of the electrolyte. Overall, electric power is generated without permanent chemical transformation.

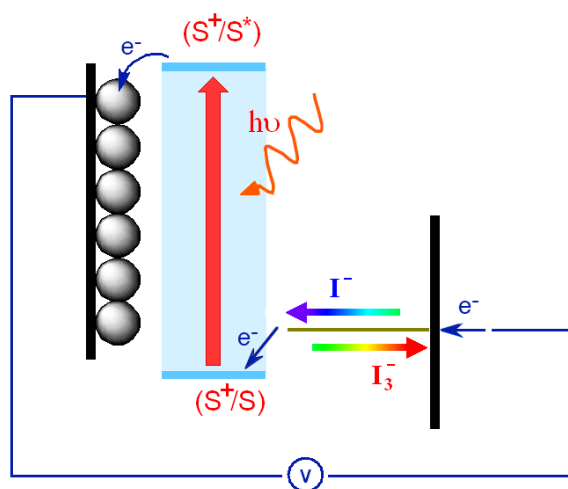


**Figure-1.14** Principle of operation of the nanocrystalline  $\text{TiO}_2$  dye-sensitized solar cells.

#### 1.4.1.4 Electron transfer processes in DSSCs

DSSCs are photoelectrochemical devices where several electron transfer (ET) processes are in parallel and in competition (figure 1.14). Since, the highest energy conversion efficiencies have been reported for a nanocrystalline  $\text{TiO}_2$  film sensitized with ruthenium polypyridyl complexes and permeated with  $\text{I}^-/\text{I}_3^-$  as the electrolyte, the following discussion will primarily focus on DSSCs with this configuration.



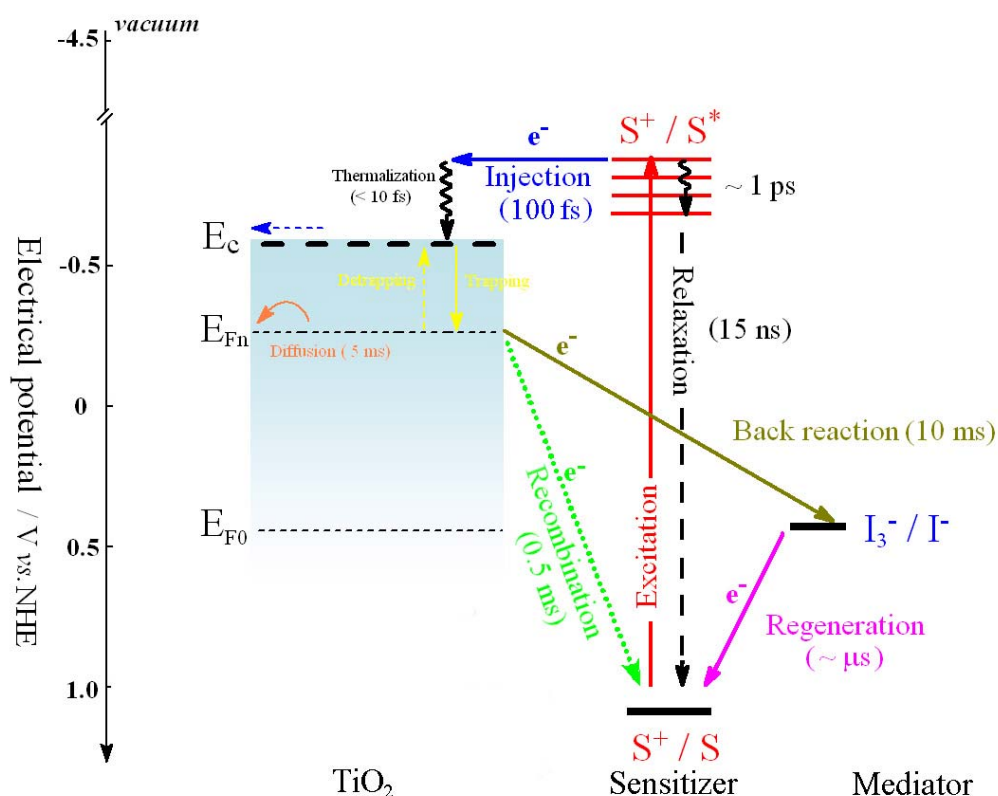


**Figure-1.15** Dynamics of different electron transfer processes in the conversion of light to electric power by a DSSC. The numbers in parentheses are representative values for each process.

Figure 1.15 shows the typical time constants of processes involved in such a DSSC device. Upon illumination, the sensitizer is photoexcited in a few femtoseconds (Eq. 1.3) and electron injection is ultrafast from S\* to TiO<sub>2</sub> (Eq. 1.4) on the subpicosecond time scale (intramolecular relaxation of dye excited states might complicate the injection process and change the timescale), where they are rapidly (less than 10 fs) thermalized by lattice collisions and phonon emissions. The nanosecond-ranged relaxation of S\* (Eq. 1.5) is rather slow compared to injection, ensuring the injection efficiency to be unity. The ground state of the sensitizer is then recuperated by I<sup>-</sup> in the microsecond domain (Eq. 1.6), effectively annihilating S<sup>+</sup> and intercepting the recombination of electron in TiO<sub>2</sub> with S<sup>+</sup> (Eq. 1.7) that happens in the millisecond time range. This is followed by the

two most important processes – electron percolation across the nanocrystalline film and the redox capture of the electron by the oxidized relay (back reaction, Eq. 1.8),  $I_3^-$ , within milliseconds or even seconds. The similarity in time constants of both processes induces a practical issue on achieving high conversion efficiencies in DSSC.

**1.4.1.5 Photovoltaic Cell Performance:**

The power conversion efficiency of the photovoltaic cell determined by the Short circuit current density ( $J_{sc}$ ), Open circuit potential ( $V_{oc}$ ), Fill Factor (FF) and the intensity of the incident light ( $I_{in}$ ) as follows:

$$Efficiency(\%) = \frac{V_{oc} \times J_{sc}}{I_{in}} \times FF \times 100$$

Usually efficiency is normalized over the effective area,  $A$  of the solar cell. The efficiency of the solar cell is calculated from the current-voltage curve (figure 1.16), produced by measuring photocurrent generated by the solar cell at different photo-induced voltages. In the photovoltaic industry, an air mass coefficient is used to standardize the incident solar radiation. This is referred as “AM” and a number. For AM 1.5 solar spectrum, the intensity of illumination is taken as  $1000 \text{ W/m}^2$ .

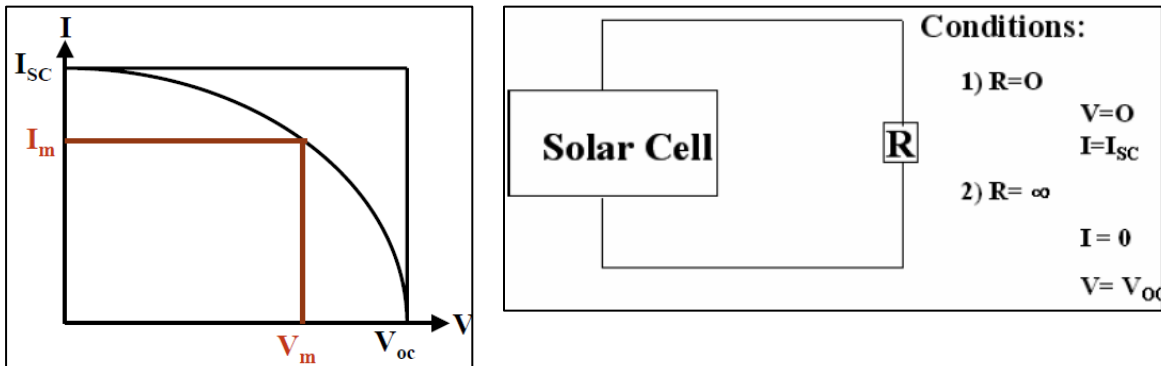


*Figure-1.16 Typical photocurrent–voltage curve obtained for solar cell.*

The fill factor of the solar cell is a measure of squareness of the I-V characteristic curve. FF is always less than 1 and is defined by the ratio of the maximum power ( $P_{\max}$ ) of the solar cell per unit area divided by the  $V_{oc}$  and  $J_{sc}$  according to

$$FF = \frac{I_m \times V_m}{I_{sc} \times V_{oc}}$$

Open circuit voltage,  $V_{oc}$  depends on  $I_{sc}$  and inversely on the recombination rates within the cell. The maximum voltage that can be obtained for DSSC is fixed for a  $TiO_2$  electrode and  $I/I_3^-$  redox mediator because the Fermi level of  $TiO_2$  depends on the electrolyte component and their concentrations. This is around 0.7-0.8 V. The short circuit current density  $J_{sc}$  can be expressed as,

$$J_{sc} = \Phi_{ET} \int qF(\lambda)[1 - r(\lambda)]LHE(\lambda)d\lambda$$

where  $\Phi_{ET}$  is electron transfer yield (averaged over wavelength) which is product of electron injection yield and the charge collection efficiency;  $F(\lambda)$  is incident photon flux density at wavelength  $\lambda$ ;  $r(\lambda)$  is the incident light loss before reaching the  $TiO_2$  film in the cell, for example, the reflection loss at interfaces; and  $LHE(\lambda)$  is the light harvesting efficiency at wavelength  $\lambda$ .

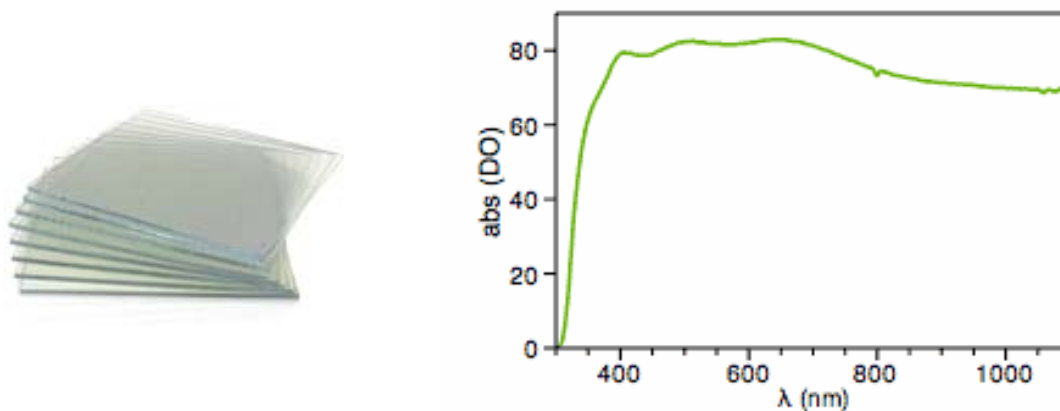
#### 1.4.1.6 Structure of DSSC

Figure 1.13 illustrates the structure of the dye sensitized solar cell. The dye sensitized solar cell consists of 5 main components: substrate, transparent conductive oxide coating (TCO), metal oxide coating, dye and electrolyte.

##### (a) Substrate

The electrode substrate used is a transparent conducting glass (TCO). It provides the mechanical integrity to the solar cell and protects it from the environment. TCO material used is usually Fluorine doped Tin Oxide (FTO) or tin doped indium oxide. This substrate should have low sheet resistance ( $10-15 \Omega / \square$ ) as this is where the electrons reach after travelling through  $TiO_2$  nanoparticles. Along with the conductivity, transparency of this substrate is also very crucial. Light has to pass through this substrate

and reach  $\text{TiO}_2$  which are loaded with dye molecules which in turn generate photo-electrons. Thus transparency and conductivity of this substrate plays an important role in fabrication of highly efficient DSSC. The anode in DSSC is Fluorine doped Tin Oxide (FTO) coated with  $\text{TiO}_2$  layers (few micron) while the cathode is FTO with a thin layer of sputtered platinum.



**Figure-1.17** TCO Sheets purchased from Solronix and its transmission data.

[<http://www.solaronix.com/products/tcolayers/tco2215>]

### Physical properties of TCO

**Table-1.1** Physical properties of TCO.

<b>Product designation:</b>	<b>TCO22-15</b>
Glass type:	Sodalime
Glass thickness	2.2 mm
Conducting layer:	FTO (fluorine tin oxide, $\text{SnO}_2:\text{F}$ )
Resistivity:	~15 ohm/square
Transmission:	> 80 % from 400 to 700 nm

**(b) Metal Oxide Layer**

The metal oxide coating ( $\text{TiO}_2/\text{ZnO}$ /binary oxides) is deposited on the top of the TCO by doctor blade coating or screen printing method. This coating provides a surface for the dye adsorption, accepts electrons from the excited dye, conducts electrons to the TCO and helps regeneration of the dye by permeating electrolyte through its structure. In order to perform these functions, the metal oxide synthesis, nanoparticle dispersion formulation and the film deposition method protocols need to be tuned meticulously.

**(c) The dye sensitizer**

The sensitizer, or dye monolayer, is the layer which interacts with the sunlight and therefore is a very important part of the DSSC. Typically the metal oxide films are immersed in the dye solution for 12 to 24 hours so that the dye molecules get adsorbed on the surface of the metal oxide nanoparticles. The structures and colours of different Ruthenium based organic dyes are shown in figure 1.18.

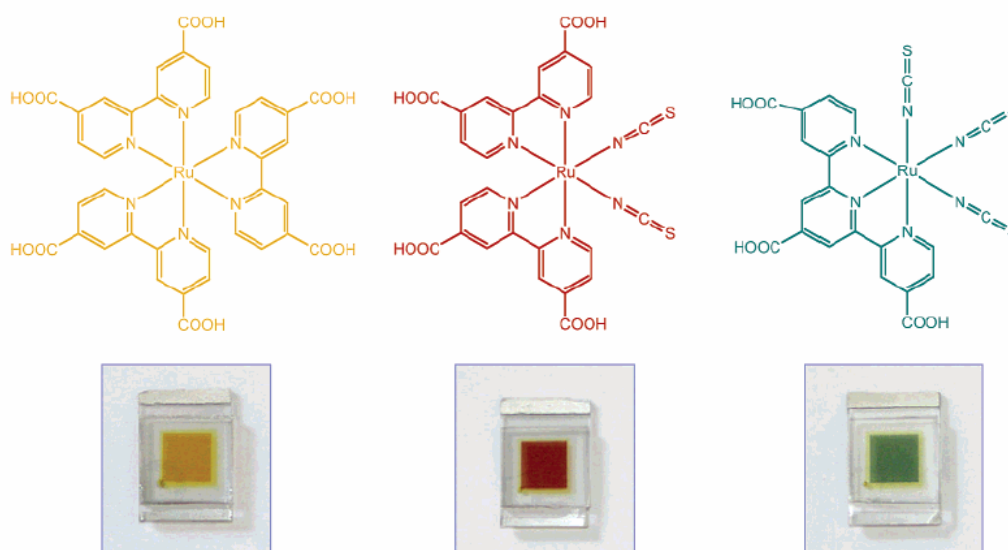


**Figure-1.18** Ruthenium based organic dyes [156]

**Ruthenizer 535-bisTBA (N719 Dye)**

Ruthenizer 535-bisTBA sensitizes very efficiently wide band-gap oxide semiconductors, like titanium dioxide, up to a wavelength of 750 nm. Ruthenizer 535-bisTBA is also

known as N719 in the literature, and has been so far one of the most efficient sensitizer in Dye Solar Cells. The structures of N719 dye is shown in figure 1.19.

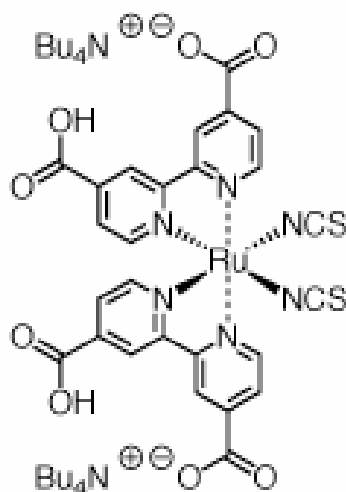


**Figure-1.19** Chemical Structure of Ruthenizer 535-bisTBA

[<http://www.solaronix.com/products/rutheniumdyes/ruthenizer535bisba>]

#### Physical properties of N719 Dye:

**Table 1.2** Physical properties of N719 Dye

<b>Product designation:</b>	<b>Ruthenizer 535 bis-TBA</b> (also known as "N719" or "dye salt")
<b>Molecular Formula:</b>	$C_{58}H_{36}O_8N_8S_2Ru$
<b>Formula Weight:</b>	1187.7 g/mol
<b>Aspect:</b>	Dark purple powder

**Ruthenizer 535 (N3 Dye)**

Ruthenizer 535 sensitizes very efficiently wide band-gap oxide semiconductors, like titanium dioxide, up to a wavelength of 750 nm. Ruthenizer 535 is also known as N3 in the literature, and has been so far one of the most efficient sensitizers in Dye Solar Cells. The structure of N3 dye is shown in figure 1.20.

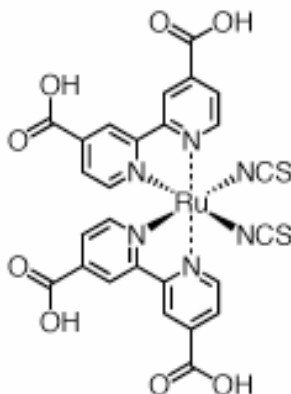


**Figure-1.20** Chemical Structure of Ruthenizer 535

[<http://www.solaronix.com/products/rutheniumdyes/ruthenizer535/>]

**Physical properties of N3 Dye**

**Table-1.3** Physical properties of N3 Dye

<b>Product designation:</b>	<b>Ruthenizer 535</b> (also known as "N3")
<b>Molecular Formula:</b>	$C_{26}H_{20}O_{10}N_6S_2Ru$
<b>Formula Weight:</b>	741.7 g/mol
<b>Aspect:</b>	Dark purple powder

**(d) The Electrolyte**

The electrolyte is a reduction-oxidation (redox) system of molecules, typically based on iodine and iodide. The electrolyte reduces the dye sensitizer after photo excitation and in turn gets reduced at the counter electrode. The iodine/iodide electrolyte is produced

simply by mixing iodine with an iodide salt in an appropriate solvent, such as acetonitrile or methoxypropionitrile. The liquid phase of the electrolyte helps to fill all of the pores and small crevices in the mesoporous electrode, allowing for rapid reduction of the dye in all places. But at the same time the solvent based electrolyte gets degraded in air and evaporates at higher temperatures (80-85<sup>0</sup>C) requiring perfect sealing of the cell.

### **1.5 Objective and outline of the thesis**

The main objective of the present work was to synthesize functionalized nanomaterials with shape and functionality control and explore them for the DSSC application. The thesis consists of five chapters including this introductory chapter; it consists of the following chapters.

The key concepts in nanoscience and a literature survey of the properties and applications of nanomaterials have been discussed in the previous sections. These constitute the **First Chapter**.

In the **Second Chapter**, a brief overview of the techniques used for the synthesis of functionalized metal oxide nanomaterials is presented. Furthermore, a general outline of the instruments and methods used for the characterization of these nanomaterials is also presented.

The **Third Chapter** discusses the synthesis of TiO<sub>2</sub> nanoparticles dressed with gold nanoparticles by the hydrothermal process by using mixed precursor and controlled conditions. We attempted to explore the application of such a synthesized nanocomposite in the context of Dye Sensitized Solar Cells. It is shown that the DSSCs made using TiO<sub>2</sub>-Au plasmonic nanocomposite yield superior performance with conversion efficiency considerably higher than that that with only TiO<sub>2</sub> nanoparticles.

In the **Fourth Chapter**, high (~7.4%) conversion efficiency is realized in DSSCs based on a hydrothermally synthesized TiO<sub>2</sub>-MWCNT nanocomposite. This represents a ~50% improvement vis-a-vis cells made with hydrothermally synthesized TiO<sub>2</sub> without

MWCNT or the Degussa P25 powder. FTIR data suggest that the -COOH groups open up on the surface of MWCNT under hydrothermal processing conditions and these conjugate with the Ti precursor to yield a composite. This integral conjugation appears to be effective in the charge-transfer process. The second part of this chapter discusses the synthesis of TiO<sub>2</sub>-Graphene nanocomposites also for the Dye Sensitized Solar Cell application.

In the **Fifth Chapter**, we report on the synthesis of various ZnO mesostructures (rods, spheres, flakes and flower-like morphologies) by hydrothermal and co-precipitation methods, and their remarkable and complete transformation into anatase TiO<sub>2</sub> mesostructures with nominally similar shapes using controlled low temperature TiCl<sub>4</sub> treatment. Various techniques are used to demonstrate the phase purity and morphology details. Based on the careful examination of the transformation of ZnO nanorods into TiO<sub>2</sub> tubes we suggest a mechanism which embodies initial formation of a thin TiO<sub>2</sub> shell on the ZnO surface by ion exchange (Ti<sup>4+</sup> - Zn<sup>2+</sup>) followed by Zn diffusion through the shell and its oxidation on the surface. We used these converted TiO<sub>2</sub> mesostructures for light harvesting in Dye Sensitized Solar Cells (DSSC) to enhance the conversion efficiency.

The **Sixth Chapter** summarizes the work described in this thesis by presenting the salient features of the work and also mentions the possible avenues for future investigations.

### 1.6 References

1. <http://www.nanotechnologyresearchfoundation.org/images/applications.jpg>.
2. E. Regis, Nano: The Emerging Science of Nanotechnology—Remaking the World-Molecule by Molecule, Little Brown and Company, Boston, **1995**.
3. C. Burda, X. Chen, R. Narayanan, M. A. El-Sayed, *Chem. Rev.*, **2005**, *105*, 1025.
4. G. Schmid, Ed.; VCH, Weinheim, **1994**.
5. A. P. Alivisatos, *J. Phys. Chem.* **1996**, *100*, 13226.
6. C. Ellert, M. Schmidt, C. Schmitt, T. Reiners, H. Haberland, *Phys. Rev. Lett.* **1995**, *75*, 1731.

## Chapter-1

7. W. P. Halperin, *Rev. Mod. Phys.* **1986**, 58, 533.
8. U. Simon, *Adv. Mater.* **1998**, 10, 1487.
9. A. P. Alivisatos, *ACS Nano*, 2008.
10. A. Henglein, *J. Phys. Chem.*, **1993**, 97, 5457.
11. Burda, C.; Chen, X.; Narayanan, R.; El-Sayed, M. A. *Chem. Rev.*, 2005, 105, 1025.
12. Kelly, K.L.; Coronado, E.; Zhao, L.L.; Schatz, G.C. *J. Phys. Chem. B*, 2003, 107, 668.
13. L. M. Liz-Marzán, *Langmuir*, **2006**, 22, 32.
14. G. Mie, *Ann. Phys.*, **1908**, 25, 377.
15. P. Mulvaney, *Langmuir*, **1996**, 12, 788.
16. M. Brust, M. Walker, D. Bethell, D.J. Schiffrin, R.J. Whyman, *Chem Commun.*, **1994**, 801.
17. M.D. Malinsky, K.L. Kelly, G.C. Schatz, R.P. VanDuyne, *J. Am. Chem. Soc.*, **2001**, 123, 1471.
18. A.C. Templeton, W.P. Wvelfing, R.W. Murray, *Acc. Chem. Res.*, **2000**, 33, 27.
19. C. D. Keating, K. M. Kovalski, M. J. Natan, *J. Phys. Chem. B.*, **1998**, 102, 9404.
20. H. Xu, E. J. Bjerneld, M. Kall, L. Borjesson, *Phy. Rev. Lett.*, **1999**, 83, 4357.
21. A. L. Crumbliss, S. C. Perine, J. Stonehuerner, K. R. Tubergen, J. Zhao, J. P. O'Daly, *Biotech. Bioeng.*, **1992**, 40, 483.
22. A. Gole, C. Dash, V. Ramakrishnan, S. R. Sainkar, A. B. Mandale, M. Rao, M. Sastry, *Langmuir*, **2001**, 17, 1674.
23. S.A. Maier, M.L. Brongersma, P.G. Kik, S. Meltzer, A.A.G. Requicha, H.A. Atwater, *Adv. Mater.*, **2001**, 13, 1501.
24. S. B. Darling, S. D. Bader, *J. Mater. Chem.*, **2005**, 15, 4189.
25. Y. W. Jun, J. W. Seo, A. Cheon, *Acc. Chem. Res.*, **2008**, 41, 179.
26. K. M. Krishnan, A. B. Pakhomov, Y. Bao, P. Blomqvist, Y. Chun, M. Gonzales, K. Griffin, X. Ji, B. K. Roberts, *J. Mater. Sci.*, **2006**, 41, 793.
27. C. P. Bean, Livingston, J. D. *J. Appl. Phys.*, **1959**, 30, S120.
28. D. L. Leslie-Pelecky, R. D. Rieke, *Chem. Mater.* **1996**, 8, 1770.
29. U. Jeong, X. Teng, Y. Wang, H. Yang, Y. Xia, *Adv. Mater.* **2007**, 19, 33.

30. P. Tartaj, *Eur. J. Inorg. Chem.*, **2009**, 333.
31. J. R. Weertman, R. S. Averback, "Nanomaterials: synthesis, properties, and applications" eds. Edelstein, A.S. Cammarata, R.C. *London institute of Phys. Publ.*, **1996**, chapter 13, 323.
32. T. Castro, R. Reifengerger, E. Choi, R. P. Andres, *Phys. rev., B, Condens. matter*, **1990**, *13*, 8548.
33. C. Noguera, *Physics and Chemistry at Oxide Surfaces*; Cambridge University Press: Cambridge, UK, **1996**.
34. H. H. Kung, *Transition Metal Oxides: Surface Chemistry and Catalysis*; Elsevier: Amsterdam, **1989**.
35. V. E. Henrich, P. A. Cox, *The Surface Chemistry of Metal Oxides*; Cambridge University Press: Cambridge, UK, **1994**.
36. A. F. Wells, *Structural Inorganic Chemistry*, 6th ed.; Oxford University Press: New York, **1987**.
37. W. A. Harrison, *Electronic Structure and the Properties of Solids*; Dover: New York, **1989**.
38. R. W. G. Wyckoff, *Crystal Structures*, 2nd ed.; Wiley: New York, **1964**.
39. M. Shelef, G. W. Graham, R. W. McCabe, In *Catalysis by Ceria and Related Materials*; Trovarelli, A., Ed.; Imperial College Press: London, **2002**; Chapter 10.
40. D. Stirling, *The Sulfur Problem: Cleaning Up Industrial Feedstocks*; Royal Society of Chemistry: Cambridge, **2000**.
41. A. Sherman, *Chemical Vapor Deposition for Microelectronics: Principles, Technology and Applications*; Noyes publications: Park Ridge, NJ, **1987**.
42. P. Ayyub, V. R. Palkar, S. Chattopadhyay, M. Multani, *Phys. Rev. B.*, **1995**, *51*, 6135.
43. (a) N. Millot, D. Aymes, F. Bernard, J. C. Niepce, A. Traverse, F. Bouree, B. L. Cheng, P. Perriat, *J. Phys. Chem. B*, **2003**, *107*, 5740. (b) J. Schoiswohl, G. Kresse, S. Surnev, M. Sock, M. G. Ramsey, F. P. Netzer, *Phys. Rev. Lett.* **2004**, *92*, 206103.
44. J. M. McHale, A. Auroux, A. J. Perrota, A. Navrotsky, *Science*, **1997**, *277*, 788.
45. H. Zhang, J. F. Bandfield, *J. Mater. Chem.*, **1998**, *8*, 2073.

## Chapter-1

46. Z. Song, T. Cai, Z. Chang, G. Liu, J. A. Rodriguez, J. Hrbek, *J. Am. Chem. Soc.*, **2003**, *125*, 8060.
47. M. D. Herná'ndez-Alonso, A. B. Hungri'a, J. M. Coronado, A. Martí'nez-Arias, J. C. Conesa, J. Soria, M. Ferná'ndez-Garci'a, *Phys. Chem. Chem. Phys.*, **2004**, *6*, 3524.
48. R. C. Cammarata, K. Sieradki, *Phys. Rev. Lett.*, **1989**, *62*, 2005.
49. X. Wang, J. Hanson, G. Liu, J. A. Rodriguez, A. Iglesias-Juez, M. Fernandez-Garcia, *J. Chem. Phys.*, **2004**, *121*, 5434.
50. A. D. Yoffre, *Adv. Phys.*, **1993**, *42*, 173.
51. L. Brus, *J. Phys. Chem.*, **1986**, *90*, 2555.
52. Albaret, T.; Finocchi, F.; Noguera, C. *Faraday Discuss.*, **2000**, *114*, 285.
53. J. A. Rodriguez, A. Maiti, *J. Phys. Chem. B*, **2000**, *104*, 3630.
54. J. A. Rodriguez, T. Jirsak, S. Chaturvedi, *J. Chem. Phys.*, **1999**, *111*, 8077.
55. T. Bredow, E. Apra, M. Catti, G. Pacchioni, *Surf. Sci.*, **1998**, *418*, 150.
56. M. Casarin, C. Maccato, A. Vittadini, *Surf. Sci.*, **1997**, *587*, 377-379.
57. C. A. Scamehorn, N. M. Harrison, M. I. McCarthy, *J. Chem. Phys.*, **1994**, *101*, 1547.
58. J. A. Rodriguez, *Theor. Chem. Acc.*, **2002**, *107*, 117.
59. J. A. Rodriguez, S. Chaturvedi, M. Kuhn, J. Hrbek, *J. Phys. Chem. B*, **1998**, *102*, 5511.
60. R. Hoffmann, *Solids and Surfaces: A Chemist's View of Bonding in Extended Structures*; VCH: New York, **1988**.
61. T. A. Albright, J. K. Burdett, M. H. Whangbo, *Orbital Interactions in Chemistry*; Wiley-Interscience: New York, **1985**.
62. E. Lucas, S. Decker, A. Khaleel, A. Seitz, S. Futzl, A. Ponce, W. Li, C. Carnes, K. J. Klabunde, *Chem. Eur. J.*, **2001**, *7*, 2505.
63. J. L. Anchell, A. C. Hess, *J. Phys. Chem.*, **1996**, *100*, 18317.
64. J. A. Rodriguez, J. Hrbek, J. Dvorak, T. Jirsak, A. Maiti, *Chem. Phys. Lett.*, **2001**, *336*, 377.
65. A. M. Ferrari, G. Pacchioni, *J. Phys. Chem.*, **1995**, *99*, 17010.
66. H. Bosh, F. Janssen, *Catal. Today*, **1988**, *2*, 369.

67. P. Forzatti, *Catal. Today*, **2000**, 62, 51.
68. M. R. Hoffman, S. T. Martin, W. Choi, D. W. Wahneman, *Chem. Rev.*, **1995**, 95, 69.
69. A. Maldoti, A. Molinari, R. Amadeni, *Chem. Rev.*, **2002**, 102, 3811.
70. K. Kalyanasendevan, M. Gratzel, D. M. Roundhill, J. P. Fackler, *Optoelectronics Properties of Inorganic Compounds*; Eds.; Plenum: New York, **1999**; pp 169-194.
71. G. Sheveglieri, Ed.; *Gas Sensors*; Kluwer: Dordrecht, **1992**.
72. R. W. Johnson, E. S. Thieles, R. H. French, *Tappi. J.*, **1997**, 80, 233.
73. L. G. Phillips, D. M. Barbeno, *J. Dairy Sci.* **1997**, 80, 2726.
74. H. Selhofer, *Vacuum Thin Films*, August **1999**, 15.
75. A. Fujishima, T. N. Rao, D. A. Tryk, *J. Photochem. Photobiol. C: Photochem. Rev.*, **2000**, 1, 1.
76. C. Sousa, F. Illas, *Phys. Rev. B*, **1994**, 50, 13974.
77. P. Bonhole, E. Gogniat, M. Gratzel, P. V. Ashrit, *Thin Solid Films*, **1999**, 350, 269.
78. H. Zhang, J. F. Banfield, *J. Phys. Chem. B*, 2000, 104, 3481.
79. X. Z. Ding, X.-H. Liu, *J. Mater. Res.*, **1998**, 13, 2556.
80. Y. Hu, H.-L. Tsai, C.-L. Huang, *Mater. Res. Eng. A.*, **2003**, 344, 209.
81. P. I. Gouma, M. J. Millis, *J. Am. Ceram. Soc.* **2001**, 84, 619.
82. R. L. Penn, J. F. Banfield, *Am. Mineral.* **1999**, 84, 1231.
83. N. Serpone, D. Lawless, R. Khairutdinov, *J. Phys. Chem.* **1995**, 98, 16646.
84. K. M. Reddy, S. V. Manorama, A. R. Reddy, *Mater. Chem. Phys.* **2002**, 78, 239.
85. E. Yagi, R. Hasiguti, *Phys. Rev. B*, **1996**, 54, 7945.
86. D. J. Smith, L. A. Bursill, M. G. Blanchin, *Philos. Magn. A*, **1984**, 50, 473.
87. J. Muscat, V. Swamy, N. M. Harrison, *Phys. Rev. B.*, **2002**, 65, 224112.
88. P. Knauth, H. L. Tuller, *J. Appl. Phys.*, **1999**, 85, 897.
89. (a) J. Joo, S. G. Kwon, T. Yu, M. Cho, J. Lee, J. Yoon, T. Hyeon, *J. Phys. Chem. B*, **2005**, 109, 15297. (b) S. Y. Chae, M. K. Park, S. K. Lee, T. Y. Kim, S. K. Kim, W. I. Lee, *Chem. Mater.*, **2003**, 15, 3326. (c) D. Chatterjee, S. Dasgupta, *J. Photochem. Photobiol. C*, **2005**, 6, 186. (d) S. Mozia, M. Tomaszewska, A. W. Morawski, *Desalination*, **2005**, 185, 449.

90. N. Mahmoodi, M. Arami, N. Limaee, N. Tabrizi, *Chem. Eng. J.*, **2005**, *112*, 191.
91. J. Park, G. Maltzahn, L. Zhang, M. P. Schwartz, E. Ruoslahti, S. N. Bhatia, M. J. Sailor, *Adv. Mater.*, **2008**, *20*, 1630.
92. M. Ni, M. K. H. Leung, D. Y. C. Leung, K. Sumathy, *Renewable Sustainable Energy Rev.*, **2007**, *11*, 401.
93. (a) A. Fujishima, *Science*, **2003**, *301*, 1673. (b) G. R. Torres, T. Lindgren, J. Lu, C. G. Granqvist, S. E. Lindquist, *J. Phys. Chem. B*, **2004**, *108*, 5995.
94. (a) M. Jakob, H. Levanon, P.V. Kamat, *Nano Lett.*, **2003**, *3*, 353. (b) Y. Ohko, T. Tatsuma, T. Fujii, K. Naoi, C. Niwa, Y. Kubota, A Fujishima, *Nature Mater.*, **2003**, *2*, 29. (c) Li et.al., *Environ. Sci. Technol.*, **2008**, *42*, 2130.
95. (a) M. Grätzel, *Nature*, **2001**, *414*, 338. (b) M. Grätzel, *MRS Bull.*, **2005**, *30*, 23.
96. Z. R. Tian, J. Liu, J. A. Voigt, B. Mckenzie, X. Huifang, *Angew. Chem., Int. Ed.*, **2003**, *42*, 413.
97. X. Wang, C. J. Summers, Z. L. Wang, *Nano Lett.*, **2004**, *4*, 423.
98. X. Fan, M. L. Zhang, I. Shafiq, W. J. Zhang, C. S. Lee and S. T. Lee, *Adv. Mater.*, **2009**, *21*, 2393.
99. M. H. Huang, Y. Wu, H. Feick, N. Tran, E. Weber and P. Yang, *Adv. Mater.*, **2001**, *13*, 113.
100. B. D. Yao, Y. F. Chan and N. Wang, *Appl. Phys. Lett.*, **2002**, *81*, 757.
101. L. E. Greene, M. Law, D. H. Tan, M. Montano, J. Goldberger, G. Somorjai and P. Yang, *Nano Lett.*, **2005**, *5*, 1231.
102. C. Liu, J. A. Zapien, Y. Yao, X. Meng, C. S. Lee, S. Fan, Y. Lifshitz and S. T. Lee, *Adv. Mater.*, **2003**, *15*, 838.
103. M. Ahmad, R. ud-Din, C. Pan and J. Zhu, *J. Phys. Chem. C*, **2010**, *114*, 2560.
104. B. Liu and H. C. Zeng, *J. Am. Chem. Soc.*, **2003**, *125*, 4430.
105. M. Guo, P. Diao and S. Cai, *J. Solid State Chem.*, **2005**, *178*, 1864.
106. W. I. Park, Y. H. Jun, S. W. Jung and G.-C. Yi, *Appl. Phys. Lett.*, **2003**, *82*, 964.
107. A. B. Hartanto, X. Ning, Y. Nakata and T. Okada, *Appl. Phys. A: Mater. Sci. Process.*, **2004**, *78*, 299.
108. W. D. Yu, X. M. Li and X. D. Gao, *Appl. Phys. Lett.*, **2004**, *84*, 2658.
109. M. Ahmad, C. Pan, J. Iqbal, L. Gan and J. Zhu, *Chem. Phys. Lett.*, **2009**, *480*, 105.

110. Y. Dai, Y. Zhang and Z. L. Wang, *Solid State Commun.*, **2003**, 126, 629.
111. M. Ahmad, C. Pan, J. Zhao, J. Iqbal and J. Zhu, *Mater. Chem. Phys.*, **2010**, 120, 319.
112. H. Yan, R. He, J. Pham and P. Yang, *Adv. Mater.*, **2003**, 15, 402.
113. Z. W. Pan, Z. R. Dai and Z. L. Wang, *Science*, **2001**, 291, 1947.
114. H. Yan, J. Johnson, M. Law, R. He, K. Knutsen, J. R. McKinney, J. Pham, R. Saykally and P. Yang, *Adv. Mater.*, **2003**, 15, 1907.
115. Y. B. Li, Y. Bando, T. Sato and K. Kurashima, *Appl. Phys. Lett.*, **2002**, 81, 144.
116. Z. L. Wang, X. Y. Kong, Y. Ding, P. Gao, W. L. Hughes, R. Yang and Y. Zhang, *Adv. Funct. Mater.*, **2004**, 14, 943.
117. P. X. Gao and Z. L. Wang, *Appl. Phys. Lett.*, **2004**, 84, 2883.
118. X. Y. Kong and Z. L. Wang, *Nano Lett.*, **2003**, 3, 1625.
119. Q. Wan, Q. H. Li, Y. J. Chen, T. H. Wang, X. L. He, J. P. Li and C. L. Lin, *Appl. Phys. Lett.*, **2004**, 84, 3654.
120. B. S. Kang, F. Y. Ren, W. Heo, L. C. Tien, D. P. Norton and S. J. Pearton, *Appl. Phys. Lett.*, **2005**, 86, 112105.
121. F. Zhang, X. Wang, S. Ai, Z. Sun, Q. Wan, Z. Zhu, Y. Xian, L. Jin and K. Yamamoto, *Anal. Chim. Acta*, **2004**, 519, 155.
122. T. L. Sounart, J. Liu, J. A. Voigt, J. Hsu, E. D. Spoeerke, Z. Tian, Y. Jiang, *Adv. Funct. Mater.*, **2006**, 16, 335.
123. Q. Zhang, C. S. Dandeneau, X. Zhou, G. Cao, *Adv. Mater.* **2009**, 21, 4087.
124. M. Saito, S. Fujihara, *Energy Environ. Sci.*, **2008**, 1, 280.
125. K. Keis, J. Lindgren, S. E. Lindquist, A. Hagfeldt, *Langmuir*, **2000**, 16, 4688.
126. Energy Information Administration, International Energy Outlook **2010**, April 2010 ([www.eia.doe.gov/oiaf/ieo/index.html](http://www.eia.doe.gov/oiaf/ieo/index.html)).
127. BP, Statistical Review of World Energy, June 2006.
128. M. A. Green, *Third Generation PhotoVoltaics: AdVanced Solar Energy ConVersion*; Springer-Verlag: Berlin, Heidelberg, **2003**.
129. W. West, *Photogr. Sci. Eng.*, **1974**, 18, 35.
130. J. Moser, *Monatsch. Chem.*, **1887**, 8, 373.
131. S. Namba, Y. Hishiki, *J. Phys. Chem.*, **1965**, 69, 774.

132. R. C. Nelson, *J. Phys. Chem.*, **1965**, 69, 714.
133. J., Bourdon *J. Phys. Chem.*, **1965**, 69, 705.
134. H. Gerischer, H. Tributsch, Ber. Bunsenges. *Phys. Chem.*, **1968**, 72, 437.
135. H. Gerischer, H. Tributsch, Ber. Bunsenges. *Phys. Chem.*, **1969**, 73, 251.
136. H. Gerischer, *Electroanal. Chem. Interfac. Electrochem.*, **1975**, 58, 263.
137. H. Tsubomura, M. Matsumura, Y. Noyamaura, T. Amamiya, *Nature*, **1976**, 261, 402.
138. W. D. K. Clark, N. Sutin, *J. Am. Chem. Soc.*, **1977**, 99, 4676.
139. S. Anderson, E. C. Constable, M. P. Dare-Edwards, J. B. Goodenough, A. Hamnett, K. R. Seddon, R. D. Wright, *Nature*, **1979**, 280, 571.
140. H. Gerischer, *Photochem. Photobiol.*, **1972**, 16, 243.
141. R. Memming, *Photochem. Photobiol.*, **1972**, 16, 325.
142. A. Fujishima, T. Watanabe, O. Tatsuoki, K. Honda, *Chem. Lett.*, **1975**, 4, 13.
143. T. S. Jayadevaiah, *Appl. Phys. Lett.*, **1974**, 25, 399.
144. A. Hamnett, M. P. Dare-Edwards, R. D. Wright, K. R. Seddon, J. B. Goodenough, *J. Phys. Chem.*, **1979**, 83, 3280.
145. M. P. Dare-Edwards, J. B. Goodenough, A. Hamnett, K. R. Seddon, R. D. Wright, *Faraday Discuss. Chem. Soc.*, **1980**, 70, 285.
146. A. Fujishima, K. Honda, *Bull. Chem. Soc. Jap.*, **1971**, 44, 1148.
147. A. Fujishima, K. Honda, *Nature*, **1972**, 238, 37.
148. D. Duonghong, N. Serpone, M. Grätzel, *Helv. Chim. Acta*, **1984**, 67, 1012.
149. J. DeSilvestro, M. Grätzel, L. Kavan, J. Moser, J. Augustynski, *J. Am. Chem. Soc.*, **1985**, 107, 2988.
150. N. Vlachopoulos, P. Liska, J. Augustynski, M. Grätzel, *J. Am. Chem. Soc.*, **1988**, 110, 1216.
151. O'Regan B.; Grätzel, M. *Nature*, 1991, 353, 737.
152. M. K. Nazeeruddin, A. Kay, I. Rodicio, R. Humphry-Baker, E. Müller, P. Liska, N. Vlachopoulos, M. Grätzel, *J. Am. Chem. Soc.*, **1993**, 115, 6382.
153. M. K. Nazeeruddin, P. Pechy, M. Grätzel, *Chem. Commun.*, **1997**, 1075.
154. B. A. Gregg, M. C. Hanna, *J. Appl. Phys.*, **2003**, 93, 3605.

## Chapter-1

155. F. Nour-Mohhamadi, S. D. Nguyen, G. Boschloo, A. Hagfeldt, T. Lund, *J. Phys. Chem. B*, **2005**, *109*, 22413.
156. M. Gratzel, *Inorg. Chem.*, **2005**, *44*, 6841.

## **Chapter-2**

### **Synthesis and Characterizations Techniques**

*This chapter presents a brief description of the nanomaterials synthesis methods used in the doctoral work, such as hydrothermal, sol-gel and co-precipitation. This follows with the discussion on various experimental tools employed to characterize the structural, optical and electrical properties of the synthesized nanomaterials. A detailed description of fabrication of Dye Sensitized Solar cells along with various properties is also included.*

## Section-I

### 2. I Synthesis Technique

During the past decade, scientists have developed techniques for synthesizing and characterizing many new materials with at least one dimension on the nanoscale, including nanoparticles, nanolayers, nanotubes and nanocomposites [1]. Still, the design and synthesis (or fabrication) of nanoscale materials with controlled properties is a significant and ongoing challenge within nanoscience and nanotechnology.

Nanoscience is still largely in the “discovery phase” wherein new materials are being synthesized on small scales (hundreds of milligrams or less) for testing specific physical properties. Typically, during this phase of development of a new technology area, researchers focus mainly on identifying new properties and applications. The nature of engineered nanomaterials and their proposed uses provides compelling reasons for the implementation of green chemistry in the development of the new materials and applications. The technology is early in development and expected to be widely applied and distributed. These materials are expected to (i) exhibit new size-based properties (both beneficial and detrimental) that are intermediate between molecular and particulate, (ii) incorporate a wide range of elemental and material compositions, including organics, inorganics, and hybrid structures, and (iii) possess a high degree of surface functionality.

The synthesis of multi-functional metal oxides nanomaterials under technological desirable low temperature conditions with controlled size, shape and pure phase remains a major task for the scientists. Soft chemistry routes represent the most attractive alternatives, because they allow good control from the molecular precursors to the final product at low processing temperatures, result in the formation of nanomaterials with high purity and compositional homogeneity with advantages such as (i) wet chemical control on oxidation states, (ii) ability to template various nanostructures, (iii) relatively cheap, (iv) able to form nano, meso and micron sized particles and thin films. The present research work is mainly on hydrothermal, sol-gel and co-precipitation methods for syntheses of oxide nanomaterials.

### **2. I.1 Hydrothermal methods**

The hydrothermal technique is becoming one of the most important tools for advanced materials processing, particularly owing to its advantages in the processing of nanostructural materials for a wide variety of technological applications such as electronics, optoelectronics, catalysis, ceramics, magnetic data storage, biomedical, biophotonics, etc. The hydrothermal technique not only helps in processing monodispersed and highly homogeneous nanoparticles, but also acts as one of the most attractive techniques for processing nano-hybrid and nanocomposite materials.

Hydrothermal processing can be defined as any heterogeneous reaction in the presence of aqueous solvents or mineralizers under high pressure and temperature conditions to dissolve and recrystallize (recover) materials that are relatively insoluble under ordinary conditions. Among various technologies available today in advanced materials processing, the hydrothermal technique occupies a unique place owing to its advantages over conventional technologies. It covers processes like hydrothermal synthesis, hydrothermal crystal growth leading to the preparation of fine to ultra fine crystals, bulk single crystals, hydrothermal transformation, hydrothermal sintering, hydrothermal decomposition, hydrothermal stabilization of structures, hydrothermal dehydration, hydrothermal extraction, hydrothermal treatment, hydrothermal phase equilibria, hydrothermal electrochemical reactions, hydrothermal recycling, hydrothermal microwave supported reactions, hydrothermal mechanochemical, hydrothermal sonochemical, hydrothermal electrochemical processes, hydrothermal fabrication, hot pressing, hydrothermal metal reduction, hydrothermal leaching, hydrothermal corrosion, and so on. The hydrothermal processing of advanced materials has lots of advantages and can be used to give high product purity and homogeneity, crystal symmetry, metastable compounds with unique properties, narrow particle size distributions, a lower sintering temperature, a wide range of chemical compositions, single-step processes, dense sintered powders, sub-micron to nanoparticles with a narrow size distribution using simple equipment, lower energy requirements, fast reaction times, lowest residence time, as well as for the growth of crystals with polymorphic modifications, the growth of crystals with low to ultra low solubility, and a host of other applications. The duration of

experiments is being reduced at least by 3-4 orders of magnitude, which will in turn, make the technique more economic. With an ever-increasing demand for composite nanostructures, the hydrothermal technique offers a unique method for coating of various compounds on metals, polymers and ceramics as well as for the fabrication of powders or bulk ceramic bodies.

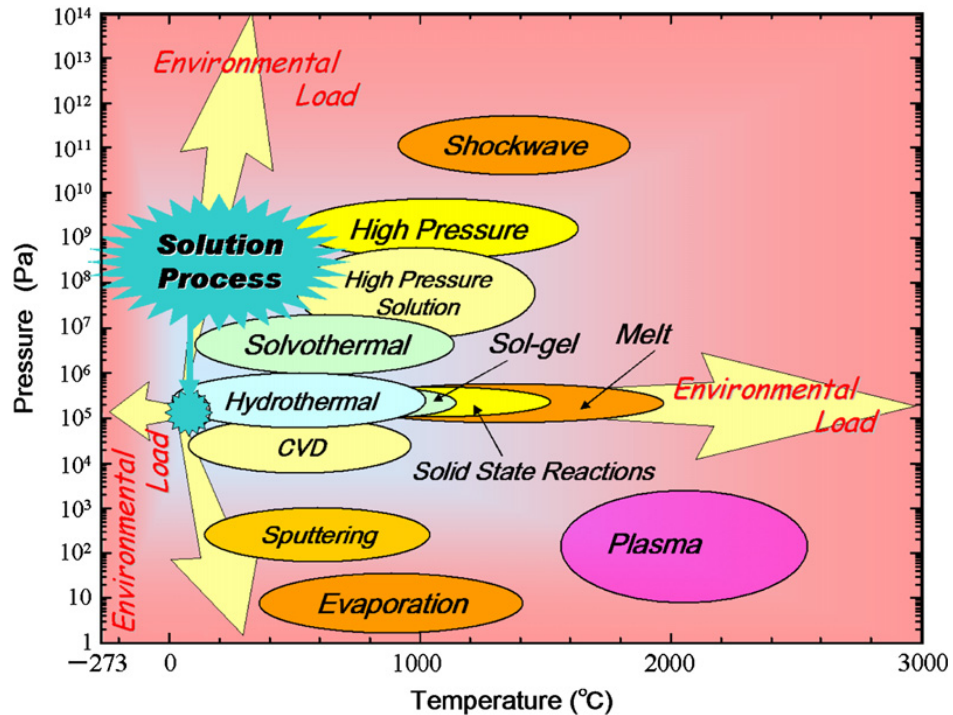


*Figure-2.1 Pressure temperature map of materials processing techniques [2].*

The hydrothermal processing of materials is a part of solution processing and it can be described as super heated aqueous solution processing. Figure 2.1 shows the pressure temperature map of various materials processing techniques [2, 3]. According to this, the hydrothermal processing of advanced materials can be considered as environmentally benign. Besides, for processing nanomaterials, the hydrothermal technique offers special advantages because of the highly controlled diffusivity in a strong solvent media in a closed system. Nanomaterials require control over their physicochemical characteristics, if they are to be used as functional materials.

Hydrothermal technology as mentioned earlier in a strict sense also covers supercritical water (SCW) or supercritical fluid (SCF) technology, which is gaining momentum in the last 1½ decades owing to its enormous advantages in the yield and speed of production of nanoparticles and also in the disintegration, transformation, recycling and treatment of various substances including toxic organics, wastes, etc. In case of supercritical water technology, water is used as the solvent in the system, whereas supercritical fluid technology is a general term when solvents like CO<sub>2</sub> and several other organic solvents are used, and because these solvents have lower critical temperature and pressure compared to water this greatly helps in processing the materials at much lower temperature and pressure conditions.

Supercritical water and supercritical fluids provide an excellent reaction medium for hydrothermal processing of nanoparticles, since they allow varying the reaction rate and equilibrium by shifting the dielectric constant and solvent density with respect to pressure and temperature, thus giving higher reaction rates and smaller particles. The reaction products are to be stable in SCF leading to fine particle formation. Further, the technique facilitates issues like energy saving, the use of larger volume equipment, better nucleation control, avoidance of pollution, higher dispersion, higher rates of reaction, better shape control, and lower temperature operations in the presence of the solvent.

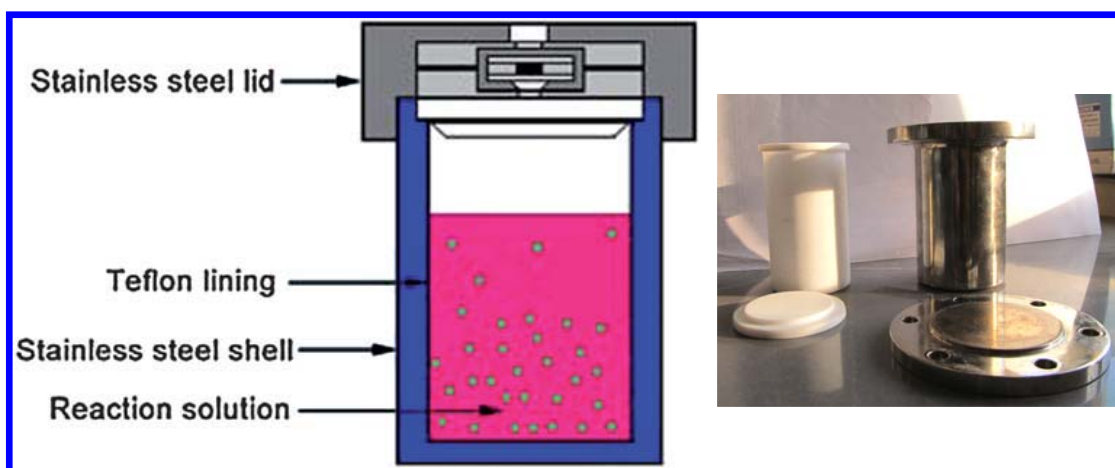


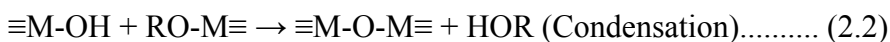
**Figure-2.2** A schematic of a Teflon-lined, stainless autoclave [4]. The inset shows the photo of Stainless steel autoclave with Teflon liner typically used in the laboratory.

Hydrothermal synthesis is normally conducted in steel pressure vessels called ‘autoclaves’ or ‘bombs’ with or without Teflon liners under controlled temperature and/or pressure with the reaction in aqueous solutions (figure-2.2). The temperature can be elevated above the boiling point of water, reaching the pressure of vapor saturation. The temperature and the amount of solution added to the autoclave largely determine the internal pressure produced.

### 2.1.2 Sol-gel technique

The sol-gel technique is one of the most widely used soft chemical methods and mainly applied for the synthesis of metal and semimetal oxides. In this process, oxides are synthesized by the formation of an oxide network directly in solution by hydrolysis of alkoxides, followed by gelation and finally by removal of the solvent [5]. In contrast to the solid-state method, a wet chemical synthesis can provide homogenous nanosized oxides of high purity at lower reaction temperatures. Sol-gel and aerogel processes are the most widely used routes and involve a colloidal sol which is converted into a gel during aging [6, 7].

The main principle of the classical sol-gel process is the controlled hydrolysis of metallo-organic compounds (alkoxides) in an organic solvent. The sol-gel process involves olation (formation of hydroxyl bridges) and oxolation (formation of oxygen bridges) reactions during hydrolysis (reactions 2.1-2.3). The oxolation condensation reaction is responsible for the formation of colloidal agglomerates, and the olation addition reaction is responsible for their aggregation into a polymeric gel.



Where R is alkyl group and M is metal or semimetal.

The gel formation depends on different parameters including the nature of starting material(s) (precursor[s]), kind of solvent, precursor concentration in the solvent, alkoxy

to water ratio, temperature of the reaction, pH, kind of catalyst, stirring and aging time. Metal alkoxides serve as starting materials and can be hydrolyzed by water. The alkoxides have been extensively used for the production of oxides and glasses. During hydrolysis, alkoxy groups are replaced by strong  $\text{OH}^-$  nucleophiles, and the following condensation and addition steps lead to the formation of oxide chains. The sol-gel synthesis goes through the formation of a sol of colloidal particles or units in a solution, gelation of the sol by the agglomeration of these particles or sub-units into a big gel network structure, removing of the solvent, and heat treatment to transfer gel into solid. Depending on reaction conditions, the sol particles may grow further or form gel. The sol-gel process can be used for the preparation of a variety of materials (figure 2.3).

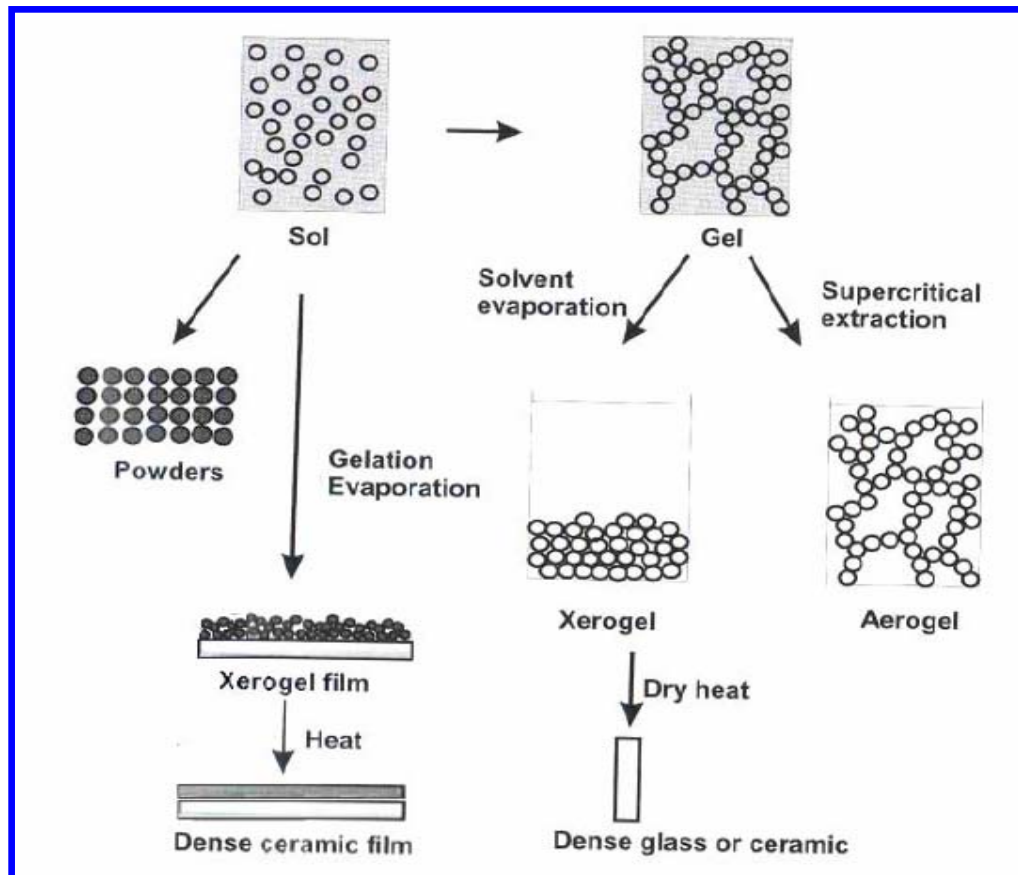


**Figure-2.3** Production options for the Sol-gel Process [8]

The drying of the sol gives powders. The application of dip-coating or spin-coating leads to the preparation of the thin films. The removal of the solvent by drying causes the shrinking of the gel and significant reduction in the volume due to increasing capillary forces. The high capillary pressure in the pores causes the collapse of the gel network structure and the production of less porous powder (xerogel). In contrast, the supercritical extraction when the solvent is removed above its critical temperature preserves the structure of the gel network and yields a highly porous material (aerogel). Dense ceramic material or glass can be produced by sintering the xerogel or aerogel.

### **2. I.3 Co-Precipitation Method**

The kinetics of nucleation and particle growth in homogeneous solutions can be adjusted by the controlled release of the anions and cations. Careful control of the kinetics of the precipitation can result in monodisperse nanoparticles. Once the solution reaches a critical supersaturation of the species forming particles, only one burst of nuclei occurs. Thus, it is essential to control the factors that determine the precipitation process, such as the pH and the concentration of the reactants and ions.

Organic molecules are used to control the release of the reagents and ions in the solution during the precipitation process. The particle size is influenced by the reactant concentration, pH, and temperature.

### **2. I.4 Fabrication of Dye Sensitized Solar Cells**

The fabrication process of DSSC involves multiple steps as follows.

1. Preparation of the paste of nanocrystalline metal oxide powder ( $\text{TiO}_2$ ,  $\text{ZnO}$  etc.).
2. Deposition of metal oxide film onto TCO coated substrate.
3. Post heat treatment and dye soaking of the metal oxide film.
4. Assembly of the film (anode) with Pt coated substrate (cathode) and electrolyte into the solar cell.

The most crucial step is the preparation of the paste from nanocrystalline metal oxide powder. The viscosity of paste is controlled by polymer binders such as Polyethylene Glycol, and organic surfactants as Triton X-100. This paste is spread on a conducting Fluorine-doped Tin Oxide (FTO) coated glass using Doctor Blade technique so as to

form a uniform film of desired thickness. This film is then annealed at 450°C temperature to improve the connectivity amongst nanoparticles. These annealed films are then dipped in Ru-based organic dye solution for 24 hours for TiO<sub>2</sub> films and 2 hours for ZnO films. Figure 2.4 shows different steps involved in the fabrication of DSSC, from slurry making to preparing dyed films for characterization. Final DSSC is prepared by assembly of working electrode (i.e. dye coated film) with a counter electrode (i.e. platinum coated FTO) with a liquid electrolyte between two electrodes. The electrolytes were used with 0.6 M 1-hexyl-2,3-dimethyl-imidazolium iodide, 0.1 M LiI, 0.05 M I<sub>2</sub>, and 0.5 M 4-tert-butylpyridine in methoxyacetonitrile.

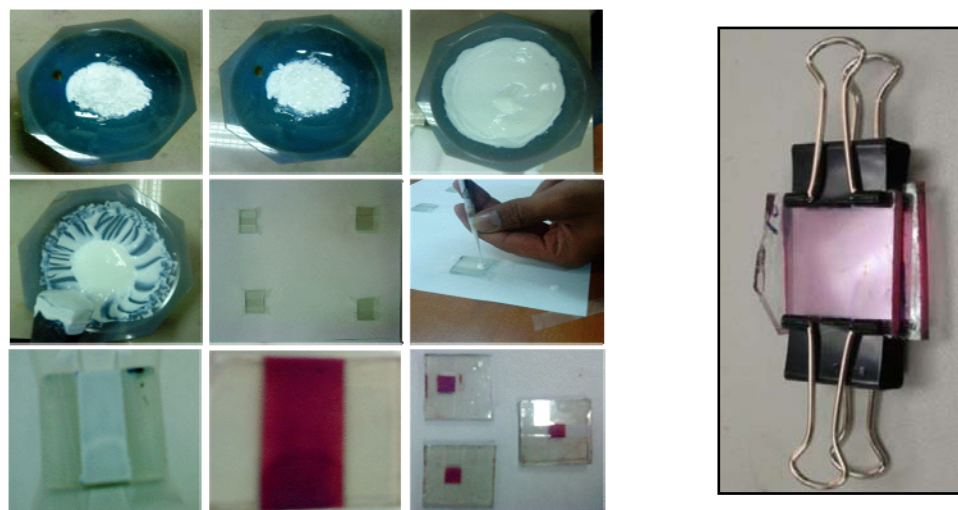


**Figure-2.4** *A systematic process of doctor blade method with at right side DSSC in practice.*

## Section-II

### 2. II Materials Characterisation Techniques

The synthetic methods discussed above have reached significant maturity in terms of homogeneity in the structural/electronic properties of the particles forming the solid, as well as in the size distribution, still much work is needed to obtain full control over the synthesis variables and their influence in the final semiconducting oxide material prepared especially in large scale. Problems related to oxide stoichiometry or the presence of impurities and amorphous phases coexisting with the crystalline one are often encountered. A glimpse into these problems indicate that structural and electronic properties as well as the primary particle size distribution are strongly dependent on the preparation method at the state of the art; a first goal is to perform a detailed and full characterization of the particular solid yielded by the specific preparation method. To do this in a systematic way, one needs a diverse array of characterization techniques. An important issue is the correct interpretation of the experimental results obtained by characterization tools. To help in reaching this goal, in this section we will describe the most often used techniques and the specific consequences that nanostructure induces in their corresponding physicochemical observables. This part of the chapter is devoted in explaining the basic principles on which different techniques are based and their application to understanding various aspects of formation of nanomaterials. In general, the individual characterization technique should not be invasive, but should be able to provide all quantitative details of the structure or composition. Few of such techniques are discussed below.

#### 2. II. 1 X-ray diffraction (XRD)

X-ray crystallography is a valuable tool for obtaining structural parameters of metal oxides [9]. X-ray diffraction (XRD) is a rapid analytical technique primarily used for phase identification of a crystalline material and can provide information on unit cell dimensions. XRD patterns come from the interference pattern of elastically dispersed X-ray beams by atom cores (figure 2.5) and, in the case of materials with moderate to long-range order, contain information that arises from the atomic structure and the particle characteristics (for example, size, strain, defects etc.).

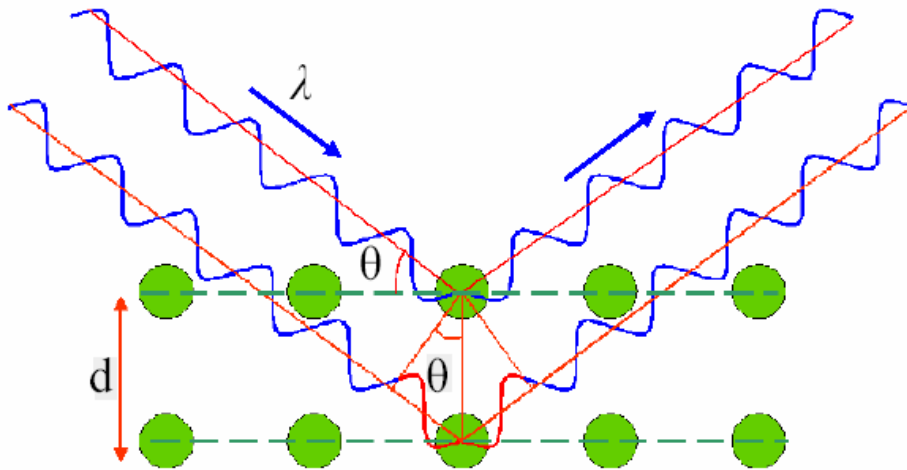


**Figure-2.5** Representation of Diffraction of X-rays by crystal planes.

Powder diffraction patterns are typically plotted as the intensity of the diffracted X-rays vs. the angle  $2\theta$ . Peaks will appear in the diffraction pattern at  $2\theta$  values when constructive interference is at a maximum, that is, when Bragg's Law (eq. 2.4) is satisfied.

$$n\lambda = 2d \sin\theta \dots \dots \dots (2.4)$$

In this experiment, we will be observing first order ( $n = 1$ ) diffraction of X-rays with a wavelength of  $1.54056 \text{ \AA}$ . By measuring the  $2\theta$  values for each diffraction peak, we can calculate the d-spacing (the distance between the diffracting planes) for each diffraction peak.

Recent analyses of particle characteristics rely on least squares refinement of the whole powder diffraction profile, although there are several useful approximations that give some of these characteristics from individual peaks. The pattern is represented as a superposition of peaks where the peak position depends on the cell parameters, and the peak width is a sum of instrument parameters, particle size parameters and strain related parameters. The particle size ( $D$ ) is calculated using Scherrer's formula:

$$D = k \lambda / \beta \cos\theta$$

Where,  $k$  = Scherrer's Constant  $\approx 0.9$ ,  $\lambda$  representing the wavelength (Cu-K $\alpha$ ,  $\lambda = 1.542 \text{ \AA}$ ),  $\beta$  = Full Width at Half Maximum (FWHM) and  $\theta$  representing the diffraction angle.

## 2. II. 2 UV-VIS Spectroscopy

UV-Visible spectroscopy measures the intensity of absorption of near-ultraviolet and visible light by a sample. Ultraviolet and visible light are energetic enough to promote the outer electrons in an atomic, molecular or material system to higher energy levels depending on the specific nature of the electronic states of a given material. In semiconductors, when the incident photon energy exceeds the band gap energy of the materials, absorption takes place and signal is recorded by the spectrometer whereas in metals when the surface free electrons vibrate coherently with the incident frequency then resonant absorption takes place. This spectrometer can operate in two modes (i) transmission and (ii) reflection mode. In transmission mode usually thin films and colloidal nanoparticles well-dispersed in solvent are used. The optical measurements for opaque thin films and those nanoparticles which are not dispersible in solvents are done in diffuse reflectance (DRS) mode. Reflectance spectra provide information about the scattering and absorption coefficient of the samples and hence their optical properties.

**Instrument:** The light from the source is alternatively split into one of two beams by a chopper; one beam is passed through the sample and the other through the reference (figure 2.6). The detector, which is often a photodiode, alternates between measuring the sample beam and the reference beam. Some double beam instruments have two detectors, and the sample and reference beam are measured at the same time. In other instruments, the two beams pass through a beam chopper which blocks one beam at a time.

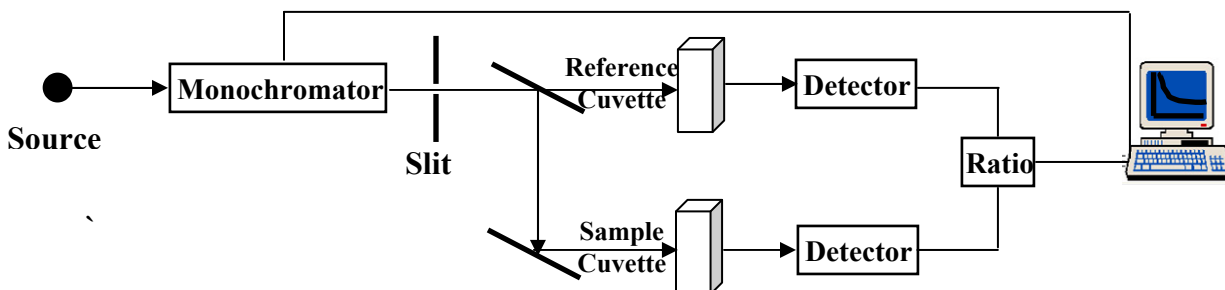


*Figure-2.6 Schematics of UV-VIS Spectrophotometer in Transmission Mode.*

**Broadening of spectral transitions:** The possible sources for the signal broadening: (a) Doppler Broadening: Random motion of nanoparticles in the liquids and gaseous samples causes their absorption and emission frequencies to show a Doppler shift and hence the spectrum lines are broadened. This effect is more pronounced in liquids than gaseous samples due to significant collisions in solutions. In the case of solids, the motions of the particles are more limited in extent and less random in direction, so that solid phase spectra are often sharp but show evidence of interactions by the splitting of the lines into two or more components. (b) Heisenberg's Uncertainty Principle: If a system exists in an energy state for a limited time ' $\delta t$ ' seconds, then the energy of that state will be uncertain (fuzzy) to an extent ' $\delta E$ ' and is given by  $\delta E \times \delta t \approx h/2\pi \approx 10^{-34}$  J.s, where  $h$  = Planck's Constant. Usually life time of excited state is  $10^{-8}$  sec, i.e.  $10^8$  Hz uncertainty in the radiation frequency which is, in fact, small as compared to UV-Vis frequency regime ( $10^{14} - 10^{16}$  Hz).

**Intensity of Spectral lines:** There are three main factors that decide the intensity of spectral lines: (i) *Transition probability*: The likelihood of a system in one state changing to another state which is usually governed by quantum mechanical selection rules. (ii) *Population of states*: The number of atoms/molecules initially in the state from which the transition occurs. It is governed by the equation:  $N_{\text{upper}} / N_{\text{lower}} = \exp(-\Delta E/kT)$ ; Where,  $\Delta E = E_{\text{upper}} - E_{\text{lower}}$ ,  $T$  = temperature (K),  $k$  = Boltzman's Constant =  $1.38 \times 10^{-23}$  J/K. (iii) *Concentration and path length*: Clearly since sample is absorbing energy from a beam of radiation, the more sample the more beam traverses, the more energy will be absorbed from it. Besides the amount of the sample, the concentration of the sample is also deciding factor for the energy absorption. Based on this, Beer-Lambert law, which is often written as:

$$I / I_0 = \exp(-\kappa cl) \quad \text{or} \quad I / I_0 = 10^{-\epsilon cl} = T$$

Where,  $\kappa$  = constant, for particular spectroscopic transition under consideration.

Where  $T$  = transmittance =  $I / I_0$ ,  $\epsilon$  = molar absorption coefficient.

Inverting above equation and taking logarithms,

$$I_0 / I = 10^{\epsilon cl} \quad \text{Or} \quad \log(I_0 / I) = \epsilon cl = A,$$

Where,  $A$  = absorbance / optical density

Thus, absorbance is directly proportional to the concentration, where the path length and molar extinction coefficient is suppose to be constant for the particular measurement. The source used for the UV and visible light are deuterium and tungsten lamps respectively and the detector used is usually PMT.

### 2. II. 3 Raman Spectroscopy

Raman spectroscopy is a powerful tool to analyze structural/morphological properties of solid oxides at a local level, given the strong sensitivity of the phonon characteristics to the crystalline nature of the materials [10].

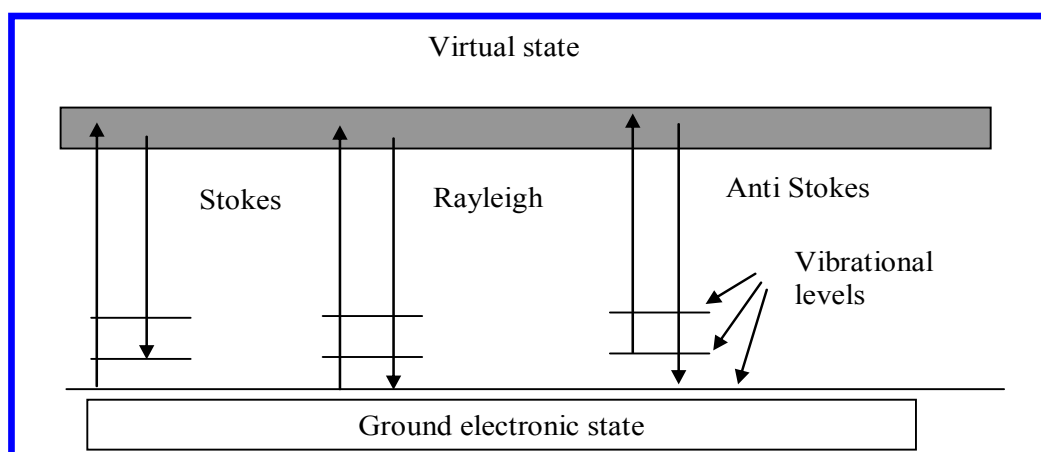


**Figure-2.7** Energy level diagram for Raman scattering; (a) Stokes Raman scattering (b) anti-Stokes Raman scattering [11].

When light encounters molecules in air, the predominant mode of scattering is elastic scattering, called Rayleigh scattering [11]. This scattering is responsible for the blue color of the sky; it increases with the fourth power of the frequency and is consequently more effective at short wavelengths. It is also possible for the incident photons to interact with the molecules in such a way that energy is either gained or lost so that the scattered photons are shifted in frequency. Such inelastic scattering is called Raman scattering.

Like Rayleigh scattering, the Raman scattering depends upon the polarizability of the molecules. For polarizable molecules, the incident photon energy can excite vibrational

modes of the molecules, yielding scattered photons, which are diminished in energy by the amount of the vibrational transition energies. A spectral analysis of the scattered light under these circumstances will reveal spectral satellite lines below the Rayleigh scattering peak at the incident frequency. Such lines are called "Stokes lines". If there is significant excitation of vibrational excited states of the scattering molecules, then it is also possible to observe scattering at frequencies above the incident frequency. These lines, generally weaker, are called anti-Stokes lines (Figure 2.7).

Since the Raman Effect depends upon the polarizability of the molecule, it can be observed for molecules, which have no net dipole moment and therefore produce no pure rotational spectrum. This process can yield information about the moment of inertia and hence the structure of the molecule. In Raman scattering, an intense monochromatic light source (laser) can give scattered light, which includes one or more "sidebands" that are offset by rotational and/or vibrational energy differences. This is potentially very useful for remote sensing, since the sideband frequencies contain information about the scattering medium, which could be useful for identification. The Raman bands are the characteristics of the structure and gives valuable information about the structure, size and crystal surface area [12].

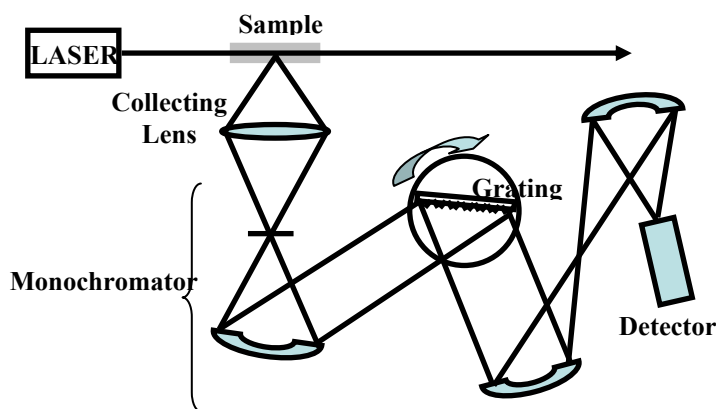


**Figure-2.8** *Schematic of Raman Spectrometer*

Raman Spectrometer (figure 2.8) consists of Laser beam (very narrow, monochromatic, coherent and powerful) which when passed through the cell, usually a narrow glass or

quartz tube filled with the sample, light get scattered sideways from the sample, which is collected by a lens and passed into a grating monochromator. The signal is measured by a sensitive PMT and after amplification; it is usually processed by a computer which plots the Raman spectrum.

### **2. II. 4 Fourier Transform IR Spectroscopy**

FTIR (Fourier Transform Infrared) Spectroscopy, or simply FTIR Analysis, is a technique that provides information about the chemical bonding or molecular structure of materials, whether organic or inorganic and identifies chemical bond functional groups by the absorption of infrared radiation which excites vibrational modes in the bond. This spectrum appears only when the vibrations amongst bonded atoms produces a change in the permanent electric dipole moment of the molecule/solid. It is reasonable to suppose that the more polar a bond, the more intense will be IR spectrum arising from the vibrations of that bond [13, 14].

The spectrophotometer consists of mainly source, monochromator and detector. The source is in some form of filament (e.g. Nernst Filament, made of a spindle of rare earth oxides or globar filament, made of carborundum rod) which is maintained at red- or white-heat by an electric current. The monochromator guides IR beam and focuses to the sample. The detectors are based on either temperature (bolometer/thermometer) or conductivity rise at given frequency (PbS).

FTIR has considerably speeded and improved the spectroscopy in the IR region in general and in particular far IR region i.e. below  $400\text{ cm}^{-1}$  where good deals of useful molecular information is contained, is usually called as 'Energy Limited' region, where sources become weak and detectors insensitive, resulting poor signal to noise ratio. The advantage of using FTIR is that the whole spectrum is obtained across the entire frequency range at once with constant resolving power over entire range. The technique works on the fact that bonds and groups of bonds vibrate at characteristic frequencies. A molecule that is exposed to infrared rays absorbs infrared energy at frequencies which are characteristic to that molecule. During FTIR analysis, a spot on the specimen is subjected

to a modulated IR beam. The specimen's transmittance and reflectance of the infrared rays at different frequencies is translated into an IR absorption plot consisting of reverse peaks. The resulting FTIR spectral pattern is then analyzed and matched with known signatures of identified materials in the FTIR library. Well-dispersed nanoparticles solutions were drop-coated onto Si (111) wafers and air-dried; however powdered samples were mixed with the standard KBr powder. The FTIR measurements of these samples were carried out on a Perkin Elmer Spectrum One FTIR spectrometer operated in the diffuse reflectance mode at a resolution of  $4\text{ cm}^{-1}$ .

### **2. II. 5 Transmission electron microscopy (TEM)**

Transmission electron microscopy (TEM) is one of the most powerful and versatile techniques for the characterization of nanostructured systems. Its unique characteristics allow one to achieve atomic resolution of crystal lattices as well as to obtain (with the assistance of energy-dispersive X-ray spectroscopy (EDS) complementary techniques) chemical and electronic information at the sub-nanometer scale. The line diagram of a typical TEM column is shown in figure 2.9. In TEM, a thin specimen is illuminated with electrons in which the electron intensity is uniform over the illuminated area. The interaction of an electron beam with a solid specimen results in a number of elastic or inelastic scattering phenomena (backscattering or reflection, emission of secondary electrons, X-rays or optical photons, and transmission of the undeviated beam along with beams deviated as a consequence of elastic – single atom scattering, diffraction - or inelastic phenomena). The TEM technique is dedicated to the analysis of the transmitted or forward-scattered beam. Such a beam is passed through a series of lenses, among which the objective lens mainly determines the image resolution, to obtain the magnified image. In low resolution TEM, the objective aperture will be adjusted for selection of the central beam (containing the less-scattered electrons) or of a particular diffracted (or scattered in any form) beam to form the bright-field or dark-field image, respectively. In high resolution TEM (HRTEM), which is usually performed in bright-field mode, the image is formed by collecting a few diffracted beams in addition to the central one.

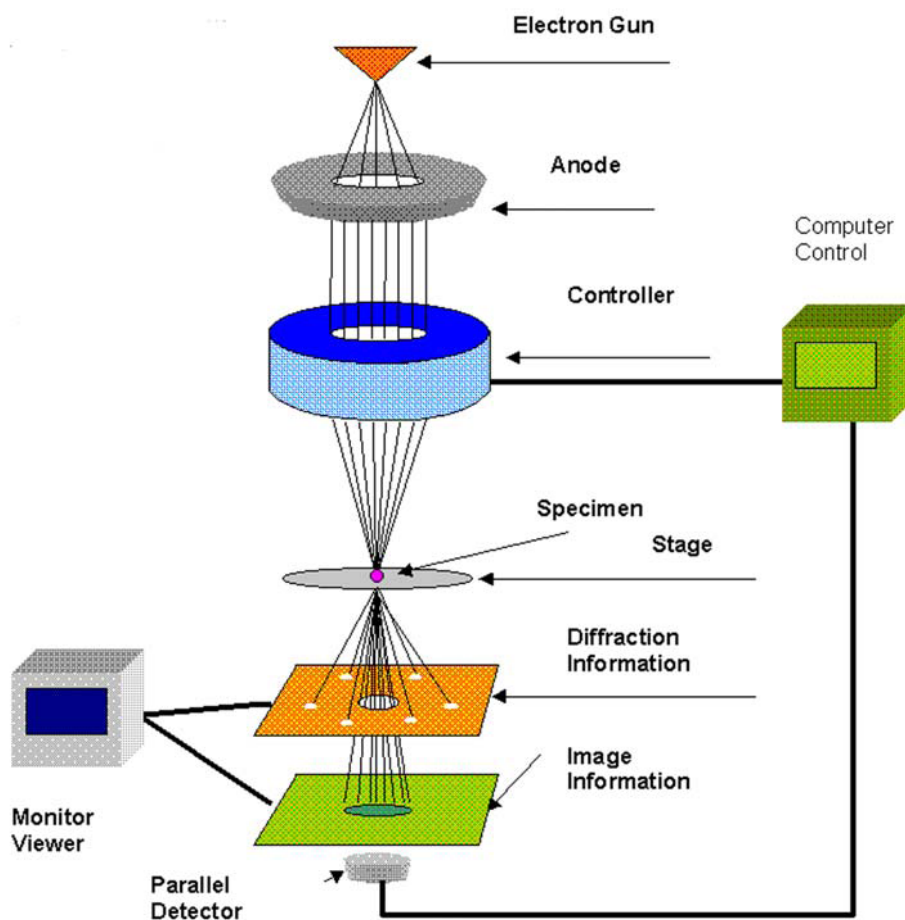


**Figure 2.9** Schematic diagram of the Transmission Electron Microscope.

[\[http://www.rpi.edu/dept/materials/COURSES/NANO/shaw/Page5.html\]](http://www.rpi.edu/dept/materials/COURSES/NANO/shaw/Page5.html)

Angular distribution of scattering can be viewed in the form of scattering patterns, usually called diffraction patterns, commonly referred to as selected area electron diffraction (SAED). Spatial distribution of scattering can be observed as contrast in images of the specimen. The advantage of this arrangement is the possibility of directly viewing the area from which the diffraction pattern arises. Further, Kikuchi patterns obtained by inelastic scattering of electrons is also very useful for understanding the crystallographic orientation as these are rigidly attached to a crystal plane and therefore move in the diffraction pattern when the crystal is tilted.

Many materials require extensive sample preparation and thinning procedures to produce a sample thin enough to be electron transparent, and changes in the structure may be caused during this process. Also the field of view is relatively small, raising the possibility that the region analysed may not be characteristic of the whole sample. Also there is potential that the sample may be damaged by the electron beam, particularly in the case of biological materials. Despite these limitations, TEM has been the technique of choice due to atomic-level resolution leading direct visual information of size, shape, dispersion and structure. Further, when coupled with SAED, the technique can provide important information on the crystallographic directions in the structures, helpful to understand the growth kinetics [15].

### **2. II. 6 Scanning Electron Microscope (SEM)**

Scanning Electron Microscopy is extremely useful for the direct observations of surfaces because they offer better resolution and depth of field than optical microscope. A typical schematic of a SEM is shown in figure 2.10. The two major components of an SEM are the electron column and control console [16]. The electron column consists of an electron gun and two or more electron lenses, which influence the path of electrons travelling down an evacuated tube. The control console consists of a cathode ray tube viewing screen and computer to control the electron beam. The purpose of electron gun is to provide a stable beam of electrons. Generally, tungsten or Lanthanum hexaboride ( $\text{LaB}_6$ ) thermionic emitters are used as electron gun. The spot size from a tungsten gun is too large to produce a sharp image unless electron lenses are used to demagnify it and place a much smaller focused electron spot on the specimen.

When the electron beam impinges on the specimen, many types of signals are generated and any of these can be displayed as an image. The two signals most often used to produce SEM images are secondary electrons (SE) and backscattered electrons (BSE). Most of the electrons are scattered at large angles (from  $0^\circ$  to  $180^\circ$ ) when they interact with the positively charged nucleus. These elastically scattered electrons usually called 'backscattered electrons' (BSE) are used for SEM imaging. Some electrons scatter

inelastically due to the loss in kinetic energy upon their interaction with orbital shell electrons.

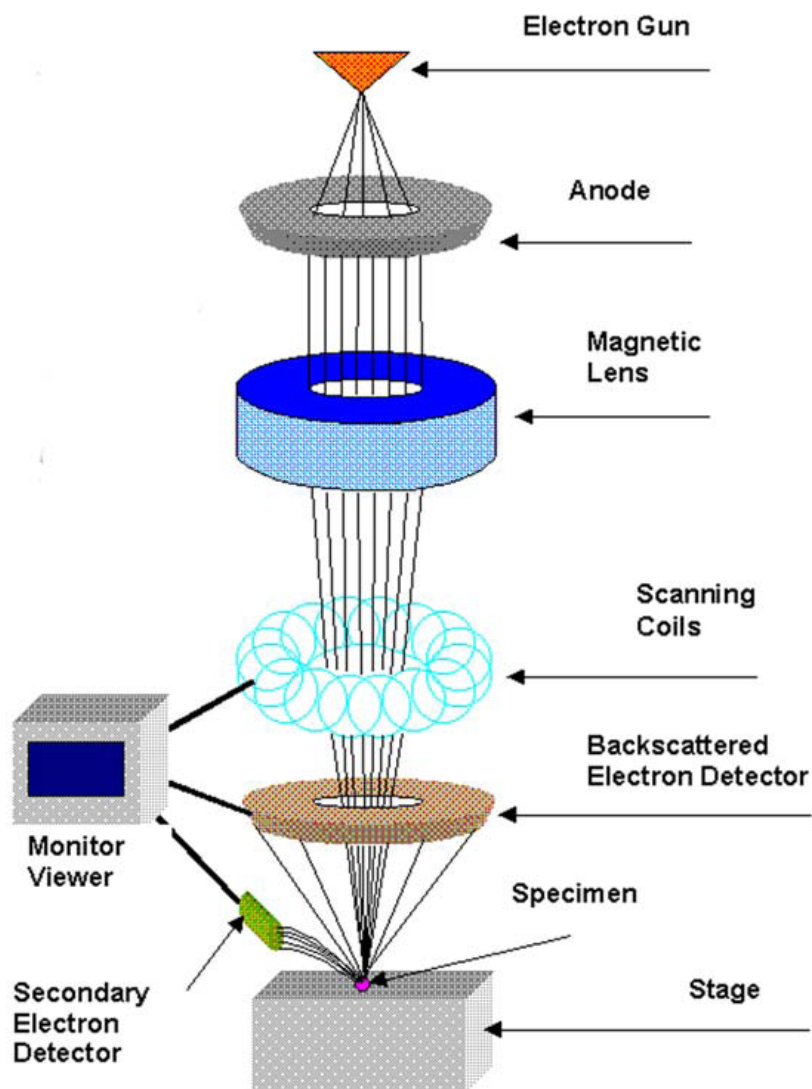


**Figure-2. 10** Schematic diagram of the Scanning Electron Microscope.

[<http://www.rpi.edu/dept/materials/COURSES/NANO/shaw/Page5.html>]

Incident electrons may knock off loosely bound conduction electrons out of the sample. These are secondary electrons (SE) and along with backscattered electrons are widely used for SEM topographical imaging. Both SE and BSE signals are collected when a

positive voltage is applied to the collector screen in front of detector. When a negative voltage is applied on the collector screen only BSE signal is captured because the low energy SEs are repelled. Electrons captured by the scintillator/ photomultiplier are then amplified and used to form an image in the SEM. If the electron beam knocks off an inner shell electron, the atom rearranges by dropping an outer shell electron to an inner one. This excited or ionized atom emits an electron commonly known as the Auger electron. Recently Auger electron spectroscopy (AES) is useful to provide compositional information. Instead of excited atom releasing Auger electron, it can release a photon of electromagnetic radiation. If the amount of energy released is high, the photon will be an X-ray photon. These electrons are characteristic of the sample and can be used for analysis. This type of analysis is known as Energy Dispersive analysis of X-rays (EDAX).

## 2. II. 7 Dye sensitized solar cells (DSSC) characterization

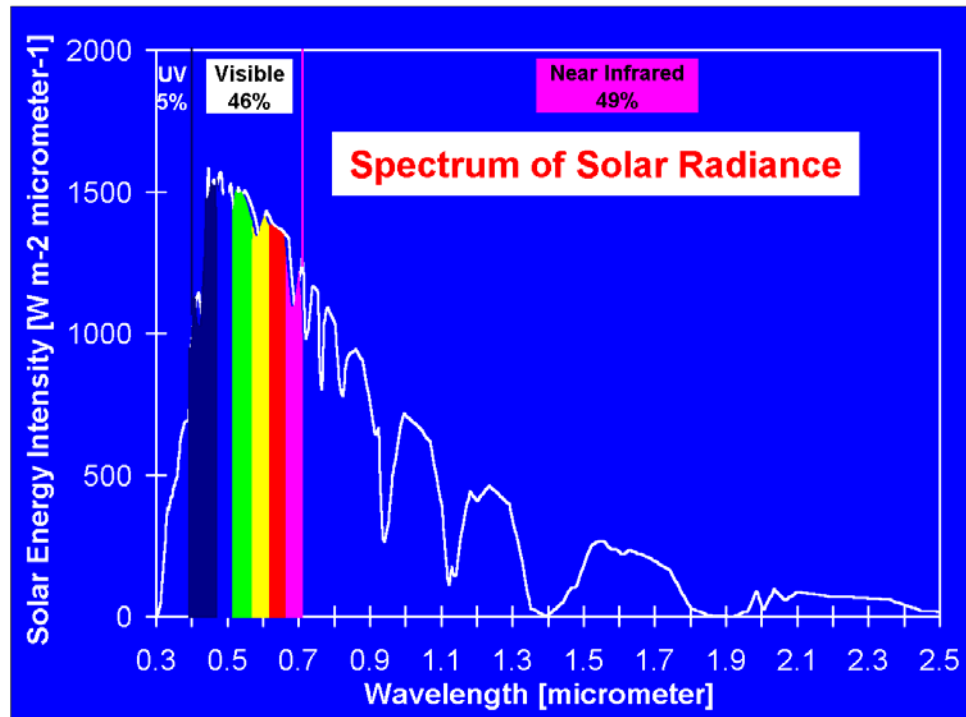


**Figure-2.11** the solar radiation spectrum of the sun as a function of wavelength.

## Chapter-2

The solar radiation spectrum is shown in figure 2.11 as the irradiance of the sun as a function of wavelength. The sun emits light with a range of wavelengths from the ultraviolet and visible to the infrared. It peaks in the visible, resembling the spectrum of a blackbody at a temperature of 5760 K. It is, however, influenced by atmospheric absorption and the position of the sun. Ultraviolet light is filtered out by ozone, and water and CO<sub>2</sub> absorb mainly in the infrared making dips in the solar spectrum at 900, 1100, 1400, and 1900 nm (H<sub>2</sub>O) and at 1800 and 2600 nm (CO<sub>2</sub>). When skies are clear, the maximum radiation strikes the earth's surface when the sun is directly overhead, having the shortest path length through the atmosphere. The path length is called the air mass (AM) and can be approximated by  $AM = 1/\cos\theta$ , where,  $\theta$  is the angle of elevation of the sun. In figure 2.12 the air-mass value AM 0 equates to isolation at sea level with the Sun at its zenith. AM 1.0 represents sunlight with the Sun at zenith above the Earth's atmosphere and absorbing oxygen and nitrogen gases. AM 1.5 is the same, but with the Sun at an oblique angle of 48.2°, which simulates a longer optical path through the Earth's atmosphere; AM 2.0 extends that oblique angle to 60.1°. The standard solar spectrum used for efficiency measurements of solar cells is AM 1.5 G (global).

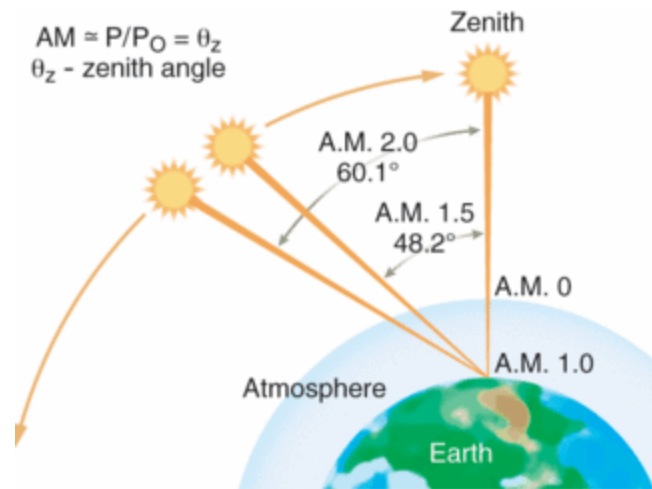


**Figure-2.12** Air-Mass calculations for 1 Sun measurements.

[\[http://www.optoiq.com/index/photronics-technologies-applications/lfw-isplay/lfw-article-display/286515/articles/laser-focus-world/volume-43/issue-3/features/photovoltaics-nhancements-enable-solar-simulators-to-shed-light-on-new-photovoltaic-designs.html.\]](http://www.optoiq.com/index/photronics-technologies-applications/lfw-isplay/lfw-article-display/286515/articles/laser-focus-world/volume-43/issue-3/features/photovoltaics-nhancements-enable-solar-simulators-to-shed-light-on-new-photovoltaic-designs.html)

This spectrum is normalized so that the integrated irradiance (the amount of radiant energy received from the sun per unit area per unit time) is  $1000 \text{ W m}^{-2}$ . The irradiance varies depending on the position of the sun, orientation of the Earth, and sky conditions. One also distinguishes sunlight in direct or diffuse light. The direct component can be concentrated, which increases the solar cell efficiency by increasing cell voltage outputs. Diffuse light arises by scattering of the sunlight in the atmosphere. This fraction is around 15% on average [17] but larger at higher latitudes and in regions with a significant amount of cloud cover. Materials with rough surfaces such as DSCCs are relatively better suited for diffuse light than perfectly flat surfaces and are less sensitive to movements of the sun.

### 2. II. 7. 1 Solar Simulator

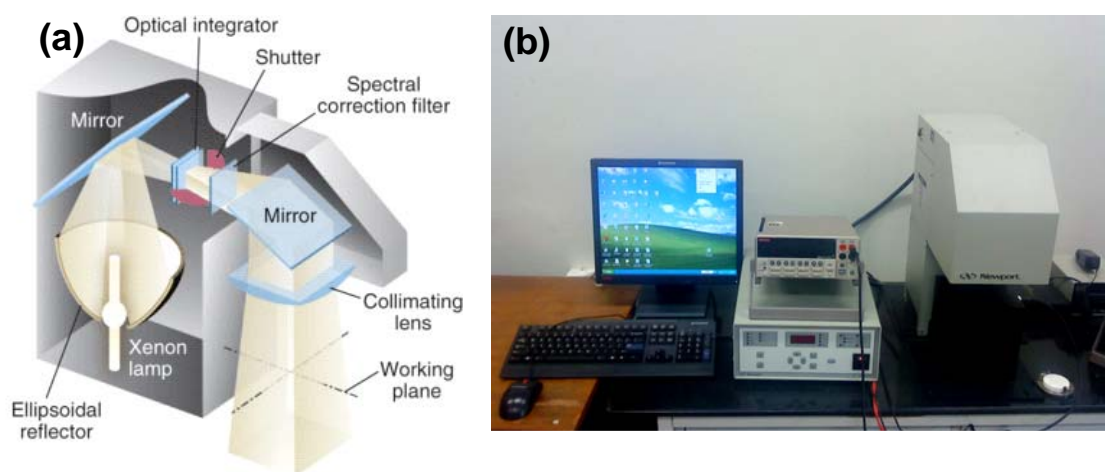


**Figure-2.13** (a) Schematic diagram of Solar Simulator and (b) Newport Solar Simulator with I-V measurement set up.

[\[http://www.optoIQ.com/index/photronics-technologies-applications/lfw-isplay/lfw-article-display/286515/articles/laser-focus-world/volume-43/issue-3/features/photovoltaics-enhancements-enable-solar-simulators-to-shed-light-on-new-photovoltaic-designs.html.\]](http://www.optoIQ.com/index/photronics-technologies-applications/lfw-isplay/lfw-article-display/286515/articles/laser-focus-world/volume-43/issue-3/features/photovoltaics-enhancements-enable-solar-simulators-to-shed-light-on-new-photovoltaic-designs.html)

A solar simulator (also known as artificial sun) is a device that provides illumination approximating natural sunlight. The purpose of the solar simulator is to provide a controllable indoor test facility under laboratory conditions used for the testing of solar cells, plastics, and other materials and devices. The simulator starts with a xenon arc lamp with various output powers, with the illumination area ranging from  $2 \times 2$  inch to  $8 \times 8$  inch. For example, a 300 W,  $2 \times 2$  inch, solar simulator can provide output densities of up to  $2800 \text{ W/m}^2$ , or nearly three times the typical solar irradiance level at sea level with an Air Mass (AM) equivalent of 1.0.

The simulator also include a control that allows the output levels to be increased or decreased while maintaining the proper spectral ratios necessary to simulate solar irradiance. An ellipsoidal reflector collects the lamp output, and a collection mirror directs the light through a single-blade shutter to an optical integrator that ensures uniformity variations of less than 2% across the simulator's output beam. Beam uniformity is heavily dependent on two design considerations: proper alignment of the optical elements and the optical integrator. The integrator is a monolithic optic that effectively homogenizes the collimated light to within uniformity values listed in international photovoltaic testing standards. The light then passes through the AM spectral-correction filter as shown in figure 2.13.

## 2. II. 7. 2 Solar Cell Efficiency Measurements (I-V Measurements)

### Current-voltage characterization

Standard current-voltage measurement of a DSSC determines the current voltage response of the device, i.e. current-voltage characteristics, in the dark and under different light intensities. In the dark, the applied voltage, bias, on the device generates a current that flows in the direction opposite to that of the photocurrent. This reverse current is usually called the dark current. For an ideal diode, the dark current  $I_{\text{dark}}$  relates to voltage with Eq. 2.5.

$$I_{\text{dark}} = I_S (e^{qV/k_B T} - 1) \quad (2.5)$$

where  $I_S$  is the saturation current of the diode (typically  $10^{-7}$ - $10^{-9}$  A),  $V$  is the voltage applied on the terminals of the cell and  $q$  is the elementary charge.

Under illumination, the current-voltage characteristics follow

$$I = I_{ph} - I_S (e^{qv/k_B T} - 1) = I_{ph} - I_S (e^{V/V_T} - 1) \quad (2.6)$$

where  $I_{ph}$  is the photocurrent that depends on irradiation intensity and  $V_T$  is often referred to as the thermal voltage that equals  $k_B T/q$ . For non-ideal devices, an ideality factor,  $m$ , is used to describe the weaker dependence of dark current on voltage.

$$I = I_{ph} - I_S (e^{mV/V_T} - 1) \quad (2.7)$$

An experimental I-V curve is shown in figure 2.14, together with the power curve. The following parameter can be derived with the I-V curve.

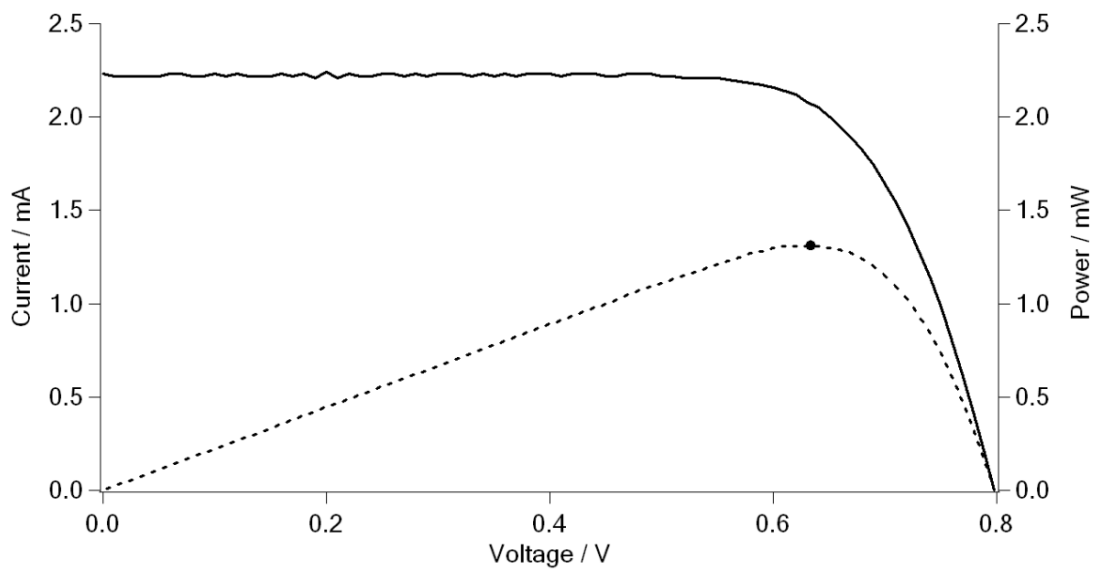


**Figure-2.14** A typical I-V curve in the experiment. The dotted line shows the power output at different bias. The dark big dot indicates the maximum power point.

### 2. II. 7. 2 .1 Open-circuit voltage (V<sub>OC</sub>)

The open circuit voltage (V<sub>OC</sub>) is the maximum voltage, when the circuit resistance has caused any current to cease flowing.

The V<sub>OC</sub> is measured under the condition when there is no external load connected, i.e. the circuit is broken or open. In this condition, there is no external current flow between the two terminals of the device, i.e.  $I = 0$  and  $V = V_{OC}$ . From eq. 2.7,

$$I_{ph} - I_S (e^{mV/V_T} - 1) = 0 \quad (2.8)$$

$$V_{OC} = mV_T \ln (I_{ph}/I_S + 1) \cong mV_T \ln (I_{ph}/I_S) \quad (2.9)$$

Voc increases logarithmically with the photocurrent and light intensity.

**2. II. 7. 2 .2 Short-circuit current (I<sub>SC</sub>)**

The short circuit current density (I<sub>SC</sub>) is the maximum current through the circuit when there is no resistance (and hence no voltage).

The I<sub>SC</sub> is measured at the condition when the applied voltage, V, equals zero. From Eq. 2.7,

$$I_{SC} = I_{ph} \quad (2.10)$$

I<sub>SC</sub> increases linearly with the light intensity.

**2. II. 7. 2 .3 Fill factor (FF)**

The power is calculated as the product of I × V and the maximum power point is labeled with the dot in figure 2.14. At this point, the device delivers the highest power output with the voltage, V<sub>m</sub> and current, I<sub>m</sub>.

$$V_m = V_{OC} - mV_T \ln (V_m/V_T + 1) \quad (2.11)$$

The fill factor (FF) is defined as the ratio  $FF = \frac{V_m I_m}{V_{OC} I_{SC}}$

to describe how the maximum power rectangle fits under the I-V characteristics.

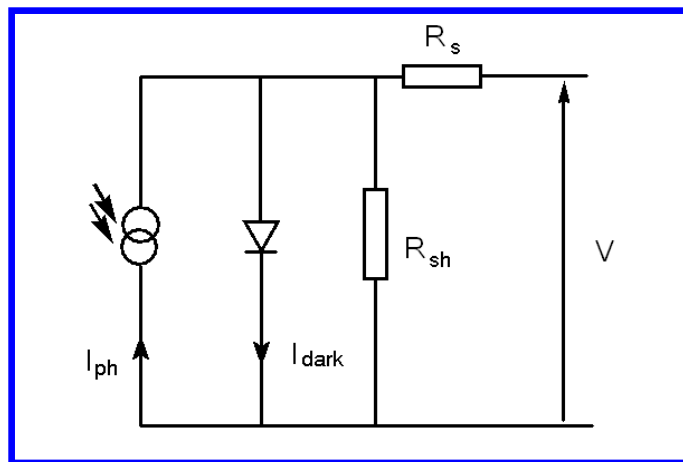


**Figure-2.15** A simplified equivalent circuit for DSSC. Series and shunt resistances are taken into account.

Typical FF of DSC ranges from 0.6 to 0.8 depending on the individual device and usually increases with the decreasing light intensity. It is also influenced by the series resistance ( $R_s$ ) arising from the internal resistance and resistive contacts of the cell and parallel resistance ( $R_{sh}$ ) from the leakage of the current. Figure 2.15 illustrates a simplified equivalent circuit for DSSC in which  $R_s$  and  $R_{sh}$  are present. For an efficient solar cell, we need a small  $R_s$  but a large  $R_{sh}$  since, a large  $R_s$  and a small  $R_{sh}$  decrease the FF dramatically.

#### 2. II. 7. 2. 4 Solar-to-electric-power conversion efficiency ( $\eta$ )

The efficiency  $\eta$  of the device is the parameter that is associated with the performance of the device. It is defined as the ratio of the maximum power ( $P_{max}$ ) to the incident sunlight power ( $P_s$ ).

$$\eta = \frac{I_m V_m}{P_s} = \frac{I_{sc} V_{oc} FF}{P_s} \quad (2.12)$$

$P_s$  is an important experimental parameter and in order to compare different results, standard test condition is always used for all the devices in this work. This condition includes AM 1.5 spectrum illumination with an incident power density of  $100 \text{ mW cm}^{-2}$  and a test temperature of 298 K.

#### 2. II. 7. 3 Incident photon-to-current conversion efficiency (IPCE) Measurements

Another fundamental measurement of the performance of a solar cell is the “external quantum efficiency”, which in the DSSC community is normally called the incident photon to current conversion efficiency (IPCE). The IPCE value corresponds to the photocurrent density produced in the external circuit under monochromatic illumination of the cell divided by the photon flux that strikes the cell. From such an experiment the IPCE as a function of wavelength can be calculated from

$$IPCE = \frac{J_{sc}(\lambda)}{e\Phi(\lambda)} = \frac{1240 J_{sc}(\lambda) [\text{A cm}^{-2}]}{\lambda [\text{nm}] P_s(\lambda) [\text{W cm}^{-2}]} \quad (2.13)$$

where  $e$  is the elementary charge. IPCE values provide practical information about the monochromatic quantum efficiencies of a solar cell.



*Figure-2.16 Newport IPCE measurement systems.*

**2. II. 7. 4 Electrochemical Impedance Spectroscopy (EIS)**

In order to study the electron transport and charge recombination in the porous semiconducting metal oxide films Electrochemical Impedance Spectroscopy (EIS) measurements were performed [18].

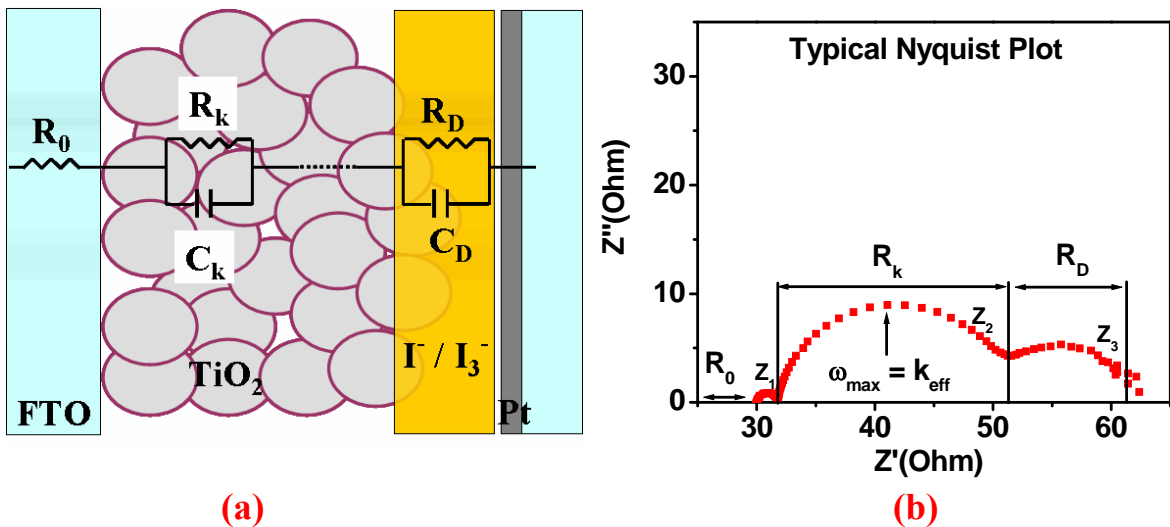


*Figure-2.17 (a) Schematics diagram of various interfaces involved in DSSC (b) Typical Nyquist plot of DSSC.*

The frequency range chosen for the measurement was from  $10^{-2}$  Hz to  $10^6$  Hz with an amplitude of 10 mV. The impedance spectrum of DSSC (Nyquist plot) mainly consists of 3 semicircles attributed to the impedances for the Pt| Electrolyte ( $Z_1$ ),  $\text{TiO}_2$ |Dye|electrolyte ( $Z_2$ ) and the diffusion of  $\text{I}_3^-$  ( $Z_3$ ) in the electrolyte, respectively, as depicted in figure 2.17(a).

The resistance elements  $R_0$ ,  $R_k$ , and  $R_D$  are described as the real part of  $Z_1$ ,  $Z_2$  and  $Z_3$ , respectively shown in figure 2.17 (b). It is found that the resistance element  $R_0$  in the high frequency range over 1 MHz is influenced by the sheet resistance of TCO and the contact resistance between the TCO and nanoparticle film.

The parameters of significance to the cell performance can be extracted from the impedance data from (Nyquist plot) as follows:

a)  $k_{\text{eff}}$  is estimated from the peak frequency  $\omega_{\text{max}}$  of the central arc, which describes the rate of recombination of electron in the film.

b)  $\tau_{\text{eff}}$  is the inverse of  $k_{\text{eff}}$  which gives the information about the lifetime of electron throughout the working electrode.

c)  $R_k$  is the diameter of the central arc which gives the charge transfer resistance including recombination of electrons with  $\text{I}_3^-$  at the  $\text{TiO}_2$  / electrolyte interface.

d)  $D_{\text{eff}}$  is the effective diffusion coefficient of electrons is calculated as,

$$D_{\text{eff}} = (R_k / R_w) L^2 k_{\text{eff}},$$

Where  $L$  is the thickness of working electrode and for true circle  $R_k \gg R_w$ .

e)  $R_D$  is the DC resistance of diffusion of  $\text{I}_3^-$  in electrolyte calculated from the diameter of the third arc (low frequency in the mHz range).

f)  $\text{Con}$  describes the charge transport resistance and its recombination rate along the entire thickness of working electrode and is calculated as

$$\text{Con} = R_k L k_{\text{eff}}.$$

## 2. III References

1. Nanostructured Materials, Processing, Properties and Applications; Koch, C. C., Ed.; Noyes Publications: Norwich, New York, **2002**.
2. M. Yoshimura, W. Suchanek, K. Byrappa, *Mater. Res. Soc. Bull.*, USA, **2000**, 25,17.

3. K. Byrappa, T. Adschiri, *Progress in Crystal Growth and Characterization of Materials*, **2007**, 53, 117e166.
4. F. Xu, L. Sun, *Energy Environ. Sci.*, **2011**, 4, 818.
5. J. Gopalakrishnan, *Chemistry of Materials*, **1995**, 7, 1265.
6. L. G. Hubert-Pfalzgraf, S. Daniele, J.M. Decams, *J. Sol-Gel Sci. Technol.*, **1997**, 8, 49.
7. X. Wang, Z. Zhang, and S. Zhou, *Mater. Sci. Eng. B: Solid-State Mater. Adv. Technol.*, **2001**, B86, 29.
8. U. Schubert and N. Hüsing, *Synthesis of Inorganic Materials*, Wiley-VCH, **2000**, pp. 396.
9. Wyckoff, R. W. G. *Crystal Structures*, 2nd ed.; Wiley: New York, **1964**.
10. R. Loudon, *Adv. Phys.* **2001**, 50, 813.
11. D. A. Long, *Raman Scattering*, McGraw Hill Book Company, New York, **1977**.
12. (a) M. Fernandez-Garcia, A. Martinez-Arias, J. C. Hanson, J. A. Rodriguez, *Chem. Rev.* **2004**, 104(9), 4063. (b) J. L. Anchell, A. C. Hess, *J. Phys. Chem.* **1996**, 100, 18317.
13. C. N. Banwell, E. M. McCash, *A Book: Fundamentals of Molecular Spectroscopy*, 4th Ed., Tata McGraw Hill Publishing Co. Ltd., **2002**.
14. J. Coates, *Interpretation of Infrared Spectra: A Practical Approach*, *Encyclopedia of Analytical Chemistry*, R.A. Meyers (Ed.), 10815, John Wiley & Sons Ltd, **2000**.
15. (a) J. Duan, S. Yang, H. Liu, J. Gong, H. Huang, X. Zhao, R. Zhang, Y. J. Du, *Am. Chem. Soc.*, **2005**, 127, 6180. (b) Y. Ding, Z. L. Wang, *J. Phys. Chem. B.*, **2004**, 108, 12280.
16. G. Lawes, *Scanning electron microscopy and X-ray microanalysis: Analytical chemistry by open learning*, John Wiley & sons, **1987**.
17. J. Nelson, *The Physics of Solar Cells*; Imperial College Press: London, **2003**.
18. M. Adachi, M. Sakamoto, J. Jiu, Y. Ogata, S. Isoda, *J Phys. Chem. B.*, **2006**, 110, 13872.

## Chapter-3

### Semiconductor-Metal (TiO<sub>2</sub>-Au) Nanocomposites for DSSC Application

*Anatase TiO<sub>2</sub> nanoparticles dressed with gold nanoparticles were synthesized by hydrothermal process by using mixed precursor and controlled conditions. Diffused Reflectance spectra (DRS) reveal that in addition to the expected TiO<sub>2</sub> interband absorption below 360 nm gold surface plasmon feature occurs near 564 nm. It is shown that the dye sensitized solar cells made using TiO<sub>2</sub>-Au plasmonic nanocomposite yield superior performance with conversion efficiency (CE) of ~6% (no light harvesting), current density ( $J_{SC}$ ) of ~13.2 mA/cm<sup>2</sup>, open circuit voltage ( $V_{oc}$ ) of ~0.74 V and fill factor (FF) 0.61; considerably better than that with only TiO<sub>2</sub> nanoparticles (CE ~5%,  $J_{SC}$  ~12.6 mA/cm<sup>2</sup>,  $V_{oc}$  ~0.70V, FF ~ 0.56).*

### 3.1 Introduction

Semiconducting metal oxides have gained prominence in recent years in view of their several interesting and application-worthy properties in the arena of optoelectronic applications [1-3]. An application of particular interest based on nano-meso-porous metal oxide photoanodes is dye sensitized solar cells (DSSC) discovered by O'regan and Gratzel in 1991 [4]. Since then several research efforts have been expended on manipulating the corresponding architecture involving inorganic and organic systems as well as various interfaces so as to enhance the cell performance [5-9]. Although the concept of using functional nanocomposites involving metals (or semiconductors) with metal oxides has been attempted in this context, the metal based composites do not appear to have been fully explored. Kamat et al. have shown that electron transfer occurs from semiconductor to Au in colloidal solutions<sup>10</sup>. Noble metals deposited on semiconductor particles have been shown to improve photocatalytic electron transfer processes at the semiconductor interface [11]. Wood et al. examined the photoinduced interaction between a semiconductor and Au, and concluded that the role of Au is primarily to accept electrons from the photo-excited semiconductors [12]. They explored the behavior of Au and Pt with ZnO and concluded that Pt establishes Ohmic type contact while Au-ZnO is a Schottky type contact. Dhas, et al. reported that ZnO nanoflowers loaded with Au NPs yield solar energy conversion efficiency of ~2.5%, considerably higher than the unloaded nanoflowers [7]. Snaith and coworkers have recently outlined a strategy for incorporating metal nanoparticles with strong surface plasmon resonance into dye-sensitized solar cells that overcomes four main issues related to the introduction of metal nanoparticles into the bulk of a solar cell, namely a) charge recombination within the metal, b) thermal stability during processing, c) chemical stability, and d) control of metal nanoparticle dye chromophore separation to inhibit non-radiative quenching [13]. This new plasmonic photovoltaic system has thus led to enhanced light absorption and photocurrent generation in dye-sensitized solar cells.

In this work, we have hydro-thermally synthesized anatase TiO<sub>2</sub> nanoparticles and TiO<sub>2</sub>-Au nano-composites and have made DSSCs using these. The DSSCs made with TiO<sub>2</sub>-Au nanocomposite yield a far superior performance than cells made with only TiO<sub>2</sub>

nanoparticles. Various processes such as interfacial charge transfer and stability of interfaces can greatly influence the ability of a semiconductor-metal composite to sustain charge separation. We present results of different measurements and outline the possible origin of this effect.

## 3.2 Experimental Methods

### 3.2.1 Preparation of TiO<sub>2</sub>-Au Nanocomposite

The TiO<sub>2</sub> nanoparticles attached with Au NPs were synthesized by hydrothermal route using high purity Titanium tetra isopropoxide (TIP) and HAuCl<sub>4</sub>. For obtaining TiO<sub>2</sub>-Au nanocomposite 1ml of TIP was hydrolysed in a mixed solvent of 10ml of ethanol and 10ml of de-ionized water under stirring. Then, 10ml of 0.6M urea aqueous solution was added dropwise to the stirred solution. 1ml of 0.1M HAuCl<sub>4</sub> aqueous solution was introduced, and the resulting solution mixture was transferred into a Teflon lined stainless steel autoclave. It was then sealed and maintained at 180°C for 18h. After the reaction a pink colored solid powder was recovered by centrifugation followed by washing with distilled water and ethanol to remove the residual ions in the final product and, then, the powder was finally dried at 60 °C in air for 10 h. The same protocol was followed to prepare TiO<sub>2</sub> nanoparticles without the addition of HAuCl<sub>4</sub> solution.

The TiO<sub>2</sub> and TiO<sub>2</sub>-Au nanocomposite films were made by the doctor blade method and the films were then annealed at 450 °C for 30 min. The thickness of TiO<sub>2</sub>-Au nanocomposite films was ~12 μm. For sensitization, the TiO<sub>2</sub> and TiO<sub>2</sub>-Au nanocomposite films were impregnated with 0.5 mM N719 dye in ethanol for 24 h at room temperature. The sensitizer-coated TiO<sub>2</sub> films were washed with ethanol. The electrolytes were used with 0.6 M 1-hexyl-2, 3-dimethylimidazolium iodide, 0.1 M LiI, 0.05 M I<sub>2</sub>, and 0.5 M 4-tert-butylpyridine in methoxyacetonitrile.

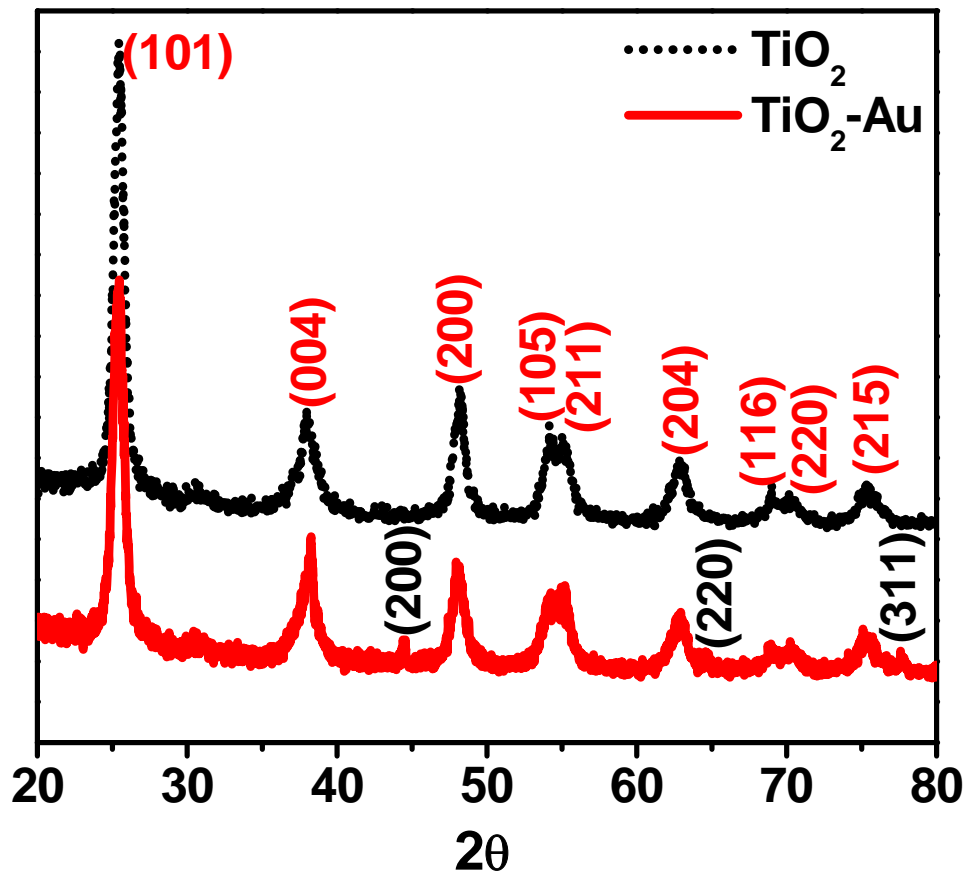
**3.2.2 Characterization.** X-ray diffraction patterns of the powders were recorded using X'pert pro PAN analytical diffractometer using Ni filtered Cu K $\alpha$  radiation ( $\lambda = 1.5418$  Å). Optical properties of the nanoparticles were studied by UV-Visible-NIR spectrophotometer in diffuse reflectance mode over the spectral range of 190 to 1400 nm.

The measurements were carried out on a Jasco V-570 spectrophotometer. The Raman spectra of the synthesized materials were studied using Horiba Jobin Yvon LabRAM HR System. High-resolution transmission electron microscopy (HRTEM) was performed on FEI Tecnai 300kV. TEM and Elemental Mapping on TiO<sub>2</sub>-Au composite was carried out at 200 keV and electron spot size of 2.2 nm and the data was collected for 5 min.

**3.2.3 Measurements.** The J-V characteristics were measured by irradiation with 100 mW/cm<sup>2</sup> (450Wxenon lamp, Newport Instruments), 1 sun AM 1.5, simulated sunlight as a solar simulator. The current was measured using a Kiethley 2420 source. Measurements of the incident-photon-to-current conversion efficiency (IPCE) were carried out without bias illumination with respect to a calibrated Melles-Friot silicon diode. IPCE was measured by changing the excitation wavelength (photoncounting spectrometer, ISS Inc., and Kiethley 2400 source meter). Electrochemical Impedance Spectroscopy (EIS) was measured by using Autolab PGSTAT30 (Eco-Chemie).

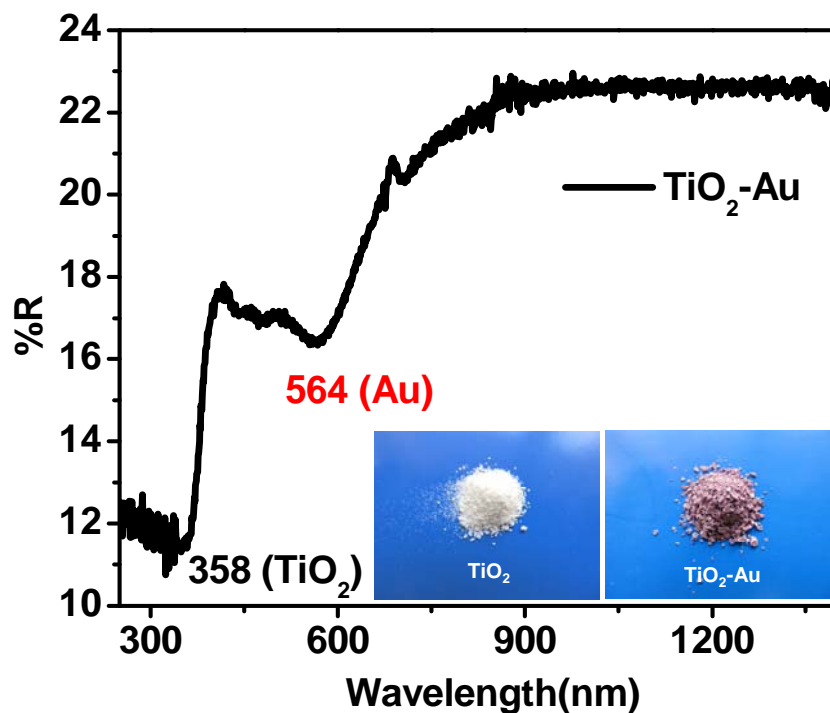
### 3.3 Results and Discussion

Figure 3.1 compares the XRD patterns for TiO<sub>2</sub> NPs with TiO<sub>2</sub>-Au nanocomposite. The peaks in figure 3.1(a) (dashed curve) at 25.4 (101), 38.1 (004), 48.1 (200), 54.2 (105), 55.0 (211), 62.8 (204), 69.1 (116), 70.3 (220) and 75.4 (215) (PCPDFWIN # 211 272) clearly represent the anatase TiO<sub>2</sub> phase. The tiny peaks at 38.1 (111) (overlapping with the TiO<sub>2</sub> (004)), 44.4 (200), 64.6 (220) and 77.6 (311) in the full red curve of figure 3.1(a) are attributed to metallic gold (PCPDFWIN # 040784) in the TiO<sub>2</sub>-Au nanocomposite. Presence of gold nanoparticles can also be clearly elucidated by Diffused Reflectance Spectra (DRS).



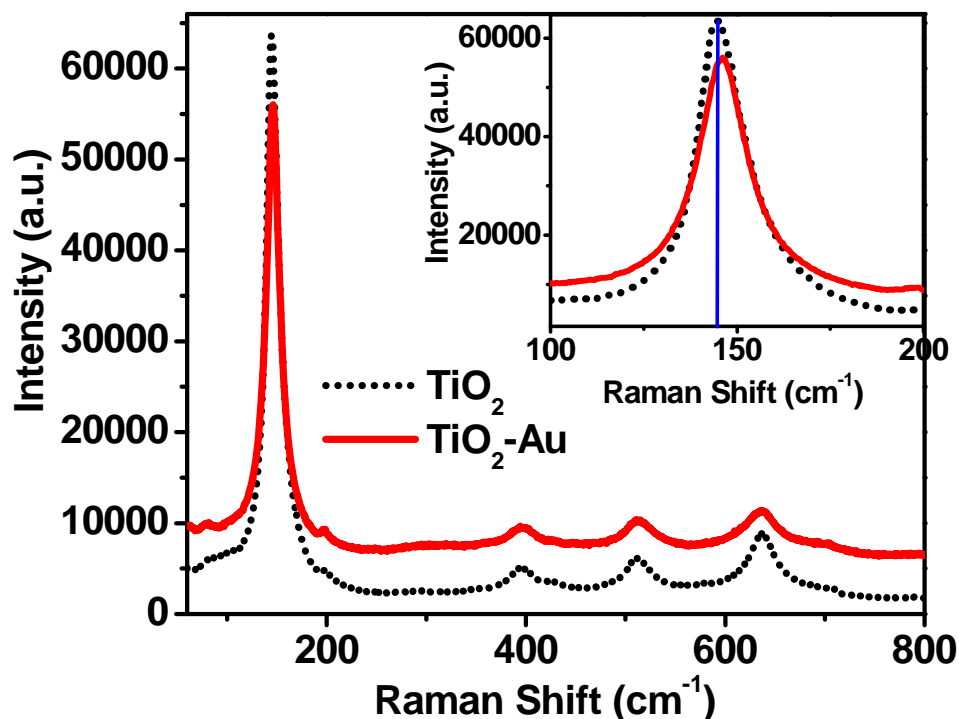
**Figure-3.1** X-ray diffraction (XRD) patterns of TiO<sub>2</sub> (short dotted line) and TiO<sub>2</sub>-Au (solid line) nanocomposite.

Figure 3.2 shows the diffused reflectance spectrum (DRS) for TiO<sub>2</sub>-Au nanocomposite. In addition to the strong interband absorption feature for anatase titania at 358 nm, a peak at ~ 564 nm corresponding to the surface plasmon absorption due to Au nanoparticles testifies to the formation of the nanocomposite. The inset in figure 3.2 shows the corresponding photos of pure TiO<sub>2</sub> and TiO<sub>2</sub>-Au samples. It can be seen that the color of pure TiO<sub>2</sub> and TiO<sub>2</sub>-Au samples is white and dark pink, respectively, which further indicates that the TiO<sub>2</sub>-Au sample contains metallic gold nanoparticles.



**Figure-3.2** Diffused reflectance Spectra (DRS) of  $\text{TiO}_2$ -Au nanocomposite. The inset shows corresponding photos of the pure  $\text{TiO}_2$  and  $\text{TiO}_2$ -Au composite samples.

The Raman spectra for  $\text{TiO}_2$  and  $\text{TiO}_2$ -Au nanocomposite powders are shown in figure 3.3. These spectra were measured at room temperature. The observed modes at  $\sim 145 \text{ cm}^{-1}$  ( $E_{g(1)}$ ),  $199 \text{ cm}^{-1}$  ( $E_{g(2)}$ ),  $396 \text{ cm}^{-1}$  ( $B_{1g(1)}$ ),  $511 \text{ cm}^{-1}$  (combination of  $A_{1g}$  and  $B_{1g(2)}$ ) and  $638 \text{ cm}^{-1}$  ( $E_{g(3)}$ ) can be assigned to the Raman active modes of the anatase crystal [14]. As seen from the inset, it is interesting to note that the Raman peak at  $\sim 145 \text{ cm}^{-1}$  is seen to have shifted towards higher wave-number for the case of  $\text{TiO}_2$ -Au nanocomposite sample. This can be attributed to the strain induced by Au loading and also possibly to small change in the crystallite size [15].



**Figure-3.3** Raman spectra for  $\text{TiO}_2$  (short dotted line) and  $\text{TiO}_2\text{-Au}$  (solid line) nanocomposite. Inset shows specific region of the data on expanded scale.

The TEM data of the  $\text{TiO}_2\text{-Au}$  nanocomposites are shown in figure 4. The image in figure 3.4(a) shows the nanoparticle size is in the range of  $\sim 15\text{-}20$  nm. The TEM image of selected area elemental scan of  $\text{TiO}_2\text{-Au}$  nanocomposite is shown in figure 3.4(b). The elemental mapping was carried out at 200 keV and electron spot size of 2.2 nm. The data were collected for 5 min. The elemental scans shown in figure 3.4(c) & (d) clearly reveal the presence of both Au and  $\text{TiO}_2$  NPs in the nanocomposites. From the elemental scans it can be noted that the Ti and Au locations bear strict correlation in the  $\text{TiO}_2\text{-Au}$  nanocomposite with the feeble Au signal (due to small concentration) being on the periphery of the  $\text{TiO}_2$  NPs. The energy dispersive x-ray (EDX) data shown in figure 3.5 further confirms the presence of Au in the  $\text{TiO}_2\text{-Au}$  nanocomposites.

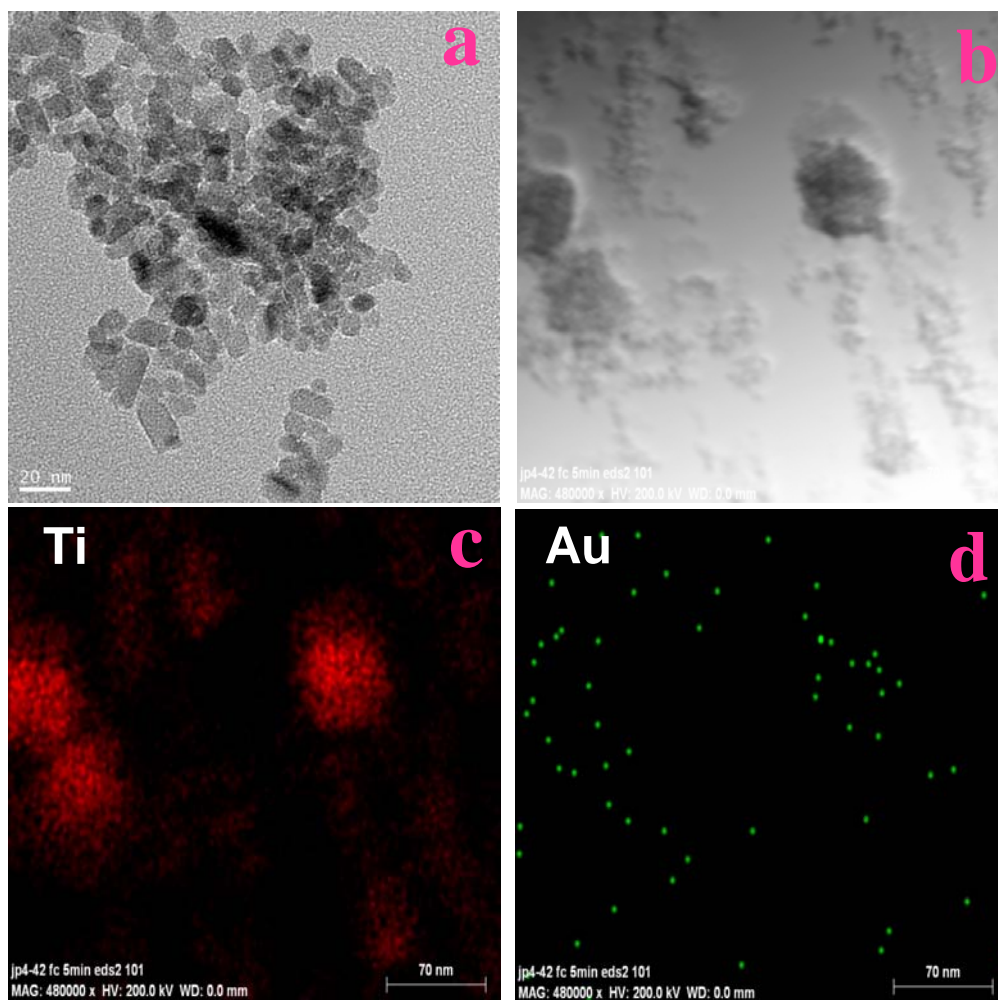


**Figure-3.4** (a) TEM image of selected area elemental scan of Au decorated TiO<sub>2</sub> nanoparticles revealing positions of Ti (b), Au(c) elements in sample.

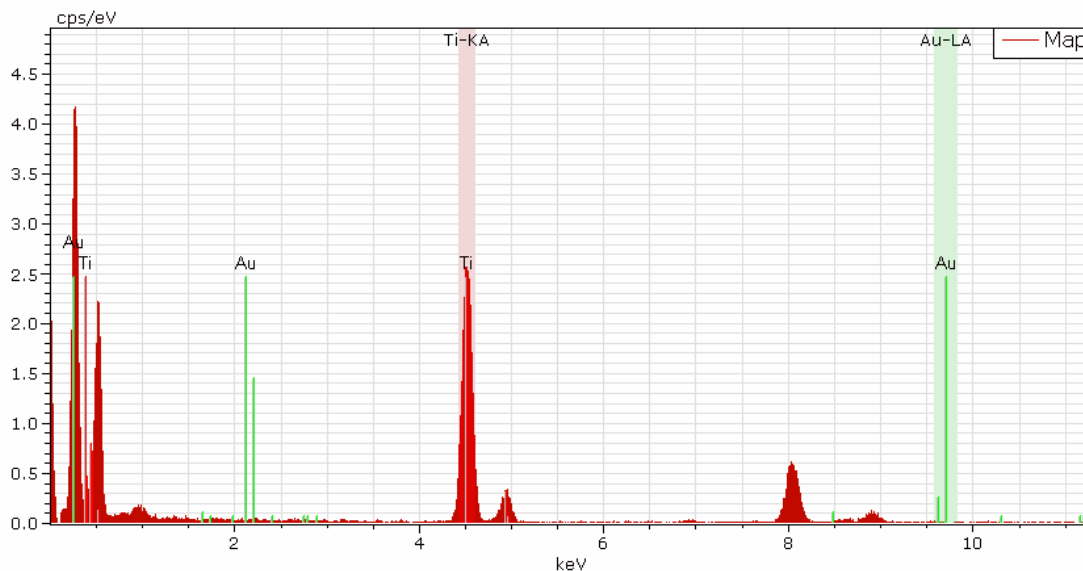


**Figure-3.5** The energy dispersive x-ray (EDX) data of TiO<sub>2</sub>-Au nanocomposites.

We evaluated the performance of the TiO<sub>2</sub> and TiO<sub>2</sub>-Au nanocomposite for photovoltaic application by recording the IPCE at different incident wavelengths of light which was calculated from the equation,  $IPCE (\%) = 1240 J_{SC} / \lambda P_{in}$ , where  $J_{SC}$  is the short-circuit current density,  $\lambda$  is the wavelength of the incident light and  $P_{in}$  is the power of the incident light. Figure 3.6 shows the difference in the IPCE spectra between the TiO<sub>2</sub>-Au and TiO<sub>2</sub> cases as a function of the wavelength. Interestingly the peak in this difference spectrum appears in the Au Plasmon region reflected in the DRS spectrum (figure 3.2). It should also be noted that some enhancement is seen in the longer wavelength region which can emanate from the plasmonic absorption in anisotropic Au nanostructures which could develop in the film formation and annealing during solar cell fabrication. This selective enhancement in the photocurrent generation efficiency in the Au plasmonic absorption regions is indicative of the fact that the attachment of metal nanoparticles is beneficial for enhanced absorption (local field enhancement) and/or charge separation.

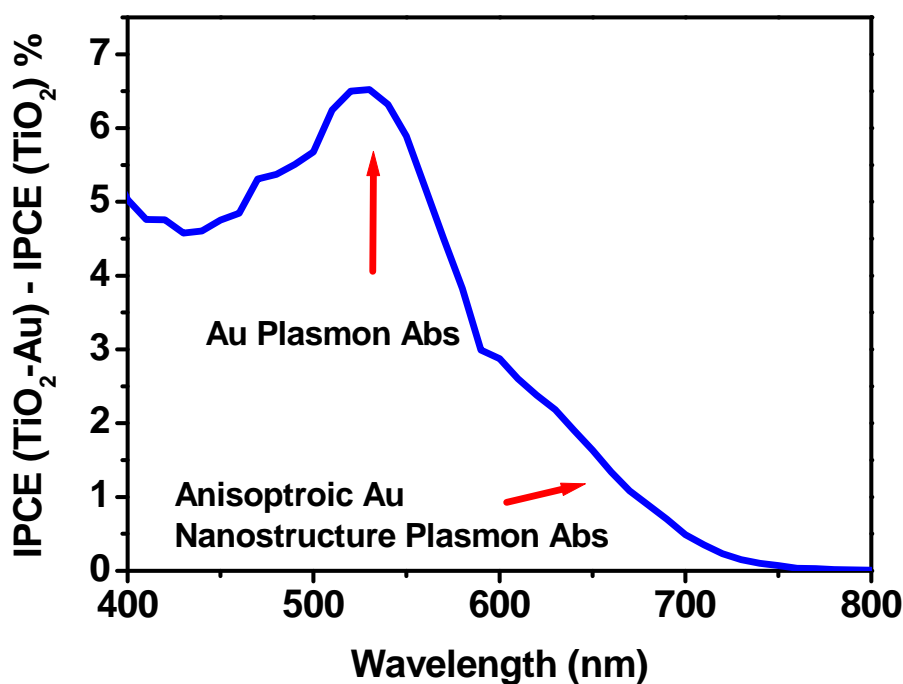


**Figure-3.6** The difference in the IPCE spectra between the  $\text{TiO}_2\text{-Au}$  and  $\text{TiO}_2$  cases as a function of the wavelength.

The cell performance of the DSSCs based on only  $\text{TiO}_2$  based and the  $\text{TiO}_2\text{-Au}$  nanocomposite electrodes was examined under 1 sun AM 1.5 simulated sunlight with an active area of  $0.25 \text{ cm}^2$ . Figure 3.7 and Table 3.1 compare the J-V characteristics for DSSCs prepared with the  $\text{TiO}_2\text{-Au}$  nanocomposite and  $\text{TiO}_2$  NPs electrodes. The inset shows corresponding photos of the pure  $\text{TiO}_2$  and  $\text{TiO}_2\text{-Au}$  composite films on FTO. It can be seen that for the case of nanocomposite the short circuit current density ( $J_{\text{SC}}$ ) is about  $13.2 \text{ mA}\cdot\text{cm}^{-2}$  which is higher than that for  $\text{TiO}_2$  nanoparticles case. Higher  $J_{\text{SC}}$  value in case of  $\text{Au-TiO}_2$  composite can be assigned to plasmon induced charge transfer from gold nanoparticles to  $\text{TiO}_2$ <sup>16</sup>. The open circuit voltage ( $V_{\text{OC}}$ ) of  $\text{TiO}_2\text{-Au}$  nanocomposite is 0.74V and that for the  $\text{TiO}_2$  nanoparticles case is 0.70 V. Also the fill factor is higher for the case of  $\text{TiO}_2\text{-Au}$  films ( $\sim 61\%$ ) than the case of  $\text{TiO}_2$  film (56%). Increase in  $V_{\text{OC}}$  and Fill Factor can be correlated with decreased electron-hole recombination at  $\text{TiO}_2\text{:Au-dye-electrolyte}$  interface [17]. The optimized mean efficiency

obtained by our procedure for TiO<sub>2</sub> nanoparticles film is about 5.0 % (no light harvesting). After Au loading on TiO<sub>2</sub> nanoparticles, the conversion efficiency is improved from 5.0% to 6.0% (almost 20% enhancement). Addition of Au NPs is thus seen to reduce the e-h recombination centers generally attributed to the oxygen vacancies in TiO<sub>2</sub> in the surface layers. Also, the Au plasmon mode energetically overlaps with dye absorption zone possibly rendering charge into the TiO<sub>2</sub> nanoparticles [16].

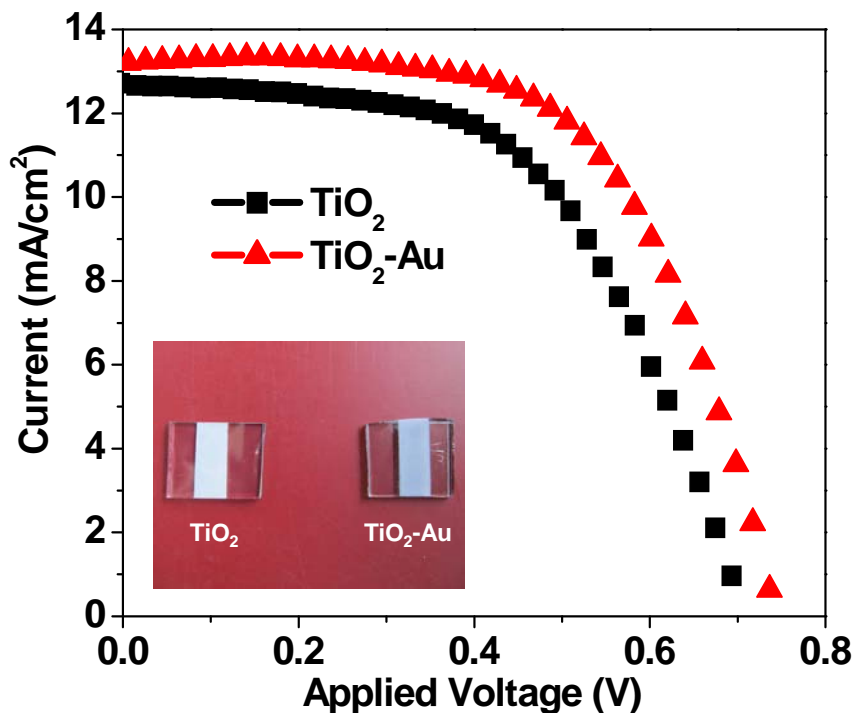
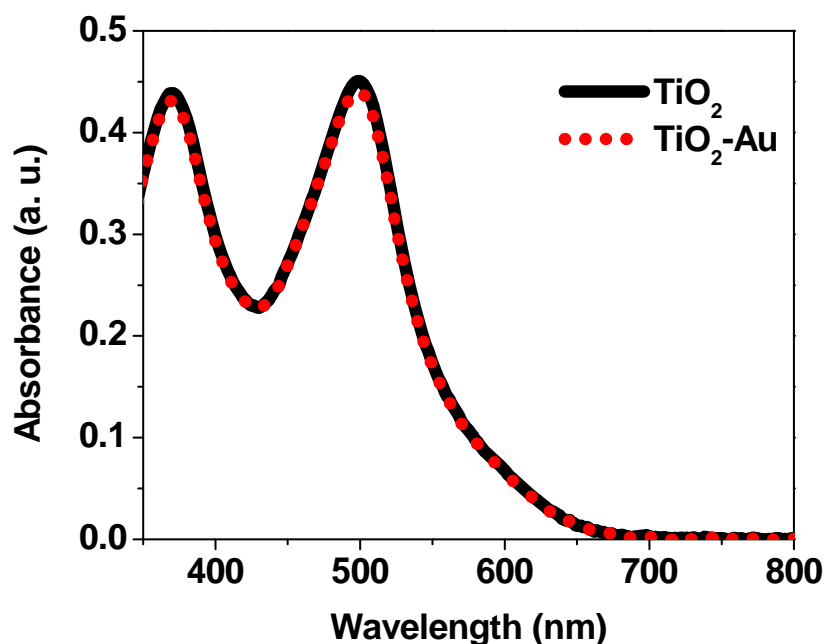


**Figure-3.7** J-V characteristics for TiO<sub>2</sub> nanoparticles and TiO<sub>2</sub>-Au nanocomposite. The inset shows corresponding photos of the pure TiO<sub>2</sub> and TiO<sub>2</sub>-Au composite films on FTO.

**Table-3.1** Performance Parameters of DSSCs fabricated with TiO<sub>2</sub> nanoparticles and TiO<sub>2</sub>-Au

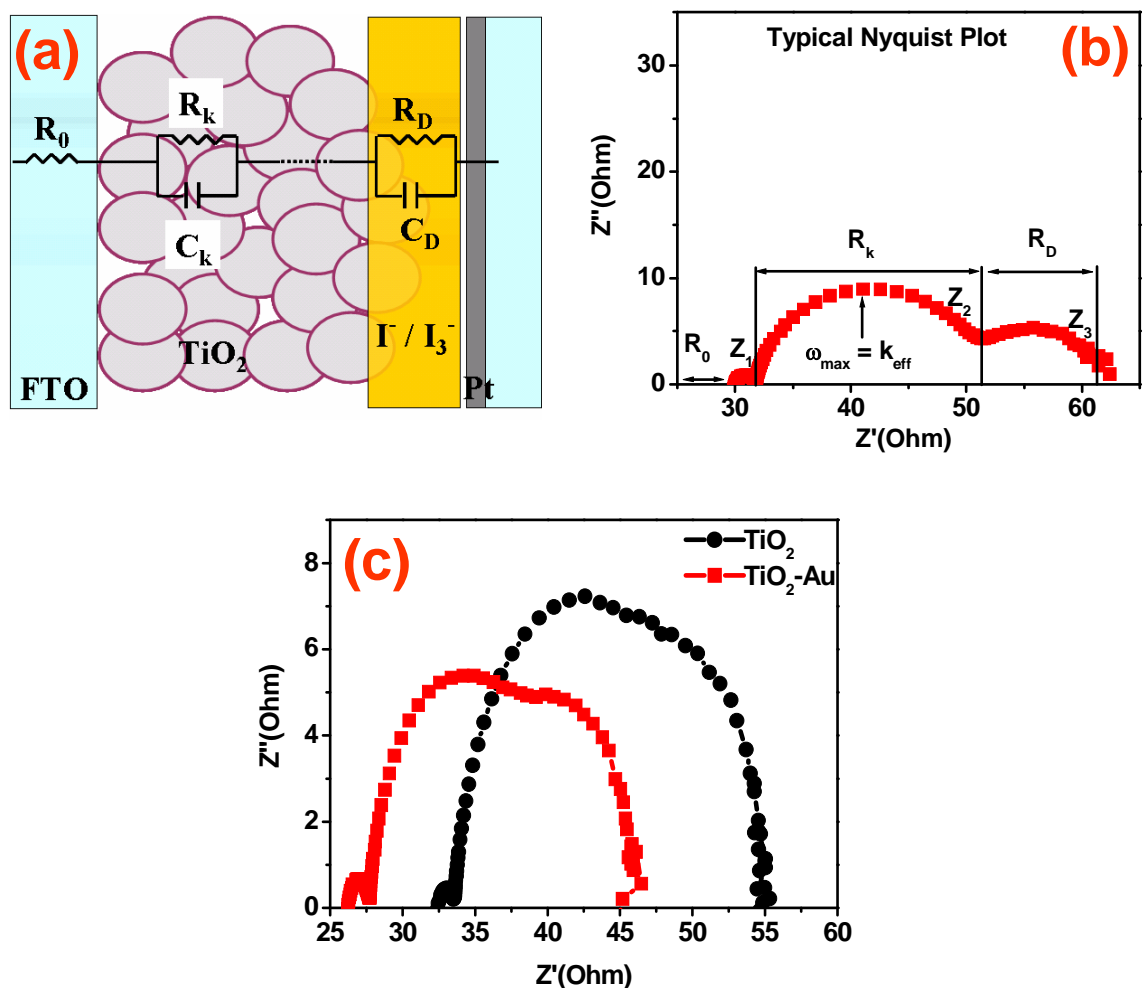
Samples	V <sub>OC</sub> (V)	J <sub>SC</sub> (mA/cm <sup>2</sup> )	Fill Factor	Eff(%)
TiO <sub>2</sub>	0.70	12.6	56.0	5.0 ± 0.2
TiO <sub>2</sub> -Au	0.74	13.2	61.0	6.0 ± 0.2

Figure 3.8 shows absorptions of solutions containing the dye detached from the  $\text{TiO}_2$  and  $\text{TiO}_2$ -Au nanocomposite films (all with  $1.5 \text{ cm}^2$  area) in 10 mL of  $\text{H}_2\text{O}$  with 1 mM KOH. We can calculate from Figure 8 the dye loadings of the  $\text{TiO}_2$  and  $\text{TiO}_2$ -Au nanocomposite films, which is  $\sim 2 \times 10^{-7}$  and  $\sim 2.1 \times 10^{-7} \text{ mol/cm}^2$ , respectively. It is interesting that although the dye loading of the  $\text{TiO}_2$ -Au nano-composite film is comparable to  $\text{TiO}_2$  nano-particulate film, the energy conversion efficiency of the  $\text{TiO}_2$ -Au cells is much higher. Thus other aspects pointed out above have a stronger influence.



**Figure-3.8** Absorptions of solutions containing dye detached from the  $\text{TiO}_2$  and  $\text{TiO}_2$ -Au nanocomposite films (all with  $1.5 \text{ cm}^2$  area) in a 10ml  $\text{H}_2\text{O}$  with 1mM KOH.

In order to study the electron transport and charge recombination in these  $\text{TiO}_2$  films Electrochemical Impedance Spectroscopy (EIS) measurements were performed. The frequency range chosen was from  $10^{-2}$  Hz to  $10^6$  Hz with an ac amplitude of 10 mV. The impedance spectrum of DSSC (Nyquist plot) mainly consists of 3 semicircles attributed to the impedances for the Pt| Electrolyte ( $Z_1$ ),  $\text{TiO}_2$ |Dye |electrolyte ( $Z_2$ ) and the diffusion of  $\text{I}_3^-$  ( $Z_3$ ) in the electrolyte, respectively, as depicted in figure 3.9 (a) [18].



**Figure-3.9** Electrochemical Impedance Spectroscopy (EIS) Measurements: (a) Schematic diagram showing the three interfaces, (b) Typical Nyquist Plot with specified parameters, and (c) Nyquist plot of TiO<sub>2</sub> Nanoparticles and TiO<sub>2</sub>-Au nanocomposite.

The resistance elements R<sub>1</sub>, R<sub>k</sub>, and R<sub>D</sub> are described as the real part of Z<sub>1</sub>, Z<sub>2</sub> and Z<sub>3</sub>, respectively, as shown in figure 3.9(b). It is found that the resistance element R<sub>0</sub> in the high frequency range over 1 MHz is influenced by the sheet resistance of TCO and the contact resistance between the TCO and TiO<sub>2</sub>. Figure 3.9(c) shows the Nyquist plots for the TiO<sub>2</sub> and TiO<sub>2</sub>-Au cases. From the plots it is clear that the electron transfer resistance at TiO<sub>2</sub>-Dye-electrolyte interface is decreased considerably in the case of TiO<sub>2</sub>-Au. This resistance R<sub>k</sub> i.e the diameter of the central arc which gives the charge transfer resistance including recombination of electrons with I<sub>3</sub><sup>-</sup> at the TiO<sub>2</sub> / electrolyte interface is lower

(~11  $\Omega$ ) for TiO<sub>2</sub>-Au as compared to ~14.2  $\Omega$  for TiO<sub>2</sub>.  $R_D$  (the DC resistance of diffusion of I<sub>3</sub><sup>-</sup> in electrolyte calculated from the diameter of the third arc) for the TiO<sub>2</sub>-Au nanocomposite is less than that for the TiO<sub>2</sub> based film. This leads to the higher efficiency, since other parameters are nominally comparable to the nanoparticle case.

**Table-3.2** Properties determined by Electrochemical Impedance Spectroscopy Measurements.

Name	$k_{\text{eff}}$ (s <sup>-1</sup> )	$\tau_{\text{eff}}$ (s)	$R_k$ ( $\Omega$ )	$D_{\text{eff}}$ (cm <sup>2</sup> s <sup>-1</sup> )	Con ( $\Omega$ cm s <sup>-1</sup> )	$R_D$ ( $\Omega$ )
TiO <sub>2</sub>	2.656	0.37	14.22	5.438 x 10 <sup>-5</sup>	0.453	6.98
TiO <sub>2</sub> -Au	3.85	0.26	10.93	6.06 x 10 <sup>-5</sup>	0.504	6.6

### 3.4 Conclusions

In conclusion, TiO<sub>2</sub> nanoparticles loaded with Au nanoparticles are hydrothermally in situ synthesized and are shown to yield solar energy conversion efficiency of ~6%, considerably higher than the unloaded TiO<sub>2</sub> nanoparticles without light harvesting. The transport improvement is revealed by electrochemical impedance spectroscopy which brings out that the charge transfer resistance including recombination of electrons with I<sub>3</sub><sup>-</sup> at the TiO<sub>2</sub> / electrolyte interface is lower for TiO<sub>2</sub>-Au as compared to unloaded TiO<sub>2</sub> nanoparticles. Different characterizations are employed to elucidate the probable causes of the observations.

### 3.5 References

1. A. Hochbaum, P. Yang, *Chem. Rev.*, **2010**. *110*, 527.
2. J. Nowotny, *Energy Environ. Sci.*, **2008**. *1*, 565.
3. H. Arakawa, K. Sayama, *Res. Chem. Intermed.* **2000**. *26*, 145.
4. B. O'Regan, M. Gratzel, *Nature*, **1991**. *23*, 737.
5. A. Hagfeldt, G. Boschloo, L. Sun, L. Kloo, H. Pettersson, *Chem. Rev.*, **2010**. *110*, 6595.

6. Q. Zhang, C.S. Dandeneau, X. Zhou, G. Cao, *Adv. Mater.*, **2009**, *21*, 4087.
7. V. Dhas, S. Muduli, S. Agarkar, A. Rana, B. Hannover, R. Banerjee, S. Ogale, *Solar Energy*, **2011**, *85*, 1213.
8. V. Dhas, S. Muduli, W. Lee, S.H. Han, S. Ogale, *Appl. Phys. Lett.*, **2008**, *93*, 243108-3.
9. S. Muduli, W. Lee, V. Dhas, S. Mujawar, M. Dubey, K. Vijayamohanan, S.H. Han, S. Ogale, *ACS Appl. Mater. Interfaces*, *2009*, *1*, 2030.
10. P. V. Kamat, B. Shanghavi, *J. Phys. Chem. B*, **1997**, *101*, 7675.
11. V. Subramanian, E. Wolf, P. V. Kamat, *J. Phys. Chem. B*, **2001**, *105*, 11439.
12. A. Wood, M. Giersig, P. Mulvaney, *J. Phys. Chem. B.*, **2001**, *105*, 8810.
13. M. D. Brown, T. Suteewong, R.S. Santosh, V. D'Innocenzo, A. Petrozza, M. Lee, U. Wiesner, H. J. Snaith, *Nano Lett.*, **2011**, *11*, 438.
14. A. Golubovic, M. Scepanovic, A. Kremenovic, S. Askrabic, V. Berec, Z. Dohcevic-Mitrovic, Z. V., Popovic, *J Sol-Gel Sci Technol.*, **2009**, *49*, 311.
15. Q. Xiang, J. Yu, B. Cheng, H. C. Ong, *Chem. Asian J.*, **2010**, *5*, 1466.
16. L. Du, A. Furube, K. Yamamoto, K. Hara, R. Katoh, M. Tachiya, *J. Phys. Chem. C*, **2009**, *113*, 6454.
17. M. Law, L. E. Greene, A. Radenovic, T. Kuykendall, J. Liphardt, P. Yang, *J. Phys. Chem. B*, **2006**, *110*, 22652.
18. M. Adachi, M. Sakamoto, J. Jiu, Y. Ogata, S. Isoda *J Phys. Chem. B.*, **2006**, *110*, 13872.

## **Chapter-4**

### **TiO<sub>2</sub>-MWCNTs/Graphene Nanocomposites for DSSC Application**

*The simple laboratory protocol is developed for the synthesis of TiO<sub>2</sub>-MWCNT and TiO<sub>2</sub>-Graphene nanocomposites by hydrothermal route. Several characterizations have been employed to reveal the nature of the modification imparted to the MWCNTs and Graphene under hydrothermal processing conditions. It is observed that these nanocomposites show higher conversion efficiency in dye-sensitized solar cells as compared to hydrothermally synthesized TiO<sub>2</sub> without MWCNT and Graphene.*

## 4.1 Introduction

Many conventional materials, such as metals, ceramics, and plastics, cannot fulfill all requirements for new technologies seeking to solve the world's most immediate problems related to energy and the environment. In many cases, however, the combination of two materials can show properties superior to those of their individual constituents. A well-known example is inorganic fiber-reinforced polymer composites, which in recent years have become ubiquitous in applications where lightweight, tough materials are required, including aerospace, high-end automotive and sporting equipment. Decreasing the size of the inorganic units to the same level as the organic building blocks has led to more homogeneous materials, which allowed a further refinement of material properties on the molecular level. This has resulted in the introduction of organic-inorganic hybrids, such as metal organic frameworks. In contrast to nanocomposites, which simply combine the individual properties of the components, these hybrid materials merge the properties of the components in a way that creates new properties distinct from those of either building block. [1, 2] The last two decades have seen the development of some new types of hybrid materials, such as nanocomposites and metal oxide frameworks, and their implementation in various applications that require.

This chapter is divided into two sections: hydrothermal synthesized (I) TiO<sub>2</sub>-MWCNTs nanocomposites and (II) TiO<sub>2</sub>-Graphene nanocomposites for photovoltaic applications.

## 4-I Section-I

### TiO<sub>2</sub>-MWCNTs Nanocomposites

#### 4-I.1 Introduction

Dye-sensitized solar cell (DSSCs) represents a key class of cell architecture that has emerged as a promising candidate for the development of next generation solar cells [3, 4]. With suitable engineering and optimization of the nanostructure for its optical, electrical and morphological properties, its porosity, light harvesting characteristics etc. these cells have been shown to deliver fairly high power efficiencies [3, 5, 6]. This compounded with the low materials/processing cost and the ease of manufacturing has led to significant efforts in recent years to improve their performance. The efficiency of collection of the photo-generated carriers at the two electrodes is a critical factor in the device performance. It is determined by the competition between the electron transport to the anode and electron transfer to I<sub>3</sub><sup>-</sup> ions in the electrolyte. In order to improve the efficiency of DSSCs, various ideas have been pursued. These include deposition of a thin tunneling barrier layer on the substrate [7-9], incorporation of an ultrathin layer of insulating oxide on the surface of the meso-porous film of TiO<sub>2</sub> [10], concurrent use of different dyes for co-sensitization [11], post-treatment using TiCl<sub>4</sub> precursor [12,13], etc. A bi-layer structure involving an additional light harvesting layer is also employed widely because it confines the incident light within the electrode enhancing the photocurrent density [14-16]. One of the major bottlenecks that often limits the performance of these solar cells is the efficiency of electron transport across the nanoparticulate network because the inter-particle interface scattering encountered during the electron transit effectively enhances electron recombination before their efficient collection at the electrode surface. It is to reduce such undesirable effects dramatically that suggestions have been made and experimented upon using extended charge carrier pathways such as nanotubes, nanorods, flowers etc. as integrated elements of the cell architecture [17,18]. Such geometric forms can either be added in a simple physical mixture with nanoparticulates which eventually get sintered together by adequate thermal processing, or nanocomposites of extended and particular structures can be preformed and used for making the cells. The latter one is an attractive proposition because it gives

avenues to engineer the structural and electrical characteristics of the interfaces during the synthesis protocol itself. Several attempts have been made using both strategies and enhancements in efficiencies have been realized [5, 6]. One category of extended quasi 1D material that has attracted considerable attention in this regard is the carbon nanotubes (CNTs) for its good and controllable electrical characteristics and compatible band line-ups with metal oxide nanosystems of interest such as  $\text{TiO}_2$ ,  $\text{ZnO}$  etc. [19-29]

Chen et al. synthesized CNTs- $\text{TiO}_2$  nanocomposites by hydrolysis wherein formation of  $\text{TiO}_2$  and its compounding with CNTs happened almost simultaneously with interface formation via polar oxygenated groups, though these authors did not report on photovoltaic or photocatalytic measurements [30]. Lee et al. used nanocomposites of preprocessed multi wall carbon nanotubes (MWCNTs) with carboxylic acid groups and  $\text{TiO}_2$  nanoparticles (NPs) synthesized via Sol-Gel process for DSSCs and obtained conversion efficiency of 4.97 % with 0.1 wt % CNT [26]. Kamat and co-workers have done significant work on nanocomposites of single walled CNTs (SWCNTs) with  $\text{TiO}_2$  in the context of photovoltaic and photocatalytic applications. They have demonstrated efficiency enhancements and have also elucidated the attendant mechanisms of photo-induced charge separation and carrier transport to the collecting electrodes [19-21]. Yen et al. used a modified acid catalyzed sol-gel method to synthesize MWCNTs- $\text{TiO}_2$  nanocomposites and examined them for DSSCs performance. They emphasized the importance of optimum CNTs loading to realize efficiency of 4.62% [23]. Lee et al. have also realized DSSCs efficiency of 5.02 % using MWCNTs- $\text{TiO}_2$  nanocomposites, which projects improvement by ~50% over the case without MWCNT [25]. More recently Sawatsuk et al have shown improvement in the efficiency of DSSC by almost 60% by a simple mixing process [31].

In the present work we have employed hydrothermal route to synthesize  $\text{TiO}_2$ -MWCNTs nanocomposites and have realized significant enhancement in the power conversion efficiency of DSSCs (7.4%). Using various characterizations we analyze the possible origin of the observed effects. It is useful to mention here that the hydrothermal process, in which the chemical reaction could take place under auto-generated pressure upon

heating, is efficient to achieve crystalline phase at relatively low temperatures [32, 33]. It is suggested that the high pressure can render denser materials with less defects and good crystallinity as compared to other milder routes.

## 4-I.2 Experimental

**4-I.2.1 Materials.** Chemical agents were purchased from Aldrich Co. and the  $\text{RuL}_2(\text{NCS})_2:(\text{TBA})_2$  (L=2,2'-bipyridine-4,4'-dicarboxylic acid, TBA=tetrabutylammonium) (N719) were purchased from Solaronix Co. and used as received. MWCNTs (95% purity) having diameter 20-40nm and length 5-15 $\mu\text{m}$  were obtained from Monald Tech. (India). Fluorine-doped  $\text{SnO}_2$  (FTO) electrode (sheet resistance 8 ohm/square, transmittance 77% in the visible range) were obtained from Pilkington TEC Glass. For preparation of reference DSSCs, commercial  $\text{TiO}_2$  were obtained from Degussa (P25). High purity water (Milli-Q, Millipore) was used for all experiments. The FTO electrodes were washed with acetone, ethanol and deionized (18.2  $\text{M}\Omega\cdot\text{cm}$ ) water in an ultrasonication bath for 15 min with a final wash in *i*-propanol.

### 4-I.2.2 Preparation of $\text{TiO}_2$ -MWCNT nanocomposite

The  $\text{TiO}_2$ -MWCNTs nanocomposite was prepared by using hydrothermal method. Titanium Isopropoxide (2 ml) was hydrolyzed by adding sufficient amount of deionized water and then a few milligrams of MWCNTs were added to the above solution followed by sonication for 5 minutes. The solution was then transferred to Teflon lined autoclave vessel along with 3ml of  $\text{H}_2\text{SO}_4$  (1M). This autoclave vessel was kept at 175 °C for 24 hours. The resulting product was washed thoroughly with deionized water and dried at 50 °C in a dust proof environment to produce grayish powder of  $\text{TiO}_2$ -MWCNTs nanocomposite.

### 4-I.2.3 Characterization

The various techniques such as X-ray diffraction (XRD, Philips X'Pert PRO), Raman (Horiba Jobin Yvon LabRAM HR System), Transmission Electron Microscopy (TEM), Field-Emission Scanning Electron Microscope (FE-SEM, Hitachi S-4200), FT-IR spectroscopy (Perkin Elmer Spectra One) were used to characterize the samples.

Formation of TiO<sub>2</sub>-MWCNTs nanocomposite films was carried out by the doctor blade method, and then annealed at 450 °C for 30 min. Thickness of TiO<sub>2</sub>-MWCNTs nanocomposite films was ~ 12 microns. For sensitization, the TiO<sub>2</sub>-MWCNTs nanocomposite films were impregnated with 0.5 mM N719 dye in ethanol for 24 h at room temperature. The sensitizer-coated TiO<sub>2</sub> films were washed with ethanol.

**4-I.2.4 Measurements.** The J-V characteristics were measured by irradiation with 100 mW/cm<sup>2</sup> (450 W Xenon lamp, Oriel Instruments) 1 sun AM 1.5 simulated sunlight as a solar simulator in the presence of a water filter. Current was measured using Kiethley 2400 source. The electrolytes were used with 0.6 M 1-hexyl-2, 3-dimethyl-imidazolium iodide, 0.1 M LiI, 0.05 M I<sub>2</sub>, and 0.5 M 4-tert-butylpyridine in methoxyacetonitrile. The measurements of incident-photon-to-current conversion efficiency (IPCE) were carried out without bias illumination with respect to a calibrated Melles-Friot silicon diode. IPCE was measured by changing the excitation wavelength (Photon counting spectrometer, ISS Inc. and Kiethley 2400 source meter).

## 4-I.3 Results and Discussion

### 4-I.3.1 Crystal Structure of TiO<sub>2</sub>-MWCNTs nanocomposite

Figure 4.1 compares the XRD patterns for TiO<sub>2</sub> NPs and TiO<sub>2</sub>-MWCNTs nanocomposite synthesized by hydrothermal route. The peaks in figure 4.1 at 25.3 (101), 37.8 (004), 48.2 (200) and 54.1 (105) (PCPDFWIN # 211 272) clearly represent the anatase TiO<sub>2</sub> phase, with a tiny amount of (110) rutile phase contribution (PCPDFWIN # 211 276) observed at 27.22. The 100% XRD peak intensity for CNT (PCPDFWIN # 411 487) is expected at 26.38 (002), which is not apparent due to its small amount in the composition of TiO<sub>2</sub>-MWCNTs (as well as its low Z as compared to the dominant Ti (high Z) O<sub>2</sub>), but the same can be clearly elucidated by Raman analysis as discussed later. As indicated in the inset, we did see a tiny but definitive shift in the XRD peak positions possibly suggesting strain (and particle size) effects originating in the integration between the TiO<sub>2</sub> NPs and the MWCNTs surface. It also suggests that our process leads to real integration across the interface rather than formation of a mere mixture, as we bring out more conclusively via Raman and FT-IR analysis.

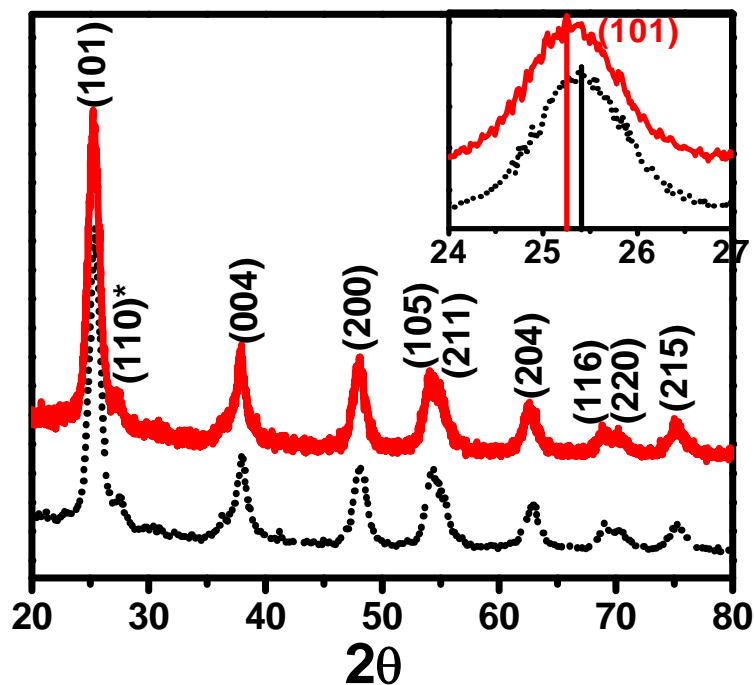


**Figure-4.1** X-ray diffraction (XRD) patterns of  $\text{TiO}_2$  (short dotted line) and  $\text{TiO}_2$ -MWCNT (solid line) nanocomposite.

The Raman spectra for  $\text{TiO}_2$  and  $\text{TiO}_2$ -MWCNTs nanocomposite powders are shown in figure 4.2. The Raman spectrum for the case of pure  $\text{TiO}_2$  shows clear signatures at about  $397.2\text{ cm}^{-1}$ ,  $514.6\text{ cm}^{-1}$  and  $641\text{ cm}^{-1}$ , as expected [34], while for pure MWCNTs case the Raman features are observed at  $1325\text{ cm}^{-1}$  and  $1571.5\text{ cm}^{-1}$ , as reported [27]. As seen from the inset, clear signatures of MWCNTs are also noted in the  $\text{TiO}_2$ -MWCNTs nanocomposite spectrum, along with those for  $\text{TiO}_2$  in that spectral region. Interestingly, the main three features ( $397.2\text{ cm}^{-1}$ ,  $514.6\text{ cm}^{-1}$  and  $641\text{ cm}^{-1}$ ) in the Raman spectrum representative of anatase  $\text{TiO}_2$  are broadened in the case of the  $\text{TiO}_2$ -MWCNTs nanocomposite sample as compared to the only  $\text{TiO}_2$  case. Such broadening can occur due to strain gradients originating from interface integration or particle size distribution, and has been observed in other nanocomposite systems with MWCNT [31, 35]. In thin films it is well known that strain effects can extend to several nanometers into materials (critical thickness) depending on the lattice misfit. In the present case one has a molecular

substrate on which the TiO<sub>2</sub> nanoparticles are getting chemically anchored. It is difficult to define strain in precise terms in this organic-inorganic complex interface system. However given the nanoscopic nature of the particles that leads to higher concentration of surface atoms and attendant phonon softening, one could expect strain gradients to extend almost over the particle dimension which in our case is around 8-10 nm. We believe that in addition to strain the Raman line broadening could occur due to particle size distribution [36]. Indeed in the present case, since the MWCNT concentration is small it is possible that in addition to heterogeneous nucleation on the MWCNT surface, some nanoparticles could grow via homogeneous nucleation and may have a different size distribution. Admittedly more work will be needed to resolve the precise origin of the broadening.

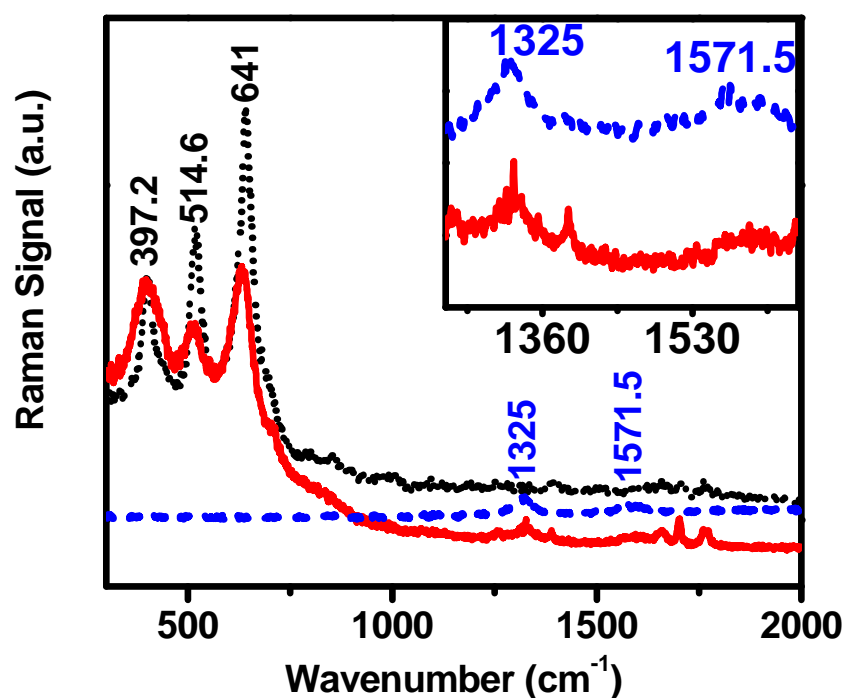


**Figure-4.2** Raman spectra for MWCNTs (dashed line), TiO<sub>2</sub> (short dotted line) and TiO<sub>2</sub>-MWCNTs (solid line) nanocomposite. Inset shows specific region of the data on expanded scale.

#### 4-I.3.2 Morphological Characterization

Figure 4.3a shows the TEM image of TiO<sub>2</sub> nanoparticles synthesized by the hydrothermal process without incorporation of MWCNT. The mean particle size is about 8-10 nm and the particles are faceted suggesting good crystallinity as expected in a hydrothermal process. Figure 4.3b shows TEM image of MWCNTs used in the experiment indicating its dimensions (Diameter ~20-40nm and length ~5-15 $\mu$ m). The integration between MWCNT and TiO<sub>2</sub> nanoparticles discussed above can be visualized from the FE-SEM data shown in figure 4.3c. A very uniform growth with excellent TiO<sub>2</sub> NPs coverage can be clearly seen. As will be discussed next, hydrothermal processing environment surface modifies MWCNTs to enable such growth. We now address the issue of possible modification imparted by the hydrothermal treatment used to prepare the nanocomposite to examine the possible routes for interface integration of growing TiO<sub>2</sub> NPs on its surface.

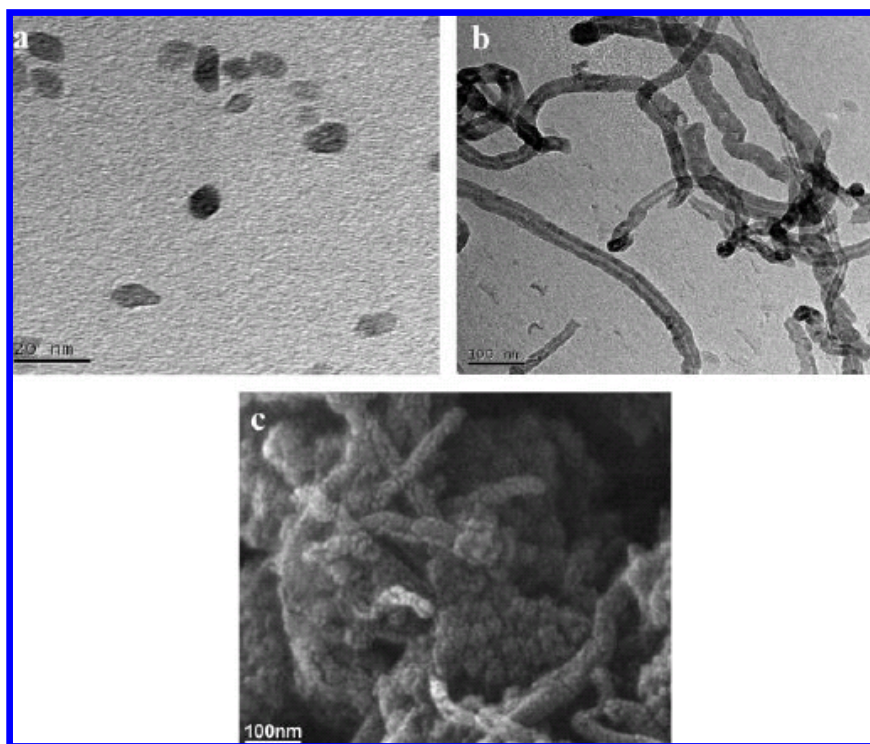


**Figure-4.3** Transmission electron micrograph (TEM) images of (a) TiO<sub>2</sub> nanoparticles, (b) MWCNT. The FE-SEM data showing integrated growth of TiO<sub>2</sub> on MWCNTs is shown in (c).

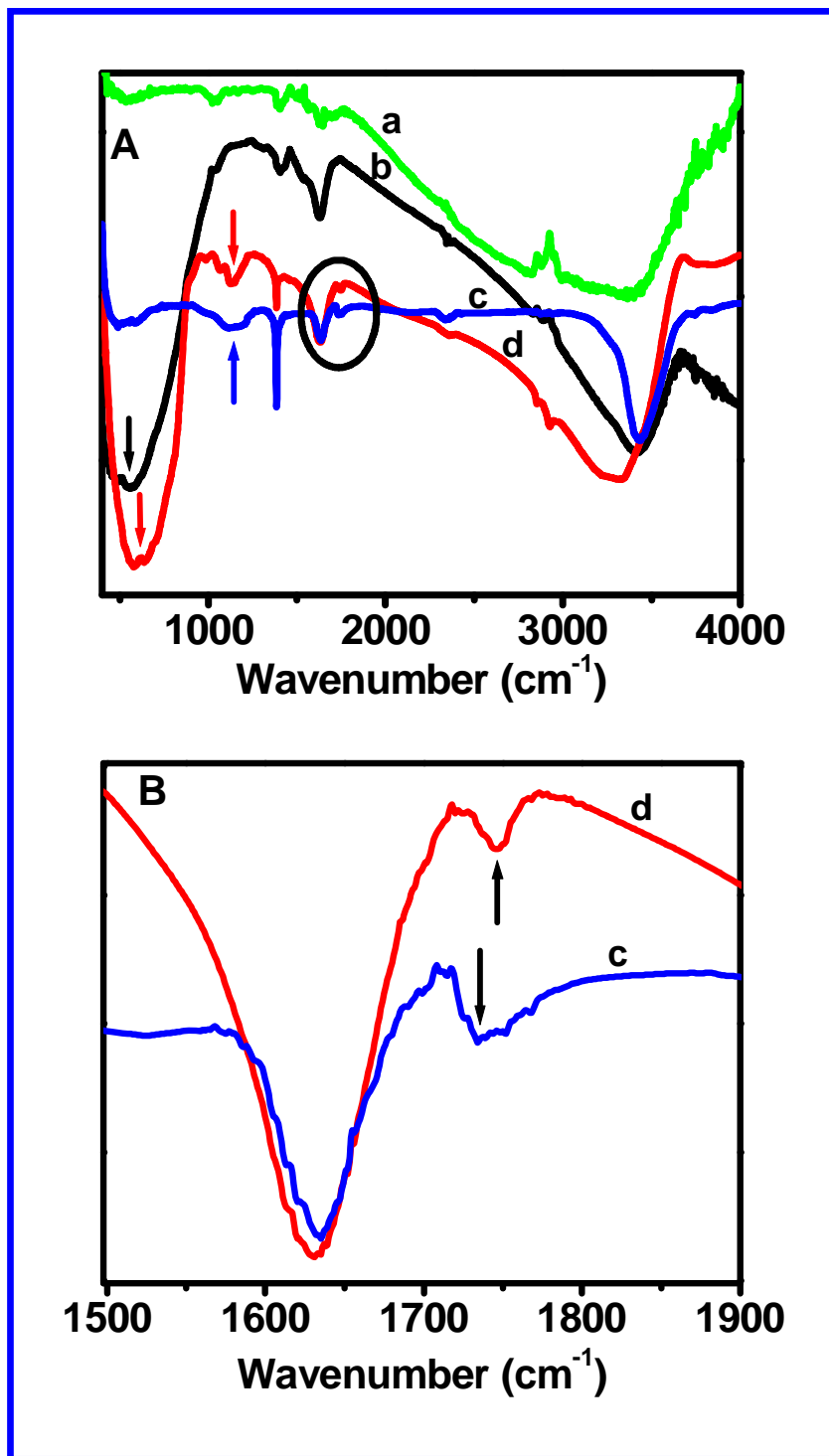


**Figure-4.4** FT-IR data for the (a) pristine MWCNTs, (b)  $\text{TiO}_2$  nanoparticles, (c) hydrothermally processed MWCNTs and (d)  $\text{TiO}_2$ -MWCNTs nanocomposites.

### 4-I.3.3 FT-IR spectra

Figure 4.4A shows the FTIR data of (a) pristine MWCNTs, (b) TiO<sub>2</sub> nanoparticles, (c) hydrothermally processed MWCNTs and (d) TiO<sub>2</sub>-MWCNTs nanocomposites. The bonding between Ti–O is clearly represented in the region near 500 cm<sup>-1</sup>. It is interesting to note from the black and red arrows in this region that the mean position of the signature shifts from about 520 cm<sup>-1</sup> in the TiO<sub>2</sub> case to about 612 cm<sup>-1</sup> for the TiO<sub>2</sub>-MWCNT composite. This can be attributed to different size distributions and possibly levels of strains in the two cases. Interestingly, only in the cases of hydrothermally processed samples involving MWCNT (namely, MWCNT and TiO<sub>2</sub>-MWCNT) we note clear signatures centered near 1143 cm<sup>-1</sup> and 1735 cm<sup>-1</sup>. The signature near 1143 cm<sup>-1</sup> is in the fingerprint region, hence difficult to assign uniquely. However, the occurrence of the signature near 1735 cm<sup>-1</sup> (see circled region) with contribution in the region around 3400 cm<sup>-1</sup> (OH stretch, which also overlaps with other contributions) together indicate the presence of –COOH group only in the hydrothermally processed cases involving MWCNT [37]. From figure 4.4B it can be noted that in the TiO<sub>2</sub>-MWCNT nanocomposite the same signature appears a bit shifted to 1745 cm<sup>-1</sup>, suggesting the effect of conjugation of TiO<sub>2</sub> on the modified MWCNT surface. Other characteristic bands including the sharp one near 1380 cm<sup>-1</sup> are generated due to different mineralizer residues used in the hydrothermal process. In the light of this result, we now address the issue of possible modification imparted by the hydrothermal treatment used to prepare the nanocomposite to examine the possible routes for interface integration of growing TiO<sub>2</sub> NPs on its surface.

Due to the –OH group on Ti-precursor and the C–O, C=O and O–C=O groups opened up on the surface of MWCNTs due to hydrothermal treatment, properly integrated nanocomposites can form naturally through some physicochemical actions involving van der Waals force, H- bonding and other bonding types. For example, the –OH group on Ti-precursor may possibly react with the –OH and –COOH groups on MWCNT surface in removing H<sub>2</sub>O contained in wet fresh composites. Thus the bonding of the form C–O–Ti or O=C–O–Ti might form through the dehydration reaction among the groups on the two materials [30]. As indicated in the figure 4.4B, the shift of carbonyl group (C=O)

from  $1735\text{ cm}^{-1}$  (in hydrothermally processed MWCNTs) to  $1745\text{ cm}^{-1}$  (in  $\text{TiO}_2$ -MWCNTs nanocomposites) indicates the interaction of carboxylate group with Ti-precursor. In figure 4.5 we present a schematic of the suggested process.

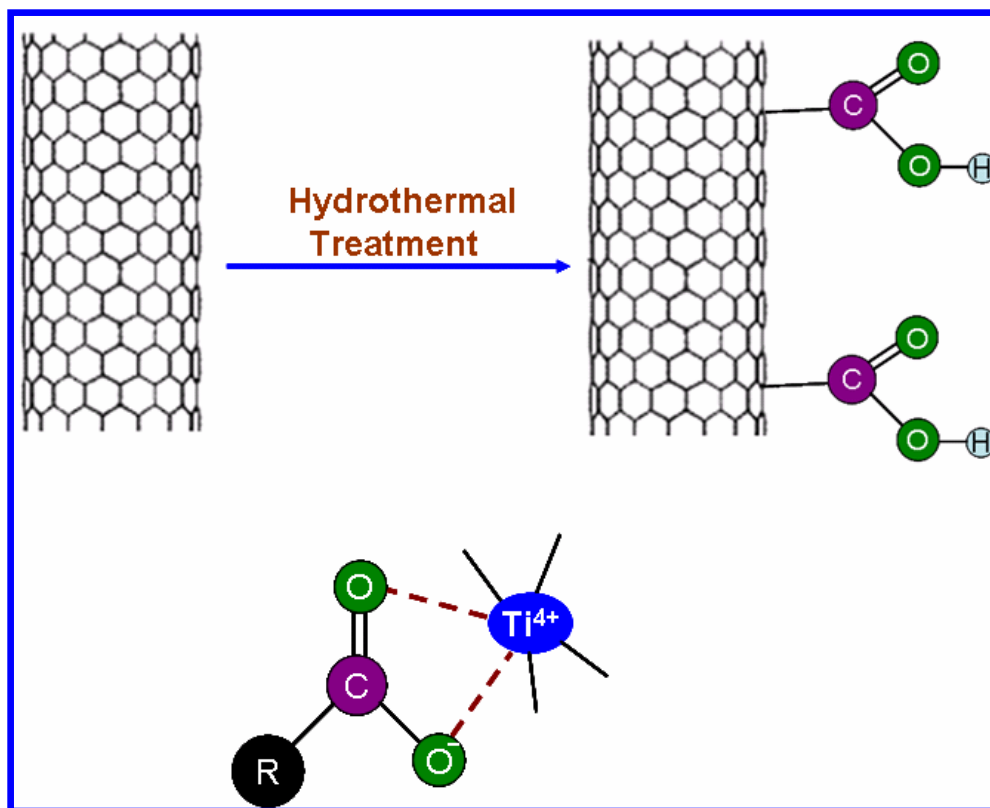


**Figure-4.5** Schematic of functionalisation of MWCNTs under hydrothermal treatment and the attachment of functionalized MWCNTs with  $\text{TiO}_2$  nanoparticles (R belongs to MWCNTs).

We evaluated the performance of the  $\text{TiO}_2$ -MWCNTs nanocomposite as an electrode for photovoltaic application by recording the IPCE at different incident wavelengths of light. As a reference cells, commercial  $\text{TiO}_2$  films were prepared by P25 (Degussa). Figure 4.6 shows IPCE spectra as a function of wavelength for the P25 and  $\text{TiO}_2$ -MWCNTs samples which was calculated from the equation,  $\text{IPCE} (\%) = 1240 J_{SC} / \lambda P_{in}$ , where  $J_{SC}$  is the short-circuit current density,  $\lambda$  is the wavelength of the incident light and  $P_{in}$  is the power of the

incident light. The absolute IPCE for TiO<sub>2</sub>-MWCNTs is significantly higher than that for P25 over the entire wavelength region, which is in good agreement with the observed higher short-circuit photocurrent density ( $J_{sc}$ ) as shown later. Both these electrodes exhibit an IPCE maximum corresponding to the absorption maximum of the Ru (II) complex. The IPCE response at all wavelengths is enhanced from ~ 47 % to ~ 70% as a result of introducing MWCNTs scaffold in the mesoscopic TiO<sub>2</sub> film. Factors controlling the IPCE in DSSCs solar cells have been discussed in detail by several research groups [20]. Suppressing the back electron transfer and improving the electron transport within the nanostructured TiO<sub>2</sub> film (which directly increases ( $J_{sc}$ ) short-circuit current) are regarded as the two most important factors controlling the overall IPCE of the cell. Enhancement in the photoconversion efficiency in the present experiments suggests that charge collection and transport in these films are considerably improved by incorporating MWCNTs in the network in the form of integrated nanocomposite.

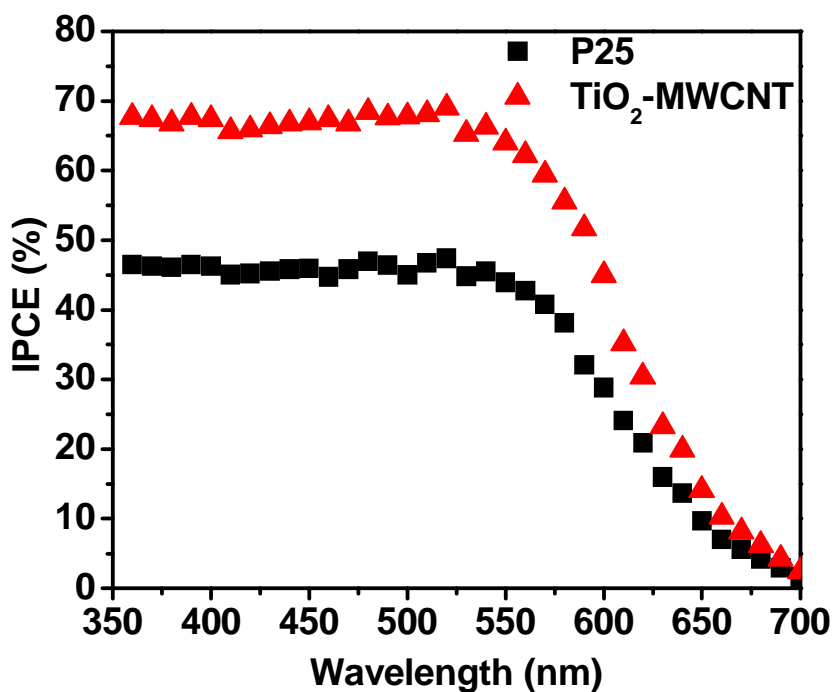


**Figure-4.6** IPCE data for TiO<sub>2</sub>-MWCNTs nanocomposite as compared to the corresponding P25 data.

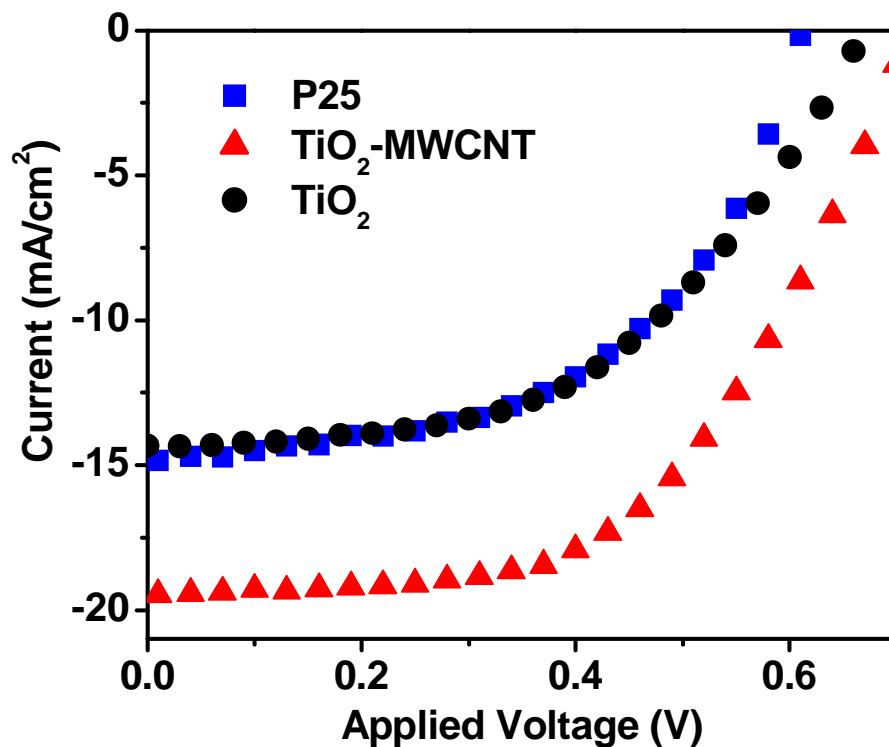


**Figure-4.7** J-V characteristics for TiO<sub>2</sub>-MWCNT nanocomposite as compared to the corresponding cases of P25 and hydrothermally synthesized TiO<sub>2</sub> nanoparticles without MWCNT.

**Table-4.1** Performance Parameters of DSSCs fabricated with P25, TiO<sub>2</sub> nanoparticles and TiO<sub>2</sub>-MWCNTs.

Name	V <sub>oc</sub> (V)	J <sub>sc</sub> (mA/cm <sup>2</sup> )	Fill Factor (FF)	Efficiency (η)
Degussa P25	0.61	14.9	0.52	4.73
TiO <sub>2</sub>	0.70	14.33	0.51	4.90
TiO <sub>2</sub> -MWCNT	0.70	21.9	0.49	7.37

The cell performances of the DSSCs based on the MWCNTs-TiO<sub>2</sub> nanocomposite electrodes were measured under 1 sun AM 1.5 simulated sunlight with an active area of

0.25 cm<sup>2</sup>. Figure 4.7 and Table 4.1 compare the J–V characteristics for DSSCs prepared with the nanocomposite electrodes (MWCNT wt % 0.2), TiO<sub>2</sub> nanoparticles and with P25. It can be seen that for the case of nanocomposite the  $J_{sc}$  is about 22 mA cm<sup>-2</sup> which is almost 47 % higher than that for P25 and 53 % higher than that for TiO<sub>2</sub> nanoparticles. The open-circuit voltage ( $V_{oc}$ ) is 0.70 V (same as compared to TiO<sub>2</sub> nanoparticles) and 0.61 V for P25. As a result, the energy conversion efficiency of the cells made from our nanocomposite is 56 % higher (= 7.37%) than that for P25 (= 4.73 %) and 51 % higher than that for TiO<sub>2</sub> nanoparticles (= 4.9%). It is useful to mention here that the wt% of MWCNT for which the results are given here is roughly near optimum from the standpoint of efficiency. The efficiency was seen to fall almost by almost a factor of two upon increasing the wt.% of MWCNT to 0.5% (presumably due to adverse dye loading effect discussed later). A plot of the power conversion efficiency as a function of the MWCNT concentration has been given in figure 4.8.

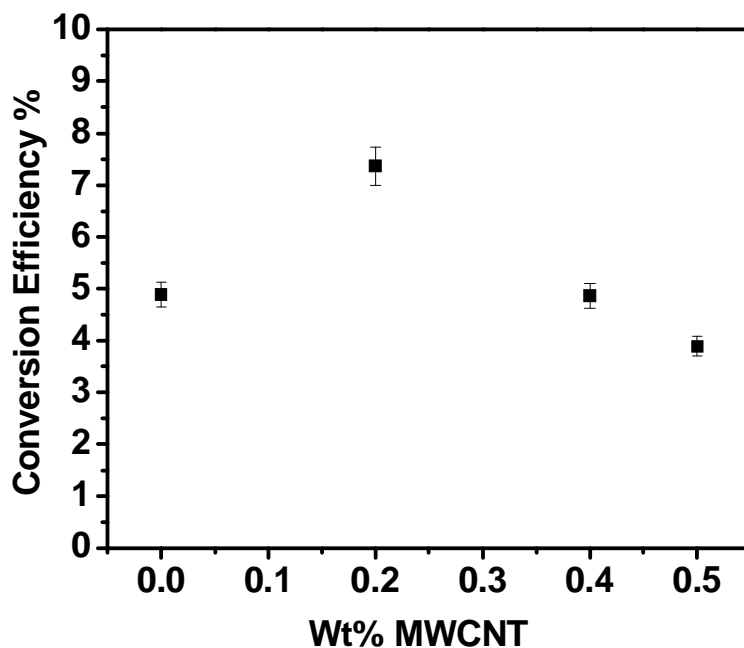


**Figure-4.8** A plot of the power conversion efficiency as a function of the MWCNT concentration.

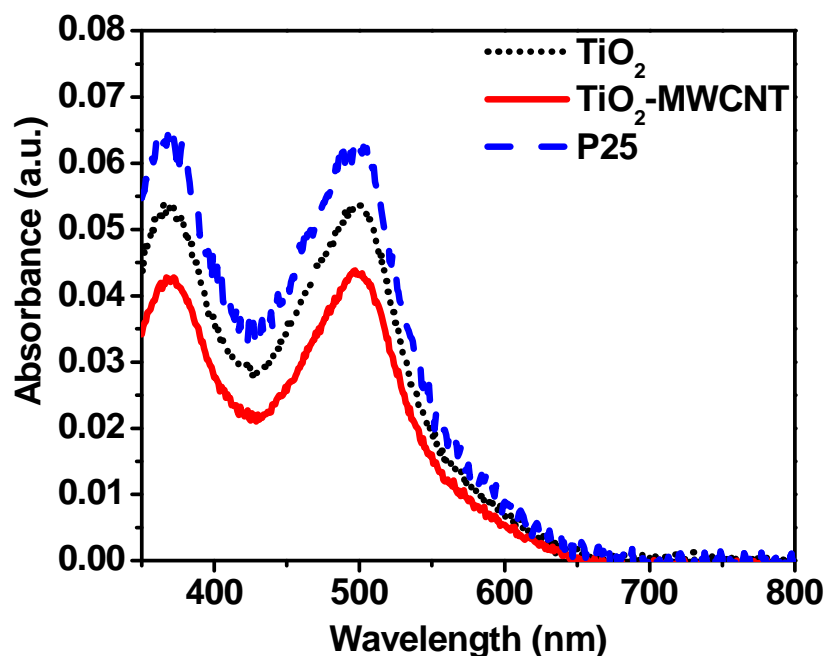


**Figure-4.9** Absorptions of solutions containing dye detached from the  $\text{TiO}_2$  (short dotted line),  $\text{TiO}_2$ -MWCNTs (solid line) nanocomposite, and P25 (dashed line) films (all with  $1\text{cm}^2$  area) in a 10ml  $\text{H}_2\text{O}$  with 1mM KOH.

Figure 4.9 shows absorptions of solutions containing dye detached from the  $\text{TiO}_2$  (short dotted line),  $\text{TiO}_2$ -MWCNTs nanocomposites (solid line) and P25 (dashed line) films (all with  $1\text{cm}^2$  area) in a 10ml  $\text{H}_2\text{O}$  with 1mM KOH. We can calculate from figure 4.9 the dye loadings of the P25,  $\text{TiO}_2$  and  $\text{TiO}_2$ -MWCNTs nanocomposite films, which are  $4.5 \times 10^{-8}$ ,  $4.1 \times 10^{-8}$  and  $3.37 \times 10^{-8}$  mol/ $\text{cm}^2$ , respectively. It is interesting that although the dye loading of  $\text{TiO}_2$ -MWCNT nanocomposite is less as compared to P25 and  $\text{TiO}_2$  nanoparticles, the energy conversion efficiency of the cells made from the nanocomposite is higher than both. This can be attributed to an improved charge carriers transport afforded by MWCNT and possibly lower recombination as well. We believe that the effective molecular and thereby electronic coupling realized in our hydrothermal synthesis process is responsible for the significant enhancement of conversion efficiency.

## 4-II Section-II

### TiO<sub>2</sub>-Graphene Nanocomposites

#### 4-II.1 Introduction

As emerging electronic and optoelectronic systems require the development of new devices with multifunctionality, various research activities have been focused on the synthesis of novel materials and their integration into device platforms [38, 39]. One example is the use of one-dimensional (1D) forms of inorganic materials (including nanowires and carbon nanotubes) in flexible and transparent electronics [40-42]. In this application, the 1D material provides a significant enhancement in the mechanical flexibility and optical transparency, while their single crystalline structures hold promise for high device performance. In addition to 1D nanostructures graphene, the two-dimensional (2D) layer of carbon atoms has attracted much attention due to its excellent properties including good electrical and thermal conduction [43-45], mechanical strength and elasticity [46], and optical transparency [47, 48]. Recent achievement of large-area graphenes (single and multilayer types) has found use in a variety of applications such as capacitors [49, 50], liquid crystalline displays [51], nanoelectromechanical resonators [52], various types of films/papers/membranes [53-55], polymer composites [56, 57], and as scaffolds for environmental sorbents [58-60] and catalysts [61]. However, the applications of both materials are limited by their intrinsic properties. In this regard, the hybridization of different types of materials is crucial as it can enable versatile and tailor-made properties with performances far beyond those of the individual materials. Especially for graphene, hybridization with semiconductor nanostructures enables the construction of three dimensional architectures and the imposition of multifunctionalities [62]. With this in mind, graphene-based nanocomposites with metal nanoparticles (platinum [63-65], palladium [64, 66], gold [67], copper [68]) and metal oxides (titania [69-72], clay [73, 74], silica [71, 75], polyoxometallates [58], birnessite manganese oxide [76], cobalt oxide [61], zinc oxide [77]) have recently been reported. Such inorganic nanomaterial-graphene composites can be prepared conceptually from two different solution based approaches: an in situ preparation of the inorganic component in the

presence of a graphene dispersion/solution, or from solution mixing of the two previously prepared components. The *in situ* synthesis approach toward ceramic oxide-graphene materials has been limited to cobalt oxide- [61], manganese oxide- [76] and titanium oxide-graphene oxide [70, 72] composites.

Here we demonstrate the synthesis of nanocomposite hybrid materials composed of TiO<sub>2</sub> nanoparticles formed on graphene layers by hydrothermal route. The DSSCs made with TiO<sub>2</sub>-Graphene nanocomposite yield a superior performance than cells made with only TiO<sub>2</sub> nanoparticles. We present results of different measurements and outline the possible origin of this effect.

### **4-II.2 Experimental**

#### **4-II.2.1 Preparation of TiO<sub>2</sub>-Graphene nanocomposite**

The synthesis protocol is same as that used for the TiO<sub>2</sub>-MWCNT nanocomposites whereas graphene is used in place of MWCNT. The nanocomposite was prepared by using hydrothermal method. Titanium Isopropoxide (2 ml) was hydrolyzed by adding sufficient amount of deionized water and then a few milligrams of Graphene were added to the above solution followed by sonication for 5 minutes. The solution was then transferred to Teflon lined autoclave vessel along with 3ml of H<sub>2</sub>SO<sub>4</sub> (1M). This autoclave vessel was kept at 175 °C for 24 hours. After this, the reaction was allowed to cool and the solid products were centrifuged and washed three times with water, once with ethanol, and then collected and dried at 50 °C to produce grayish powder of TiO<sub>2</sub>-Graphene nanocomposite.

#### **4-II.2.2 Characterization techniques**

X-ray diffraction patterns of the powder samples were scanned in the 2θ range of 10-80° on a Philips X'pert pro PAN analytical powder diffractometer employing Ni filtered Cu Kα radiation (λ = 1.5418 Å). Phase identification was determined from the PXRD patterns using PCPDFWIN software. Raman spectroscopy was done by using Horiba Jobin Yvon LabRAM HR System. TEM measurements were performed on a Tecnai F-30 instrument operated at an accelerating voltage of 300 kV. The samples for TEM analysis

were prepared by drying the drops of the TiO<sub>2</sub>-Graphene nanocomposite solutions on carbon coated copper grids. Image processing evaluation was performed with the help of micrograph Gatan software. Atomic force Microscopy (AFM) measurement was carried out using RHK Technology (SPM 100). The formation of TiO<sub>2</sub>-Graphene nanocomposite films was carried out by the doctor blade method, and the films were then annealed at 450 °C for 30 min. The thickness of TiO<sub>2</sub>-Graphene nanocomposite films was ~ 12µm. For sensitization the TiO<sub>2</sub>-MWCNT nanocomposite films were impregnated with 0.5 mM N719 dye in ethanol for 24 h at room temperature. The sensitizer-coated nanocomposite films were washed with ethanol.

### **4-II.2.3 I-V Measurements**

I-V characteristics were measured by irradiation with 100 mW/cm<sup>2</sup>, 1 sun AM 1.5, and simulated sunlight as a solar simulator. The current was measured using a Kiethley 2420 source. The electrolyte used was 1 M 1-hexyl-2, 3-dimethyl-imidazolium iodide, 0.05 M LiI, 0.05 M I<sub>2</sub>, and 0.5 M 4-tert-butylpyridine in acetonitrile.

## **4-II.3 Results and Discussion**

### **4-II.3.1 X-ray Diffraction**

Figure 4.10 shows the powder X-ray diffraction patterns of TiO<sub>2</sub> and TiO<sub>2</sub>-Graphene nanocomposite samples. The peaks in figure 4.10(a) at 25.28 (101), 37.80 (004), 48.18 (200) and 54.09 (105) clearly represent pure anatase TiO<sub>2</sub> phase (PCPDFWIN # 211 272). The 100% XRD peak intensity for Graphene (PCPDFWIN # 411 487) is expected at 26.38 (002), which is not apparent because of its small amount in the composition of TiO<sub>2</sub>-Graphene [as well as its low Z as compared to the dominant TiO<sub>2</sub> (high Z)], but the same can be clearly elucidated by Raman analysis as discussed later.

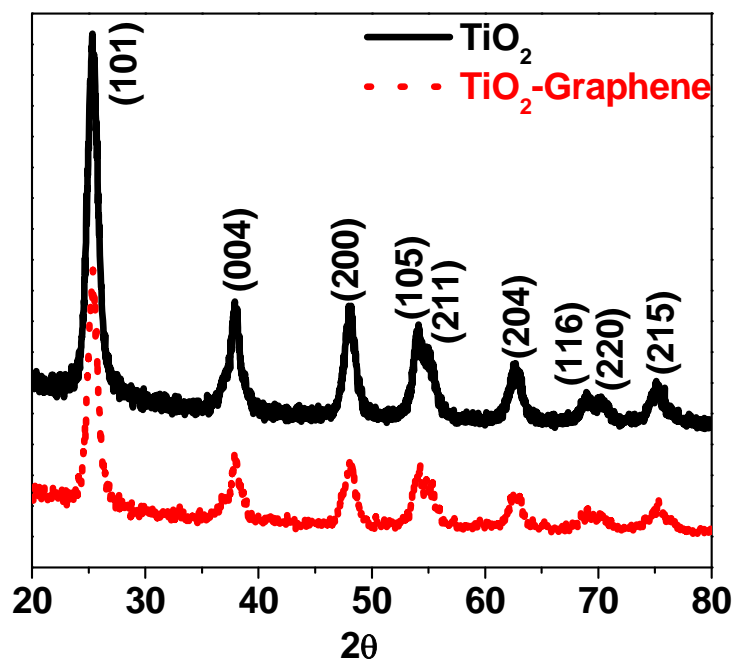


**Figure-4.10** XRD patterns of  $\text{TiO}_2$  (solid line) and  $\text{TiO}_2$ -Graphene (short dotted line) nanocomposite.

#### 4-II.3.2 Raman Spectroscopy

Figure 4.11 shows the Raman spectra for the  $\text{TiO}_2$  nanoparticles,  $\text{TiO}_2$ -Graphene nanocomposites and pristine graphene. The spectra for the case of pure  $\text{TiO}_2$  show clear signatures at about  $407 \text{ (B1g) cm}^{-1}$ ,  $517.5 \text{ (A1g + B1g) cm}^{-1}$  and  $637.5 \text{ (Eg) cm}^{-1}$ , which are in accordance with the bands observed for anatase  $\text{TiO}_2$ , as expected [34] while for the pure graphene case, the Raman features are observed at  $1328$  and  $1583.5 \text{ cm}^{-1}$ , corresponding to the D - and G -bands, respectively as reported [78]. The clear signatures of graphene are also noted in the  $\text{TiO}_2$ -Graphene nanocomposite spectrum, along with those for  $\text{TiO}_2$  in that spectral region.

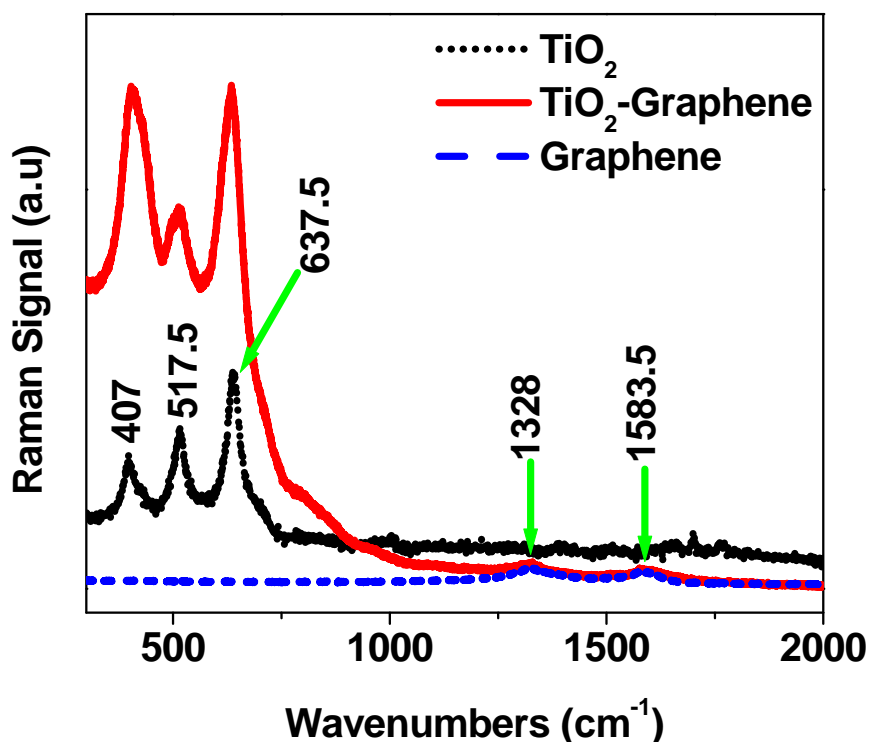


**Figure-4.11** Raman spectra for graphene (dashed line),  $\text{TiO}_2$  (short dotted line), and a  $\text{TiO}_2$ -Graphene nanocomposite (solid line).

#### 4-II.3.3 Transmission Electron Microscopy (TEM) Data

Hydrothermally synthesized  $\text{TiO}_2$ -Graphene nanocomposites were further examined using Transmission Electron Microscopy (TEM), as seen in figure 4.12(a, b). The obtained composite retained the two-dimensional sheet structure with micrometers-long wrinkles after the hydrothermal reaction. It is clearly seen that the graphene sheets were decorated uniformly by the  $\text{TiO}_2$  nanoparticles indicating the strong interaction between the nanoparticles and Graphene. Such morphology seems like a gem-decorated silk. High-resolution TEM (HRTEM) suggests that each nanoparticle is in fact composed of very small crystallites on the order of  $\sim 10\text{-}12$  nm in size that appear to be crystallographically aligned in the same orientation, as seen in figure 4.12(c, d).

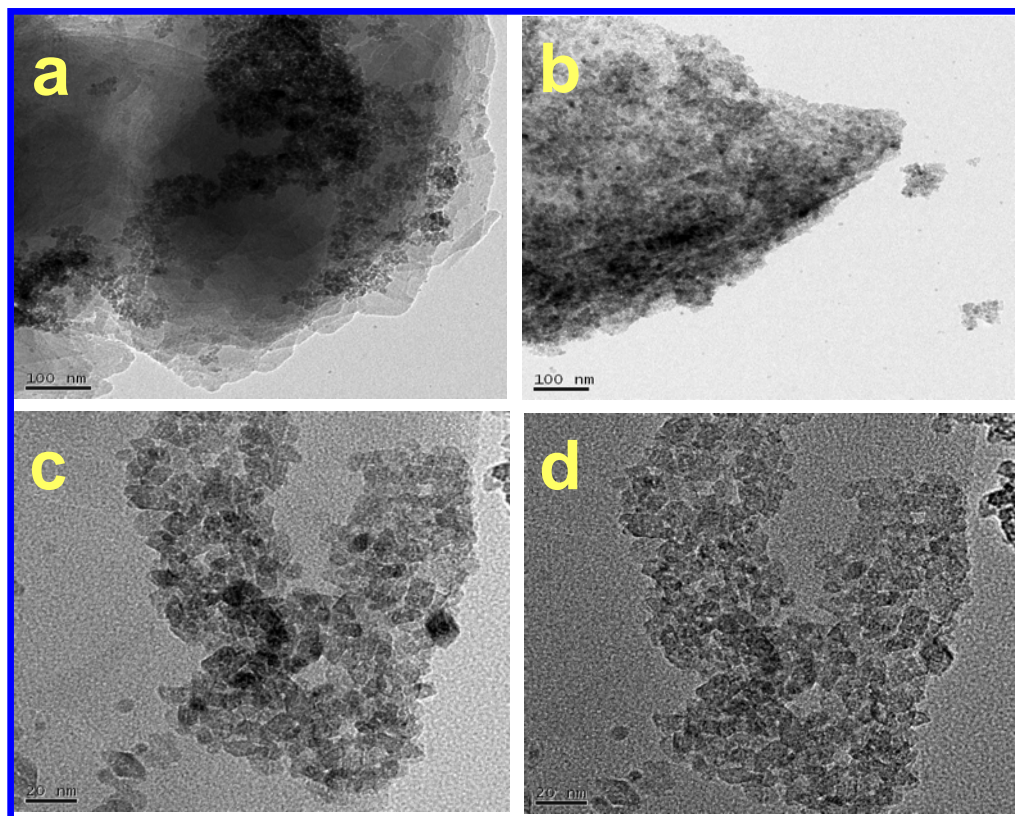


**Figure-4.12** (a, b) TEM and (b, d) HR-TEM images of TiO<sub>2</sub>-Graphene nanocomposites.

#### 4-II.3.4 Atomic Force Microscopy (AFM) Study

The atomic force microscopy studies were carried out using a commercial high vacuum SPM system by RHK technologies (SPM 100). The sample for AFM is prepared by dispersing a small amount of TiO<sub>2</sub> decorated graphene in Ethanol and drop-casted on atomically flat mica substrate. The topography is recorded in contact mode using a very soft cantilever (spring constant  $\sim 0.2$  N/m). Figure 4.13 (a) shows the total scanned region of sample. It is clearly seen the separated sheets of graphene decorated by TiO<sub>2</sub> nanoparticles. The magnified image figure 4.13 (b) & (c) show clear graphene sheets where TiO<sub>2</sub> nanoparticles could be resolved. Interestingly, the further resolved image as shown in figure 4.13 (d) seems two single graphene sheets one over the other which is shown by marked white line. Apparently, these results are completely consistent with the above TEM results.

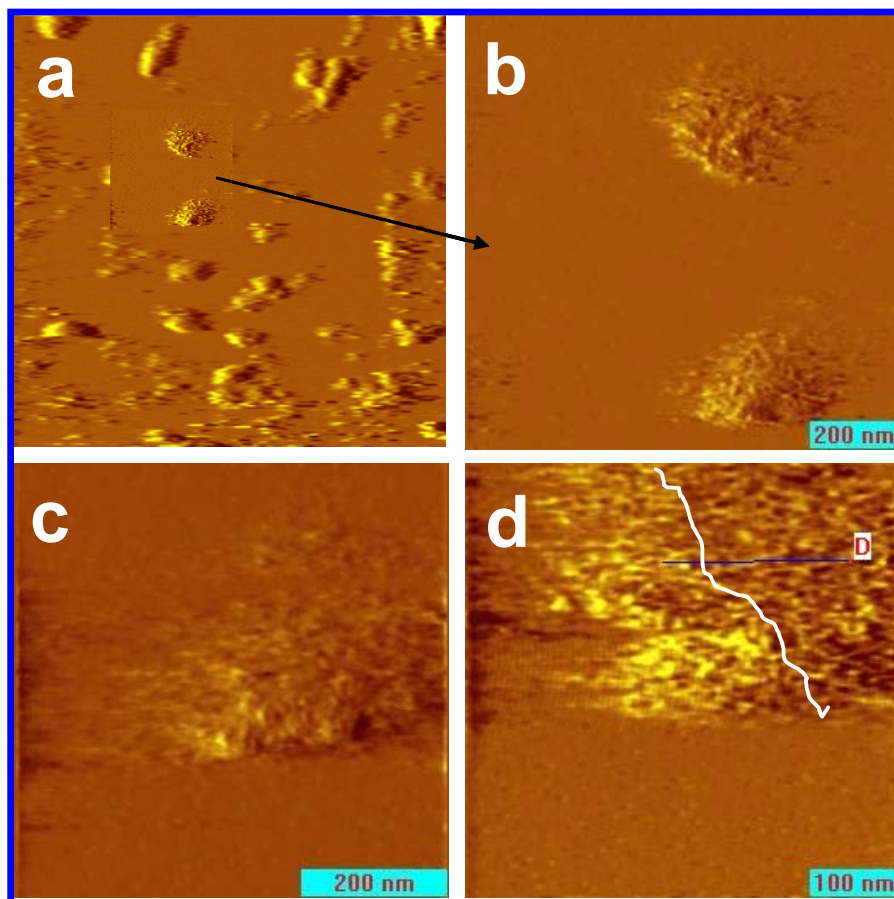


**Figure-4.13** Atomic Force Microscopy (AFM) images of TiO<sub>2</sub>-Graphene nanocomposites.

Figure 4.14 and Table 4.2 compare the solar cell characteristics for DSSCs prepared with electrodes made of TiO<sub>2</sub> NPs without Graphene and TiO<sub>2</sub>-Graphene nanocomposites with an active area of 0.25 cm<sup>2</sup>. It can be seen that for the case of the nanocomposite, J<sub>SC</sub> is about 15.2 mA/cm<sup>2</sup>, which is almost 29% higher than that for TiO<sub>2</sub> NPs. The open-circuit voltage (V<sub>oc</sub>) of TiO<sub>2</sub>-Graphene nanocomposite is 0.69 V is same as that compared to TiO<sub>2</sub> NPs. The optimized mean efficiencies obtained by our procedure for TiO<sub>2</sub>-Graphene nanocomposites is about 6.1%, which is almost 24.5% higher than that for TiO<sub>2</sub> NPs(4.9%). The enhancement of efficiency for the case of nanocomposites is due to an improved charge-carrier transport afforded by Graphene and possibly a lower recombination as well.

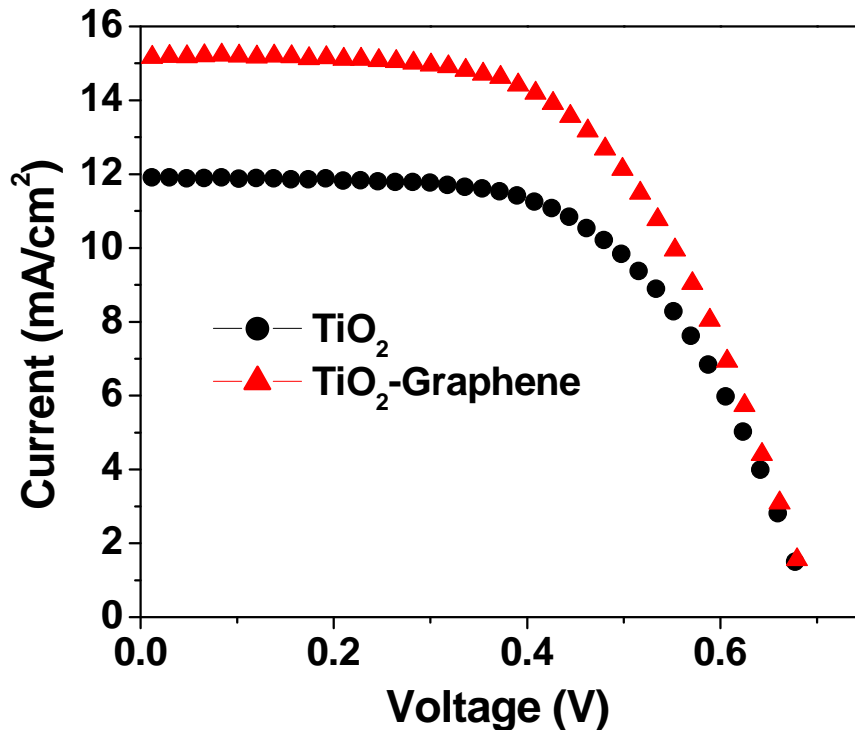


**Figure-4.14** J-V characteristics for a TiO<sub>2</sub>-Graphene nanocomposite as compared to the corresponding cases of hydrothermally synthesized TiO<sub>2</sub> NPs without Graphene.

**Table-4.2** Performance Parameters of DSSCs Fabricated with Hydrothermally Synthesized TiO<sub>2</sub> NPs without Graphene, and TiO<sub>2</sub>-Graphene Nanocomposite Powder.

Name	V <sub>oc</sub> (V)	J <sub>sc</sub> (mA/cm <sup>2</sup> )	Fill Factor (FF)	Efficiency (η)
TiO <sub>2</sub>	0.69	11.8	59.4	4.9
TiO <sub>2</sub> -Graphene	0.69	15.2	58	6.1

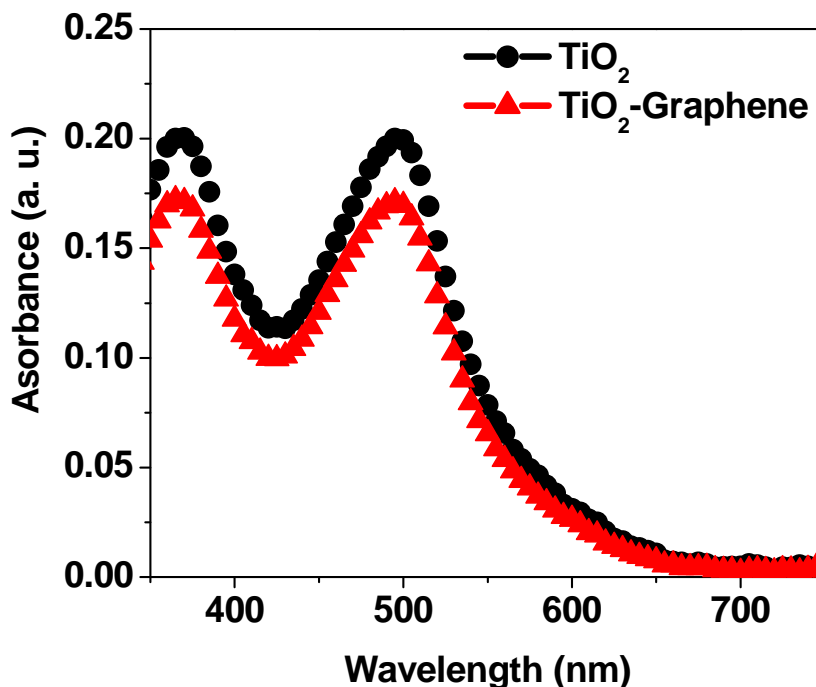


**Figure-4.15** Absorptions of solutions containing dye detached from the  $\text{TiO}_2$  (solid line) and  $\text{TiO}_2$ -Graphene (short dotted line) nanocomposite, films (all with  $1\text{cm}^2$  area) in a  $10\text{ml H}_2\text{O}$  with  $1\text{mM KOH}$ .

Figure 4.15 shows absorptions of solutions containing dye detached from the  $\text{TiO}_2$ ,  $\text{TiO}_2$ -Graphene nanocomposite films (all with  $1\text{cm}^2$  area) in  $10\text{ mL}$  of  $\text{H}_2\text{O}$  with  $1\text{ mM KOH}$ . We can calculate from figure 4.15 the dye loadings of the  $\text{TiO}_2$  and  $\text{TiO}_2$ -Graphene nanocomposite films, which are  $\sim 9.1 \times 10^{-8}$  and  $\sim 7.7 \times 10^{-8}$   $\text{mol}/\text{cm}^2$ , respectively. It is interesting that the dye loading of  $\text{TiO}_2$ -Graphene nanocomposite is less as compared to  $\text{TiO}_2$  nanoparticles, but the energy conversion efficiency of the cells made from the nanocomposite is higher than  $\text{TiO}_2$  nanoparticles. This can be attributed to an improved charge carriers transport afforded by Graphene and possibly lower recombination as well.

## 4.2 Conclusions

High ( $\sim 7.4\%$ ) conversion efficiency is realized in DSSCs based on a hydrothermally synthesized  $\text{TiO}_2$ -MWCNT nanocomposite. This represents a  $\sim 50\%$  improvement vis-a-

vis cells made with hydrothermally synthesized TiO<sub>2</sub> without MWCNT or Degussa P25 powder. FTIR data suggest that the -COOH groups open up on the surface of MWCNT under hydrothermal processing conditions and these conjugate with the Ti precursor to yield a composite. This integral conjugation appears to be effective in the charge-transfer process. Although MWCNT appears to reduce dye loading to some extent, the efficient charge transfer from TiO<sub>2</sub> to MWCNT and the efficient electron transport by the latter appears to help to improve the efficiency by 50%.

Enhancement in the conversion efficiency is realized in dye-sensitized solar cells using hydrothermally synthesized TiO<sub>2</sub>-Graphene nanocomposites as compared to hydrothermally synthesized TiO<sub>2</sub> without graphene. TEM images shows the graphene sheets were decorated uniformly by the TiO<sub>2</sub> nanoparticles indicating the strong interaction between the nanoparticles and Graphene. Several characterizations have been employed to reveal the nature of the modification imparted to the graphene under hydrothermal processing conditions.

### 4.3 References

1. G. Kickelbick, *Hybrid Materials: Synthesis, Characterization and Application*; Wiley-VCH: Weinheim, Germany, **2007**.
2. C. Sanchez, P. Gomez-Romero, *Functional Hybrid Materials*; Wiley VCH: Weinheim, Germany, **2004**.
3. B. O'Regan, M. Gratzel, *Nature*, **1991**, *23*, 737.
4. M. Grätzel, *J. Photochem. Photobiol. C-Photochem. Rev.* **2003**, *4*, 145.
5. Q. Zhang, Chou, T.; Russo, B.; Jenekhe, S.; Cao, G. *Angew. Chem. Int. Ed.* **2008**, *47*, 2402.
6. H. Koo, Y. Kim, Y. Lee, W. Lee, K. Kim, N. Park, *Adv. Mater.* **2008**, *20*, 195.
7. P. J. Cameron, L. M. Peter, *J. Phys. Chem. B*, **2003**, *107*, 14394.

8. J. Xia, N. Masaki, K. Jiang, Y. Wada, S. Yanagida, *Chem. Lett.* **2006**, 35, 252.
9. J. Xia, N. Masaki, K. Jiang, S. Yanagida, *Chem. Commun.* **2007**, 138.
10. E. Palomares, J. N. Clifford, S. A. Haque, T. Lutz, J. R. Durrant, *J. Am. Chem. Soc.* **2003**, 125, 475.
11. J. N. Clifford, E. Palomares, M. K. Nazeeruddin, R. Thampi, M. Grätzel, J. R. Durrant, *J. Am. Chem. Soc.* **2004**, 126, 5670.
12. N.-G. Park, G. Schlichthörl, J. van de Lagemaat, H. M. Cheong, A. Mascarenhas, A. J. Frank, *J. Phys. Chem. B*, **1999**, 103, 3308-3314.
13. P. M. Sommmeling, B. C. O'Regan, R. R. Haswell, H. J. P. Smit, N. J. Bakker, J. J. T. Smits, J. M. Kroon, J. van Roosmalen, A. M. *J. Phys. Chem. B*, 2006, 110, 19191.
14. Z.S. Wang, H. Kawauchi, T. Kashima, H. Arakawa, *Coord. Chem. Rev.* **2004**, 248, 1381.
15. S. Ito, S. M. Zakeerudiin, R. Humphry-Baker, P. Liska, P. Charvet, P. Comte, M. K. Nazeeruddin, P. Péchy, M. Takata, H. Miura, S. Uchida, M. Grätzel, *Adv. Mater.* **2006**, 18, 1202.
16. S. Hore, C. Vetter, R. Kern, H. Smit, A. Hinsch, *Sol. Energy Mater. Sol. Cells*, **2006**, 90, 1176.
17. C. Jiang, X. Sun, G. Ko, D. Kwong, J. Wang, *Appl. Phys. Lett.* **2007**, 90, 263501/1-3.
18. G. Mor, O. Varghese, M. Paulose, K. Shankar, C. Grimes, *Sol. Energy Mater. Sol. Cells*, **2006**, 90, 2011.
19. A. Kongkanand, R. Domínguez, P. Kamat, *Nano Lett.* **2007**, 7, 676.
20. P. Brown, K. Takechi, P. Kamat, *J. Phys. Chem. C*, **2008**, 112, 4776.
21. A. Kongkanand, P. Kamat, *ACS NANO*, **2007**, 1, 13.

22. S. Jang, R. Vittal, K. Kim, *Langmuir*, **2004**, *20*, 9807.
23. C. Yen, Y. Lin, S. Liao, C. Weng, C. Huang, Y. Hsiao, C. Ma, M. Chang, H. Shao, M. Tsai, C. Hsieh, C. Tsai, F. Weng, *Nanotechnology*, **2008**, *19*, 1.
24. S. Kim, S. Jang, R. Vittal, J. Lee, K. Kim, *J. Appl. Electrochem.* **2006**, *36*, 1433.
25. K. Lee, C. Hu, H. Chen, K. Ho, *Sol. Energy Mater. Sol. Cells*, **2008**, *92*, 1628.
26. T. Lee, P. Alegaonkar, J. Yoo, *Thin Solid Films*, **2007**, *515*, 5131.
27. Y. Zhu, H. Elim, Y. Foo, T. Yu, Y. Liu, W. Ji, J. Lee, Z. Shen, A. Wee, J. Thong, C. Sow, *Adv. Mater.* **2006**, *18*, 587.
28. F. Vietmeyer, B. Seger, P. Kamat, *Adv. Mater.* **2007**, *19*, 2935.
29. X. Yan, B. Tay, Y. Yang, W. Yung, *J. Phys. Chem. C*, **2007**, *111*, 17254.
30. L. Chen, B. Zhang, M. Qu, Z. Yu, *Powder Technology*, **2005**, *154*, 70.
31. T. Sawatsuk, A. Chindaduang, C. Sae-kung, S. Pratontep, G. Tumcharern, *Diamond & Related Materials*, **2009**, *18*, 524.
32. K. Byrappa, T. Adschiri, *Progress in Crystal Growth and Characterization of Materials*, **2007**, *53*, 117.
33. J. Beusen, M. Van Bael, H. Van den Rul, J. D'Haen, J. Mullens, *Journal of the European Ceramic Society*, **2007**, *27*, 4529.
34. H. Choi, Y. Jung, S. Kim, *Bull. Korean Chem. Soc.* **2004**, *25*, 426.
35. Y. Zhu, Izaac H. Elim, Y. Foo, T. Yu, Y. Liu, W. Ji, J.Y. Lee, Z. Shen, A. T. S. Wee, J. T. L. Thong, Sow C. H. *Adv. Mater.* **2006**, *18*, 587.
36. C. Xu, P. Zhang, L. Yan, *J. Raman Spectrosc.* **2001**, *32*, 862.
37. R. M. Silverstein, G. C. Bassler, T. C. Morrill, *Spectroscopic Identification of Organic Compounds, 3rd ed.; John Wiley and Sons: New York, 1974.*

38. N. Stutzmann, R. H. Friend, H. Sirringhaus, *Science*, **2003**, 299, 1881.
39. G. Thomas, *Nature*, **1997**, 389, 907.
40. (a) K. Bradley, J.-C. P. Gabriel, G. Gruner, *Nano Lett.* **2003**, 3, 1355. (b) Q. Cao, S.-H. Hur, Z.-T. Zhu, Y. Sun, C. Wang, M. Meitl, M. Shim, J. A. Rogers, *Adv. Mater.* **2006**, 18, 304.
41. M. C. McAlpine, R. S. Friedman, S. Jin, K.-h. Lin, W. U. Wang, C. M. Lieber, *Nano Lett.* **2004**, 3, 1531.
42. (a) X. Duan, C. Niu, V. Sahi, J. Chen, J. W. Parce, S. Empedocles, J. L. Goldman, *Nature*, **2003**, 425, 274. (b) X. Duan, *MRS Bull.* **2007**, 32, 134.
43. A. K. Geim, K. S. Novoselov, *Nat. Mater.* **2007**, 6, 183.
44. (a) K. S. Novoselov, A. K. Geim, S. V. Morozov, D. Jiang, Y. Zhang, S. V. Dubonos, I. V. Grigorieva, A. A. Firsov, *Science*, **2004**, 306, 666. (b) K. S. Novoselov, A. K. Geim, S. V. Morozov, D. Jiang, M. I. Katsnelson, I. V. Grigorieva, S. V. Dubonos, A. A. Firsov, *Nature*, **2005**, 438, 197.
45. Y. Zhang, Y.-W. Tan, H. L. Stormer, P. Kim, *Nature*, **2005**, 438, 201.
46. C. Lee, X. Wei, J. W. Kysar, J. Hone, *Science*, **2008**, 321, 385.
47. G. Eda, G. Fanchini, M. Chhowalla, *Nat. Nanotechnol.* **2008**, 3, 270.
48. D. Li, M. B. Müller, S. Gilje, R. B. Kaner, G. G. Wallace, *Nat. Nanotechnol.* **2008**, 3, 101.
49. M. D. Stoller, S. J. Park, Y. W. Zhu, J. H. An, R. S. Ruoff, *Nano Lett.* **2008**, 8, 3498.
50. S. R. C. Vivekchand, C. S. Rout, K. S. Subrahmanyam, A. Govindaraj, C. N. R. Rao, In Graphene-Based Electrochemical Supercapacitors, 10th National Symposium in Chemistry: Bangalore, India, Feb 01-03, **2008**; Bangalore, India, **2008**; pp 9-13.

51. P. Blake, P. D. Brimicombe, R. R. Nair, T. J. Booth, D. Jiang, F. Schedin, L. A. Ponomarenko, S. V. Morozov, H. F. Gleeson, E. W. Hill, A. K. Geim, K. S. Novoselov, *Nano Lett.* **2008**, *8*, 1704.
52. J. S. Bunch, A. M. van der Zande, S. S. Verbridge, I. W. Frank, D. M. Tanenbaum, J. M. Parpia, H. G. Craighead, P. L. McEuen, *Science*, **2007**, *315* (5811), 490.
53. D. A. Dikin, S. Stankovich, E. J. Zimney, R. D. Piner, G. H. B. Dommett, G. Evmenenko, S. T. Nguyen, R. S. Ruoff, *Nature*, **2007**, *448*, 457.
54. S. Park, K. S. Lee, G. Bozoklu, W. Cai, S. T. Nguyen, R. S. Ruoff, *ACS Nano*, **2008**, *2*, 572.
55. T. J. Booth, P. Blake, R. R. Nair, D. Jiang, E. W. Hill, U. Bangert, A. Bleloch, M. Gass, K. S. Novoselov, M. I. Katsnelson, A. K. Geim, *Nano Lett.* **2008**, *8*, 2442.
56. S. Stankovich, D. A. Dikin, G. H. B. Dommett, K. M. Kohlhaas, E. J. Zimney, E. A. Stach, R. D. Piner, S. T. Nguyen, R. S. Ruoff, *Nature*, **2006**, *442*, 282.
57. T. Ramanathan, A. A. Abdala, S. Stankovich, D. A. Dikin, M.; Herrera-Alonso, R. D. Piner, D. H. Adamson, H. C. Schniepp, X. Chen, R. S. Ruoff, S. T. Nguyen, I. A. Aksay, R. K. Prud'homme, L. C. Brinson, *Nat. Nanotechnol.* **2008**, *3*, 327.
58. C. Petit, T. J. Bandosz, *J. Phys. Chem. C*, **2009**, *113*, 3800.
59. M. Seredych, T. J. Bandosz, *J. Phys. Chem. C*, **2007**, *111*, 15596.
60. M. Seredych, T. J. Bandosz, *J. Colloid Interface Sci.* **2008**, *324*, 25.
61. C. Xu, X. Wang, J. W. Zhu, X. J. Yang, L. Lu, *J. Mater. Chem.* **2008**, *18*, 5625.
62. (a) D. Y. Cai, M. Song, C. X. Xu, *Adv. Mater.* **2008**, *20*, 1706. (b) A. P. Yu, P. Ramesh, X. B. Sun, E. Bekyarova, M. E. Itkis, R. C. Haddon, *Adv. Mater.* **2008**, *20*, 4740. (c) V. C. Tung, L.-M. Chen, M. J. Allen, J. K. Wassei, K. Nelson, R. B. Kaner, Y. Yang, *Nano Lett.* **2009**, *9*, 1949.

63. (20) Y. C. Si, E. T. Samulski, *Chem. Mater.* **2008**, *20*, 6792.
64. C. Xu, X. Wang, J. W. Zhu, *J. Phys. Chem. C*, **2008**, *112*, 19841.
65. B. Seger, P. V. Kamat, *J. Phys. Chem. C*, *2009*, *113*, 7990.
66. A. Mastalir, Z. Kiraly, M. Benko, I. Dekany, *Catal. Lett.* **2008**, *124*, 34.
67. R. Muszynski, B. Seger, P. V. Kamat, *J. Phys. Chem. C*, **2008**, *112*, 5263.
68. N. A. Luechinger, E. K. Athanassiou, W. J. Stark, *Nanotechnology*, **2008**, *19*, 6.
69. G. Williams, B. Seger, P. V. Kamat, *ACS Nano*, **2008**, *2*, 1487.
70. W. Q. Peng, Z. M. Wang, N. Yoshizawa, H. Hatori, T. Hirotsu, *Chem. Commun.* **2008**, 4348.
71. Y. H. Chu, M. Yamagishi, Z. M. Wang, H. Kanoh, T. Hirotsu, *Microporous Mesoporous Mater.* **2009**, *118*, 496.
72. D. H. Wang, D. W. Choi, J. Li, Z. G. Yang, Z. M. Nie, R. Kou, D. H. Hu, L. V. Saraf, J. G. Zhang, I. A. Aksay, J. Liu, *ACS Nano*, **2009**, *3*, 907.
73. C. Nethravathi, J. T. Rajamathi, N. Ravishankar, C. M. Wang, C. Shivakumara, M. Rajamathi, *Langmuir*, **2008**, *24*, 8240.
74. C. Nethravathi, B. Viswanath, C. Shivakumara, N. Mahadevaiah, M. Rajamathi, *Carbon*, **2008**, *46*, 1773.
75. Y. H. Chu, Z. M. Wang, M. Yamagishi, H. Kanoh, T. Hirotsu, Y. X. Zhang, *Langmuir*, **2005**, *21*, 2545.
76. X. J. Yang, Y. Makita, Z. H. Liu, K. Ooi, *Chem. Mater.* **2003**, *15*, 1228.
77. G. Williams, P. V. Kamat, *Langmuir*, **2009**, *25*, 13869.
78. Timothy N. Lambert, Carlos A. Chavez, Bernadette Hernandez-Sanchez, Ping Lu, Nelson S. Bell, Andrea Ambrosini, Thomas Friedman, Timothy J. Boyle, David R. Wheeler, Dale L. Huber, *J. Phys. Chem. C*, **2009**, *113*, 19812.

## Chapter-5

### TiCl<sub>4</sub> Treatment of TiO<sub>2</sub> and ZnO

*We report on the synthesis of various ZnO mesostructures (rods, spheres, flakes and flower-like morphologies) by hydrothermal and co-precipitation methods and their remarkable and complete transformation into anatase TiO<sub>2</sub> mesostructures with nominally similar shapes using controlled low temperature TiCl<sub>4</sub> treatment. Various techniques are used to demonstrate the phase purity and morphology details. Based on the careful examination of the transformation of ZnO rods into TiO<sub>2</sub> tubes we suggest a mechanism which embodies initial formation of a thin TiO<sub>2</sub> shell on the ZnO surface by ion exchange (Ti<sup>4+</sup> - Zn<sup>2+</sup>) followed by Zn diffusion through the shell and its oxidation on the surface. We used these converted TiO<sub>2</sub> mesostructures for light harvesting in Dye Sensitized Solar Cells (DSSC) to enhance the conversion efficiency.*

## 5-I Section-I

### TiCl<sub>4</sub> treatment of TiO<sub>2</sub> Nanoparticles for DSSC

#### 5-I.1 Introduction

In Dye-sensitized solar cells (DSSC), the functionalities of charge generation and transport are no longer combined in one material but separated in different materials, i.e., a sensitizing dye, a (wide band gap) semiconductor (TiO<sub>2</sub>), and a liquid redox electrolyte. The performance in DSSCs is mainly influenced by the fabrication conditions, the morphology and particle size of the mesoporous TiO<sub>2</sub> layer[1], recombination rate at the interfaces<sup>[5]</sup>, light harvesting performance of dyes[3], thermally resistant transparent-conducting-oxide (TCO) [4], and electrolytes[5]. A known method to improve the performance of the solar cells is a post-treatment of the TiO<sub>2</sub> film in which an extra layer of TiO<sub>2</sub> is grown onto the TiO<sub>2</sub> nanoparticles constituting the film. Different explanations of the working principle of this coating have been reported [6-9]. These hypotheses concern increased surface area [6], improved electron transport [6], light scattering [7], TiO<sub>2</sub> purity [8], and dye anchoring [9]. The post-treatment has been carried out using several TiO<sub>2</sub> precursors and methods: TiCl<sub>3</sub> electrodeposition [10] and titanium isopropoxide [11] and titanium tetrachloride (TiCl<sub>4</sub>) post-treatment [6-9, 12]. The latter results in the highest efficiency increase for the solar cells [13]. The TiCl<sub>4</sub> treatment results in an improvement in photocurrent, normally between 10% and 30%. In this study the post-treatment of nanocrystalline TiO<sub>2</sub> films with TiCl<sub>4</sub> and its effects on the TiO<sub>2</sub> properties and solar cell performance have been investigated.

#### 5-I.2 Experimental Method

Cells were fabricated as in the previous chapter. TiO<sub>2</sub> particles were synthesized by using a simple hydrothermal method. 2ml of Titanium Isopropoxide was hydrolysed by adding 100ml of deionised water and then sonicated for 5 minutes. The solution was transferred to Teflon lined autoclave vessel along with 3ml of H<sub>2</sub>SO<sub>4</sub> (1M). This autoclave vessel was kept at 175°C for 24 hours. The resulting product was washed thoroughly with deionised water and dried at 50°C in a dust proof environment to produce powder of TiO<sub>2</sub> nanoparticles. Doctor blading method was employed to make the TiO<sub>2</sub> nanoparticles

films and study the DSSCs. After making the films, these were annealed at 450°C for 60 min. Then the post-treatment with  $\text{TiCl}_4$  has been applied to freshly sintered  $\text{TiO}_2$  films according to literature procedures [12]. An aqueous stock solution of 2 M  $\text{TiCl}_4$  was diluted to 0.05 M. Sintered electrodes were immersed into this solution and stored in an oven at 70 °C for 30 min in a closed vessel. After flushing with demineralized water and drying, the electrodes were sintered again at 450 °C for 30 min. The profiles and film thickness for  $\text{TiO}_2$  films have been determined using a Dektak 150 stylus profilometer (Veeco Instruments). The thickness of the  $\text{TiO}_2$  nanoparticle films was found to be  $\sim 12\mu\text{m}$ . For sensitization, the films were impregnated with 0.5 mM N719 dye (purchased from Solaronix under the name Ruthenium 535) in ethanol for 24 h at room temperature. The samples were then rinsed with ethanol to remove excess dye on the surface and were air-dried at room temperature. This was followed by redox electrolyte addition and top contact of Pt coated FTO as discussed earlier. The electrolyte used was 1 M 1-hexyl-2, 3-dimethyl-imidazolium iodide, 0.05 M LiI, 0.05 M  $\text{I}_2$ , and 0.5 M 4-tert-butylpyridine in acetonitrile. I-V characteristics were measured using a solar simulator (Newport) at 100  $\text{mW}/\text{cm}^2$  (1 sun AM 1.5).

### 5-I.3 Results and discussion

Figure 5.1 shows the X-ray diffraction (XRD) patterns of  $\text{TiO}_2$  and  $\text{TiCl}_4$  treated  $\text{TiO}_2$  on FTO (Fluorine doped Tin Oxide) substrate (i.e. pure anatase phase of  $\text{TiO}_2$ ). As can be seen from the XRD pattern, the  $2\theta$  values at 25.4 (101), 38.1 (overlapping with FTO (37.6)), 48.1 (200), 54.2 (overlapping with FTO (54.6)), 55.0 (211), 62.8 (204) (PCPDFWIN # 211 272) correspond to anatase  $\text{TiO}_2$ . There is no extra peak for the case of  $\text{TiCl}_4$  treated  $\text{TiO}_2$ . The peaks at 26.3, 31.6, 33.6, 37.6, 51.45, 54.6, 61.5 and 65.4 correspond to the XRD pattern of FTO substrate as shown in figure 5.1.

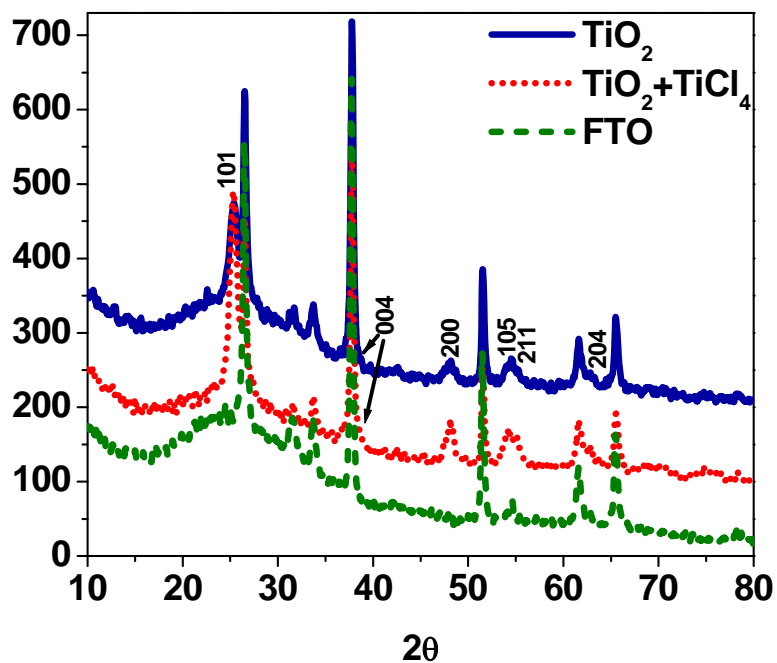


**Figure-5.1** XRD data of  $\text{TiO}_2$ ,  $\text{TiCl}_4$  treated  $\text{TiO}_2$  and FTO.

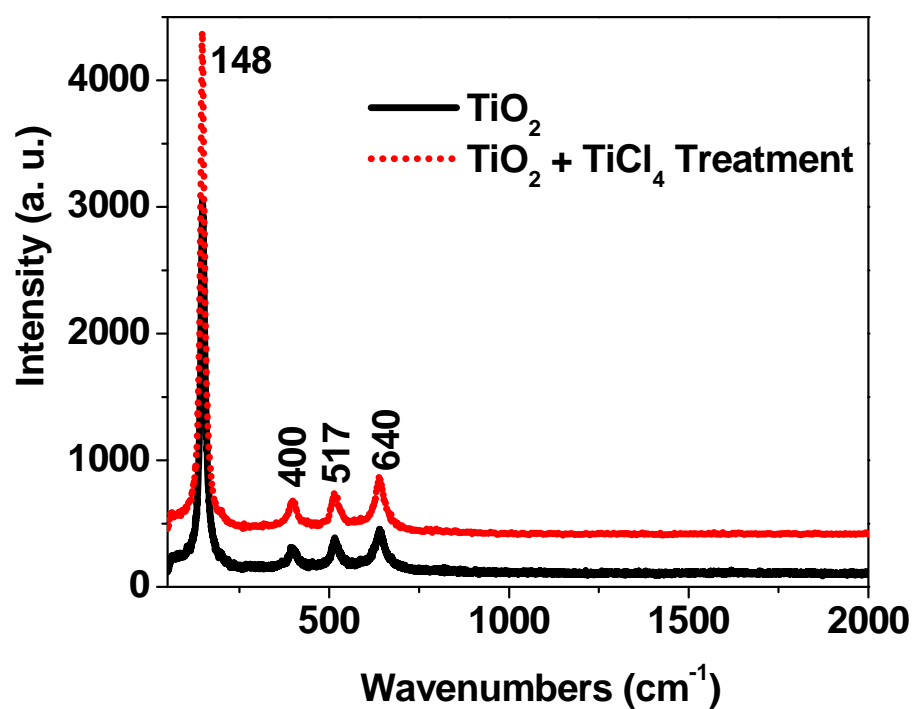


**Figure-5.2** Raman spectra of  $\text{TiO}_2$  and  $\text{TiCl}_4$  treated  $\text{TiO}_2$  films on FTO.

The Raman spectra for  $\text{TiO}_2$  and  $\text{TiCl}_4$  treated  $\text{TiO}_2$  are shown in figure 5.2. These spectra were measured at room temperature. The observed modes at  $\sim 145 \text{ cm}^{-1}$  ( $E_{g(1)}$ ),  $199 \text{ cm}^{-1}$  ( $E_{g(2)}$ ),  $396 \text{ cm}^{-1}$  ( $B_{1g(1)}$ ),  $511 \text{ cm}^{-1}$  (combination of  $A_{1g}$  and  $B_{1g(2)}$ ) and  $638 \text{ cm}^{-1}$  ( $E_{g(3)}$ ) can be assigned to the Raman active modes of the anatase crystal [14]. There is no additional peak observed after  $\text{TiCl}_4$  treatment of  $\text{TiO}_2$ .

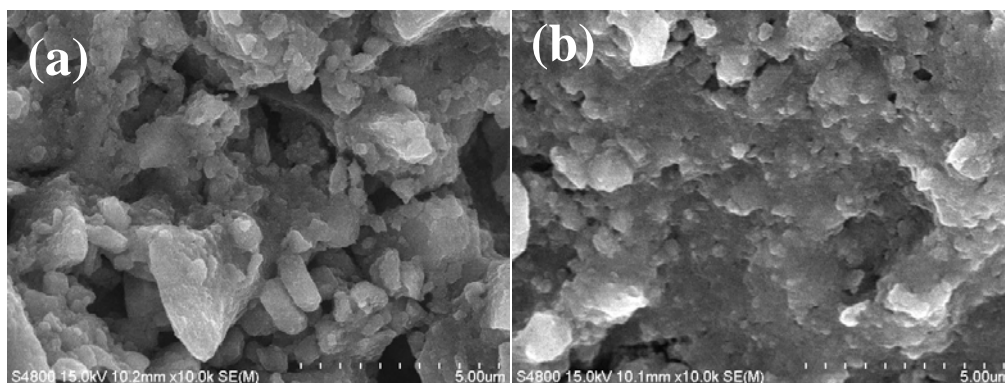


**Figure-5.3** FE-SEM Image of (a) Untreated Film (b)  $\text{TiCl}_4$  treated  $\text{TiO}_2$  Film

Figure 5.3 shows the FE SEM images of the untreated and treated  $\text{TiO}_2$  films. From the images it is clear that after  $\text{TiCl}_4$  treatment there is deposition of thin layer of  $\text{TiO}_2$  on the already existing  $\text{TiO}_2$  which gives a compact nature and good necking between particles. This reduces the porosity of the film but at the same time improves the interconnectivity between particles so as to reduce hopping of electrons within film.

Figure 5.4 shows scanning probe microscopic studies of bare and  $\text{TiCl}_4$  treated  $\text{TiO}_2$  film. These measurements were carried in high vacuum conditions ( $10^{-6}$  torr) using SPM 100 (RHK Technologies.) The AFM studies were carried in contact mode using a cantilever of spring constant 0.2 N/m. The force distance (F-D) curve for  $\text{TiCl}_4$  treated films resemble to F-D curves commonly observed on firm surfaces compared to diffused spectra on untreated films. These results clearly indicate surface modification with a fair increase in surface properties leading to higher compactness after  $\text{TiCl}_4$  treatment.

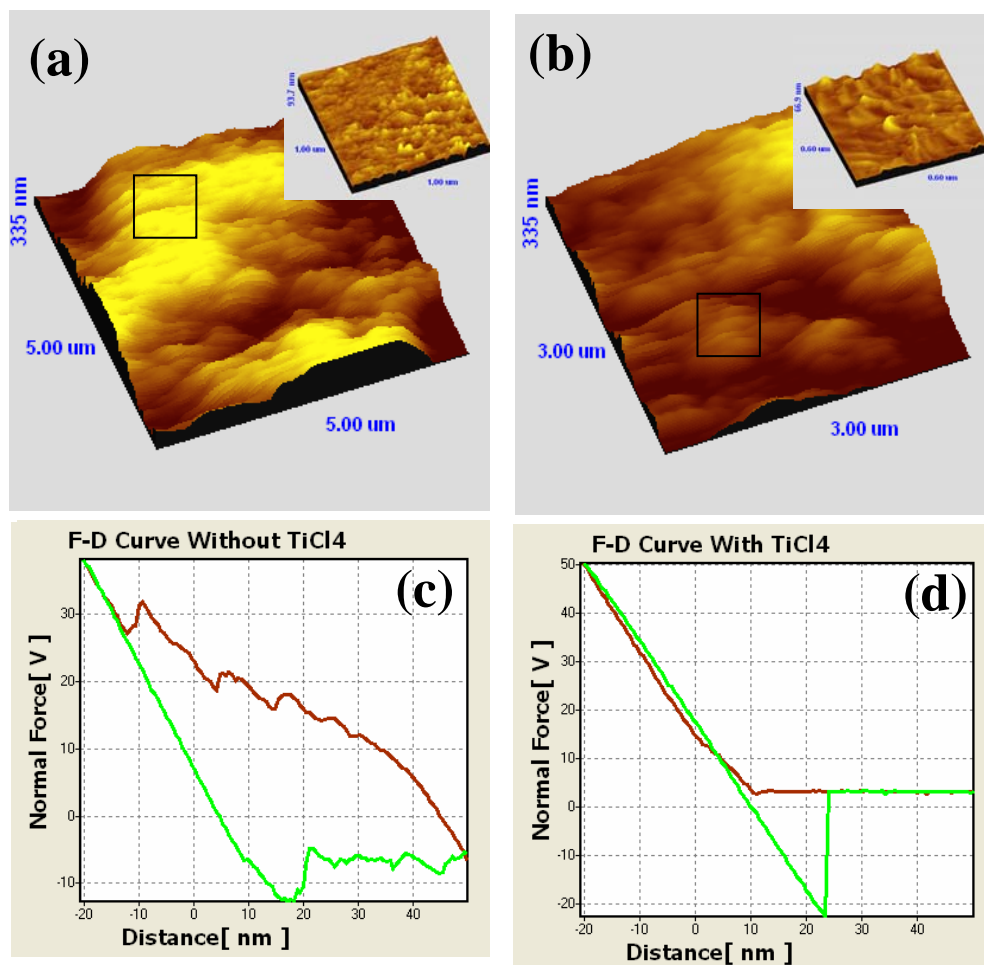


**Figure-5.4** AFM Topography of (a) without TiCl<sub>4</sub> & (b) with TiCl<sub>4</sub> treated TiO<sub>2</sub> films, and F-D Curves for (c) without TiCl<sub>4</sub> and (d) with TiCl<sub>4</sub> treated TiO<sub>2</sub> films.

Figure 5.5 shows the I–V characteristics of the TiO<sub>2</sub> nanoparticle films with and without the TiCl<sub>4</sub> treatment. The cells were measured with an active area of 0.25 cm<sup>2</sup>. The numbers shown are the average of three cells for each treatment. Within the treatment groups, the cells were quite reproducible. As shown in Table 5.1, the short circuit current density ( $J_{SC}$ ) was improved from 10.2 mA cm<sup>-2</sup> to 14.0 mA cm<sup>-2</sup> by the TiCl<sub>4</sub> treatment, which is almost 37% higher than that for without TiCl<sub>4</sub> treatment of TiO<sub>2</sub> nanoparticles. The enhancement in current density is due to a small over layer on the particle surface has formed which improves the transport through the particle-particle contacts after TiCl<sub>4</sub>

treatment. Another possibility is that the add-layer covers up specific impurities, defects, or crystal facets, which catalyze the recombination reaction on the original particles. The optimized mean efficiency obtained by our procedure for TiO<sub>2</sub> nanoparticles film is about 4.3 %. After TiCl<sub>4</sub> treatment, the conversion efficiency is improved from 4.3% to 5.4% (almost 25% enhancement).

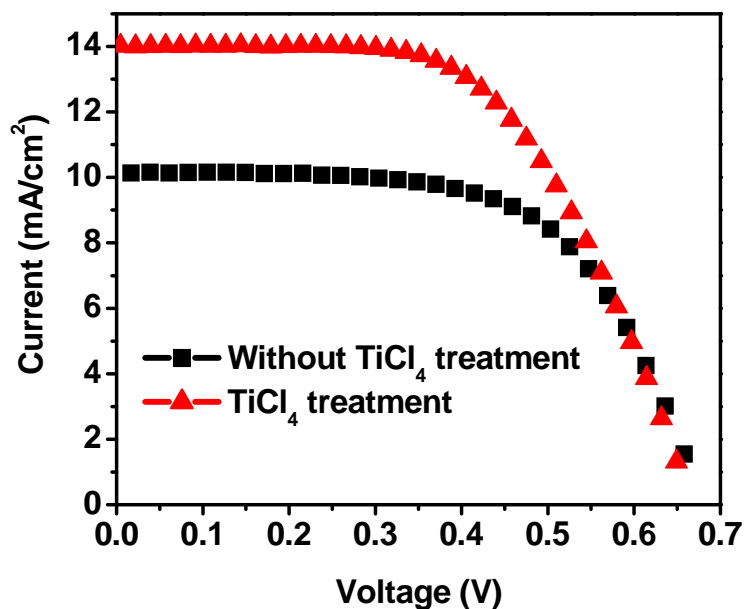


**Figure-5.5.** Current–voltage characteristics of hydrothermally synthesized TiO<sub>2</sub> nanoparticle Films with and without TiCl<sub>4</sub> treatment

**Table 5.1** IV Results for with and without TiCl<sub>4</sub> Treatment of TiO<sub>2</sub> nanoparticles.

Name	V <sub>oc</sub> (V)	J <sub>sc</sub> (mA/cm <sup>2</sup> )	Fill Factor (FF)	Efficiency (η)
TiO <sub>2</sub>	0.67	10.2	62	4.3
TiO <sub>2</sub> -TiCl <sub>4</sub>	0.66	14.0	58.1	5.4

Figure 5.6 shows absorptions of solutions containing dye detached from the  $\text{TiCl}_4$  treated and without  $\text{TiCl}_4$  treated  $\text{TiO}_2$  films (all with  $2 \text{ cm}^2$  area) in 10 mL of  $\text{H}_2\text{O}$  with 1 mM KOH. We can calculate from figure 5.6 the dye loadings of the  $\text{TiCl}_4$  treated and without  $\text{TiCl}_4$  treated  $\text{TiO}_2$  films, which are  $6 \times 10^{-8}$  and  $5 \times 10^{-8} \text{ mol/cm}^2$ , respectively. The significant enhancement in dye loading for  $\text{TiCl}_4$  treated case is attributed to increased surface area and roughness factor due to formation of the additional thin layer of tiny  $\text{TiO}_2$  nanoparticles on and within the film.

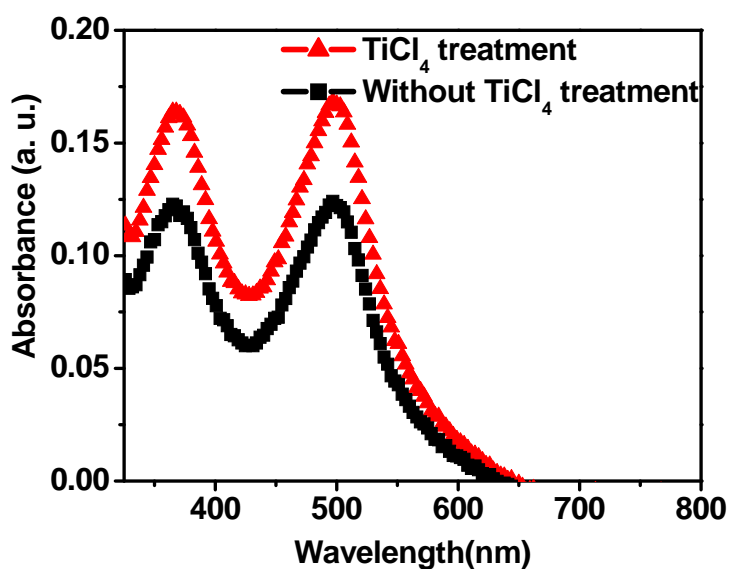


**Figure-5.6** Optical Absorption of solutions containing dye detached from doctor bladed films of different cases of interest (film area of  $2 \text{ cm}^2$  dye extracted in 10 mL of 1 mM KOH)

## 5-II Section-II

### ZnO based DSSC

#### 5-II.1 Introduction

As stated earlier, dye-sensitized solar cells (DSSCs) have demonstrated promise for solar-energy conversion to electricity because of their low fabrication cost, easy manufacture process, and relatively high efficiency [15]. The primary photovoltaic (PV) material for DSSCs today is TiO<sub>2</sub>, for which conversion efficiencies greater than 11% have been successfully achieved [16]. Compared to TiO<sub>2</sub>, zinc oxide (ZnO) is a rather unique wide band gap metal oxide for various reasons, and is also being actively explored as an alternative material [17-23]. ZnO has higher electron mobility ( $\sim 205\text{-}1000\text{ cm}^2\text{ V}^{-1}\text{ s}^{-1}$ ) than TiO<sub>2</sub> ( $\sim 0.1\text{-}4\text{ cm}^2\text{ V}^{-1}\text{ s}^{-1}$ ), enabling faster diffusion transport of photoinjected electrons when employed as the electrode in DSSCs [24]. In addition, ZnO can be easily processed into various nanostructures, such as nanoparticles [25], nanowires [26, 27], nanotubes [28], and tetrapods [29], providing numerous options for optimizing the electrode morphology so as to improve the charge collection. However, the conversion efficiency of ZnO-based DSSCs reported so far still remains lower than those fabricated from TiO<sub>2</sub>, leaving plenty of room to improve the efficiency through structural and morphology modification of the electrode.

One way to enhance the efficiency of ZnO-based cells is to construct one-dimensional nanostructures that produce more direct electron transport path so as to increase electron diffusion length and reduce the charge recombination rate [26-28, 30]. To this end, aligned nanowire/nanorod arrays [26], individual nanowires [27], and inorganic core/shell nanowire architectures [31] have been fabricated as the anode, with which an efficiency of 2.4% was achieved in the most successful case [26, 31]. Another approach is to improve the light-harvesting capability of the film by taking the optical enhancement effects, i.e., additional admixing of submicrometer-sized ZnO particles as the light-scattering centers and/or direct introduction of a light-scattering layer in the photoelectrode film [32-34]. Particularly, ZnO aggregates composed of nanosized crystallites can be used as efficient light scatters, offering relatively large specific surface

area framework, and removing the adverse effect caused by the lowered adsorption of dye-molecules in the film. For the case employing hierarchical structure of ~300 nm ZnO colloids, such approach can increase the conversion efficiency up to 3.5% [34]. In this work, different ZnO nanonanostructures were synthesized by hydrothermal and co-precipitation methods using different capping agents and examined its implications for solar energy conversion.

### **5-II.2 Experimental Method**

#### **5-II.2.1 Synthesis of ZnO nanoflowers by hydrothermal method**

The ZnO nanoflowers used in this study were synthesized by a hydrothermal route using high purity zinc acetate and NaOH. For obtaining ZnO flower, a 150 ml, 0.01M aqueous solution of zinc acetate was prepared and magnetically stirred for 10 min. After the dissolution of zinc acetate, 6 ml of 6.67M aqueous solution of NaOH was added to the above solution. Then this solution was transferred into a Teflon lined stainless steel autoclave. It was then sealed and maintained at 180 °C for 2 h. After the reaction a white colored solid powder was recovered by centrifugation followed by washing with distilled water and ethanol to remove the residual ions in the final product and, then, the powder was finally dried at 60 °C in air for 5 h.

#### **5-II.2.2 Preparation of ZnO nanostructures by using different capping Agents**

0.02M aqueous solution of zinc acetate was prepared and magnetically stirred for 5 minutes. 0.5gm of capping agents (citric acid & polyvinyl pyrrolidone) was dissolve in 10ml of de-ionized water and then 10 ml of 2M aqueous solution of NaOH was added drop wise to the above solution. A white colored solid powder was obtained and recovered by centrifugation followed by washing with de-ionized water. Then, the powder was finally dried at 60 °C in air for 10 h.

#### **5-II.2.3 Fabrication of dye-sensitized solar cell**

Doctor blading method was employed to make the ZnO nanostructure films and study the DSSCs. After making the films they were annealed at 450°C for 60 min. For sensitization, the films were impregnated with 0.5 mM N3 dye in ethanol for 2 h at room temperature.

The samples were then rinsed with ethanol to remove excess dye on the surface and were air-dried at room temperature. This was followed by redox electrolyte addition and top contact of Pt coated FTO. The electrolyte used was 1 M 1-hexyl-2, 3-dimethylimidazolium iodide, 0.05 M LiI, 0.05 M I<sub>2</sub>, and 0.5 M 4-tert-butylpyridine in acetonitrile.

**5-II.3 Characterization:** The synthesized ZnO nanostructures were characterized by X-ray diffraction (XRD; Philips X'Pert PRO), Scanning Electron Microscopy (SEM) and field-emission scanning electron microscopy (FESEM; Hitachi S-4200). The J-V characteristics were measured by irradiation with 100 mW/cm<sup>2</sup> (450W xenon lamp, Newport Instruments), 1 sun AM 1.5, simulated sunlight as a solar simulator. The current was measured using a Kiethley 2420 source meter.

#### 5-II.4 Results and discussions

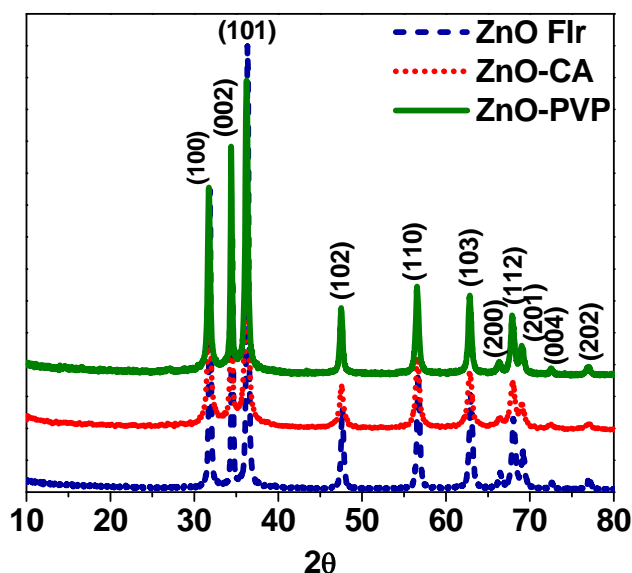


**Figure-5.7** XRD data of ZnO nanoflowers(Short dashed), ZnO capped by Citric Acid(Short dotted) and ZnO capped by Polyvinyl Pyrrolidone (Solid line).

Figure 5.7 shows the XRD data of ZnO nanoflowers (Short dashed), ZnO capped by Citric Acid (Short dotted) and ZnO capped by Polyvinyl Pyrrolidone (Solid line). As can be seen from the XRD pattern, the  $2\theta$  values at 31.76(100), 34.4(002), 36.26(101),

47.53(102), 56.59(110), 62.8(103), 66.37(200), 67.95(112), 69.21(201), 72.56(004) and 77.06(202) correspond to wurtzite ZnO nanostructures (PCPDFWIN # 800075).

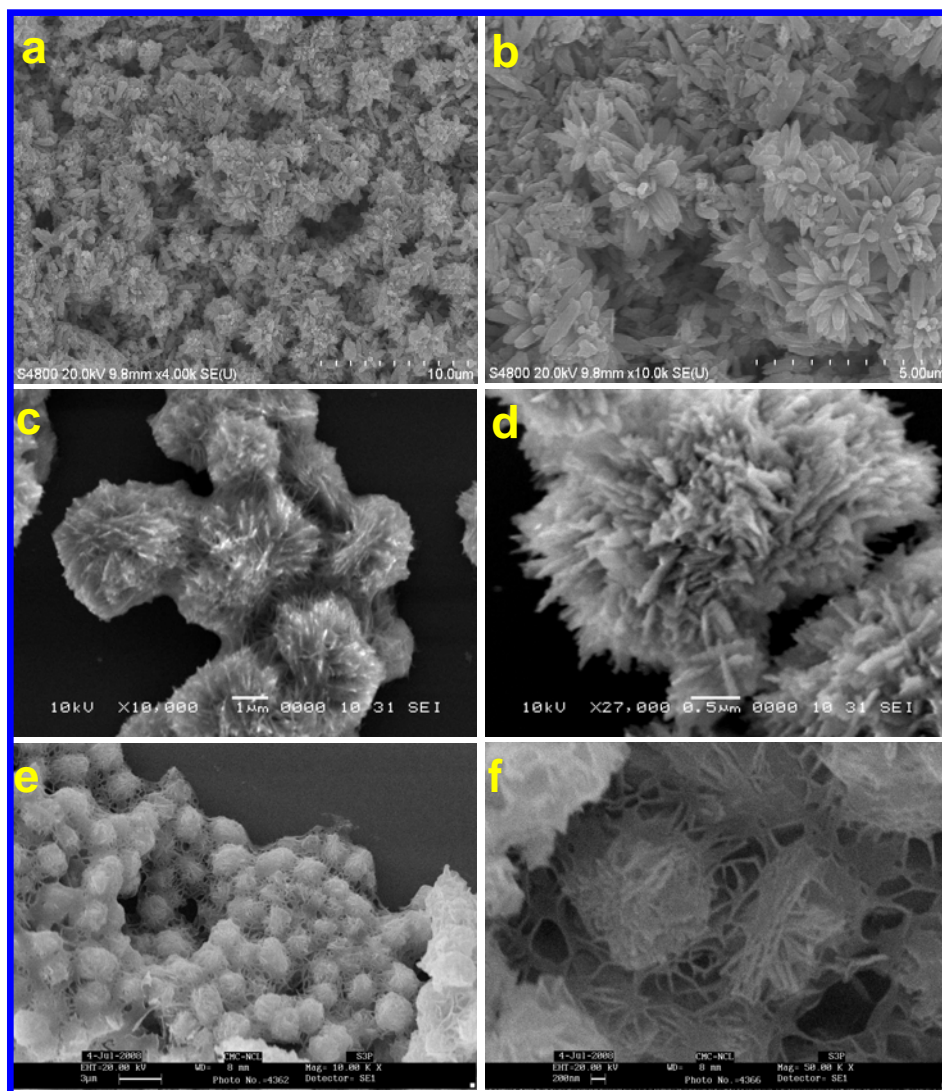


**Figure-5.8** (a, b) FE-SEM images of ZnO nanoflowers, (c, d) SEM images of ZnO capped by Citric Acid and (e, f) SEM images of ZnO capped by Polyvinyl Pyrrolidone.

The field-emission scanning electron microscopy (FESEM) images of ZnO nanoflower are shown in figure 5.8 (a, b). Figure-(c, d) & (e, f) are the Scanning Electron Microscopy (SEM) of ZnO capped by citric acid and polyvinyl pyrrolidone respectively.

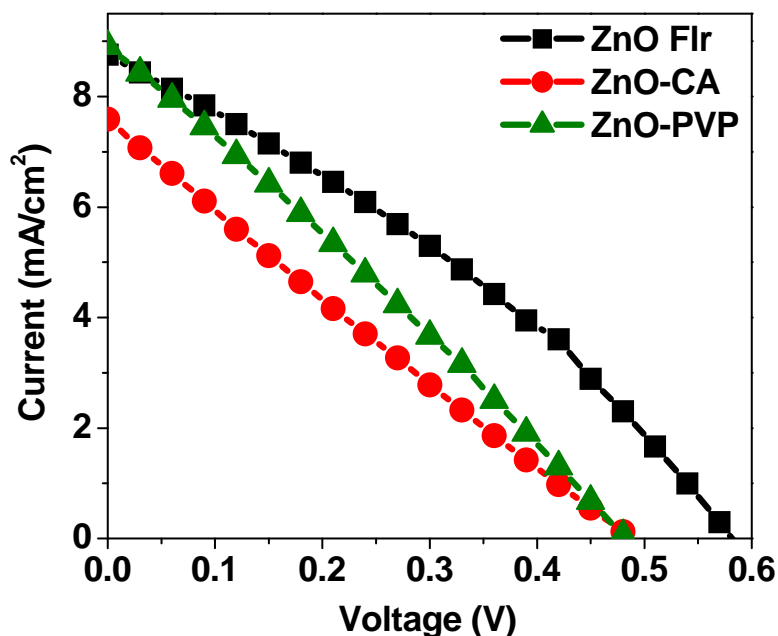


**Figure-5.9** J-V characteristics for dye-sensitized ZnO nanoflower, ZnO capped by citric acid and polyvinyl pyrrolidone films.

**Table-5.2** Photovoltaic properties of dye-sensitized ZnO-nanoflower, ZnO capped by citric acid and polyvinyl pyrrolidone films.

<i>Names</i>	<i>Voc (V)</i>	<i>Jsc (mA/cm<sup>2</sup>)</i>	<i>Fill Factor</i>	<i>Efficiency (%)</i>
ZnO Flr	0.58	8.75	32	1.6
ZnO Capped by CA	0.49	7.6	24	0.9
ZnO Capped by PVP	0.48	8.9	27	1.2

Figure 5.9 shows typical J-V curves for the two cases of interest under the illumination ( $I=100 \text{ mW/cm}^2$ ). Table 5.2 summarizes the solar cell parameters. The efficiency values for the ZnO-nanoflower case is 1.6% and for the cases of ZnO capped by citric acid and poly vinyl pyrrolidone are 0.9% and 1.2% respectively.

### 5-III Section-III

## **TiCl<sub>4</sub> Treatment of ZnO Mesostructures for Shape Preserving Chemical Transformations for DSSC Applications**

### **5-III.1 Introduction**

Titanium dioxide (TiO<sub>2</sub>) is perhaps one of the most widely used transition metal oxides in diverse applications due to its variety of unique and application-worthy properties [35]. With the growing emphasis of the current science and technology on nanomaterials due to their unique and novel property domains, considerable efforts have been expended over the past decade to synthesize various metal oxides (including TiO<sub>2</sub>) in the form of different phases, shapes, and functions using a variety of soft chemical and physical synthesis techniques. Depending on the use of a particular process, specific precursors/radicals, capping agents, temperature, pressure etc. a particular morphology of the nanosystem evolves [35-41]. In the context of different applications such as photovoltaics, catalysis, electro-optics etc., controlled nanocrystal growth is intensely researched. In addition to the size and composition, the shape control of nanomaterials is an important variable to adapt to the properties for various applications. However, different oxides have their specific symmetry-dependent crystal growth habits which make the proposition of developing specific desired (shape) morphology a non-trivial proposition. For instance, ZnO can grow more easily into anisotropic structures [42-47] while TiO<sub>2</sub> does not, unless efforts are made for facet control via selective capping.

Literature survey shows that the chemical transformation of inorganic nanocrystalline solids via diffusion or exchange of atoms is emerging as an attractive approach for nanostructure engineering in recent years. In particular, for transforming one ionic nanocrystal into another hetero-interfaced nanostructure, cation exchange reaction is shown to be a very useful process [48-57]. The pioneering work of Alivisatos et al. [48,50, 55, 56] is noteworthy in this context. It is generally assumed that the anionic structure of the crystal is conserved, while the cations undergo replacement during the exchange reaction due to their relatively smaller size and higher mobility. For instance,

the morphology composed of a CdSe nanocrystal embedded in a CdS rod (CdSe/ CdS) was exchanged to a PbSe/PbS nanorod via a Cu<sub>2</sub>Se/Cu<sub>2</sub>S structure keeping the seed size and position within the nanorod preserved [56]. The morphology change in the cation exchange reactions of metal chalcogenide nanocrystals, CdE to M<sub>x</sub>E<sub>y</sub> (E = S, Se, Te and M = Pd, Pt) has been investigated by Son et al. [57] Brock et al. [58] have synthesized Ag<sub>2</sub>Se wet gel monoliths by an ion exchange reaction of a monolithic CdSe wet gel and converted the same to an aerogel by drying under supercritical conditions. Herein we have synthesized ZnO mesostructures (rods, spheres, flakes and flower-like morphologies) by using hydrothermal and co-precipitation methods, and have converted these to TiO<sub>2</sub> mesostructures by simple TiCl<sub>4</sub> treatment. Interestingly, in all cases, this process is seen to exhibit a remarkable nominally shape-preserving property. The converted TiO<sub>2</sub> mesostructures were used for light harvesting function in a Dye-Sensitized Solar Cells (DSSCs) for higher conversion efficiency. A significant jump in the solar conversion efficiency was achieved with such light harvesting.

TiCl<sub>4</sub> treatment of nanoparticulate TiO<sub>2</sub> films has been researched by several groups [59, 60], especially by O'Regan and Bakker, in the context of the dye sensitized solar cell application, and a significant improvement in cell efficiency has been demonstrated following such a treatment. However, there have not been many studies on the possible beneficial use of such a treatment for other oxides. ZnO has attracted considerable interest of the DSSC community due to its unique set of optoelectronic properties however the corresponding DSSC efficiencies are quite low. The pioneering work by Yang and coworkers [61] showed that DSSCs based on ZnO nanowire/TiO<sub>2</sub> core-shell structures have higher charge separation yields. It is now known that TiO<sub>2</sub> coating of ZnO nanostructure improves the DSSC efficiency, and in most cases such coating is applied by the expensive atomic layer deposition method. Only recently, Atienzar et al. reported a simple TiCl<sub>4</sub> treatment that led the surface coating of TiO<sub>2</sub> on ZnO core (equivalent of the TiCl<sub>4</sub> post treatment of TiO<sub>2</sub> structured materials) leading to improved DSSC performance [62]. However, no details were provided about the effects of TiCl<sub>4</sub> on ZnO morphology. Recently, the effect of TiCl<sub>4</sub> treatment on porous ZnO photoelectrode has also been examined by Murakami et al. [63]

### 5-III.2 Experimental Section

**Materials:** The chemical agents were purchased from Aldrich Co. and Merck Chemicals. The  $\text{RuL}_2(\text{NCS})_2/(\text{TBA})_2$  (N719; L = 2,2'-bipyridine-4,4'-dicarboxylic acid and TBA = tetrabutylammonium) and the fluorine-doped  $\text{SnO}_2$  (FTO) electrode (sheet resistance 15 ohm/square) were purchased from Solaronix Co. For the preparation of reference DSSCs, commercial  $\text{TiO}_2$  was obtained from Degussa (P25). High-purity water (Milli-Q, Millipore) was used for all experiments. The FTO electrodes were washed with acetone, ethanol, and deionized (18.2  $\text{M}\Omega\cdot\text{cm}$ ) water in an ultrasonication bath for 15 min with a final wash in isopropyl alcohol.

#### 5-III.2.1 Preparation of ZnO Flowers

The ZnO flowers used in this study were synthesized by hydrothermal route using high purity zinc acetate and NaOH. For obtaining ZnO flower, a 150 ml, 0.01M aqueous solution of zinc acetate was prepared and magnetically stirred for 10 min. After the dissolution of zinc acetate, 6 ml of 6.67 M aqueous solution of NaOH was added to the above solution. Then this solution was transferred into a Teflon lined stainless steel autoclave. It was then sealed and maintained at 180 °C for 2 h. After the reaction a white colored solid powder was recovered by centrifugation followed by washing with distilled water and ethanol to remove the residual ions in the final product. Then the powder was finally dried at 60 °C in air for 5 h.

#### 5-III.2.2 Preparation of ZnO rods on FTO and ITO

Zinc acetate, Zinc nitrate, Hexamethylene tetramine (HMT) and Sodium Hydroxide Pellets were used as precursors for ZnO rod growth. Zinc acetate solution (5 mM concentration) was prepared in methanol and was kept under stirring at 65 °C for 45 min. Then sodium hydroxide solution (30 mM concentration, prepared in Methanol) was added drop wise till the solution attained slight milky color and was used as seed solution. Fluorine doped tin oxide (FTO) and Indium doped tin oxide (ITO) glass plates (2.5 cm × 2.5 cm) were used as substrates for growth of ZnO nanorods. The substrates were mounted on the spin coater having a preset rotation speed of 2500 rpm for 30 sec and then spin coating was carried out using freshly prepared seed solution. The process

was repeated continuously until the transparent substrate turned slightly opaque. Finally the substrates were annealed at 300<sup>0</sup>C for 1 hr for better adherence of ZnO nanoparticles which act as nucleating sites for the growth of ZnO nanorods.

For facile growth of ZnO rods, equimolar solutions of Zinc Nitrate (25 mM) and hexamethylene tetramine (HMT 25 mM)) were separately prepared using de-ionized water as solvent. The seeded substrates were immersed into the solution and the solution temperature was maintained at 95 <sup>0</sup>C under slow stirring. The depositions were carried out for time duration of 3 hour. Finally, the deposits were annealed at 300 <sup>0</sup>C for 1 hr for removal of moisture and for improving the adhesion.

### **5-III.2.3 Preparation of ZnO spheres and flakes**

The ZnO sphere like morphology was synthesized at room temperature by co-precipitation method using zinc acetate, polyvinyl pyrrolidone and sodium hydroxide. 0.02M aqueous solution of zinc acetate was prepared and magnetically stirred for 5minutes. 0.5gm of polyvinyl pyrrolidone (capping agents) was dissolved in 10ml of de-ionized water and added to the zinc acetate solution. Then 10 ml of 2M aqueous solution of NaOH was added drop wise to the above solution. A white colored solid powder was obtained and recovered by centrifugation followed by washing with de-ionized water. Then, the powder was finally dried at 60 °C in air for 10 h. The ZnO flakes were obtained from a commercial source (Smart NanoZ, Pune, India).

### **5-III.2.4 Preparation of TiO<sub>2</sub> Nanoparticles**

Nanocrystalline TiO<sub>2</sub> was prepared by using a simple hydrothermal method. 2 ml of Titanium Isopropoxide was hydrolyzed by adding 100 ml of deionized water and then sonicated for 5 minutes. The solution was transferred to Teflon lined autoclave vessel along with 3ml of H<sub>2</sub>SO<sub>4</sub> (1M). This autoclave vessel was kept at 175 °C for 24 Hrs. The resulting product was washed thoroughly with deionized water and dried at 50°C in a dust proof environment to produce the powder of TiO<sub>2</sub> nanoparticles.

### 5-III.2.5 Fabrication of dye sensitized solar cell

Doctor blading method was employed to first make the TiO<sub>2</sub> nanoparticle film (thickness ~7 μm) and then an over layer of ZnO flowers film (thickness ~8 μm). The total thickness of the film was ~15 μm. After making such films they were annealed at 450 °C for 60 min. Then these films were treated with TiCl<sub>4</sub> solution (50mM) at 70 °C followed by second annealing at 450 °C for 30 min. After TiCl<sub>4</sub> treatment, the total thickness of the film was found to be reduced from ~15 μm to ~11 μm. Same thickness (~11 μm) of TiCl<sub>4</sub> treated TiO<sub>2</sub> nanoparticle and P25 (Degussa) films were made for comparison. The films were impregnated with 0.5 mM N719 dye in ethanol for 24 h at room temperature. The samples were then rinsed with ethanol to remove excess dye on the surface and were air-dried at room temperature. This was followed by redox electrolyte addition and top contact of Pt coated FTO. The electrolyte used was 1 M 1-hexyl-2, 3-dimethyl-imidazolium iodide, 0.05 M LiI, 0.05 M I<sub>2</sub>, and 0.5 M 4-tert-butylpyridine in acetonitrile. The J-V characteristics were measured by exposure to 100 mW/cm<sup>2</sup> (450W xenon lamp, Newport Instruments), 1 sun AM 1.5, simulated sunlight by a solar simulator. The current was measured using a Kiethley 2420 source meter.

### 5-III.2.6 TiCl<sub>4</sub> Treatment of ZnO Structured Films

The ZnO structured films directly grown on FTO and ITO by chemical method as described earlier were treated by TiCl<sub>4</sub> solution (50mM) at 70 °C for 30 min. Then these films were washed with D.I. water carefully followed by annealing at 450 °C for 30 min. The other ZnO films made from nanoscale powder samples were made on FTO by doctor blading method (thickness ~12 μm) and then treated by TiCl<sub>4</sub> solution to convert anatase TiO<sub>2</sub> nanostructures via ion exchange reaction using a similar procedure. Interestingly it was noted that the total thickness of the film gets reduced from ~12 μm to ~7 μm after the TiCl<sub>4</sub> treatment. The reduction of thickness after TiCl<sub>4</sub> treatment can be attributed to some soluble reaction products, which get washed out during the process. We employed exchange reaction to convert ZnO to TiO<sub>2</sub> in Scheme 1.

**Scheme 1.** Reaction Used to Convert ZnO to TiO<sub>2</sub>.



The reaction occurs via cation exchange between  $Zn^{2+}$  and  $Ti^{4+}$  ions. These exchange reactions can be qualitatively understood in terms of hard-soft acid-base theory (soft acids react faster and form stronger bonds with soft bases, whereas hard acids react faster and form stronger bonds with hard bases, all other factors being equal).  $Ti^{4+}$  is a harder acid than  $Zn^{2+}$ . Thus  $Ti^{4+}$  binds strongly with the  $O^{2-}$  anion to form  $TiO_2$ . The conversion of ZnO structured material to  $TiO_2$  structured materials is strongly favored by a thermodynamic driving force of about -249 kJ/mole [64].

### 5-III.3 Characterization

Various techniques such as X-ray diffraction (XRD; Philips X'Pert PRO), Raman spectroscopy (Horiba Jobin Yvon LabRAM HR System), Diffused Reflectance Spectra (DRS, Jasco V-570 spectrophotometer), Scanning Electron Microscopy (SEM) and field-emission scanning electron microscopy (FESEM; Hitachi S-4200) were used to characterize the samples.

### 5-III.4 Results and discussions

Figure 5.10 shows the X-ray diffraction (XRD) patterns of ZnO Flower (Flr) and  $TiCl_4$  treated ZnO Flr film on the glass substrate. As can be seen from the XRD pattern, the  $2\theta$  values at 31.8, 34.4, 36.3, 47.6, 56.6, 62.8, 67.9 and 69.2 correspond to wurtzite ZnO (PCPDFWIN # 800075). The XRD data for the case of  $TiCl_4$  treated ZnO show clear signatures of pure anatase  $TiO_2$  phase (PCPDFWIN # 211 272) at 25.3, 37.9, 48.2, 54.1, 55.2 and 62.9. The complete absence of ZnO peaks clearly indicates that following the stated  $TiCl_4$  treatment, the ZnO phase converts fully to anatase  $TiO_2$ . Several other morphologies such as spheres, flakes etc. were also studied and the corresponding XRD data are presented in figure 5.11. These too exhibit complete transformation to anatase  $TiO_2$  form.

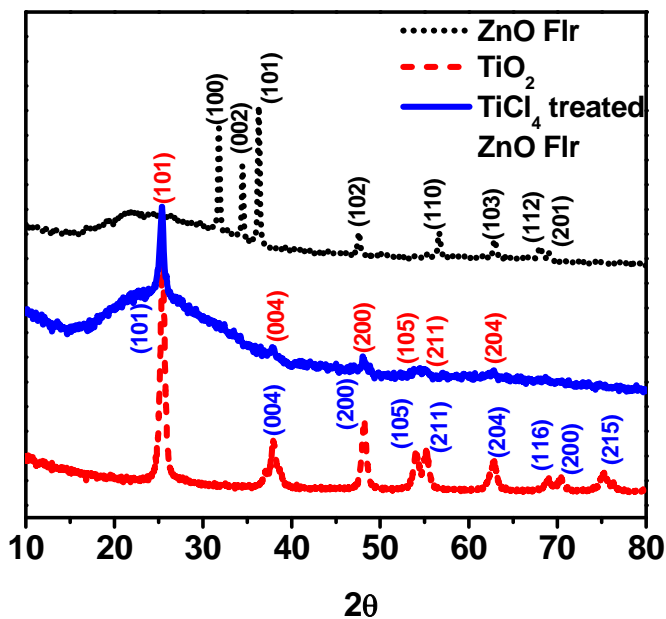


**Figure-5.10** XRD data of ZnO, TiCl<sub>4</sub> treated ZnO and FTO.

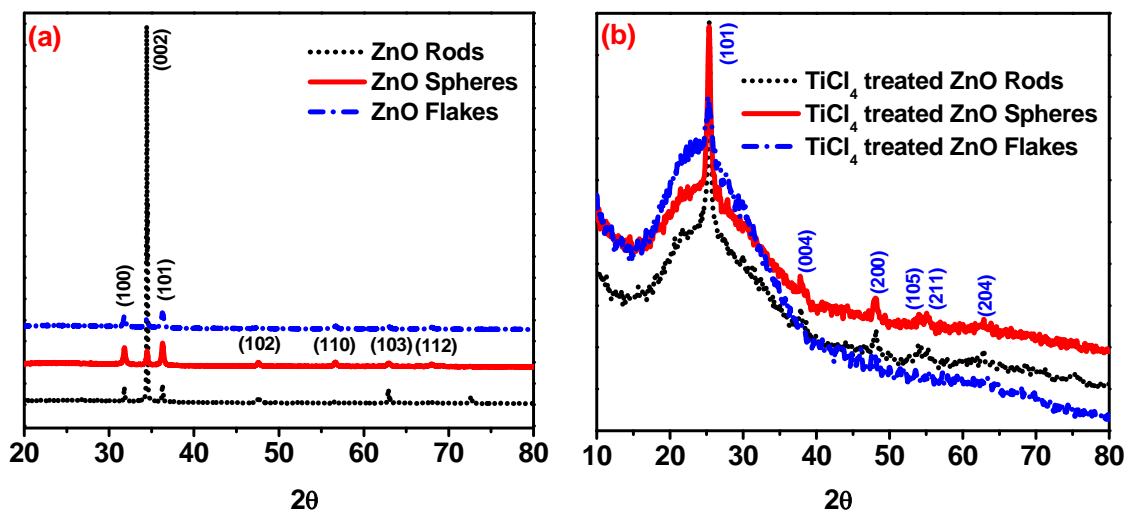


**Figure-5.11** XRD data of (a) ZnO (Rods, Spheres, Flakes), (b) TiCl<sub>4</sub> treated ZnO (Rods, Spheres, Flakes)

The Raman spectrum for ZnO Flr and TiCl<sub>4</sub> treated ZnO Flr is shown in figure 2. The Raman spectrum for the case of ZnO in Figure 2 (inset) shows the clear signatures at about 376 and 435 cm<sup>-1</sup> expected for this oxide [65]. The Raman peaks at 148.2, 401, 518 and 642 cm<sup>-1</sup> in Figure 2 are characteristic of pure anatase TiO<sub>2</sub> phase [14]. No peak

corresponding to ZnO was observed after  $\text{TiCl}_4$  treatment of ZnO, which indicates complete conversion from ZnO to anatase  $\text{TiO}_2$  by the stated  $\text{TiCl}_4$  treatment. The Raman spectra of other  $\text{TiCl}_4$  treated ZnO structured materials are shown in figure 5.13.

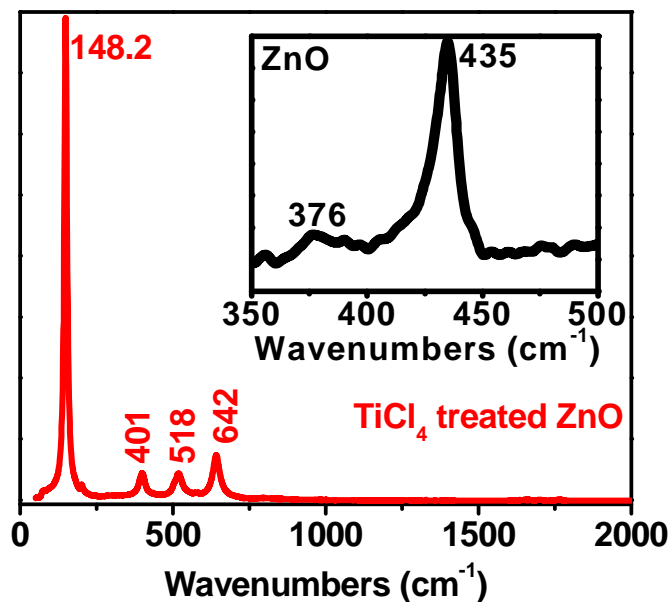


**Figure-5.12** Raman spectra of  $\text{TiCl}_4$  treated ZnO Flr and ZnO Flr (inset).

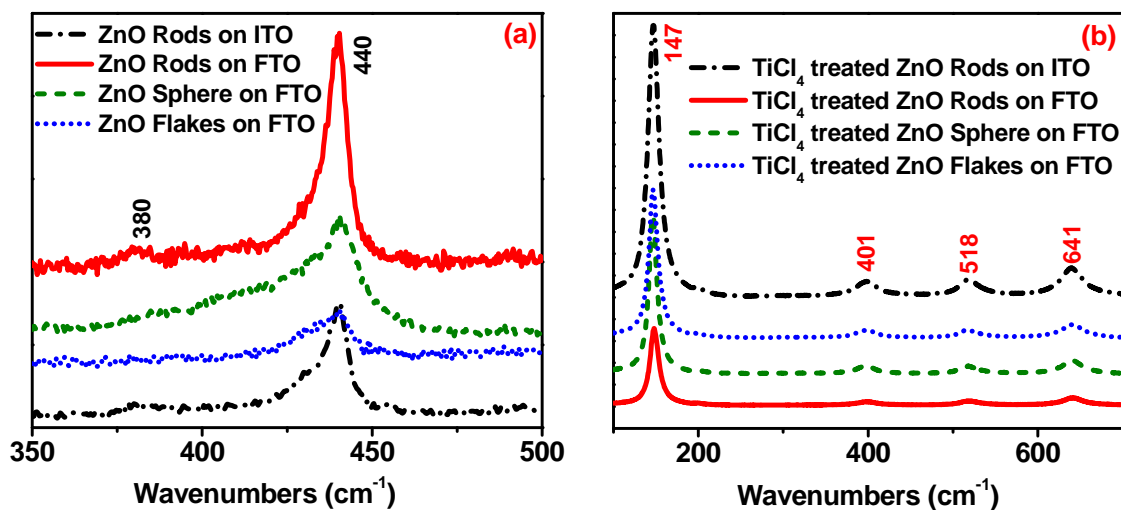


**Figure-5.13** Raman Spectra of (a) ZnO (Rods, Spheres and Flakes) and (b)  $\text{TiCl}_4$  treated ZnO (Rods, Spheres and Flakes).

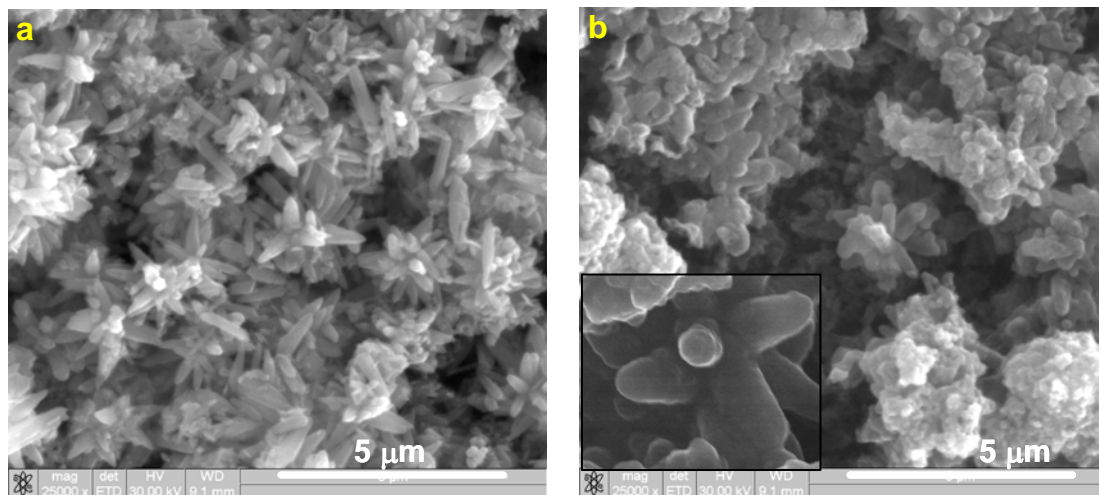


**Figure-5.14** (a) and (b) present the respectively SEM images of ZnO Flr and  $\text{TiCl}_4$  treated ZnO Flr. The inset Figure (b) is the zoomed-in version of one of the flowers of  $\text{TiO}_2$  ( $\text{TiCl}_4$  treated ZnO Flr).

Figure 5.14(a) and (b) present the SEM images of ZnO Flr film and  $\text{TiCl}_4$  treated ZnO Flr film, respectively, which clearly confirms that the morphology remains nominally intact after the  $\text{TiCl}_4$  treatment of ZnO Flr. Interestingly the latter  $\text{TiCl}_4$  treated case for which XRD shows pure anatase  $\text{TiO}_2$  phase is seen to retain the flower like morphology of the parent ZnO mesostructure, implying a nominally shape preserving chemical transformation. It is observed that in Figure 3(b) the necking between the flowers takes place after the  $\text{TiCl}_4$  treatment of ZnO Flr which is helpful for the transport of electrons in DSSC as discussed later. Such dense branched hierarchical morphology is of great value in nanoparticle films for solar cell and other optoelectronic applications for reasons of good charge carrier transport and light harvesting effects. The inset of figure 14(b) shows a zoomed-in version of one of the flowers of  $\text{TiO}_2$  ( $\text{TiCl}_4$  treated ZnO Flr).

The shape preserving transformation of ZnO Flr to  $\text{TiO}_2$  Flr seen here must occur through the cation exchange reaction between  $\text{Zn}^{2+}$  and  $\text{Ti}^{4+}$  ions as anticipated and mentioned earlier [48, 57]. Figure 5.15 shows the energy dispersive x-ray (EDX) data for the image of figure 5.14(b) indicating a complete absence of Zinc for the case of  $\text{TiCl}_4$  treated ZnO

consistent with complete ion exchange. The XPS data shown in figure 5.16 further confirm the complete absence of Zn in the case of  $\text{TiCl}_4$  treated ZnO.

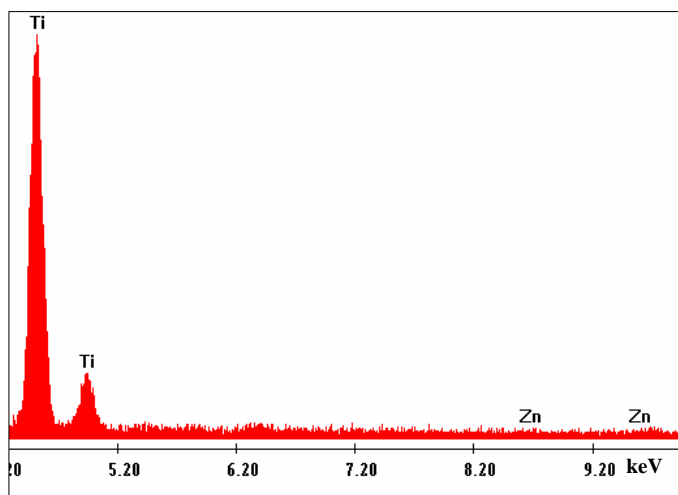


**Figure-5.15** The energy dispersive x-ray (EDX) data of  $\text{TiCl}_4$  treated ZnO.

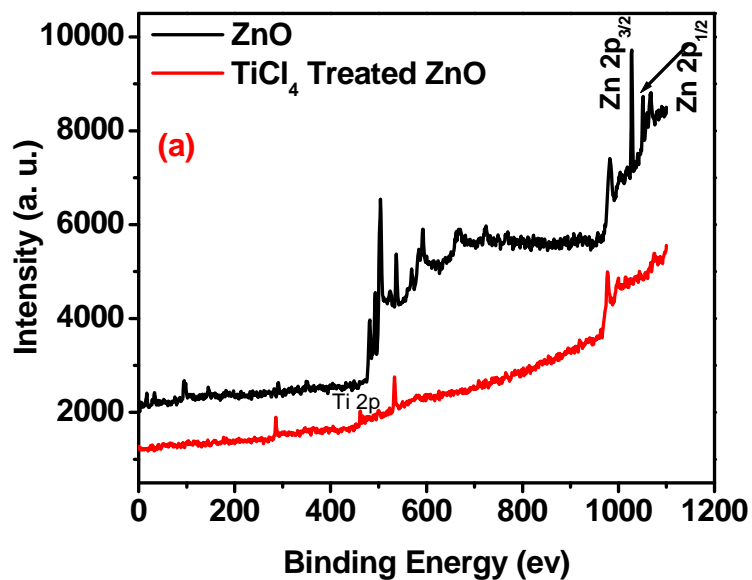


**Figure-5.16** XPS data of (a) ZnO and  $\text{TiCl}_4$  treated ZnO.

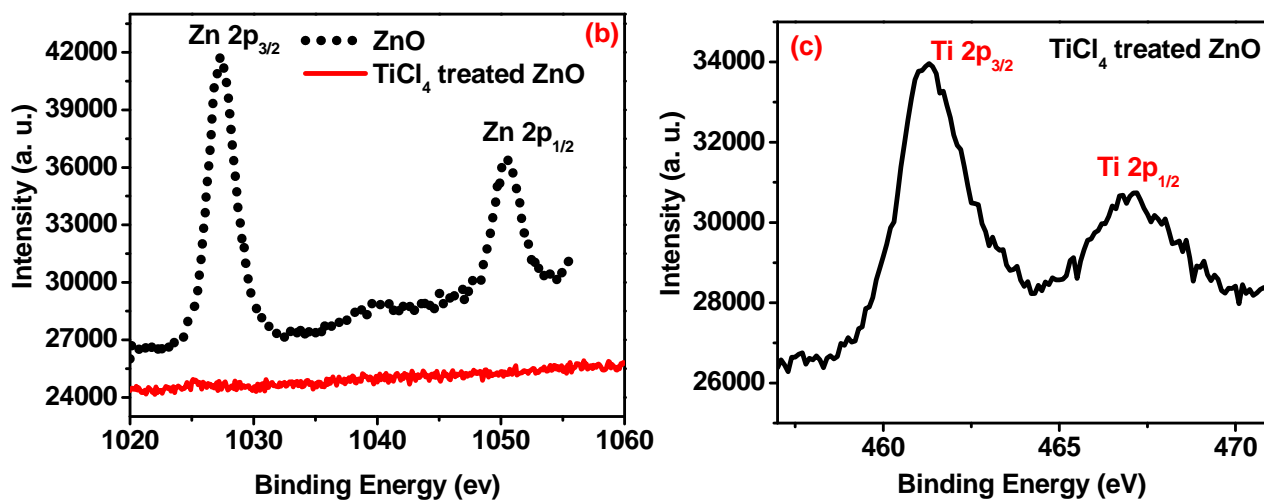


**Figure-5.16** XPS data of (b) Presence and absence of Zn in ZnO and TiCl<sub>4</sub> treated ZnO respectively, and (c) Presence of Ti in TiCl<sub>4</sub> treated ZnO.

The FE-SEM image of hexagonal shaped ZnO rods on FTO substrate is shown in figure 5.17(a). After TiCl<sub>4</sub> treatment of ZnO rods on FTO, all the ZnO rods are seen to get converted to anatase TiO<sub>2</sub> structure of nominally similar shape (figure 5.17(b)) but interestingly as hollow tubes. The schematic diagram of suggested mechanism involving conversion of ZnO rods to hollow anatase TiO<sub>2</sub> tubes is shown in figure 5.17(c). During the TiCl<sub>4</sub> treatment, all the Ti<sup>4+</sup> ions are first adsorbed on the surface of ZnO rods and then Ti<sup>4+</sup> ions and Zn<sup>2+</sup> ions are exchanged slowly among themselves via ion exchange mechanism [56-58]. There may be two possible scenarios for this ion exchange reaction (i) the new Ti<sup>4+</sup> ions adsorbed on ZnO rods diffuse inward continuously, resulting in a directional migration of the reaction interface towards the core, or (ii) The Ti<sup>4+</sup> ion diffusion is limited and core species (Zn<sup>2+</sup>) diffuse outward, generating a void space inside the rods [66]. The Zn<sup>2+</sup> ions exchanged by Ti<sup>4+</sup> ions would combine with Cl<sup>-</sup> ions present in the solution to form ZnCl<sub>2</sub> (which is soluble in water thereby coming out as side-product) whereas the Ti<sup>4+</sup> ions would take the place of Zn<sup>2+</sup> via diffusion to form TiO<sub>2</sub> as major product.

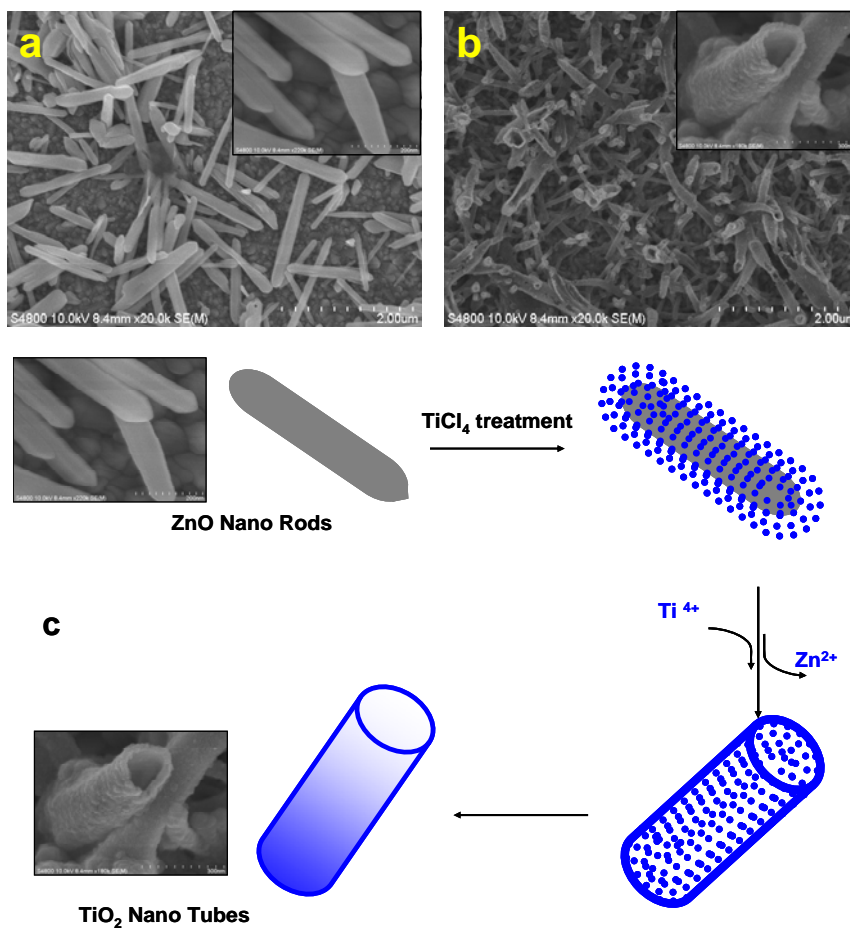


**Figure-5.17** FE-SEM of ZnO rods and (b) TiCl<sub>4</sub> treated ZnO rods on FTO and (c) schematic diagram of mechanism involving conversion of ZnO rods to TiO<sub>2</sub> hollow tubes by TiCl<sub>4</sub> treatment of ZnO rods.

Figure 5.18 (a) and (c) show the SEM images of ZnO rods on ITO substrate which are properly aligned. It is observed that by changing the substrates from FTO to ITO during the synthesis process, the growth and alignment of ZnO rods are different. The TiCl<sub>4</sub> treatment of ZnO rods on ITO substrate is shown in figure 5.18(b) and (d) which are similar when the same are on FTO substrate. After TiCl<sub>4</sub> treatment, all the ZnO rods on ITO are seen to have been converted to TiO<sub>2</sub> hollow rods keeping the alignment conserved. The process of conversion of ZnO rods to TiO<sub>2</sub> rods on ITO keeping the alignment conserved basically follow the same ion exchange mechanism which is discussed above.

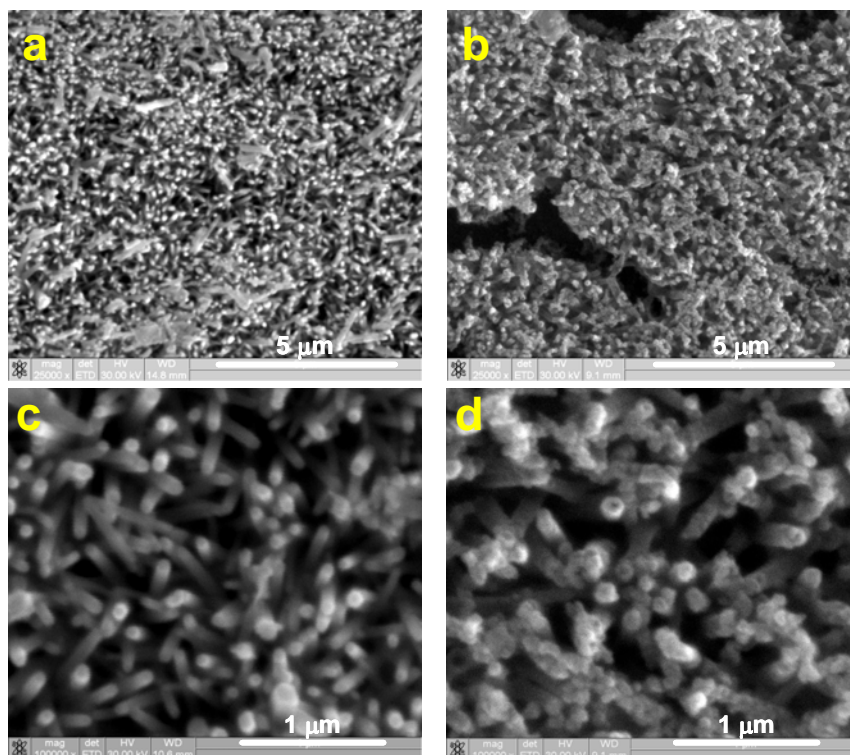


**Figure-5.18** SEM Data of ZnO rods (a) & (c) and  $\text{TiCl}_4$  treated ZnO Rods (b) & (d) on ITO.

The BET surface area data on the ZnO Flr system before and after its conversion into anatase  $\text{TiO}_2$  Flrs is Table 5.3. The area is seen to be enhanced from about  $5.9 \text{ m}^2/\text{gm}$  to  $30.5 \text{ m}^2/\text{g}$ , i.e. by a factor of about 5. This is consistent with change from a rod to a tube structure which would increase the area by a factor of about 2; the extra multiplying factor being added by the roughness enhancement.

Table-5.3 The BET Surface area measurements of ZnO Flr and  $\text{TiCl}_4$  Treated ZnO Flr.

Name	Surface Area( $\text{m}^2/\text{g}$ )
ZnO Flr	5.9
$\text{TiCl}_4$ treated ZnO Flr	30.5

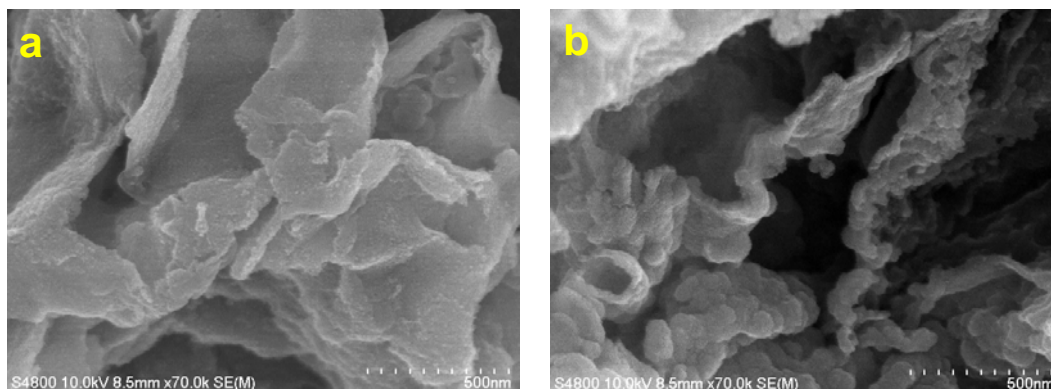
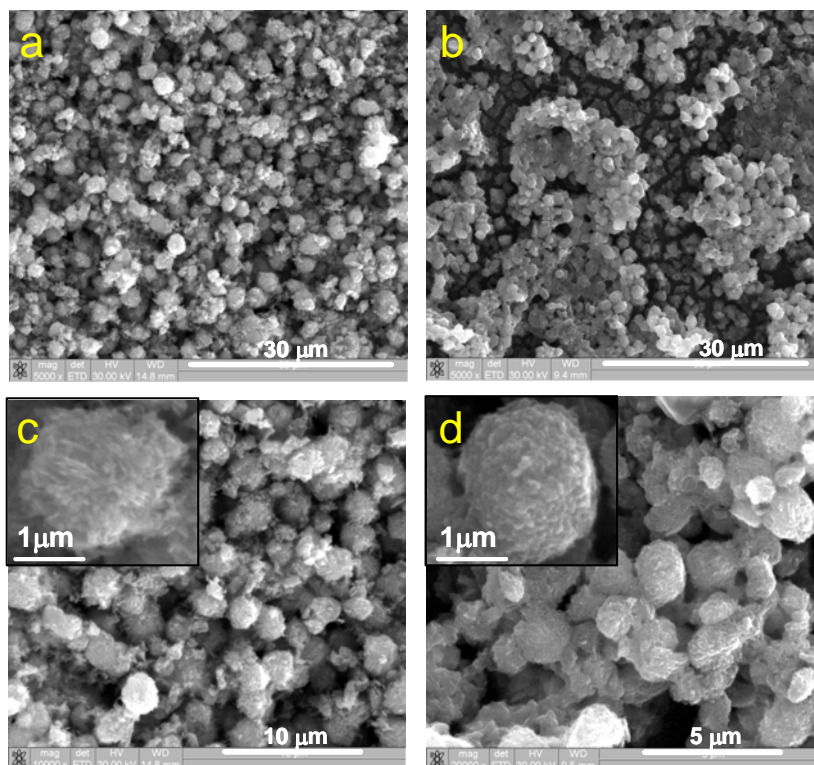


Figure-5.19 FE-SEM of ZnO flakes (a) and  $\text{TiCl}_4$  treated ZnO flakes (b) on FTO.

In figure 5.19(a), flake-like morphology of ZnO is shown, which was achieved by a special synthesis protocol. Very interestingly, by using the  $\text{TiCl}_4$  treatment of these ZnO flakes, flake-like  $\text{TiO}_2$  structures could be obtained, replicating the original morphology, as shown in figure 5.19(b).



**Figure-5.20** SEM Data of ZnO capped with PVP (a) & (c) and  $\text{TiCl}_4$  treated ZnO capped with PVP (b) & (d) on FTO

The SEM images of the hierarchically structured ZnO synthesized at room temperature by using poly vinyl pyrrolidone as capping agent are shown in figure 5.20(a) and (c). The inset of figure 5.20(c) is the magnified SEM image of the ZnO mesostructure. These hierarchically structured ZnO were converted to anatase TiO<sub>2</sub> with diameter ranging from 1 μm to 2 μm by TiCl<sub>4</sub> treatment keeping the morphology broadly conserved, as shown in figure 5.20(b) and (d). The zoomed version of one of the TiO<sub>2</sub> mesostructure is shown in the inset of figure 5.20(d). All these examples collectively show that the suggested treatment is not only facile but versatile in transforming oxide phase by preserving shapes in the broad sense.

TiO<sub>2</sub> mesostructures have been used in Dye Sensitized Solar Cells (DSSC) as light harvesters because of enhanced light scattering in the visible region thereby enhancing the path length of incident light within the nanocrystalline TiO<sub>2</sub> electrode [67-69]. In order to investigate the role of TiO<sub>2</sub> mesostructures obtained after TiCl<sub>4</sub> treatment of ZnO mesostructures as light harvesters in TiO<sub>2</sub> based DSSC, double layer structures (TZFT film) were made with 7 μm thick nanocrystalline anatase TiO<sub>2</sub> with an over layer (4 μm) of TiCl<sub>4</sub> treated ZnO Flr (implying effectively an anatase TiO<sub>2</sub> flower morphology). TiCl<sub>4</sub> treated films (~11 μm thick) with only nanocrystalline TiO<sub>2</sub> and the commercial Degussa P25 without such an over-layer were also prepared under similar conditions for comparison. All films had an active area of 0.25 cm<sup>2</sup>.

Figure 5.21 and Table 5.4 compares the photovoltaic characteristic of all the three cases. The optimized mean efficiencies obtained by our procedure for P25 and Nanocrystalline TiO<sub>2</sub> are about 5.2% and 5.4%, respectively. After TiCl<sub>4</sub> treated ZnO is introduced as an over layer, the conversion efficiency improved from 5.4% to 6.9%, a 28% increment. It is important mention here that higher efficiencies have been reported in the literature even for the nano-TiO<sub>2</sub> and P25 cases using the same dye, but achieving such efficiencies requires simultaneous optimization of several parameters and significant experience and skill in cell architecture design. In this work the emphasis is on shape preserving transformation and our attempt here is to demonstrate the possible use of such anisotropic

TiO<sub>2</sub> architectures in device improvements; the observed enhancement being significant within our current skill set in device making.

It can be seen that the open circuit voltage ( $V_{OC}$ ) of TZFT film (0.78 V) is almost 18% higher than that for TiO<sub>2</sub> nanocrystalline film (0.66 V) and P25 film (0.67 V). Also the fill factor is higher for the case of TZFT films (~ 63 %) than the case of TiO<sub>2</sub> film (58 %) and P25 (~ 60 %). Increase in  $V_{OC}$  and Fill Factor can be correlated with decreased electron-hole recombination at TiO<sub>2</sub>-dye-electrolyte interface [61].

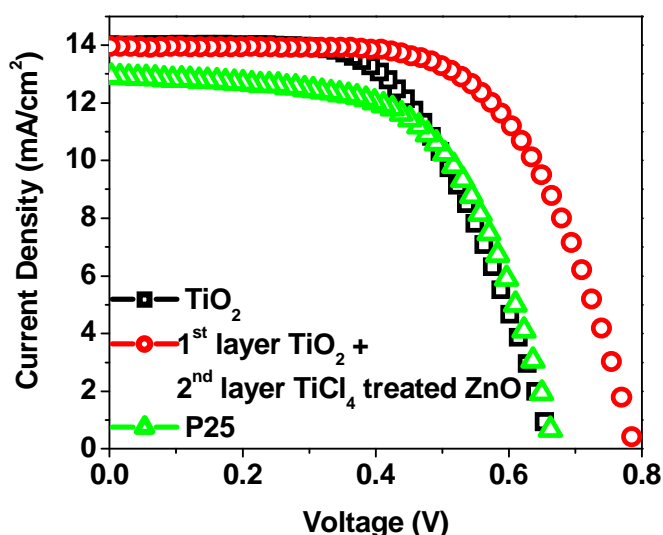


Figure-5.21 Comparison of Solar cell characteristics for DSSCs made with the nanocrystalline TiO<sub>2</sub>-layer-based TiCl<sub>4</sub> treated ZnO Flr over layer with Nanocrystalline TiO<sub>2</sub> and commercial Degussa P25.

**Table-5.4** Photovoltaic properties of dye-sensitized solar cells.

Name	Voc(V)	Jsc (mA/cm <sup>2</sup> )	Fill factor(FF)	Efficiency ( $\eta$ ) %
Degussa P25	0.67	12.9	60.5	5.2
TiO <sub>2</sub>	0.66	14.0	58.1	5.4
1 <sup>st</sup> layer TiO <sub>2</sub> + 2 <sup>nd</sup> layer TiCl <sub>4</sub> treated ZnO Flr	0.78	14.0	62.8	6.9

The thickness of all films of DSSC were ~11  $\mu$ m

Decreased recombination in TZFT film can be attributed to high quality of TiO<sub>2</sub> Flr (over layer) formed after TiCl<sub>4</sub> treatment of ZnO Flr [70]. It has been shown that the TiO<sub>2</sub> formed after TiCl<sub>4</sub> treatment has conduction band edge potential 80 mV lower than conventional TiO<sub>2</sub> nanoparticles thereby causing 20 fold decreases in electron-electrolyte recombination rate constant [52] which is responsible for increase in Voc. No substantial increment in J<sub>SC</sub> was observed for the case of TZFT films. The short circuit current density (J<sub>SC</sub>) for TZFT film is 14 mA/cm<sup>2</sup> which is about the same as that for the case of the TiO<sub>2</sub> film (12.9 mA/cm<sup>2</sup> for P25). This can be attributed to less dye adsorption in the TZFT films.

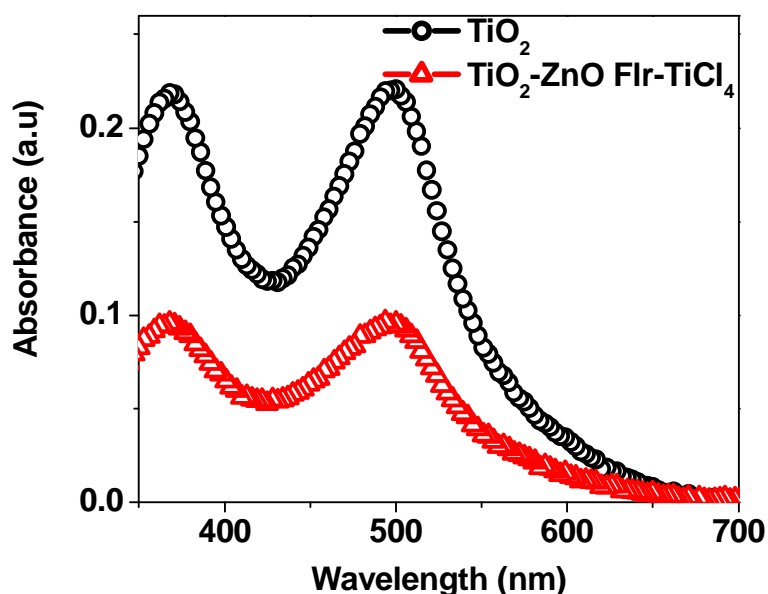


**Figure-5.22** Optical Absorption of solutions containing dye detached from doctor bladed films of different cases of interest (film area of 1.6 cm<sup>2</sup> dye extracted in 10 mL of 1 mM KOH).

In order to quantify the amount of dye adsorbed we measured the absorptions of solutions containing dye detached from the TiO<sub>2</sub> and TZFT films. We can calculate from figure 5.22 the dye loading of the TiO<sub>2</sub> and TZFT films, which have values of  $8.9 \times 10^{-8}$  and  $4.7 \times 10^{-8}$  mol/cm<sup>2</sup>, respectively. It is interesting that although the dye loading of the TZFT film is far less (by almost 50%) as compared to the TiO<sub>2</sub> nanocrystalline film, still the

current density for TZFT remains the same ( $\sim 14 \text{ mA/cm}^2$ ). In order to investigate this aspect further we measured the diffused reflectance spectra (DRS) for the  $\text{TiO}_2$  and TZFT films without dye. It is observed (figure 5.23 (a)) that the (diffused) reflectance of TZFT film is higher than that of nanocrystalline  $\text{TiO}_2$  film. This implies improved scattering of  $\text{TiO}_2$  Flrs (over layer) formed after  $\text{TiCl}_4$  treatment of ZnO Flrs which enhances the path length of light within the nanocrystalline  $\text{TiO}_2$ .

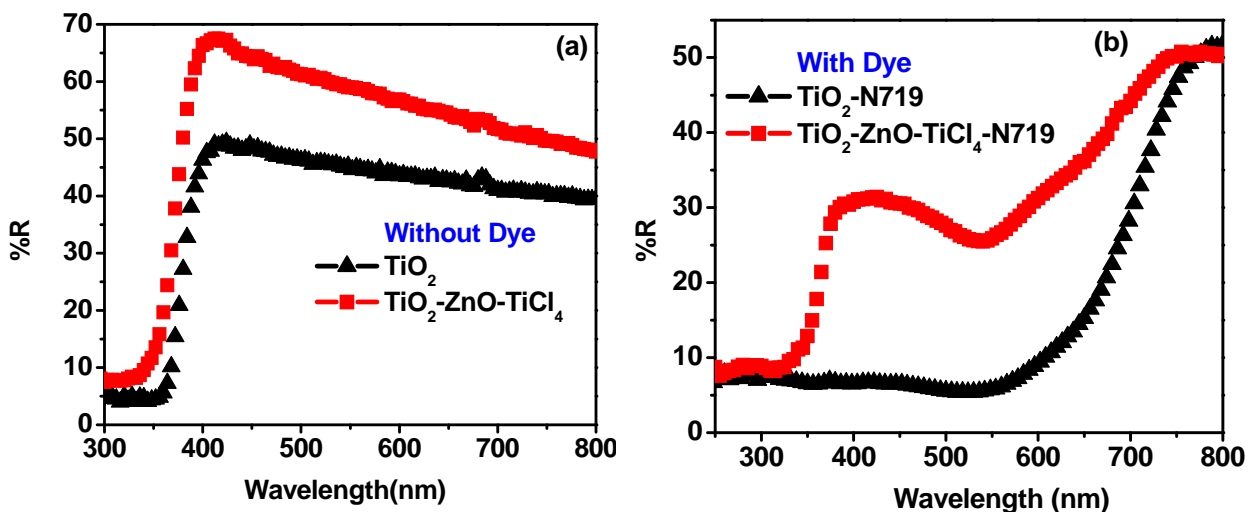


**Figure-5.23** Diffused reflectance spectra of the nanocrystalline  $\text{TiO}_2$  and TZFT films (a) without and (b) with adsorbed N-719 dye.

Since the DSSC systems contain dye adsorbed films, the DRS of dye adsorbed films was recorded for gaining further insights. As shown in figure 5.23 (b), after dye adsorption on the films the reflectance values for the TZFT and the nanocrystalline  $\text{TiO}_2$  film decrease significantly, which is mainly due to light absorption by the dye molecules. However, the dye-adsorbed TZFT film exhibits a substantially higher reflectance than the dye adsorbed nanocrystalline  $\text{TiO}_2$  film which is due to low dye adsorption of the TZFT film (as discussed earlier) and the strong light scattering effect of the over layer of  $\text{TiCl}_4$  treated ZnO Flr on the first layer of  $\text{TiO}_2$  nanoparticle (TZFT film) [67-69]. This shows that the decrease in current density due to less dye adsorption is counterbalanced by the enhancement in current density due to improved light scattering effect of  $\text{TiO}_2$  Flr over layer in TZFT films thereby keeping current density almost the same. Therefore, the

enhancement of efficiency in TZFT films can be attributed to both increase in  $V_{OC}$  and improved light scattering effect within the film.

### 5-III Conclusions

In Conclusion, ZnO mesostructures (rods, spheres, flakes and flower-like morphologies) are converted to anatase  $TiO_2$  mesostructures by a simple  $TiCl_4$  treatment and this process exhibits a remarkable nominally shape-preserving property. Thus, for the case of ZnO flowers and spheres, anatase  $TiO_2$  flowers and spheres are obtained, respectively, albeit with small changes in morphology details. Interestingly anatase  $TiO_2$  hollow rod like structures are obtained by  $TiCl_4$  treatment of ZnO rods. Post-treatment appearance of Raman peaks at 148.2, 401, 518 and 642  $cm^{-1}$  that are the characteristics of pure anatase  $TiO_2$  phase clearly indicates the complete conversion of ZnO structures to anatase  $TiO_2$ . It is observed that the morphology conversions of ZnO to  $TiO_2$  are due to the ion exchange reaction i.e. between  $Zn^{2+}$  and  $Ti^{4+}$ . These converted  $TiO_2$  mesostructures are used for light harvesting to absorb more photons from sunlight in Dye-sensitized Solar Cells for better conversion efficiency.

### 5-IV Reference

1. S. Ito, T. Kitamura, Y. Wada, S. Yanagida, *Sol. Energy Mater. Sol. Cells*, **2003**, 76, 3.
2. S.S. Kim, J.H. Yum, Y.-E. Sung, *J. Photochem. Photobiol. Chem.*, **2005**, 171, 269.
3. D.P. Hagberg, T. Edvinsson, T. Marinado, G. Boschloo, A. Hagfeldt, L. Sun, *Chem. Commun.*, **2006**, 2245.
4. T. Kawashima, T. Ezure, K. Okada, H. Matsui, K. Goto, N. Tanabe, *J. Photochem. Photobiol., A*, **2004**, 164, 199 .
5. H. Kusama, H. Arakawa, *J. Photochem. Photobiol. A*, 2004, 164, 103.
6. C. J. Barbe, F. Arendse, P. Comte, *J. Am. Ceram. Soc.*, **1997**, 80, 3157.
7. N. G. Park, G. Schlichthörl, J. v. d. Lagemaat, H. M. Cheong, A. Mascarenhas, A. Frank, *J. Phys. Chem. B*, **1999**, 103, 3308.
8. M. K. Nazeeruddin, A. Kay, I. Rodicio, R. Humphry-Baker, E. Müller, P. Liska, N. Vlachopoulos, M. Graetzel, *J. Am. Chem. Soc.*, **1993**, 115, 6382

9. L. Y. Zeng, S. Y. Dai, K. J. Wang, X. Pan, C. W. Shi, L. Guo, *Chin. Phys. Lett.*, **2004**, *21*, 1835.
10. L. Kavan, B. O'Regan, A. Kay, M. Graätzel, *J. Electroanal. Chem.*, **1993**, *346*, 291.
11. D. Menzies, R. Gervini, Y. B. Cheng, G. P. Simon, L. Spiccia, *J. Aust. Ceram. Soc.*, **2003**, *39*, 108.
12. S. Ito, P. Liska, P. Comte, R. L. Charvet, P. Pe'chy, U. Bach, L. Schmidt-Mende, S. M. Zakeeruddin, A. Kay, M. K. Nazeeruddin, M. Graätzel, *Chem. Commun.*, **2005**, 4351.
13. A. Kay, Solar cells based on dye-sensitized nanocrystalline TiO<sub>2</sub> electrodes. Thesis, Ecole Polytechnique Federale de Lausanne, **1994**.
14. H. C. Choi, Y. M. Jung and S. B. Kim, *Vibrational Spectroscopy*, **2005**, *37*, 33.
15. H. Xu, X. Tao, D.-T. Wang, Y.-Z. Zheng, J.-F. Chen, *Electrochim. Acta*, **2010**, *55*, 2280.
16. M. Gratzel, *Inorg. Chem.*, **2005**, *44*, 6841.
17. E. M. Kaidashev, M. Lorenz, H. Wenckstern, A. Rahm, H.C. Semmelhack, K.H. Han, G. Benndorf, C. Bundesmann, H. Hochmuth, M. Grundmann, *Appl. Phys. Lett.*, **2003**, *82*, 3901.
18. K. Keis, E. Magnusson, H. Lindström, S.E. Lindquist, A. Hagfeldt, *Sol. Energy Mater. Sol. Cells*, **2002**, *73*, 51.
19. M. Law, L.E. Greene, J.C. Johnson, R. Saykally, P. Yang, *Nat. Mater.* **2005**, *4*, 455.
20. K. S. Kim, Y.S. Kang, J. H. Lee, Y.J. Shin, N.G. Park, K.S. Ryu, S.H. Chang, *Bull. Korean Chem. Soc.*, **2006**, *27*, 295.
21. P.A. Du, H.H. Chen, Y. C. Lu, *Appl. Phys. Lett.* **89** (2006) 253513.
22. K. Keis, J. Lindgren, S.E. Lindquist, A. Hagfeldt, *Langmuir*, **2000**, *16*, 4688.
23. E. Hosono, S. Fujihara, I. Honma, H.S. Zhou, *Adv. Mater.* **2005**, *17*, 2091.
24. Q. Zhang, C. S. Dandeneau, X. Zhou, G. Cao, *Adv. Mater.* **2009**, *21*, 4087.
25. H. Rensmo, K. Keis, H. Lindstrom, S. Sodergren, A. Solbrand, A. Hagfeldt, S. E. Lindquist, L. Wang, M. Muhammed, *J. Phys. Chem. B*, **1997**, *101*, 2598.
26. M. Guo, P. Diao, X. Wang, S. Cai, *J. Solid State Chem.*, **2005**, *178*, 3210.

27. Y. Gao, M. Nagai, T.-C. Chang, J.-J. Shyue, *Cryst. Growth Des.*, **2007**, *7*, 2467.
28. M. Guo, P. Diao, S. Cai, *Chin. Chem. Lett.*, **2004**, *15*, 1113.
29. Z. Yang, T. Xu, Y. Ito, U. Welp, W. K. Kwok, *J. Phys. Chem. C*, **2009**, *113*, 20521.
30. K. Wang, J. Chen, W. Zhou, Y. Zhang, Y. Yan, J. Pern, A. Mascarenhas, *Adv. Mater.* **2008**, *20*, 3248.
31. T. W. Hamann, A. B. F. Martinson, J. W. Elam, M. J. Pellin, J. T. Hupp, *Adv. Mater.* **2008**, *20*, 1560.
32. Y.-Z. Zheng, X. Tao, L.-X. Wang, H. Xu, Q. Hou, W.-L. Zhou, J.-F. Chen, *Chem. Mater.*, **2010**, *22*, 928.
33. Zhang, Q.; Chou, T. P.; Russo, B.; Jenekhe, S. A.; Cao, G. *Adv. Funct. Mater.* **2008**, *18*, 1654.
34. T. P. Chou, Q. Zhang, G. E. Fryxell, G. Cao, *Adv. Mater.* **2007**, *19*, 2588.
35. (a) X. Chen and S. S. Mao, *Chem. Rev.* **2007**, *107*, 2891. (b) G. Pfaff and P. Reynders, *Chem. Rev.* **1999**, *99*, 1963. (c) A. Hagfeldt and M. Grätzel, *Chem. Rev.* **1995**, *95*, 49. (d) R. Zallen and M. P. Moret, *Solid State Commun.* **2006**, *137*, 154. (e) A. Fujishima and K. Honda, *Nature* **1972**, *238*, 37. (f) A. L. Linsebigler, G. Lu and J.T. Yates, Jr. *Chem. Rev.* **1995**, *95*, 735. (g) X. Wang, J. Zhuang, Q. Peng and Y.D. Li, *Nature* **2005**, *437*, 121.
36. (a) T. Sugimoto and X. Zhou, *J. Colloid Interface Sci.* **2002**, *252*, 347. (b) T. Sugimoto, X. Zhou and A. Muramatsu, *J. Colloid Interface Sci.* **2002**, *252*, 339. (c) T. Sugimoto, X. Zhou and A. Muramatsu, *J. Colloid Interface Sci.* **2003**, *259*, 53.
37. (a) X. Feng, J. Zhai and L. Jiang, *Angew. Chem. Int. Ed.* **2005**, *44*, 5115. (b) S. Yang and L. Gao, *Chem. Lett.* **2005**, *34*, 972. (c) S. Yang and L. Gao, *Chem. Lett.* **2005**, *34*, 1044. (d) S. Yang and L. Gao, *Chem. Lett.* **2005**, *34*, 964. (e) A. R. Armstrong, G. Armstrong, J. Canales, R. Garcí'a and P. G. Bruce, *Adv. Mater.* **2005**, *7*, 862.
38. (a) A. R. Armstrong, G. Armstrong, J. Canales, R. Garcí'a and P.G. Bruce, *Angew. Chem., Int. Ed.* **2004**, *43*, 2286. (b) J. N. Nian and H. S. Teng, *J. Phys.*

- Chem. B* **2006**, *110*, 4193. (c) M. Wei, Y. Konishi, H. Zhou, H. Sugihara and H. Arakawa, *Chem. Phys. Lett.* **2004**, *400*, 231.
39. (a) D. V. Bavykin, A. A. Lapkin, P. K. Plucinski, J. M. Friedrich and F. C. Walsh, *J. Phys. Chem. B* **2005**, *109*, 19422. (b) G. Gundiah, S. Mukhopadhyay, U. G. Tumkurkar, A. Govindaraj, U. Maitra and C. N. R. Rao, *J. Mater. Chem.* **2003**, *13*, 2118. (c) Y. Lan, X. Gao, H. Zhu, Z. Zheng, T. Yan, F. Wu, S. P. Ringer and D. Song, *Adv. Funct. Mater.* **2005**, *15*, 1310. (d) D. V. Bavykin, J. M. Friedrich and F. C. Walsh, *Adv. Mater.* **2006**, *18*, 2807.
40. K. Saravanan, K. Ananthanarayanan and P. Balaya, *Energy Environ. Sci.*, **2010**, *3*, 939.
41. J.-H. Huang, H.-Y. Wei, K.-C. Huang, C.-L. Chen, R.-R. Wang, F.-C. Chen, K.-C. Ho and C.-W. Chu, *Energy Environ. Sci.*, **2010**, *3*, 654.
42. T. L. Sounart, J. Liu, J. A. Voigt, Julia W. P. Hsu, E. D. Spoeerke, Z. Tian and Y. Jiang, *Adv. Funct. Mater.*, **2006**, *16*, 335.
43. S. Cho, S.-H. Jung and Kun-Hong Lee, *J. Phys. Chem. C*, **2008**, *112*, 12769.
44. Q. Zhang, C. S. Dandeneau, X. Zhou and G. Cao, *Adv. Mater.*, **2009**, *21*, 4087.
45. T. L. Sounart, J. Liu, J. A. Voigt, M. Huo, E. D. Spoeerke and B. McKenzie, *J. Am. Chem. Soc.* **2007**, *129*, 15786.
46. F. Xu and L. Sun, *Energy Environ. Sci.*, **2011**, *4*, 818.
47. H.-M. Cheng and W.-F. Hsieh, *Energy Environ. Sci.*, **2010**, *3*, 442.
48. D. H. Son, S. M. Hughes, Y. Yin and A. P. Alivisatos, *Science* **2004**, *306*, 1009.
49. T. Mokari, A. Aharoni, I. Popov and U. Banin, *Angew. Chem., Int. Ed.*, **2006**, *45*, 8001.
50. Y. Yin, R. M. Rioux, C. K. Erdonmez, S. Hughes, G. A. Somorjai and A. P. Alivisatos, *Science*, **2004**, *304*, 711.
51. P. H. C. Camargo, Y. H. Lee, U. Jeong, Z. Zou and Y. Xia, *Langmuir*, **2007**, *23*, 2985.
52. U. Jeong, J.-U. Kim, Y. Xia and Z.-Y. Li, *Nano Lett.*, **2005**, *5*, 937.
53. L. Dloczik and R. Koenenkamp, *Nano Lett.*, **2003**, *3*, 651.

54. R. E. Schaak, A. K. Sra, B. M. Leonard, R. E. Cable, J. C. Bauer, Y.-F. Han, J. Means, W. Teizer, Y. Vasquez and E. S. Funck, *J. Am. Chem. Soc.*, **2005**, *127*, 3506.
55. R. D. Robinson, B. Sadtler, D. O. Demchenko, C. K. Erdonmez, L.-W. Wang and A. P. Alivisatos, *Science*, **2007**, *317*, 355.
56. P. K. Jain, L. Amirav, S. Aloni and A. P. Alivisatos, *J. Am. Chem. Soc.*, **2010**, *132*, 9997.
57. S. E. Wark, C. H. Hsia and D. H. Son, *J. Am. Chem. Soc.*, **2008**, *130*, 9550.
58. Q. Yao, I. U. Arachchige and S. L. Brock, *J. Am. Chem. Soc.*, **2009**, *131*, 2800.
59. P. M. Sommeling, B. C. O'Regan, R. R. Haswell, H. J. P. Smit, N. J. Bakker, J. J. T. Smits, J. M. Kroon and J. A. M. van Roosmalen, *J. Phys. Chem. B*, **2006**, *110*, 19191.
60. B. C. O'Regan, J. R. Durrant, P. M. Sommeling and N. J. Bakker, *J. Phys. Chem. C*, **2007**, *111*, 14001.
61. M. Law, L. E. Greene, A. Radenovic, T. Kuykendall, J. Liphardt and P. Yang, *J. Phys. Chem. B* **2006**, *110*, 22652.
62. P. Atienzar, T. Ishwara, B. N. Illy, M. P. Ryan, B. C. O'Regan, J. R. Durrant, and J. Nelson, *J. Phys. Chem. Lett.* **2010**, *1*, 708.
63. N. Sakai, N. Kawashima and T. N. Murakami, *Chem. Lett.* **2011**, *40*, 162.
64. <http://chemistrytable.webs.com/enthalpyentropyandgibbs.htm>
65. Z. Li, Y. Xiong and Y. Xie, *Inorganic Chemistry*, **2003**, *42*, 8105.
66. J. Park, H. Zheng, Y.-W. Jun and A. P. Alivisatos, *J. Am. Chem. Soc.*, **2009**, *131*, 13943.
67. H.-J. Koo, Y. J. Kim, Y. H. Lee, W. I. Lee, K. Kim and N.-G. Park, *Adv. Mater.*, **2008**, *20*, 195.
68. Q. Zhang, T. P. Chou, B. Russo, S. A. Jenekhe and G. Cao, *Angew. Chem. Int. Ed.*, **2008**, *47*, 2402.
69. Y. -Z. Zheng, X. Tao, L.-X. Wang, H. Xu, Q. Hou, W.-L. Zhou and J.-F. Chen, *Chem. Mater*, **2010**, *22*, 928.
70. M. K. Nazeeruddin, A. Kay, I. Rodicio, R. Humpbry-Baker, E. Miiller, P. Liska, N. Vlachopoulos and M. Gratzel *J. Am. Chem. Soc.* **1993**, *115*, 6382.

## **Chapter-6**

### **Conclusions and Future Scope**

*This chapter contains a summary and concluding remarks for the work described in this thesis and then lays out the future scope pertaining to this work.*

## 6.1 Summary of the thesis

The technological and scientific potentials of high aspect ratio nano and meso-structures of semiconducting oxides are immense and the future of such materials is certainly bright as revealed in the present study on TiO<sub>2</sub> and ZnO. Moreover, the ultimate use of these nanostructures is strongly dependent upon the ability to precisely control their dimension, composition, surface property, phase purity and crystal structure. Related promising developments and daunting challenges are also brought out to stretch the applications of these fascinating nanomaterials in view of the nature of the emerging fundamental and technological interests of physicists, chemists and engineers. Finally, some of the future prospects and precautions for processing nanostructured materials are also explained within the broad perspective.

During the course of research work, we have investigated various methods for the synthesis of functionalized nanomaterials and their applications for dye sensitized solar cells.

The salient features of the results are as follows:

1. TiO<sub>2</sub> nanoparticles loaded with Au nanoparticles are hydrothermally *in situ* synthesized and are shown to render considerably higher solar energy conversion efficiency than the unloaded TiO<sub>2</sub> nanoparticles without light harvesting. The transport improvement is revealed by electrochemical impedance spectroscopy which brings out that the charge transfer resistance including recombination of electrons with I<sub>3</sub><sup>-</sup> at the TiO<sub>2</sub> / electrolyte interface is lower for TiO<sub>2</sub>-Au as compared to unloaded TiO<sub>2</sub> nanoparticles.
2. A simple laboratory protocol is developed for the synthesis of TiO<sub>2</sub>-MWCNT and TiO<sub>2</sub>-Graphene nanocomposites by hydrothermal route. Several characterizations have been employed to reveal the nature of the modification imparted to the MWCNTs and Graphene under hydrothermal processing conditions. It is observed that these nanocomposites show higher conversion

efficiency in dye-sensitized solar cells as compared to hydrothermally synthesized TiO<sub>2</sub> without MWCNT or Graphene.

3. Synthesis of various ZnO mesostructures (rods, spheres, flakes and flower-like morphologies) is achieved by hydrothermal and co-precipitation methods and their remarkable and complete transformation into anatase TiO<sub>2</sub> mesostructures with nominally similar shapes is realized using controlled low temperature TiCl<sub>4</sub> treatment. Various techniques are used to demonstrate the phase purity and morphology details. Based on the careful examination of the transformation of ZnO rods into TiO<sub>2</sub> tubes a mechanism is suggested which embodies initial formation of a thin TiO<sub>2</sub> shell on the ZnO surface by ion exchange (Ti<sup>4+</sup> - Zn<sup>2+</sup>) followed by Zn diffusion through the shell and its oxidation on the surface. These converted TiO<sub>2</sub> mesostructures are used for light harvesting in Dye Sensitized Solar Cells (DSSC) to enhance the conversion efficiency.

## 5.2 Scope for future work

After more than 15 years of intense research, still the physical chemistry of several of the basic operations in the DSSC device remains far from fully understood. For specific model and reference systems and controlled conditions, there is a rather detailed description in terms of energetics and kinetics. It is, however, still not possible to predict accurately how a small change to the system, that is, replacing one component or changing the electrolyte composition, will affect the DSSC performance. With time, the chemical complexity of DSSC has become clear, and the main challenge for future research is to understand and master this complexity in particular at the oxide/dye/electrolyte interface. Thus, for future research, it will be important to carefully select several reference systems that emphasize different key aspects of the device and characterize these systems in-depth with all the different techniques we have at hand.

A challenging but realizable goal for the present DSSC technology is to achieve efficiencies above 15%. Commercialization of large-scale solar cells based on

nanostructure architecture has yet to be realized. With the recent surge in interest of renewable energy we can expect major breakthroughs in developing economically viable solar energy conversion devices in the near future.

Organic dyes offer infinite possibilities for improving a wide range of properties such as molecular structure and function, efficient light-harvesting ability in different parts of the solar spectrum, control over the molecular energy levels, charge generation and separation, and molecule-to-molecule interactions. The major advantage of organic materials for solar cell applications is their low cost of production. They are easy to design with a very high light-absorbing capacity so that thinner films can be used to generate optimal photovoltaic performance. One way to improve efficiencies is by the co-adsorption of dyes with additives and by structural modification with bulky substituents which can prevent  $\pi$ - $\pi$  stacking or dye aggregation. The co-sensitization approach is also very appealing for using multiple dyes to obtain panchromatic absorption, but the fine-tuning seems to be quite difficult.

From the synthetic point of view, however, the geometric and electronic structures of the sensitizer play an important role. When all these factors are taken into account, it should be possible to design more sophisticated and appropriate dye structures that satisfy the needs of DSSC technology. DSSC technology undoubtedly has an exciting future and there are still vast opportunities to ameliorate performance. Therefore, the development of a conceptually new design for constructing metal-free dyes is an important and urgent challenge. However, control of interfacial processes and maximizing light harvesting as well as resolving long-term stability issues will be challenging and will indeed take some time yet.

## List of Publications

1. Vivek Dhas, **Subas Muduli**, Wonjoo Lee, Sung-Hwan Han and Satishchandra Ogale, Enhanced conversion efficiency in dye-sensitized solar cells based on ZnO bifunctional nanoflowers loaded with gold nanoparticles, *Appl. Phys. Lett.* 2008, 93, 243108 (Vivek Dhas and Subas Muduli contributed equally to this work).
2. **Subas Muduli**, Wonjoo Lee, Vivek Dhas, Sarfraj Mujawar, Megha Dubey, K. Vijayamohanan, Sung-Hwan Han, and Satishchandra Ogale, Enhanced Conversion Efficiency in Dye-Sensitized Solar Cells Based on Hydrothermally Synthesized TiO<sub>2</sub>-MWCNT Nanocomposites, *ACS App. Mat. & Interfaces*, 2009, 1, 2030.
3. **Subas Muduli**, Onkar Game, Vivek Dhas, Ashish Yengantiwar, and Satishchandra B. Ogale, Shape Preserving Chemical Transformation of ZnO Mesostructures into Anatase TiO<sub>2</sub> Mesostructures for Optoelectronic Applications, *Energy & Environmental Science*, 2011, DOI: 10.1039/c1ee01515j. (In Press).
4. Vivek Dhas, **Subas Muduli**, Shruti Agarkar, Abhimanyu Rana, Beatrice Hannoyer, Rahul Banerjee and Satishchandra Ogale, Enhanced DSSC performance with high surface area thin Anatase TiO<sub>2</sub> nanoleaves, *Solar Energy*, 2011, 85, 1213.
5. N. S. Chaudhari, S. S. Warule, **S. Muduli**, B. B. Kale, S. Jouen, B. Lefez, B. Hannoyerc and S. B. Ogale, Maghemite (Hematite) Core (Shell) Nanorods via Thermolysis of a molecular Solid of Fe-Complex, *Dalton Transaction*, 2011 (Accepted).

6. **Subas Muduli**, Onkar Game, Vivek Dhas, K. Vijayamohanan, K. A. Bogle, N. Valanoor and Satishchandra B. Ogale, TiO<sub>2</sub>-Au plasmonic nanocomposite for enhanced dye-sensitized solar cell (DSSC) performance (Communicated to *Solar Energy*).

### **Patents**

1. **Subas Muduli**, Vivek Dhas, Sarfraj Mujawar and Satishchandra Ogale, Preparation of titanium dioxide-multi-walled carbon nanotubes used for preparing dye sensitized solar cell, by hydrolyzing titanium compound precursor in water, sonicating, washing with water and drying, *Patent Number(s): WO2010079516-A1; IN200900048-II*.